Highly birefringent photonic crystal fibres: Linear and nonlinear effects

Ortigosa, Blanch Arturo

Award date:
2002

Awarding institution:
University of Bath

HIGHLY BIREFRINGENT PHOTONIC CRYSTAL FIBRES: LINEAR AND NONLINEAR EFFECTS

Submitted by Arturo Ortigosa Blanch
for the degree of
Doctor of Philosophy
of the University of Bath
2002

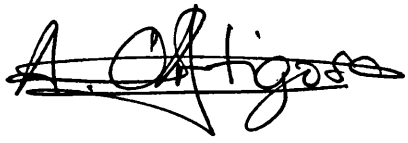

ProQuest LLC
789 East Eisenhower Parkway
P.O. Box 1346
Ann Arbor, MI 48106-1346

ABSTRACT

This thesis describes the fabrication and optical characterisation of a new class of optical fibres: Highly Birefringent photonic crystal fibres. It is shown both theoretically and experimentally that these fibres can have a very high modal birefringence, coupled with an unusual group velocity dispersion (GVD). We present independent studies of these two effects, showing that the new fibres can have a zero dispersion wavelength at visible and near infrared wavelengths, where both bulk silica and conventional fibres exhibit normal dispersion.

We have used these structures, to fabricate rocking filters in non-photosensitive highly birefringent PCF. Very good coupling efficiencies were achieved for very short lengths.

Soliton propagation using 200 fs pulses at a wavelength of 850 nm and soliton self-frequency shift in these structures have been demonstrated experimentally. Detailed experiments have been carried out to study the behavior of ultrashort pulses in photonic crystal fibers in order to elucidate the mechanisms for supercontinuum generation in these structures. When pumping with femtosecond pulses, the experimental evidence shows that, as in conventional fibers, Raman scattering leads to the break-up of higher-order solitons, which is accompanied by the generation of radiation at shorter wavelengths than the pump, leading eventually to an ultrabroad supercontinuum. The mechanism has been tested for different pumps at both sides of the zero dispersion wavelength.

Esta tesis está dedicada a Amparo, a mis padres y a Reyes por haberme aguantado y apoyado durante estos años en el exilio y a mis amigos por haber estado ahí durante todo este tiempo.

.....

There are a lot of people I should thank for their help and support during my PhD. First of all, I would like to thank my supervisor, Jonathan Knight, for his support, supervision, and the interest he has shown in me and my work during all these years.

Thanks must also go to Brian Mangan (our fabrication guru) for sharing his time, knowledge, friendship and software with me. To William Wadsworth for all the time he has spent with me in the laboratory. To John Pottage, Fetah Benabid and Γρηγορης Αντωνοπουλος for the endless discussions over coffee. To Alan George for his help and for 'lending a hand'.

To Γωργος Κακαραντζας and Antonio Díez for making my PhD 'dramatic' and for all the time we spent together inside and outside the lab.

To my friends Will Reeves, David Lawton and Jim Gregory for all the time they've spent improving my English, proof-reading this thesis and making me a *connoisseur* of English culture. I'd specially like to thank Will for his valuable help during these years on various aspects of fabrication, modelling and book keeping.

Thanks must go to Geraud Bouwmans and Caroline Malbaux (the fantastic French connection) for all the time spent doing experiments with me but mainly for being themselves.

Finally I would like to acknowledge and thank Philip Russell for his supervision and for giving me the opportunity to work in the Optoelectronics Group at Bath.

Contents

List of Figures

List of Tables

Chapter 1

Introduction

1.1 Overview

An optical fibre is a flexible glass waveguide with cylindrical symmetry designed to guide light along its length. It consists of a central region, the core, surrounded by a cladding layer with a refractive index lower than that of the core. The first working examples were made in the 1960's by Kao *et al* and the recent growth in optical telecommunications has led to massive interest in the development of next-generation fibre products.

A photonic crystal fibre (PCF) is a new type of optical fibre. Also known as 'microstructured fibres' or 'holey fibres', PCFs are all-silica optical fibres with an array of air holes running down the length of the entire fibre. First proposed in the early 90's, the first working example was reported by Knight *et al.* in 1996. Depending on the arrangement of the air hole array, the fibres can show very different guiding mechanisms: modified total internal reflection or band-gap guidance. The air hole pattern will determine as well the fibre characteristics: endlessly single mode operation for all wavelengths and single mode large mode area fibres are examples of some of the structures achieved in the past in these fibres.

This thesis presents the fabrication, characterisation and some of the applications for linear and nonlinear optics of a new family of PCFs: *Highly Birefringent*

Photonic Crystal Fibres. Chapters Two, Three and Four review previous work in this and related fields, while Chapters Five, Six, Seven and Eight present the new work done during the course of this thesis.

Highly birefringent PCFs are a new family of polarisation preserving PCFs where purposely birefringence is introduced in the structure by means of an elliptical core. The levels of birefringence achieved in these structures is much higher than those available in conventional polarisation preserving fibres. Very efficient polarisation rocking filters have been fabricated. Their linear characteristics allow the fabrication of fibres with zero dispersion wavelengths in the near infrared making them the perfect vehicle for studying nonlinear propagation of optical pulses in PCF: soliton generation and transmission can be studied in the near infrared and new physical phenomena, such as supercontinuum generation, can be studied without taking into account unwanted polarisation effects.

Chapter Two is a review of some of the basic concepts in conventional optical fibre technology. The fabrication process and the main characteristics of optical fibres will be explained. Chapter Three is dedicated to an specific field of fibre optics: Nonlinear optics in fibre optics. The fundamental concepts about soliton generation and soliton propagation will be explained. Chapter Four provides an overview on photonic crystal fibres. The fabrication, guiding mechanisms, and characterisation of these new kind of structures will be explained. The fibres fabricated during the course of this thesis are presented.

Chapter Five concerns the fabrication and characterisation of PCFs with modified dispersion. Several fibres were fabricated with zero dispersion points in the visible and near infrared and their linear characteristics tested.

Chapter Six is devoted to the fabrication and characterisation of highly birefringent PCFs. The concept of breaking the symmetry on PCF, the special fabrication procedure and the different characterisation methods needed will be explained.

Chapters Seven and Eight focus on the nonlinear work. Chapter Seven considers soliton generation and propagation in highly birefringent PCFs. The observation of massive soliton self-frequency shifts will be reported. Chapter Eight is devoted to supercontinuum generation. The mechanisms involved for generating such a

vast spectrum and the characterisation of the spectra for different parameters will be presented.

Chapter Nine will summarise the work and a discussion of future work on the subject will be presented.

Appendix A shows a list of the work published during this Thesis in peer reviewed journals and a list of publications in national and international conferences and meetings.

Chapter 2

Review of optical fibres

2.1 Introduction

Optical fibres are flexible glass waveguides with cylindrical symmetry designed to guide light along their length. The first working examples were made in the 1960's [1], since when the losses have been reduced considerably. New techniques allowed losses to be lowered to 0.2 dB/km in the 1.55 μm wavelength band and with the development of fibre amplifiers, real telecommunication networks could be implemented. Optical fibres are ideal for signal transmission as the main manufacturing material is glass which is inexpensive, abundant, enables ultra low losses and is non-conductive. That means that optical fibres are immune to most forms of external electromagnetic interference and can be used in potentially dangerous environments where the use of electrical signals could be dangerous. The growth in optical telecommunication has led to massive interest in the development of next-generation fibre products.

This Chapter provides a review of the main aspects of fibre-optic technology and performance. The fabrication method for conventional fibres, as well as the main parameters used to characterise different types of optical fibres, will be explained. Finally, the polarisation properties of optical fibres will be reviewed.

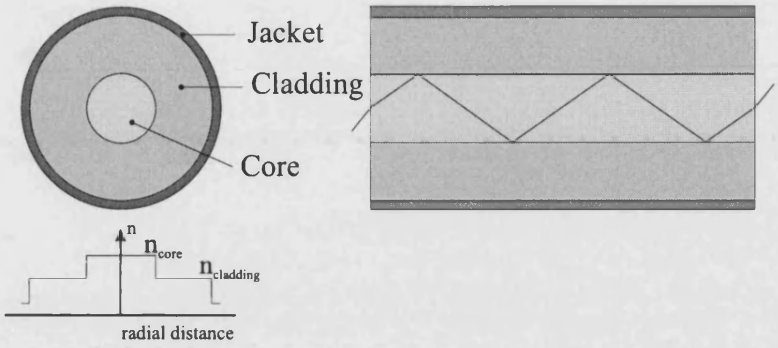

Figure 2.1: Schematic cross section, index profile and TIR mechanism of a conventional step-index optical fibre

2.2 Guidance mechanism

An optical fibre is a flexible glass waveguide with cylindrical symmetry designed to guide light along its length. It consists of a central region, the core, surrounded by a cladding layer with a refractive index lower than that of the core. When light is launched into the fibre through an end-face, it will be trapped in the waveguiding core and guided through the fibre to emerge from the other end. Guidance is achieved by total internal reflection. A ray of light will be totally internally reflected at the boundary between two dielectric media when the ray is incident from within the media with a higher refractive index (n), and the angle of incidence is greater than a critical value defined by Snell's Law as

$$\theta_c = \sin^{-1}\left(\frac{n_{cladding}}{n_{core}}\right) \tag{2.1}$$

A typical profile of a conventional optical fibre and a schematic of Total Internal Reflection (TIR) are shown in Figure 2.1. Note the index difference between the core and the cladding.

2.3 Fabrication

The material used in low-loss optical fibres is pure silica glass synthesised by fusing SiO_2 molecules. The refractive index difference between the cladding and the core regions is realised using dopants during the fabrication process. Dopants

such us GeO_2 and P_2O_5 increase the refractive index of pure silica and are suitable for the core, while materials such as boron and fluorine can be used for the cladding because they decrease its refractive index.

The fabrication of conventional optical fibres involves two stages. In the first stage, a vapor-deposition method is used to make a cylindrical preform with the desired refractive index profile and the relative core-cladding dimensions. There are several methods that can be used. The modified chemical vapour deposition (MCVD) method [2], developed at Bell Labs, is the most widely used method to fabricate optical fibre preforms. A silica tube is heated externally with a travelling flame whilst a high purity gas mixture is injected into the rotating silica tube. In the hot zone (created by the travelling torch) a gas phase reaction occurs and amorphous particles are created and deposited downstream of the hot zone. Once all the layers of dopant have been deposited, the temperature is raised and the tube is collapsed into a solid rod known as the preform.

In the second stage, the preform is drawn into fibre using a precision mechanism that feeds and then pulls the heated preform at a given speed. The preform is mounted in a precision feeding mechanism known as the preform feed which lowers it into a cylindrical furnace. After the furnace, in which the preform is heated above its softening point, the silica is pulled. A capstan (consisting in a set of wheels and springs for controlling the speed and tension of the fibre) and a drum pull and wind the fibre. It is at this stage that the final diameter of the fibre is decided (generally 125 μm). The relative core-cladding dimensions are preserved during this stage.

2.4 Characterisation of optical fibres

There are several important parameters that characterise an optical fibre. It is useful to know the core and cladding materials, its numerical aperture, how the fibre will behave for a wide range of wavelengths simultaneously, what are the losses, etc. In the next few paragraphs several important fibre parameters are described in detail [3, 4].

2.4.1 Single-mode operation

In Section 2.2 it has been explained how the guiding mechanism of an optical fibre can be explained in simple terms with the help of Snell's law. When considering electromagnetic waves, the guiding problem can be approached by considering a dielectric material (the core) surrounded by an infinite cladding layer of another dielectric material with a lower refractive index. Only solutions of the Maxwell equations that satisfy boundary conditions will propagate along the fibre. These permitted solutions of the Maxwell equations are known as the modes of the fibre. Each mode can only propagate providing that its propagation constant falls within a permitted range. When a mode can no longer propagate, it is described as cut off. All modes have a cutoff except the lowest order mode, which is called the fundamental mode.

When calculating mode cut-offs for various classes of waveguides, it is convenient to refer to the V parameter or 'normalised frequency' defined as

$$V = \frac{2\pi r}{\lambda_0}\sqrt{n_{core}^2 - n_{cladding}^2} \tag{2.2}$$

where r is the radius of the core and λ_0 is the free-space wavelength of the light source. A conventional step-index fibre will be single mode for $V < 2.405$, which is a value give by the first zero of the J_0 Bessel function. [4]

2.4.2 Numerical Aperture (NA)

Numerical aperture is an expression of the extent of the fibre's ability to accept, in its bound modes, non-normal incident rays (American National Standard T1.523-2001).

There are several factors that affect the numerical aperture of a fibre such as the physical size of the core and the refractive index profile. When working with multimode fibres a ray tracing approach can be used and, referring to Snell's law for the critical angle (see Equation 2.1), a definition based on the index difference in between core and cladding is obtained:

$$NA = \sqrt{n_{core}^2 - n_{cladding}^2} \tag{2.3}$$

When studying single mode fibres, the NA can be considered as a problem analogous to the diffraction pattern from an aperture. Then, depending on the index difference, the core radius (which would be the analog of the dimensions of the aperture in the difractional problem) and the wavelength, the dimensions of the beam will change. Therefore, the NA of single mode fibres can be understood as the divergence of the beam.

2.4.3 Effective Area

The effective area is a very important parameter when studying non-linear effects, as they are intensity dependent processes. However, it is the total optical power entering and leaving the fibre that is usually measured. Some method is required for converting between the two when comparing theoretical and experimental results. The measured optical power leaving a fibre is simply the integral of the intensity distribution over the entire fibre cross section. For a uniform intensity distribution, I, over a core of area A_{core}, the intensity could be calculated from the measured power, P_{meas} , using:

$$I = \frac{P_{meas}}{A_{core}} \tag{2.4}$$

However, the field in a single mode fibre is not evenly distributed or even fully contained within the core. It is mostly in the vicinity of the fibre axis than near the core-cladding interface and extends into the cladding to a degree depending on the actual refractive index profile. Calculating a uniform intensity in the core using Equation 2.4 would underestimate the value on the axis of the fibre and overestimate the value near the core-cladding interface.

The effective core area is a normalised profile area equivalent to the fibre mode. It is defined in terms of the electric field distribution F(x,y) and gives information about the intensity profile of the electric field in the fibre and about the dimensions of the mode in the core and the cladding in the x - y plane, i.e., in a plane perpendicular to the direction of propagation of light in the fibre. It is a single value that can be used in Equation 2.4 instead of A_{core} to calculate a value for the optical intensity. The effective area is defined as

$$A_{eff} = \frac{[\int\int |F(x,y)|^2 dxdy]^2}{\int\int |F(x,y)|^4 dxdy} \tag{2.5}$$

where F(x,y) is the amplitude and $|F(x,y)|^2$ is the intensity of the near-field of the fundamental mode.

2.4.4 Losses

There are two main loss mechanisms in optical fibres: absorption and radiation. The absorption losses are due to the interaction of the light with the material when propagating in the glass. The infra red absorption bands in silica and OH^- ions in the glass are the main effects. Radiation losses are due to light in the guided mode coupling to the cladding (usually as a result of micro and macro bending or discontinuities in the fibre structure). The biggest loss contribution comes from Rayleigh scattering. This is caused by small (compared to the wavelength of light) defects in the structure, such as irregularities arising during the fabrication process, and from the dopants used in modifying the refractive index of the glass. When working in the telecommunication window (around $1.55\mu m$), the loss due to Rayleigh scattering in silica is 0.18 dB/km and therefore ,nowadays, represents the total loss of conventional optical fibre at that wavelength together with the OH^- bands.

There is a third type of loss, confinement loss, which is mainly due to the inability of the core to confine the guided mode down the fibre. Confinement losses arise from a low index step between core and cladding or from irregularities in the core and cladding regions, but mainly for the fact of not having an infinite cladding, allowing some of the energy to leave the system. The main effect of confinement loss is the progressive leakage of the guided mode as it propagates along the fibre length.

2.4.5 Group velocity dispersion

Group velocity dispersion is a process by which an optical signal propagating in a fibre is degraded because the various frequencies of the signal have different propagation velocities within the medium. Fibre dispersion plays a critical role in propagation of short optical pulses since different spectral components associated with the pulse travel at different speeds given by the phase velocity $c/n(\omega)$.

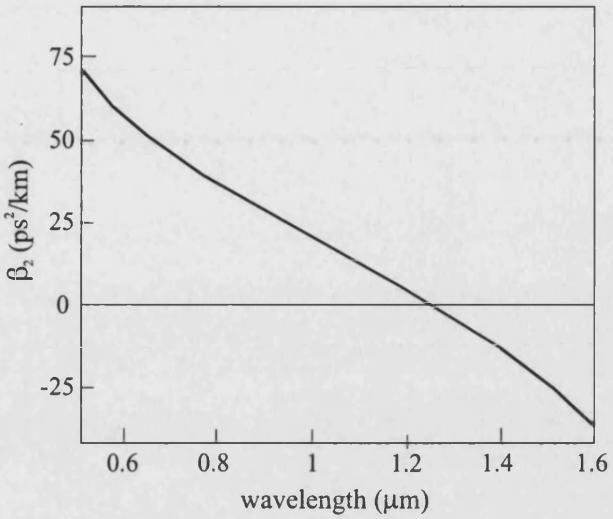

Figure 2.2: Variation of β_2 with wavelength for fused silica

Mathematically, the effects of fibre dispersion are accounted for by expanding the mode propagation constant β in a Taylor series about the centre frequency ω_0

$$\beta(\omega) = n(\omega)\frac{\omega}{c} = \beta_o + \beta_1(\omega - \omega_0) + \frac{1}{2}\beta_2(\omega - \omega_0)^2 + ... \tag{2.6}$$

where

$$\beta_1 = \frac{1}{c}\left[n + \omega\frac{dn}{d\omega}\right] = \frac{n_g}{c} = \frac{1}{v_g} \tag{2.7}$$

accounts for the pulse envelope moving at the group velocity v_g, and

$$\beta_2 = \frac{1}{c}\left[2\frac{dn}{d\omega} + \omega\frac{d^2n}{d\omega^2}\right] = \frac{\omega}{c}\frac{d^2n}{d\omega^2} \approx \frac{\lambda^3}{2\pi c^2}\frac{d^2n}{d\lambda^2} \tag{2.8}$$

which is responsible for the pulse broadening. A typical plot of β_2 for fused silica is shown in Figure 2.2. The value for β_2 can vanish at a certain wavelength and become negative for longer wavelengths. The wavelength at which $\beta_2 = 0$ is referred as the zero dispersion wavelength λ_D. In the normal dispersion regime ($\beta_2 > 0$), the higher frequency (blue) components of an optical pulse travel slower than the lower frequency (red) components. By contrast, the opposite occurs in the so-called anomalous dispersion regime($\beta_2 < 0$). The anomalous dispersion regime is of considerable interest for the study of nonlinear effects because it is in this regime that silica optical fibres can support solitons through a balance between the dispersive and nonlinear effects. The value of λ_D in a fibre will depend on fibre-design parameters such as the core radius and the core cladding

index difference[3].

2.5 Polarisation properties of optical fibres

The fundamental mode of a circularly symmetric fibre (the HE_{11}) consists on a pair of degenerate modes which are identical. When the core of the fibre becomes elliptical or when the refractive index across the core is not symmetrical, the HE_{11} mode splits into two fundamental modes. These modes are called the odd HE_{11}, designated ${}_oHE_{11}$, and the even ${}_eHE_{11}$. In common with the circular HE_{11}, both modes have no cutoff and have transverse electric fields. When the fibre has an elliptical core, the ${}_oHE_{11}$ has the electric field along the major axis and the ${}_eHE_{11}$ has it along the minor axis of the ellipse [5].

Because of the symmetry present in conventional circularly symmetric optical fibres, they do not maintain the polarization state of the guided mode along their length. Although they are nominally isotropic, small twists, bends and other stresses impose unknown and uncontrolled birefringence on the fibre, so that the polarization of the fibre output is unpredictable. Highly birefringent fibres (Hi-Bi fibres), in which strong birefringence is deliberately introduced during the fibre fabrication, are much more resilient to such environmental factors.

The polarization beat length, L_B, is a measure of the birefringence. The beat length is defined as the length in which the light experiences a 2π differential phase shift inside the fibre, i.e., the length in which, for example, linearly polarised light will return to its original state. It is defined as

$$L_B = \frac{2\pi}{\beta_x - \beta_y} = \frac{\lambda}{n_x - n_y} \tag{2.9}$$

where β_x and β_y are the propagation constants of the two modes and n_x and n_y are the refractive index that each mode sees, with shorter L_B corresponding to stronger birefringence. The importance of achieving a short beat length L_B is that perturbations affecting the fibre on a length scale longer than L_B will not disturb the propagation of light down the fibre. Therefore, when light is guided in a polarisation maintaining fibre, any bend with a radius greater that the beat length will not affect the polarisation state of the light inside the fibre.

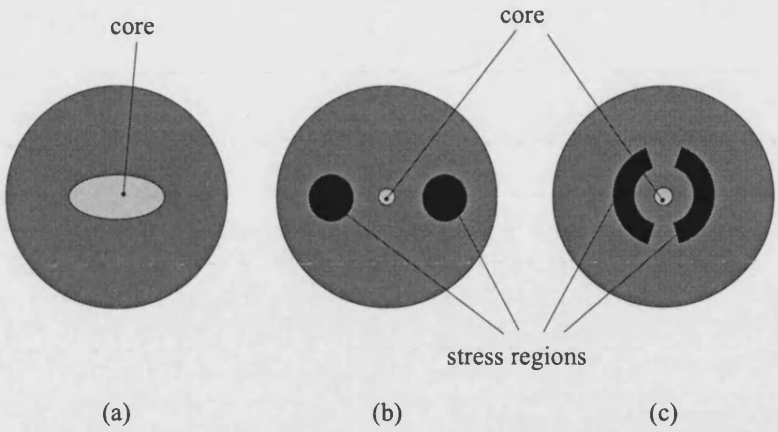

Figure 2.3: Schematic cross sections of different commercially available Hi-Bi fibres: (a) elliptical or form birefringent fibre, (b) Panda fibre and (c) Bow-Tie fibre.

The required birefringence can be achieved in two main ways. The shape of the refractive index profile defining the waveguide can be made non-circular (known as form or shape birefringence) or the material forming the fibre can itself be made birefringent, typically by introducing stresses as in Bow-Tie or Panda fibres [5, 6, 7]. Figure 2.3 shows schematic cross sections of different commercially available Hi-Bi fibres. In the form or shape birefringent case, i.e., the elliptical core fibre (a), the magnitude of the birefringence depends on the geometry of the core and the core-cladding index difference [8]. For Panda and Bow-Tie fibres the birefringence relies on the stress imposed on the structure as well as on the core-cladding index difference. These kinds of fibres are usually designed using two rods of borosilicate glass inserted on opposite sides of the fibre core at the preform stage. The modal birefringence will then depend on the location and thickness of the stress-applying elements.

When not using polarisation maintaining fibres in telecommunication systems, the unpredictability of the polarisation state using Low Birefringent fibres (Low-Bi fibres) or circularly symmetric fibres (which have a random birefringence) presents a problem. The odd and even HE_{11} modes, being two different modes, have different dispersion characteristics. Then, for a given wavelength, light can randomly couple to either of the two modes with different group velocities. This effect is referred to as polarisation mode dispersion (PMD).

For linearly polarised CW light propagating down the fibre, the randomly varying

birefringence will change the polarisation state of the light to elliptical and it will change randomly along the fibre. Most of the detection system used in telecommunications are polarisation insensitive, so the arbitrary polarisation state of the light leaving the fibre is not an issue

A problem arises when pulses propagate down the fibre. Random changes in the birefringence will induce pulse broadening as the polarisation state can be different for different parts of the pulse.

Chapter 3

Nonlinear optics in optical fibres

3.1 Introduction

This chapter is intended to be an introductory chapter to some of the main concepts in nonlinear fibre optics. Nonlinear effects resulting from the intensity dependence of the refractive index in silica will be presented. The chapter will focuss on the main nonlinear effects described in this thesis: parametric processes and soliton formation and propagation and stimulated Raman scattering. The explanation of the effects given here is based on 'Nonlinear fiber optics' by G.P. Agrawal.

Nonlinear effects resulting from the intensity dependence of the refractive index have their origin in the anharmonic motion of the electrons when an electric field E is applied. The polarisation P induced in the medium by the electric dipoles is not linear with E and satisfies the relationship

$$P = \varepsilon_0 \left(\chi^{(1)} E + \chi^{(2)} : EE + \chi^{(3)} \vdots EEE + ... \right) \tag{3.1}$$

where ε_0 is the vacuum permittivity and $\chi^{(i)} (i = 1,2,...)$ is the ith order susceptibility.

The linear susceptibility $\chi^{(1)}$ represents the dominant contribution to P. The second order susceptibility $\chi^{(2)}$ is responsible for second harmonic generation and

sum-frequency generation. $\chi^{(2)}$ vanishes for centrosymmetric media (as silica) and therefore $\chi^{(3)}$ is responsible for the lowest order nonlinear effects that can take place in optical fibres. Some important nonlinear effects in optical fibres include stimulated inelastic effects such as stimulated Raman scattering (SRS) and stimulated Brillouin scattering (SBS), and parametric processes. Third order parametric processes (they are called parametric as the optical fibre plays a passive role except for mediating the interaction) involve the nonlinear interaction among four optical waves and include phenomena such as Four Wave Mixing (FWM) and Third Harmonic Generation.

3.2 Stimulated scattering processes

Scattering processes (known as active processes because of the role played by the medium imposing the new generated frequencies) can be divided in two main types: Raman scattering and Brillouin scattering.

Raman scattering is an spontaneous effect on which a small fraction of the power of an optical field is transferred to (via optical phonons) another field whose frequency is downshifted by an amount determined by the vibrational modes of the medium. The photons can be scattered as well with higher frequencies. When the scattered photon frequency is lower than the pump frequency, this is referred as the Stokes wave, and when the frequency is up-shifted it is referred as anti-Stokes wave. When an intense pump is present, this effect becomes stimulated and an exponential growth of the Stokes band occurs. Then, it is called stimulated Raman scattering.

Brillouin scattering is very similar to Raman scattering. The difference resides on the fact that the energy and momentum transfer takes place via acoustic phonons and not optical phonons as with Raman scattering. Therefore, Brillouin scattering is due to light scattered by acoustic waves.

3.3 Parametric processes

Parametric processes can be understood in terms of the third order nonlinear polarisation $P_{NL} = \varepsilon_0 \chi^{(3)} \vdots EEE$, where E is the electric field and ε_0 is the vacuum permittivity. The total electric field corresponding to four waves of frequencies ω_1, ω_2, ω_3 and ω_4 propagating in the same direction can be written as

$$E = \frac{1}{2}\hat{x}\sum_{j=1}^{4} E_j exp\left[i(k_j z - \omega_j t)\right] + C.C \tag{3.2}$$

where $k_j = n_j\omega_j/c$ and n_j is the refractive index. Therefore, substituting 3.2 in the expression for the nonlinear polarisation yields to,

$$P_{NL} = \frac{1}{2}\hat{x}\sum_{j=1}^{4} P_j exp\left[i(k_j z - \omega_j t)\right] + C.C \tag{3.3}$$

Each one of the P_j terms consists of a large number of terms involving products of three electric fields. Of particular interest are the terms which include the phase mismatch between the fields. The processes governed by these terms will only occur if the phase matching is satisfied, that is matching the frequencies as well as the propagation constants. There are two main types of mismatch terms in P_j:

$$\phi_1 = (k_1 + k_2 + k_3 - k_4)z - (\omega_1 + \omega_2 + \omega_3 - \omega_4)t \tag{3.4}$$

$$\phi_2 = (k_1 + k_2 - k_3 - k_4)z - (\omega_1 + \omega_2 - \omega_3 - \omega_4)t \tag{3.5}$$

The term corresponding to ϕ_1 corresponds to the case in which three photons transfer energy to a single photon of frequency $\omega_4 = \omega_1 + \omega_2 + \omega_3$. This is known as third harmonic generation when $\omega_1 = \omega_2 = \omega_3$, or frequency conversion when $\omega_1 = \omega_2 \neq \omega_3$.

The term corresponding to ϕ_2 corresponds to the case in which two photons at frequencies ω_1 and ω_2 are annihilated with the simultaneous creation of two photons at frequencies ω_3 and ω_4. A common case for optical fibres is when degenerate FWM takes place, that is when $\omega_1 = \omega_2$. If $\omega_1 = \omega_2 = \omega_p$, then the phase matching condition becomes

$$\Delta k = k_3 + k_4 - 2k_p = (n_3\omega_3 + n_4\omega_4 - 2n_p\omega_p)/c = 0 \tag{3.6}$$

This effect manifests when a strong pump with frequency ω_p creates two symmetric frequency sidebands at ω_3 and ω_4 given by

$$\Omega = \omega_p - \omega_3 = \omega_4 - \omega_p \tag{3.7}$$

In analogy with stimulated Raman scattering, the sidebands are called the Stokes and anti-Stokes bands.

3.4 Pulse propagation in optical fibres

Although the value of the third order nonlinear susceptibility is very low for silica, the fact that the propagation distance in optical fibres is several of orders of magnitude bigger than the wavelength and the high nonlinearity makes it very relevant. Of special interest is the case of short intense optical pulses propagating down the fibre.

Let us consider a quasi-monochromatic field $\vec{E}(z,t)$

$$\vec{E}(z,t) = \sum_n \vec{E}_{\omega_n}(z,t)e^{-i\omega_n t} = \sum_n \vec{A}_{\omega_n}(z,t)e^{i(\vec{k}\cdot\vec{r}-\omega_n t)} \tag{3.8}$$

In the limit of small bandwidth (or slowly varying envelope) the formulation of the problem is simplified to a group of differential equations to be solved. The slowly varying envelope approximation (SVEA) can be expressed as

$$\left|\frac{\partial^2 \vec{A}(z,\omega)}{\partial z^2}\right| \ll \left|k\frac{\partial \vec{A}(z,\omega)}{\partial z}\right| \tag{3.9}$$

and means that any variation of the field in z has a much smaller frequency than the high frequency k. As the SVEA can be used, the Fourier transform of the electric field can be expressed in terms of a high frequency ω_n and a low frequency η that gives the small modulation. Using such expression for the Fourier transform of the electric field, separating the polarisation on its linear and nonlinear terms and using the Fourier transform of the linear contribution

of the polarisation, the wave equation can be written as

$$\frac{\partial^2 \vec{E}(z,t)}{\partial z^2} + \frac{1}{c^2}\int_{-\infty}^{\infty} d\eta(\omega_n+\eta)^2 \varepsilon(\omega_n+\eta)\vec{E}(z,\omega_n+\eta)e^{-i(\omega_n+\eta)t} = \mu_0 \partial_t^2 \vec{P}^{NL}(z,t) \tag{3.10}$$

The next step is to make some approximations in order to reduce the expression into a differential equation. The first approximation consists on assuming the frequency dependance of the dielectric tensor $\varepsilon(\omega)$. Once more, applying the SVEA we can do a Taylor expansion of $\varepsilon(\omega)$ (which is considered a scalar quantity as it is an isotropic medium) around ω_n. The second approximation is to make a Taylor expansion of the nonlinear polarisation term. In this case, the main term will be the first term of the expansion for $\chi^{(n)}$, as the SVEA for the temporal frequencies can be used.

Once all the approximations have been made, the final general expression is

$$\left[\frac{\partial}{\partial z} + \left(\frac{dk}{d\omega}\right)_{\omega_\sigma}\frac{\partial}{\partial t}\right]\vec{A}_{\omega_\sigma}(z,t) + \frac{i}{2}\left(\frac{d^2k}{d\omega^2}\right)_{\omega_\sigma}\frac{\partial^2}{\partial t^2}\vec{A}_{\omega_\sigma}(z,t) = \frac{i\omega_\sigma^2\mu_0}{2k_\sigma}\vec{P}^{NL}_{\omega_\sigma}(z,t)e^{-ik_\sigma z} \tag{3.11}$$

Let us assume now that a monochromatic pulse is propagating down a single mode fibre and that the only nonlinear contribution to P^{NL} is $\chi^{(3)}$. In this case, Equation 3.11 can be written as

$$\left[\frac{\partial}{\partial z} + \beta_1\frac{\partial}{\partial t} + \frac{i}{2}\beta_2\frac{\partial^2}{\partial t^2}\right]A = i\gamma|A|^2A \tag{3.12}$$

where β_1 and β_2 are the first and second derivative of k with respect to ω and

$$\gamma = \frac{\omega n_2}{A_{eff}c} = \frac{3\omega\chi^{(3)}(-\omega;\omega,-\omega,\omega)}{2cnA_{eff}} \tag{3.13}$$

If a change in the coordinate system is made and the equation is rewritten using a reference system on the pulse travelling with velocity v_g ($\tau = t - \beta_1 z$, $\zeta = z$), Equation 3.12 becomes

$$\left[\frac{\partial}{\partial \zeta} + \frac{i}{2}\beta_2\frac{\partial^2}{\partial \tau^2}\right]U = i\gamma|U|^2U \tag{3.14}$$

which is known as the Non Linear Schrödinger Equation (NLSE). Looking at the NLSE we can see that the propagation of optical pulses will be affected by two effects: (i) The chromatic dispersion of the group velocity (GVD) that will appear due to β_2 and (ii) the Self-Phase Modulation (SPM) due to the nonlinearity (γ

parameter).

3.4.1 Effect of the Group Velocity Dispersion (GVD)

The GVD is a purely lineal phenomenon which leads to a progressive broadening of the pulse as it propagates. Let us make $\gamma = 0$ in Equation 3.14. Then

$$\frac{\partial}{\partial \zeta} U = -\frac{i}{2}\beta_2 \frac{\partial^2}{\partial \tau^2} U \tag{3.15}$$

To solve this equation we can introduce the Fourier transform of $U(\zeta, \tau)$

$$U(\zeta, \tau) = \frac{1}{2\pi} \int_{-\infty}^{\infty} d\omega \tilde{U}(\zeta, \omega) e^{-i\omega\tau} \tag{3.16}$$

therefore,

$$\frac{\partial}{\partial \zeta} \tilde{U} = \frac{i}{2}\beta_2 \omega^2 \tilde{U} \tag{3.17}$$

for which the solution is

$$\tilde{U}(\zeta, \omega) = \tilde{U}(0, \omega) exp\left(\frac{i}{2}\beta_2 \omega^2 \zeta\right) \tag{3.18}$$

and then the solution for $U(\zeta, \tau)$ is

$$U(\zeta, \tau) = \frac{1}{2\pi} \int_{-\infty}^{\infty} d\omega \tilde{U}(0, \omega) e^{\left(\frac{i}{2}\beta_2 \omega^2 \zeta - i\omega\tau\right)} \tag{3.19}$$

In order to extract some of the physical meaning of this solution, let us study the case when a gaussian pulse is launched into the fibre, i.e.

$$U(0, \tau) = exp\left(-\frac{\tau^2}{2\tau_0^2}\right) \tag{3.20}$$

Then its Fourier transform will be

$$\tilde{U}(0, \omega) = \int_{-\infty}^{\infty} d\tau U(0, \tau) e^{i\omega\tau} = \sqrt{2\pi}\tau_0 exp\left[-\frac{1}{2}(\tau_0 \omega)^2\right] \tag{3.21}$$

Then, using Equation 3.19

$$U(\zeta, \tau) = \frac{\tau_0}{\sqrt{2\pi}} \int_{-\infty}^{\infty} d\omega exp\left[-\frac{1}{2}(\tau_0 \omega)^2 + \frac{i}{2}\beta_2 \omega^2 \zeta - i\omega\tau\right] = \tag{3.22}$$

$$= \sqrt{\frac{\tau_0^2}{\tau_0^2 - i\beta_2\zeta}} exp\left[-\frac{1}{2}\left(\frac{\tau^2}{\tau_0^2 - i\beta_2\zeta}\right)\right] \tag{3.23}$$

It is better to rewrite the previous expression in the form

$$U(\zeta,\tau) = |U(\zeta,\tau)|e^{i\phi(\zeta,\tau)} \tag{3.24}$$

hence,

$$|U(\zeta,\tau)| = \frac{\tau_0}{\tau_1} exp\left[-\frac{1}{2}\frac{\tau^2}{\tau_1^2}\right], \tag{3.25}$$

$$\phi(\zeta,\tau) = -signum(\beta_2)\frac{(\zeta/L_D)}{1+\zeta/L_D)^2}\frac{\tau^2}{\tau_0^2} + arctan\left(\frac{\zeta}{L_D}\right) \tag{3.26}$$

where new parameters are defined as

$$\tau_1 = \tau_0\sqrt{1+(\zeta/L_D^2)} \tag{3.27}$$

$$L_D = \frac{\tau_0^2}{|\beta_2|} \tag{3.28}$$

Therefore, it is seen that the effect of the GVD is two fold. First, it broadens the pulse from being τ_0 to being $\tau_1 > \tau_0$. The quantity L_D appears naturally and corresponds to the distance for which the pulse width of a Gaussian pulse increases $\sqrt{2}$ and depends on the fibre dispersion (β_2) and on the pulse width (τ_0). The second effect of the GVD is the appearance of a modulation in the phase (Equation 3.26) that was not present in the original pulse. This phase is dependent on τ and then the instantaneous frequency is not constant along the pulse. The instantaneous frequency is given by

$$\delta\omega = -\frac{\partial\phi}{\partial\tau} = sgn(\beta_2)\frac{2(\zeta/L_D)}{1+(\zeta/L_D)^2}\frac{\tau}{\tau_0^2} \tag{3.29}$$

At the beginning of the pulse ($\tau < 0$) the frequency shift compared to the original pulse will be positive or negative depending on the dispersion of the fibre. If the dispersion is normal ($\beta_2 > 0$) the front part of the pulse will shift towards the red (and the end towards the blue) and if the dispersion is anomalous ($\beta_2 < 0$) the opposite will occur. This effect can be related with the pulse broadening. Let us consider a pulse propagating in the normal dispersion regime. High frequencies (blue) experience a higher refractive index and therefore travel at a lower velocity. This will delay them with respect to the lower frequencies (red). At the end, the pulse will have all the high frequencies in the tail of the pulse and the low frequencies at the front, resulting in a broadening of the pulse. If the original

pulse is chirped, that is it has a certain modulation in the phase originally, the propagation will be different. If the pulse has positive chirp, as the effect of the GVD is to up-chirp the pulse, the broadening effect will be faster. If the pulse has a negative chirp, then the initial effect will be a compression of the pulse, but it will finally broaden.

3.4.2 Self phase modulation (SPM)

Let us consider now the case when the propagation distance is much shorter that the characteristic dispersion length ($L \ll L_D$). In this case we can neglect the contribution of β_2 and Equation 3.14 becomes

$$\frac{\partial}{\partial \zeta} U = i\gamma |U|^2 U \tag{3.30}$$

where its solution is

$$U(\zeta, \tau) = U(0, \tau) exp[i\gamma |U(0, \tau)|^2 \zeta] \tag{3.31}$$

Therefore, in the absence of GVD, the pulse does not broaden but it appears once more a modulation of the phase. In this case the modulation is due to the intensity of the pulse itself, and then the name self phase modulation. An effect in the instantaneous frequency appears as it did with the GVD, and is given by

$$\delta\omega = -\frac{\partial \phi}{\partial \tau} = -\gamma\zeta \frac{\partial |U(0,\tau)|^2}{\partial \tau} = \frac{\partial |u(0,\tau)|^2}{\partial \tau} \frac{\zeta}{L_{NL}} \tag{3.32}$$

where

$$L_{NL} = \frac{1}{\gamma |U(0,\tau)|^2_{max}} \tag{3.33}$$

$$|u(0,\tau)|^2 = \frac{|U(0,\tau)|^2}{|U(0,\tau)|^2_{max}} \tag{3.34}$$

L_{NL} is the distance for which the SPM starts being relevant and this characteristic length depends not only on the fibre properties but on the maximum intensity of the pulse.

Therefore, SPM introduces a chirp in the pulse but does not modified the shape of the pulse. The chirping due to SPM only 'reorders' the frequencies inside the pulse.

3.4.3 Joint effect of the Group Velocity Dispersion and Self Phase Modulation

It has been shown what the effects of the GVD and the SPM are. Each one of the phenomena have a characteristic length for which they become relevant. Let us study now the case when both effects are present. First, the effect of a continuous wave propagating down the fibre will be studied. It will be shown that the solution is not stable in the anomalous dispersion regime and leads to the generation of a pulse train. Then, the propagation of a pulse propagating down the fibre will be studied. It will be shown how stable solutions (pulses that do not change along propagation) called solitons can be found.

Modulation Instability

Let us consider a CW solution, that is $\partial_t \overline{U}(\zeta) = 0$. Then, solving the NLSE,

$$\overline{U}(\zeta) = \overline{U}_0(\zeta = 0)e^{i\phi_{NL}\zeta} \tag{3.35}$$

with

$$\phi_{NL} = \gamma|\overline{U}_0|^2 \tag{3.36}$$

The intensity of this solution does not change along the fibre, so the only dependance on ζ is for the nonlinear phase modulation. Let us assume $\overline{U}_0$ to be real. The stability of this solution can be studied by introducing a small perturbation δu, so

$$U(\zeta,\tau) = \overline{U}(\zeta) + \delta U(\zeta,\tau) = (\overline{U}_0 + u)e^{i\phi_{NL}\zeta} \tag{3.37}$$

If substituting on both sides of the equation and rearranging then

$$\left(\partial_\zeta + \frac{i}{2}\beta_2\partial_\tau^2\right) = i\gamma\overline{U}_0^2(u^* + u) \tag{3.38}$$

which is a linear equation that admits solutions like

$$u(\zeta,\tau) = u_1\cos(K\zeta - \Omega\tau) + iu_2\sin(K\zeta - \Omega\tau) \tag{3.39}$$

Then, substituting that solution in Equation 3.38 gives

$$-Ku_1 + \frac{1}{2}\beta_2\Omega^2 u_2 = 0 \tag{3.40}$$

$$-Ku_2 - \frac{1}{2}\beta_2\Omega^2 u_1 = 0 \tag{3.41}$$

which after solving gives

$$K^2 = \left(\frac{\Omega\beta_2}{2}\right)^2 (\Omega^2 + \Omega_c^2) \tag{3.42}$$

$$\Omega_c = 2\overline{U}_0\sqrt{\frac{\gamma}{\beta_2}} \tag{3.43}$$

From the above expressions, it is clearly seen that if both β_2 and γ have the same sign, Ω_c is a real quantity and then K is real as well. Then, the small perturbation will not increase and if the losses would be included, it is seen that the perturbation is progressively attenuated.

If the signs of β_2 and γ are different, then Ω_c is an imaginary quantity and then K is imaginary for values $(\Omega^2 - \Omega_c^2) < 0$. This will make the perturbation increase exponentially and therefore, any small perturbation will make the stationary solution unstable and will break the CW beam into a pulse train. In silica, γ is always greater than zero, so such modulation instability will generally appear in the anomalous dispersion regime.

Optical Solitons

After seeing what happen to a continuous solution when propagating in an optical fibre, let us consider now the case of an optical pulse propagating when both the GVD and the SPM effects are present. There are two completely different situations depending on the sign of β_2.

When in the normal dispersion regime ($\beta_2 > 0$) the chirp due to GVD and to SPM are both positive and therefore a very fast broadening of the pulse is expected. When in the anomalous dispersion regime ($\beta_2 < 0$) the chirp due to GVD and SPM have opposite signs and therefore they can compensate. When in the anomalous dispersion regime, the pulse is expected to broaden at a much lower

rate as the effect of the chirp in the pulse frequencies is in opposite directions. The solution for which both effects exactly cancel each other is known as a soliton. It can be proved that when $\gamma > 0$ and $\beta_2 < 0$ there is a stable solution for the NLSE in the form of

$$U(\zeta, \tau) = N sech(s) \tag{3.44}$$

where

$$s = \frac{1}{\sqrt{|\beta_2|}} \tau \tag{3.45}$$

and N is a natural number. $N = 1$ is known as the fundamental soliton and it is a solution that is not distorted during propagation. Solutions for $N > 1$ correspond to high order solitons and show periodic changes along their propagation.

It is worth noting that there is a stable solution of the form $\tanh(s)$ for $\beta_2 > 0$. These are called 'dark solitons' and correspond to a dark region that propagates without distortion.

In 1986 a new effect regarding solitons was experimentally observed [9] and theoretically explained [10]: the soliton self frequency shift. This effect consists on a shift towards longer wavelengths of the soliton spectrum, and can be understood in terms of stimulated Raman scattering. For very short pulses in time, the spectral width is large enough that the Raman gain can amplify the low frequency (red) spectral components of the pulse, with the high-frequency components of the same pulse acting as a pump. This process continues along the fibre and therefore the shift increases with distance.

Chapter 4

Photonic crystal fibres

4.1 Introduction

Photonic crystal fibre (PCF) is an all-silica fibre with a periodic 2-dimensional modulation of the refractive index on the scale of the optical wavelength (see Figure 4.1). The refractive index modulation is achieved with an array of air holes running down the length of the fibre [11, 12]. These types of fibres have shown many remarkable properties, mainly because of their different wave guiding mechanisms and the great versatility of the stack and fabrication process used which enables many different kinds of structures to be achieved.

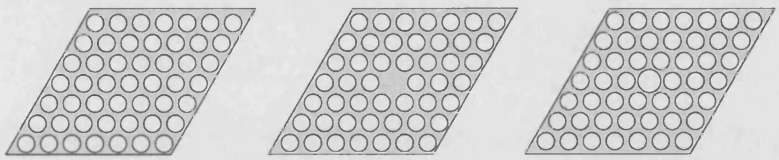

Figure 4.1: Transverse section of (a) a photonic crystal, (b) a photonic crystal with a high index defect and (c) a photonic crystal with a low index defect

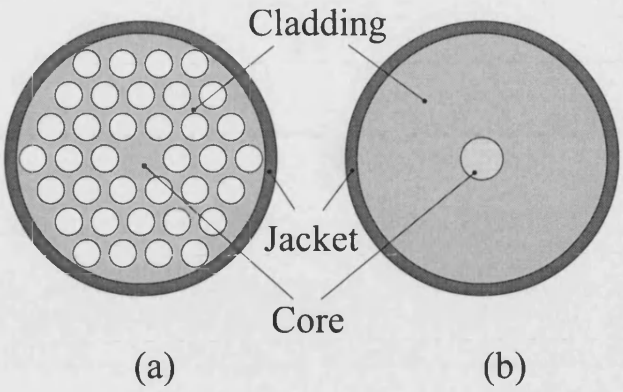

Figure 4.2: Comparison between a (a) high index PCF and (b) a conventional fibre

4.2 Properties of photonic crystal fibres

4.2.1 Guiding mechanism

Photonic crystal fibres were first proposed in 1992 but the first working example was not made until 1996 [11, 12]. It has been demonstrated that these kind of fibres can guide light not only via total internal reflection (TIR) but also via a band gap mechanism [13].

If one of the holes is missing, a 'defect' is created in the 'crystal' structure. This 'filled in' hole is referred as a high index defect and it will act as the fibre core. The structure will guide light via TIR much as in a conventional fibre (see Figure 4.2). The air-silica structure surrounding the defect has an effective refractive index that is lower than that of the pure silica forming the core and, therefore, will act as the fibre cladding [11, 12, 14].

When, instead of having one of the holes missing in the structure, a much larger hole than the rest of the air holes of the array is present (a low index defect, see Figure 4.1c) the structure can behave in a completely different way for guiding light. It can guide light via a photonic bandgap. Constructive multiple-beam interference in a periodic structure can expel light from the material for certain frequencies and directions of incidence, creating what are known as photonic bandgaps. A photonic band gap is analogous to the electronic band gap of solid-

state physics except that it applies to photons instead of electrons. If a large airhole is placed within the structure the light propagating down that hole will be 'trapped' inside, as the bandgap present in the rest of the structure does not allow the light to extend into it. The confinement of the light takes place within a hollow core. Certain wavelength bands are confined and guided down the core of the fibre, each band corresponding to the presence of a full two-dimensional band gap in the photonic crystal cladding. The presence of a two-dimensional photonic bandgap requires the fibre cladding to be a near-perfect periodic array of air holes with a high air-filling fraction and a small pitch (the distance between adjacent holes in the lattice). The trademark of photonic band gap guidance is that, when illuminated with a white light source, a brightly coloured mode will appear in the core as the band gap will only allow certain permitted wavelengths to propagate along the core region [13].

4.2.2 Endlessly single mode regime

One of the first demonstrated characteristics of PCF was the remarkably wide wavelength range in which the fibre can remain single-mode [14]. As explained in Section 2.4.1, standard step-index fibres are to have a V-value below 2.405 to be single mode. If the definition of the V value is analysed, it is seen that the 'normalised frequency' is proportional to the core-cladding index difference and inversely proportional to the wave length. That means that conventional fibres will become multi mode for wavelengths (λ_0) shorter than

$$\lambda_0 < \frac{2\pi r}{2.405}\sqrt{n_{core}^2 - n_{cladding}^2} \tag{4.1}$$

where n_{core} and $n_{cladding}$ correspond to the refractive indexes for the core and cladding regions, and r is the core radius. For example, considering the typical radius and the core-cladding index difference for standard telecommunication fibres, these are designed to be single mode for wavelengths longer than 1.27 μm. PCFs have shown a single mode regime from at least 337 nm to well beyond 1550 nm [15].

This wide range of wavelengths for which PCFs can remain single-mode can be explained using an effective refractive index model for the cladding [15]. Standard theory can be used to calculate the effective refractive index of a periodic structure

formed by two dielectric media with different refractive indices. The intensity distribution of the light in the cladding is unknown and would depend on the size and index of the core. A model was proposed which considers the effective refractive index of the fundamental mode of the photonic crystal as the refractive index of the cladding.

The fundamental mode of an infinite photonic crystal cladding is known as the fundamental space-filling mode (FSM). The FSM has the largest propagation constant (β_{FSM})that can propagate in the photonic crystal cladding without being evanescent. Any light in the cladding with a value of β greater than β_{FSM} will be evanescent. Hence, in analogy with standard fibre theory, the lower limit for a mode to be guided in a PCF will be kn_{eff}, where n_{eff} is the effective refractive index of the cladding. Hence n_{eff} is defined as,

$$n_{eff} = \frac{\beta_{FSM}}{k} \tag{4.2}$$

Then, a range of β values is available for different guided modes in the core of the PCF as long as

$$kn_{core} > \beta > \beta_{FSM} \tag{4.3}$$

When solving for FSM, it can be found that the effective index of a PCF can be expressed as

$$n_{eff} = \sqrt{n_{silica}^2 - \frac{\Lambda^2(k^2 n_{silica}^2 - \beta_{FSM})^2}{2\pi}\left(\frac{\lambda}{\Lambda}\right)^2} \tag{4.4}$$

where $k = 2\pi\ \lambda$ and Λ is the pitch or distance in between to adjacent holes [15]. At the short wavelengths (or large pitches) the effective refractive index for all filling fractions is close to that of the silica. However, at long wavelengths (or small pitch) the effective refractive index tends to a value close to an average of the cladding, and is strongly dependant on the air-filling fraction. Then, the presence of the air holes in the cladding region modulates the field distribution of the light in the core. At short wavelengths the field is sharply modulated by the presence of the air holes, but not as much when the wavelengths get longer. This is equivalent to having an effective refractive index that increases when the wavelength becomes shorter, allowing the fibre to remain in the single-mode regime.

4.3 Fabrication

In section 2.3 it was explained how conventional optical fibres are drawn in a vertical tower after preparing the glass in a MCVD machine. Photonic crystal fibres are fabricated in a vertical tower using a stack and draw technique. All the fibres fabricated during this work were drawn in the fabrication facilities available within the university. The first fibres were drawn in a vertical tower, dating from the 70's, donated by BT to the Optoelectronics Group. During the course of this work, new fabrication facilities were built in a clean room environment (as a dust-free environment is necessary in order to fabricate high quality fibres) and a new, state of the art, vertical tower was bought.

Photonic crystal fibres are fabricated using a stack and draw technique which involves no chemical processing. A summary of the fabrication process can be seen in Figure 4.3

A circular silica tube of several centimeters external diameter is drawn on the fibre-drawing tower in order to reduce its diameter down to about 1 mm. This process consists of feeding the capillary into the furnace and heat it to a temperature of around 1900°C whilst pulling it from the other end at a higher speed. The feeding mechanism (see Figure 4.4) consists of a chuck mounted on a precision lead screw that allows fine control on the feeding speed. The furnace consists of a graphite element which heats up when a current is applied to it. The furnace is purged with high purity argon as the element has to be kept in an inert atmosphere to avoid oxidisation. A gas purifier is used to reduce the impurities of the argon gas entering the furnace. Gas windows and top and bottom irises are used in order to reduce the amount of dust entering the furnace during the fabrication process. The cane puller is a set of two wheels with a precision speed control that pulls the heated silica out of the furnace (see Figure 4.4). As a result, the diameter of the capillary decreases and a number of capillaries all with the same external diameter are obtained. The same process is followed with a solid silica rod in order to get the solid canes that will act as the core. The maximum length of these capillaries depends on which tower is used for the fabrication. In the old BT tower, the length had to be under 1 m as that was the length available between the preform feed and the furnace. With the new fabrication tower, the distance is much longer so the length is not a restriction. The capillaries drawn using the new vertical tower are rarely longer than 1 m as a longer stack will

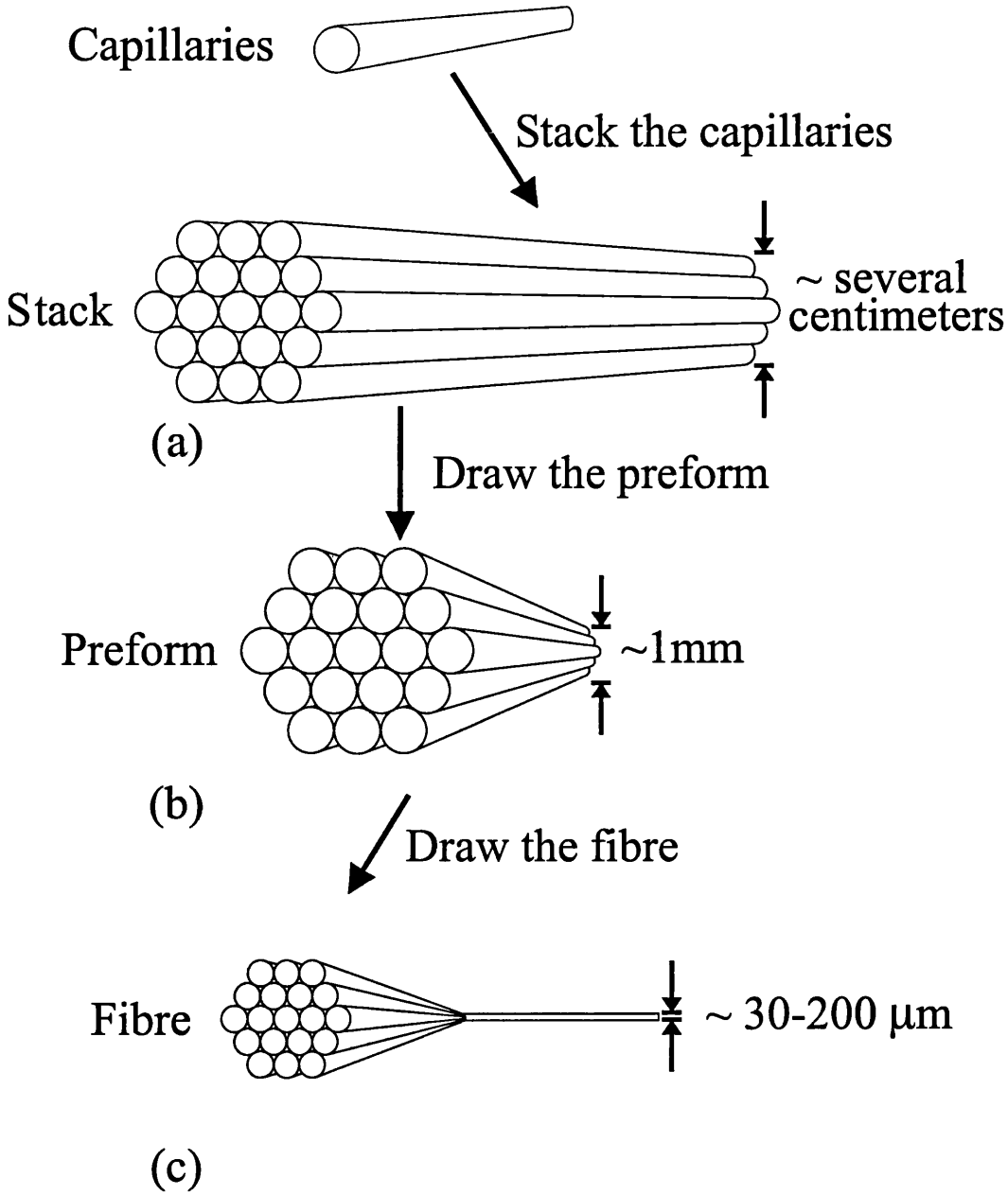

Figure 4.3: Summary of the stack and draw fabrication process for pulling a photonic crystal fibre: (a) Several capillaries are stack in order to create the structure, (b) The stack is drawn down to a preform of about one millimeter and then (c) it is drawn down to fibre

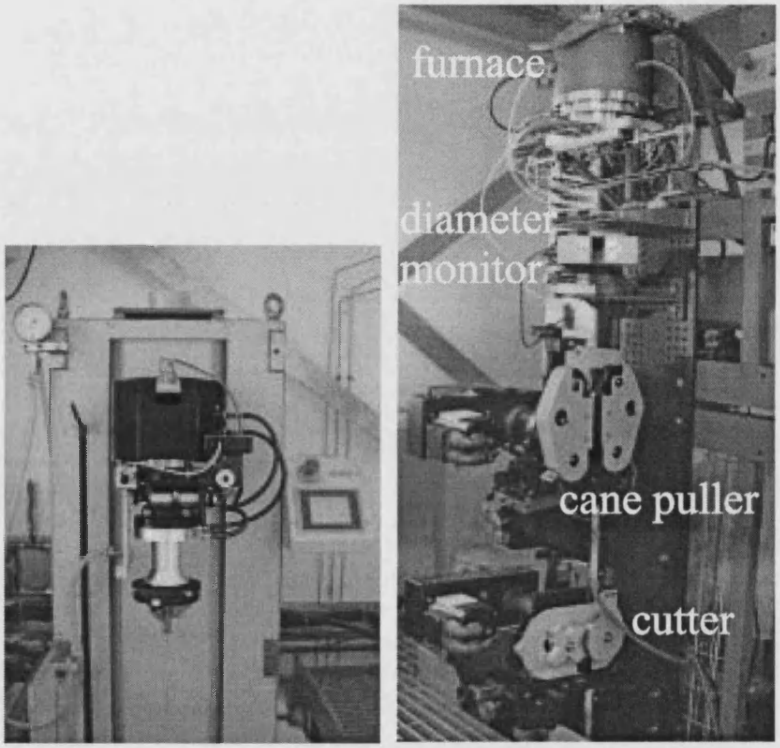

Figure 4.4: Feeding mechanism (left) and furnace, diameter monitor and cane puller (right) of the fabrication facilities

provide more preforms but at the same time it will much more difficult to stack. The statics and bending of the capillaries greatly complicate the stacking process.

Capillaries that are suitably uniform are selected and then stacked by hand forming the required array. Intentional defects, such as the solid silica core, are added during this stage.

The stack is placed in a silica tube and then drawn down on the drawing tower, as explained before, to reduce the diameter of the whole structure. Vacuum can be applied in the region between the stack and the tube to help the silica tube to collapse around the structure. This silica tube also increases the amount of silica in the structure and the stability of the stack. After this stage several preforms of about 1 mm in diameter are obtained. This process can be done at different temperatures and speeds depending on the structure. When the stack consists of a large number of periods the temperature needs to be high (around 2000°C) and the drawing speed slow (cane puller at a 0.5 m/min). That way, the preform spends enough time in the furnace in order to be heated sufficiently and uniformly. When drawing PCFs with very large air holes, the process of pulling the preform is done as cold as possible. Temperature has a direct effect on the size of the air hole and therefore the hotter the furnace when drawing, the smaller the holes will be in the preform.

For the next step, the preform is placed inside another silica tube and the preform is drawn down to fibre. The mechanism for drawing down to fibre is similar to the method described above, but in this case the capstan and the drum winder control the pulling speed (see Figure 4.5). The capstan, consisting in a set of wheels and springs, controls the pulling speed as well as the tension on the drum. This allows to wind the fibre into the drums in a very compact way. The final diameter of the fiber is about 30-200 μm. A polymer coating can be applyed on the outside of the fibre. This polymer, which has to be cured using a UV lamp, increases the strength of the fibre, making it much easier to handle.

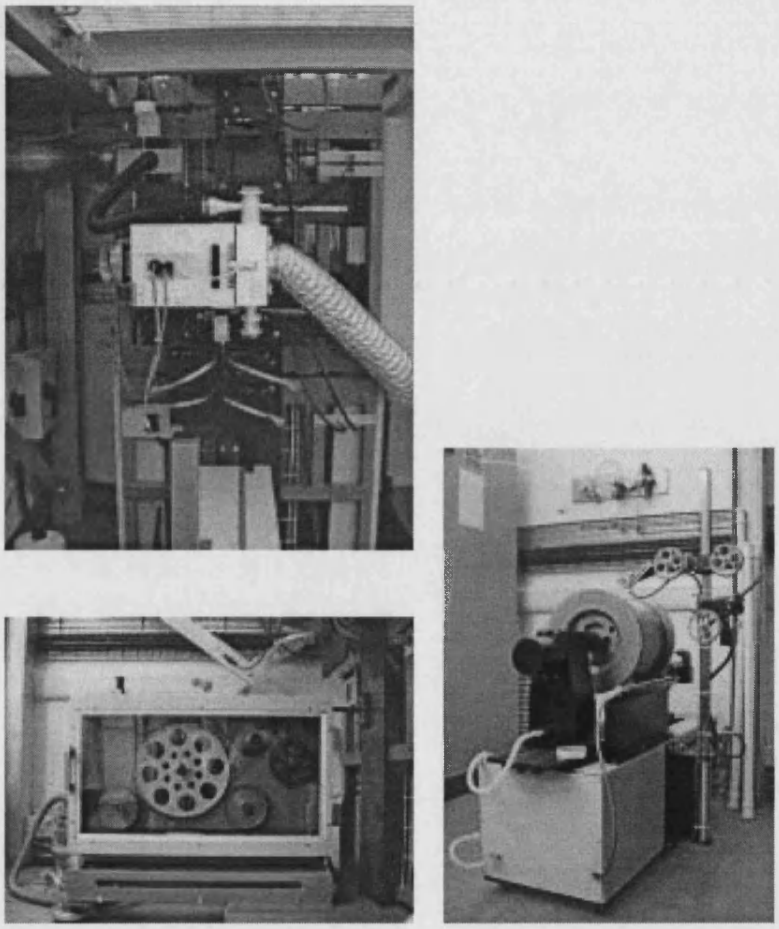

Figure 4.5: UV lamp (top), capstan (left) and drum winder (right) of the fabrication facilities

4.4 The fibres

This section is intended to be a reference section with the characteristics of all the fibres fabricated during the course of this Thesis. Being a reference section, some of the characteristics shown here will be described in more detail in the next chapters, explaining fabrication, measurement and modelling methods.

Figure 4.6 show scanning electron micrographs of all the fibres fabricated during this Thesis.

The dispersion characteristics for all the fibres and the beat length (for polarisation maintaining ones) are shown in Figures 4.7 and 4.8.

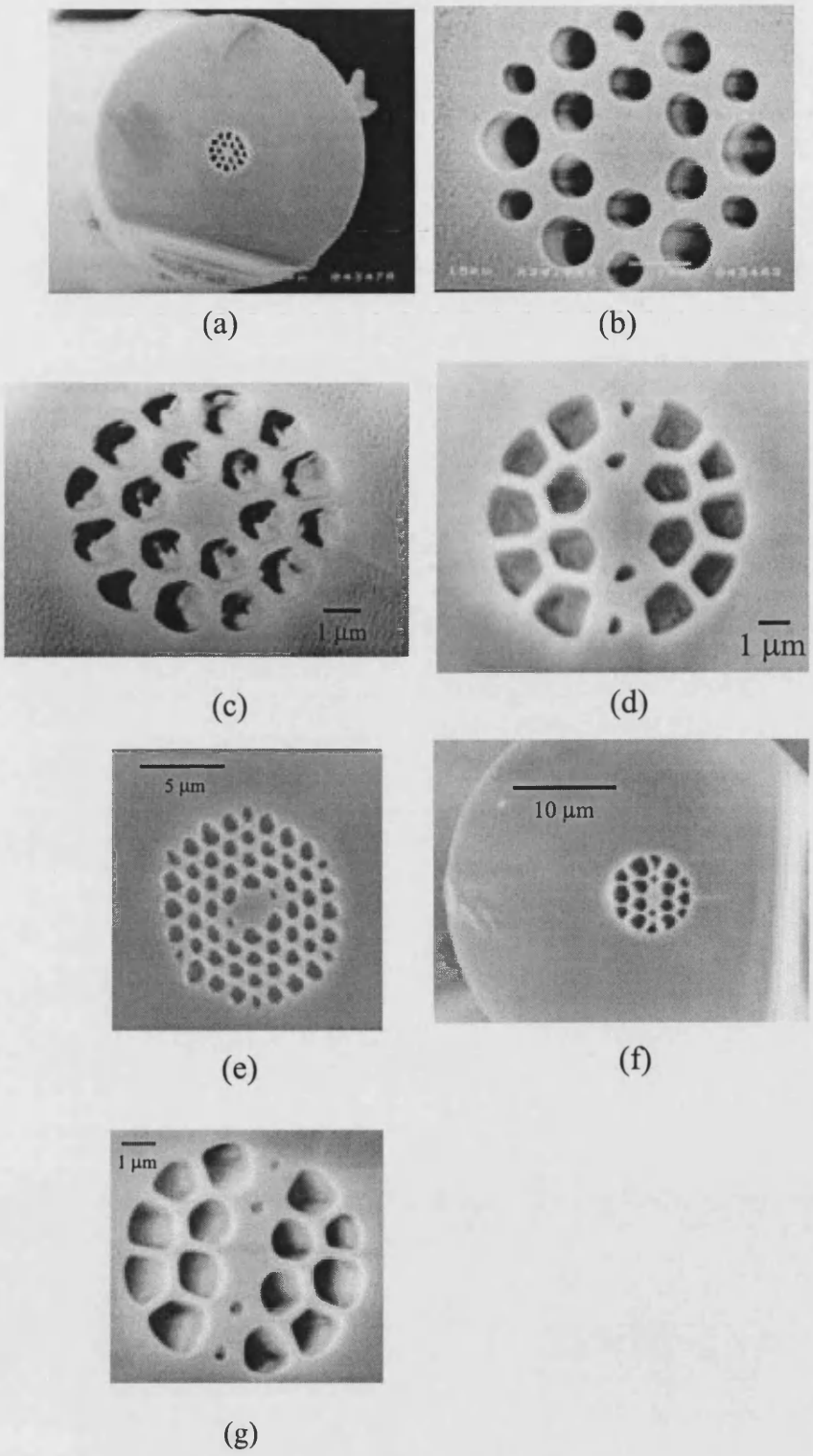

Figure 4.6: Scanning electron micrographs of (a) fibre I, (b) fibre II, (c) fibre III, (d) fibre IV, (e) fibre V, (f) fibre VI and (g) fibre VII

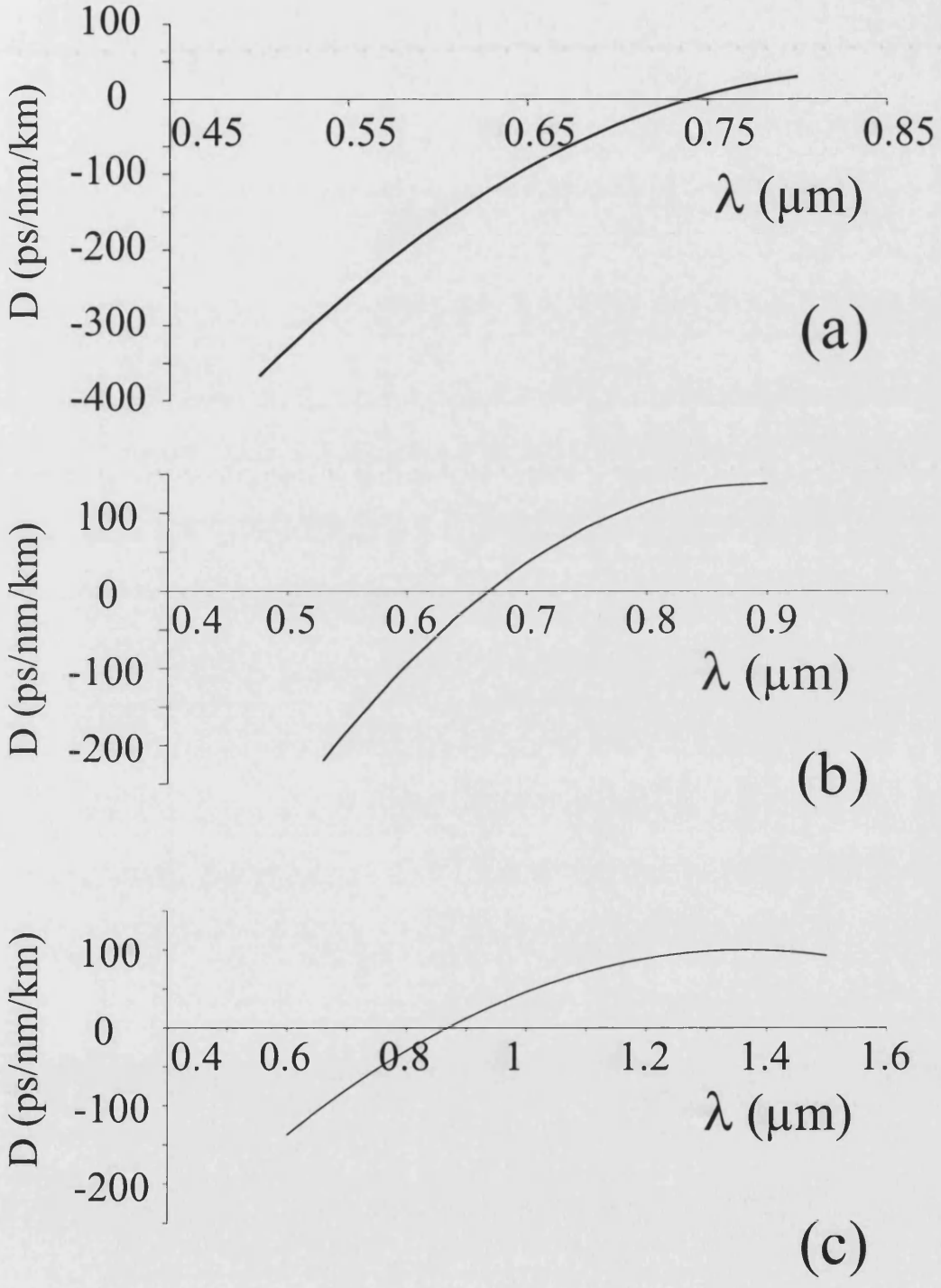

Figure 4.7: Dispersion of (a) fibre I, (b) fibre II and (c) fibre III

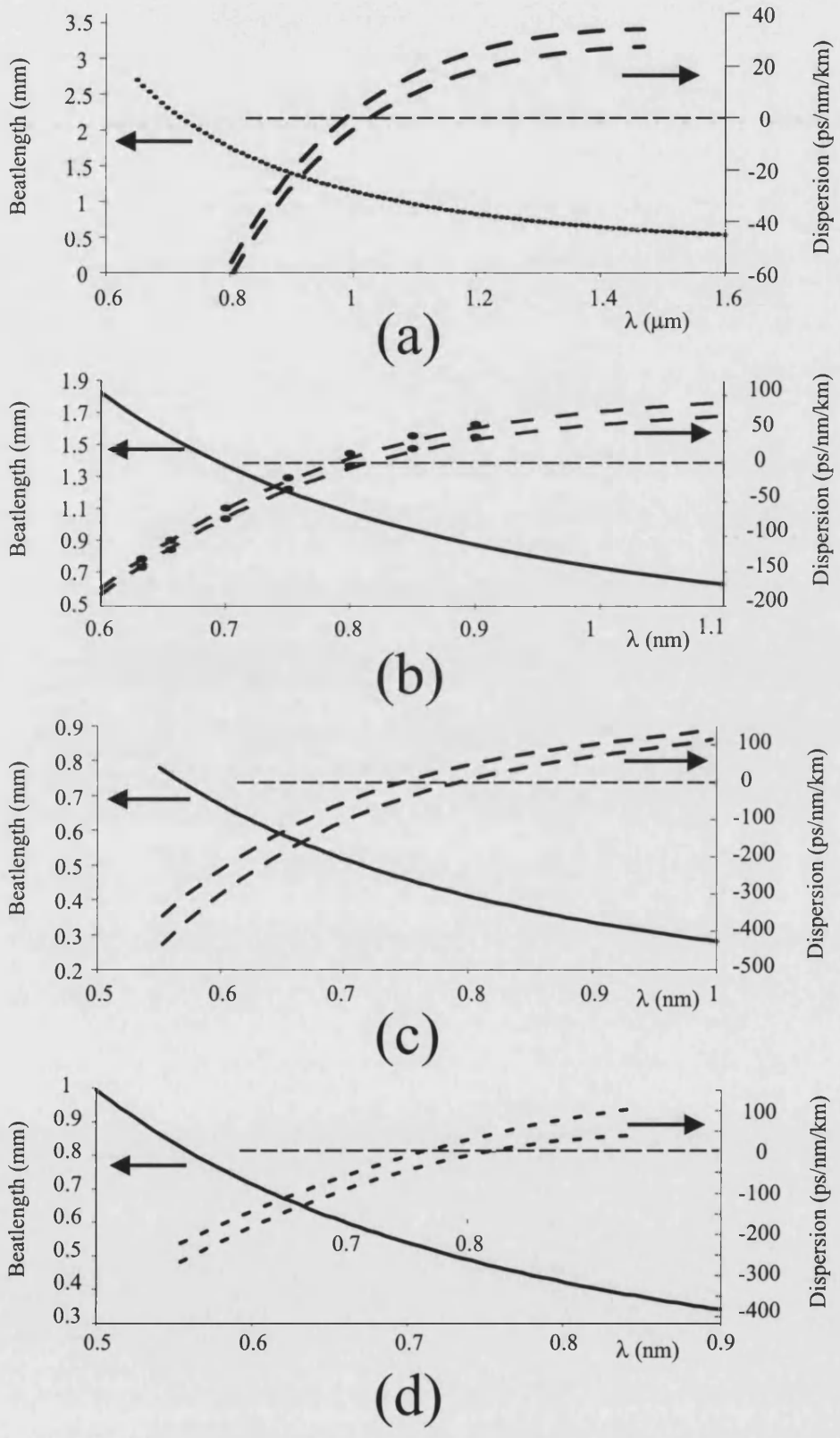

Figure 4.8: Dispersion and beat length of (a) fibre IV, (b) fibre V, (c) fibre VI and (d) fibre VII

4.4.1 Linear parameters

The definitions of the main parameters used to describe each fibre are here reminded. Table 4.1 shows the values of the main parameters for the fibres.

Fibre	Air hole size (μm)	Pitch (μm)	$\lambda_D(nm)$
I	1.2	1.6	740
II	0.6	1	668
III	1.1	1.85	840
IV	$d = 0.40$ $D = 1.16$	1.96	$\lambda_{D1} = 1020$ $\lambda_{D2} = 970$
V	$d = 0.54$ $D = 1.15$	1.46	$\lambda_{D1} = 806$ $\lambda_{D2} = 781$
VI	$d = 0.35$ $D = 1.17$	-	$\lambda_{D1} = 791$ $\lambda_{D2} = 746$
VII	$d = 0.39$ $D = 1.44$	1.51	$\lambda_{D1} = 749$ $\lambda_{D2} = 708$

Table 4.1: Parameters of the fibres fabricated during the course of this work

Dimensions

Figure 4.9 shows the convention for the different measurements that are obtained from the scanning electron micrographs.

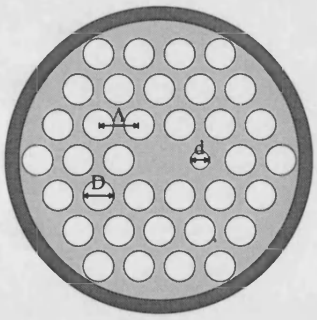

Figure 4.9: Schematic of a PCF showing the convention for air hole size and pitch

The pitch (Λ) is defined as the distance between two adjacent holes. D and d correspond to the air hole sizes.

Dispersion

The dispersion characteristics (as explained in Section 2.4.5) and, more importantly, the zero dispersion points, are given. As it will explained in the next chapters, the dispersion characteristics of the different fibres have been measured or modelled.

Birefringence

The birefringence (as explained in Section 2.5)of the fibres have been modelled. The beat length of the fibre is given by

$$L_B = \frac{2\pi}{\beta_x - \beta_y} = \frac{\lambda}{n_x - n_y} \tag{4.5}$$

4.4.2 Nonlinear parameters

There are several useful parameters when studying the nonlinear behavior of the fibres.

Effective area

The effective area (Section 2.4.3) of the fibres was measured or calculated using the definition

$$A_{eff} = \frac{[\int\int |F(x,y)|^2 dxdy]^2}{\int\int |F(x,y)|^4 dxdy} \tag{4.6}$$

Nonlinearity

The nonlinearity parameter γ (Section 3.4) is given by

$$\gamma = \frac{\omega n_2}{A_{eff} c} \tag{4.7}$$

The nonlinearity of PCFs is usually several orders of magnitude higher than that of conventional fibres. The main reason is that the effective area of the modes guided by PCFs are substantially smaller than in conventional fibres. PCF's properties allow for fabricating fibres with very small cores whilst being able to tailor a very big index step between core and cladding. This, obviously, gives a very small effective area for the guided mode.

Characteristic lengths and soliton energy

There are several characteristic lengths which are useful to know.

The nonlinear length refers to the characteristic length for which nonlinear effects become relevant. The nonlinear length L_{NL} is given by

$$L_{NL} = \frac{1}{\gamma P_0} \tag{4.8}$$

where P_0 is the input power.

The dispersion length L_D is the length of fibre for which dispersive effects become relevant. The dispersion length is given by

$$L_D = \frac{\tau_0^2}{|\beta_2|} \tag{4.9}$$

where τ_0 is the pulse length and β_2 the second derivative of β with respect to ω.

The nonlinear length and the dispersion length are compared not with the actual length of the fibre but with the effective length L_{eff} or loss length given by

$$L_{eff} = \frac{1 - e^{-\alpha L}}{\alpha} \tag{4.10}$$

where L is the length of the fibre and α the loss coefficient.

The soliton length L_s is defined as

$$L_s = \frac{\pi}{2} L_D \tag{4.11}$$

Finally, knowing L_{NL} and L_D, the soliton peak powers can be calculated as

$$N^2 = \frac{L_D}{L_{NL}} = \frac{\gamma P_0 \tau_0^2}{|\beta_2|} \tag{4.12}$$

Chapter 5

Modified group velocity dispersion in photonic crystal fibres

5.1 Introduction

Group Velocity Dispersion (GVD) in fibres plays a critical role in the propagation of short optical pulses since different spectral components associated with the pulse travel at different speeds as explained in Chapter 2. As the value of the zero GVD wavelength λ_D depends on the fibre-design parameters such as the core radius and the core cladding index difference, photonic crystal fibres are a desirable environment for modifying the dispersion of fibres. The stack and draw fabrication allows one to tailor the waveguide contribution of the GVD to compensate the material chromatic dispersion achieving anomalous dispersion where both the GVD of pure silica and that of conventional fibres is normal. At the same time, very high core-cladding index difference can be achieved with these structures [3, 16, 17].

In this chapter, a new family of PCFs with zero dispersion wavelengths in the visible and near infrared is presented. To be able to study nonlinear pulse propagation and solitons generation in PCFs, several dispersion-shifted PCFs with zero dispersion wavelength down to the wavelength range of a Ti:Sappire laser

(700-1000 nm) and into the visible were fabricated and characterised.

5.2 Group velocity dispersion of PCF

Photonic crystal fibres are single-material fibres. Tailoring the dispersion of these structures is only possible changing the waveguide contribution to the dispersion, as the material dispersion is fixed in this case. The waveguide contribution can be greatly changed as the air holes of the cladding of the PCF can be made very different in size. If the cladding of the PCF has small air holes, then the effective index of the cladding will be closer to silica than air, and the zero dispersion point will be at long wavelengths. As the air hole size increases, the effective index of the cladding decreases and the confiment in the core region increases. Then, the overall dispersion shifts towards shorter wavelengths.

Several PCFs with different parameters were fabricated. The preforms where all similar (2 period structures). The air hole size was changed using differen temperatures during the drawing process and the pitch was changed using different jacketing tubes and drawing to different final outside diameters. The fibres used were Fibre I, Fibre II and Fibre III (see Section 4.4).

5.3 Group velocity dispersion characterisation method

The group velocity dispersion measurements were carried out using a low-coherence white-light interferometric method [18]. A Michelson interferometer was set up as shown in Figure 5.1. The interferometer was set up with its usual configuration: the fibre under test was placed on one of the arms whilst the other arm was mounted with a travelling mirror in order to vary its length. A red Helium Neon laser was used for aligning purposes. Our light source was a halogen lamp and band-pass filters with a bandwidth of 10 nm were used to select the desired wavelengths.

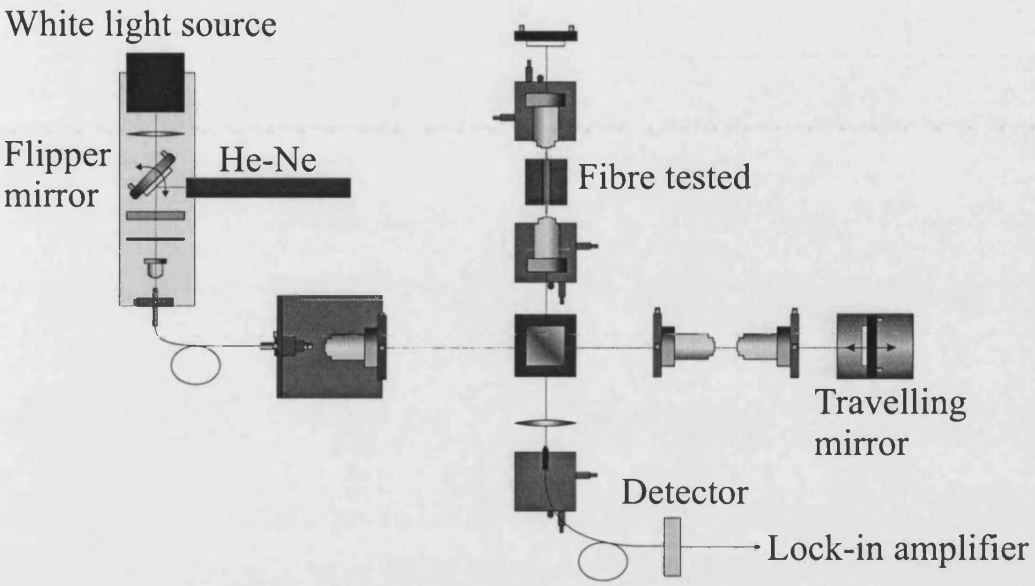

Figure 5.1: Michelson interferometer set up used to measure the group velocity dispersion

Due to the difference in optical path between both arms, an interferometric pattern appeares for each wavelength. A typical interference pattern is shown in Figure 5.2 (a).

There are two parameters which characterise an interference pattern: the period of the fringes and its visibility or envelope [19]. The shape of the envelope can be explained in terms of the Fourier transform of the wavelength dependence profile of the illuminating source. A typical wavelength profile of the band-pass filters used in the experiment and its Fourier transform is shown in Figure 5.2 (b). As seen in Figure 5.2, the x-axis corresponds to the mirror position. The position of the mirror is only important as a reference and not as an absolute value: the important parameter for us in this experiment is how the centre position of the interferogram envelope changes with wavelength.

When the optical paths in both arms are equal, then

$$\beta_{fsa} L_{fsa} = \beta_f L_f \tag{5.1}$$

where the sub index 'fsa' refers to the free space arm and 'f' refers to the arm

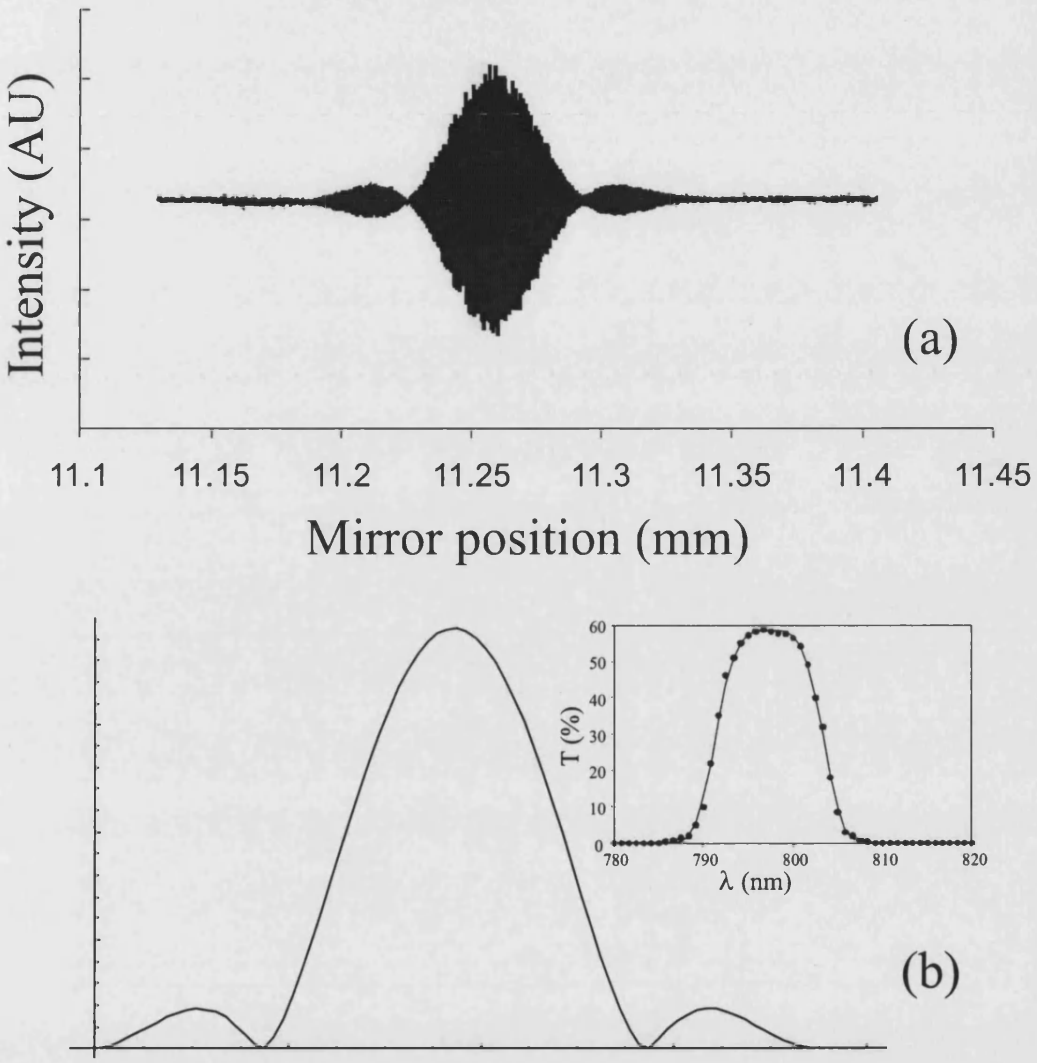

Figure 5.2: (a)Typical interference pattern recorded, and (b) typical transmission profile with wavelength of the filters used in the experiment (inset) and its Fourier transform

with the fibre on it. Then

$$L_{fsa} = \beta_f L_f \frac{\lambda}{2\pi} \tag{5.2}$$

Then, using Equation 5.1, and the relationship

$$\frac{d\beta}{d\lambda} = \frac{d\beta}{d\omega}\frac{d\omega}{d\lambda} = \frac{1}{v_g}\frac{2\pi c}{\lambda} \tag{5.3}$$

the length of the free space arm can be expressed as,

$$L_{fsa} = L_f c \frac{1}{v_g} \tag{5.4}$$

and then

$$\frac{dL_{fsa}}{d\lambda} = L_f c \frac{d}{d\lambda}\left(\frac{1}{v_g}\right) = L_f c D \tag{5.5}$$

where D is the dispersion parameter and relates to the GVD as

$$D = \frac{d\beta_1}{d\lambda} = -\frac{2\pi c}{\lambda^2}\beta_2 \tag{5.6}$$

Then for each of the fibres, we recorded the set of fringes for different wavelengths and study how the central position of the envelope changed. Then the data was analysed in order to get the dispersion characteristics and the zero GVD wavelength. A typical set of results showing the group delay associated to different wavelength filters for fibre I can be seen in Figure 5.3

5.4 Experiments

The dispersion of Fibre I was measured first. Fibre I had a hole diameter d = 1.2 μm and pitch (distance between to adjacent holes) $\Lambda = 1.6\mu m$, and two sets of data were taken for two different pieces of the same fibre. The data extracted from the interferograms shown in Figure 5.3 for the first piece is summarise in Table 5.1.

λ (μm)	0.53	0.55	0.589	0.6	0.633	0.65	0.75	0.8
Position (mm)	2.421	2.488	2.587	2.606	2.633	2.681	2.728	2.713

Table 5.1: Position of the mirror against wavelength for fibre I (d = 1.2 μm and pitch Λ = 1.6 μm)

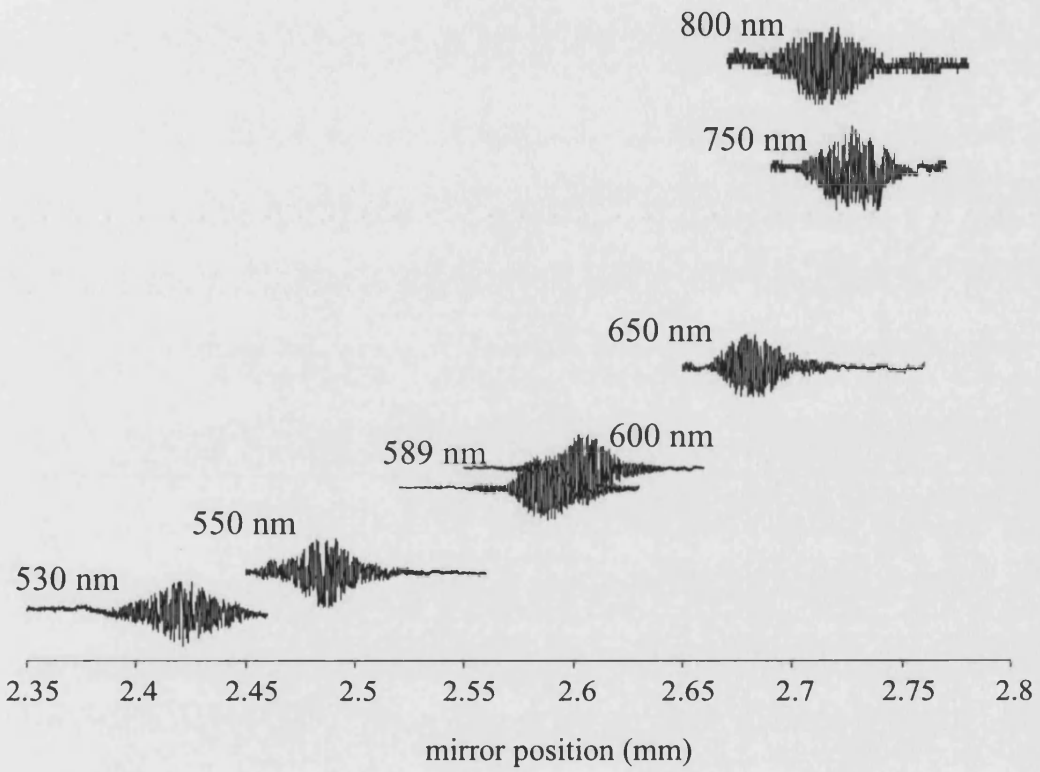

Figure 5.3: Interferograms for different band-pass filters obtained when measuring the dispersion of fibre I (d = 1.2 μm and pitch $\Lambda = 1.6\mu m$)

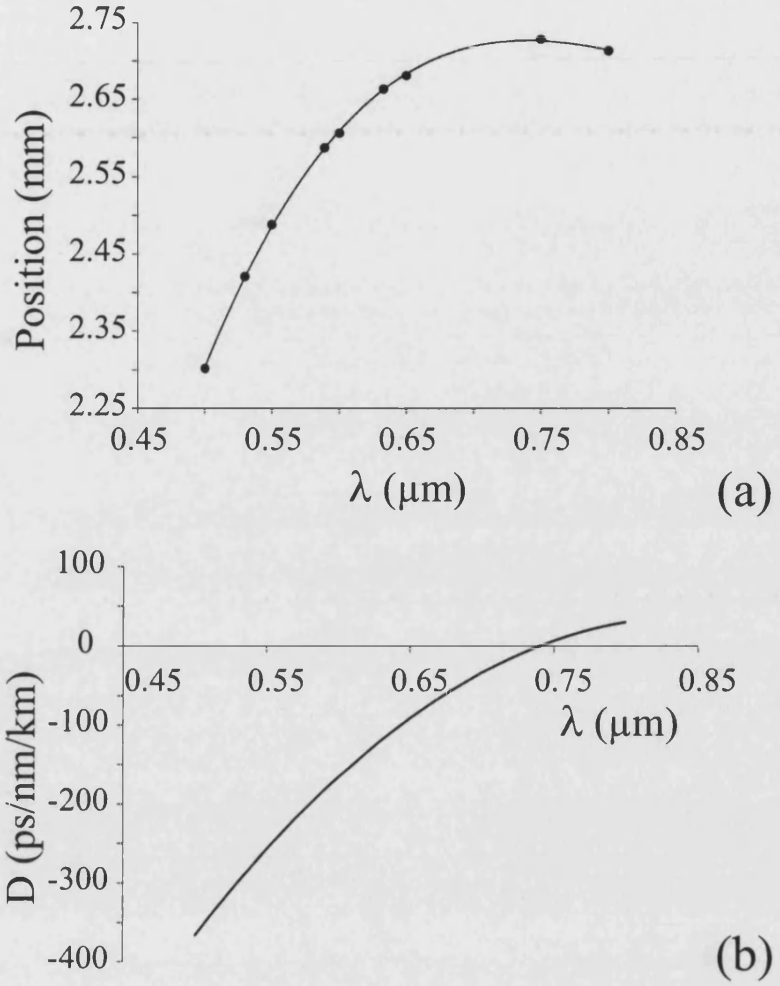

Figure 5.4: (a) Position of the center of the envelope with wavelength and (b) Dispersion of fibre I (d = 1.2 μm and $\Lambda = 1.6\mu m$)

Once the relative positions of each of the interferograms is known we can plot a curve and then differentiate it to get the Dispersion. Results are shown in Figure 5.4.

The two pieces of fibre showed similar dispersion characteristics and the zero dispersion wavelength was found to be $\lambda_D = 740nm$. Two or more pieces from different parts of the drawing process were tested in order to ensure that the fibre was sufficiently uniform. The error associated with the position of the zero dispersion wavelength is of the order of 1 nm.

The second fibre under test, fibre II, had a hole diameter d = 0.6 μm and a

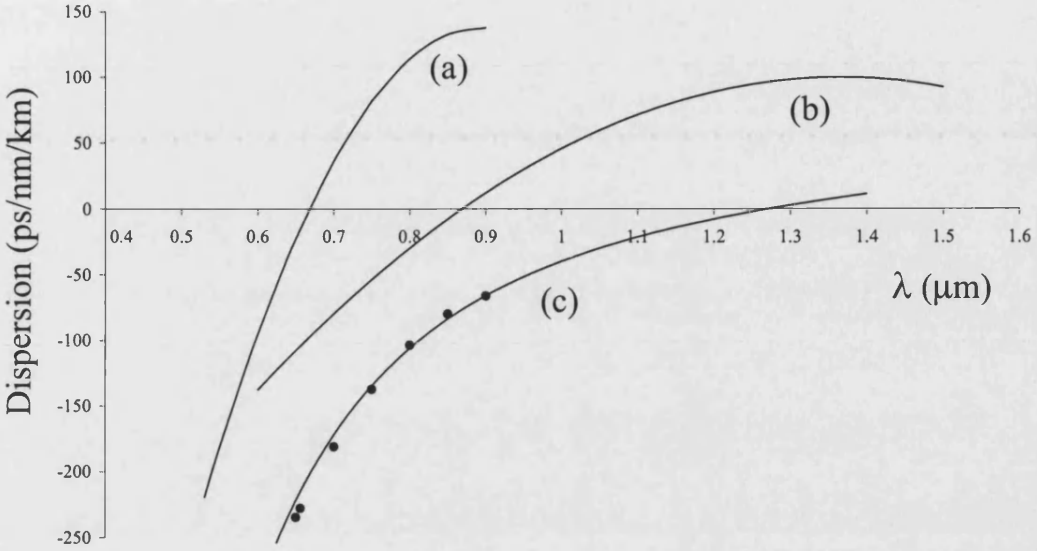

Figure 5.5: (a)Dispersion of fibre II (d = 0.6 μm and $\Lambda = 1.00\mu m$), (b)Dispersion of fibre III with d = 1.1 μm and $\Lambda = 1.85\mu m$ and (c) Dispersion characteristics of pure silica with experimental (points) and literature (line) curves compared

pitch $\Lambda = 1\mu m$. Analysing the data in the same way as previously described, the experiment showed that this fibre had a zero dispersion wavelength of $\lambda_D = 668$ nm. The results are summarized in Figure 5.5(a).

The third fibre under test was fibre III. Fibre III had a hole diameter d = 1.1 μm and pitch $\Lambda = 1.85\mu m$. This fibre was found to have $\lambda_D = 840nm$ and the results are summarized in Figure 5.5(b).

Finally, a piece of pure silica was tested, in order to compare the dispersion characteristics of it with the ones of the fibres and to test the accuracy of the method employed. The results are summarized in Figure 5.5(c). There is very good agreement between the experimental points and the curves from the literature [3].

5.5 Conclusions

Several fibres with unusual GVD characteristics have been demonstrated. It has been demonstrated that the zero dispersion wavelength of PCFs can be shifted to the visible and near infrared, where both pure silica and conventional fibres exhibit normal dispersion, by carefully choosing the parameters of the fibres. It has been shown as well that the Michelson set-up employed for the experiment is a useful tool for measuring the dispersion characteristics over a wide wavelength range.

It has been demonstrated that the dispersion of photonic crystal fibres can be shifted to different wavelengths by changing the air hole size and the core diameter. When the air hole size increases, the air-filling fraction of the cladding increases and therefore the effective refractive index decreases. This decrease in the effective refractive index makes the waveguide contribution to the dispersion to shift the dispersion from that of the material towards shorter wavelengths. The other important parameter is the core size. As the core size decreases, the zero dispersion wavelengths shifts to shorter wavelengths. Again, the waveguide contribution to dispersion is enhanced.

The unusual GVD characteristics shown by these structures has shown to have a strong effect on the non-linear response of the fibres to ultra-short optical pulses. Shifting the anomalous dispersion regime to shorter wavelengths enables the observation and study of solitons in the Ti:Sappire laser wavelength window (700-1000nm). The dispersion shifted fibres have shown as well a new nonlinear phenomenon, the generation of ultra broad (spanning up to two octaves) supercontinuum in optical fibres.

Chapter 6

Highly birefringent photonic crystal fibres: Linear characterisation and applications

6.1 Introduction

As explained in Chapter 2, in practice, conventional circularly symmetric optical fibres do not maintain the polarization state of the guided mode along their length (Section 2.5) The required birefringence can be achieved in two main ways. The shape of the refractive index profile defining the waveguide can be made non-circular (form or shape birefringence) or the material forming the fibre can itself be made birefringent, typically by introducing stresses as in bow-tie or panda fibres [5, 6, 7]. PCF can potentially be made very highly birefringent: the large index contrast enables high form birefringence, while the stack-and-draw fabrication process allows the formation of the required microstructure near the fibre core. During the course of this work, I fabricated and characterised the first intentionally birefringent PCF.

For the different experiments performed during my research studies, several Highly-Birefringent PCFs were fabricated. In this chapter, choosing one of the fibres as an example, the fabrication and characterisation techniques of these kind of structures is explained.

The last section is devoted to the fabrication and characterisation, for the first time, of a fibre rocking filter using a Highly Birefringent PCF. The mechanical twist technique employed shows that very efficient rocking filters can be fabricated using a much lower number of periods than that of rocking filters in conventional fibres.

6.2 Fabrication

When designing and fabricating a polarisation-maintaining PCF, form birefringence is a better choice for several reasons [5]. Firstly, form birefringence is based on the geometry of the core and therefore no dopants are needed in order to create stress regions. We can achieve the required structure simply by fabricating an elliptical core within the array of air holes. Secondly, form birefringence is the best option when a high index step between the core and cladding regions is achievable. This obviously is our case. Finally, the birefringence of elliptical-core fibres increases with wavelength, so one can get a better performance for longer wavelengths. This becomes specially important when designing the fibres for the telecommunication window.

There are two basic designs for fabricating the elliptical core. Both of them consist of using different air holes sizes, but one of them creates the ellipse by placing two small holes in the core vicinity and the other one places two big holes by the core region. Both schemes can be seen in Figure 6.1. During my research I have concentrated on structure (a) but it is worth noting that after our first report on these structures several other groups have been fabricating polarisation-maintaining PCFs based on configuration (b) [20, 21] or by placing two adjacent core regions [22]. In their reports they argue that they have approached the problem that way because it gives more stability on the fabrication process. Regarding this problem, we have never experienced stability problems other than the normal ones when fabricating PCFs. Another drawback of this design is that if the diameter of the big holes is not tailored appropriately it is possible to end up with a fiber that resembles more a two core structure or a fibre with a dumbbell shaped core [23, 22].

A detailed explanation of the fiber fabrication can be seen in Figure 6.2. The

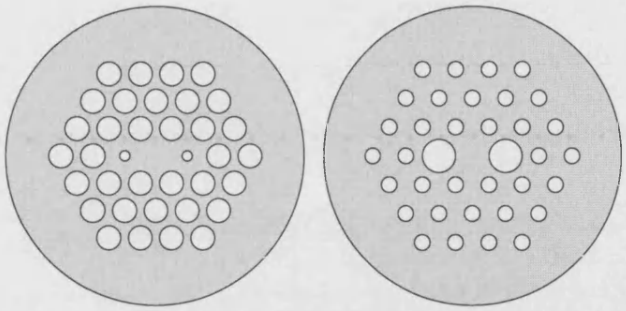

(a) (b)

Figure 6.1: Basic designs for fabricating a Highly Birefringent PCF

fibre was fabricated by stacking an array of silica capillaries and rods as explained in Chapter 4. Anisotropy was introduced into the fibre by careful positioning of capillaries with the same external diameter but different wall thicknesses, leading to different air-hole sizes in the cladding, an extra silica region in the core vicinity of the final fibre and two-fold rotation symmetry. A solid silica jacket was added to increase the diameter and strength of the fibre.

Following the stack and draw technique two different kinds of silica tubes where chosen to fabricate the capillaries. The two types correspond to ratios in between the outer diameter and wall thickness of 0.22 for the thick wall capillaries and 0.075 for the thin wall capillaries. Both kind of tubes were drawn down to the same external diameter: 1.3 mm. Once the capillaries were ready, a silica rod was drawn to the same diameter. Then the appropriate capillaries were stacked in a hexagonal close packed array carefully choosing the position of the solid rod that will act as the core and the position of the different kind of capillaries. In this case, a two period structure (a period being a ring of holes surrounding the core) with 4 holes of smaller diameter was stacked. Once the stack was ready, it was placed inside a silica tube to increase the stability of the system, and was drawn down to 1 mm preforms applying a vacuum to help the outside tube to collapse around the structure. Then, one of these preforms was placed in a second silica tube with thicker walls to add some silica to the structure and therefore being able to draw down to fibre with the desired dimensions (distance hole-to-hole just under 2 μm) whilst having a suitable external diameter.

Scanning electron micrographs of the final fibre can be seen in Figure 6.3. I will refer to this fibre as fibre IV. It shows how, with this simple two-period structure,

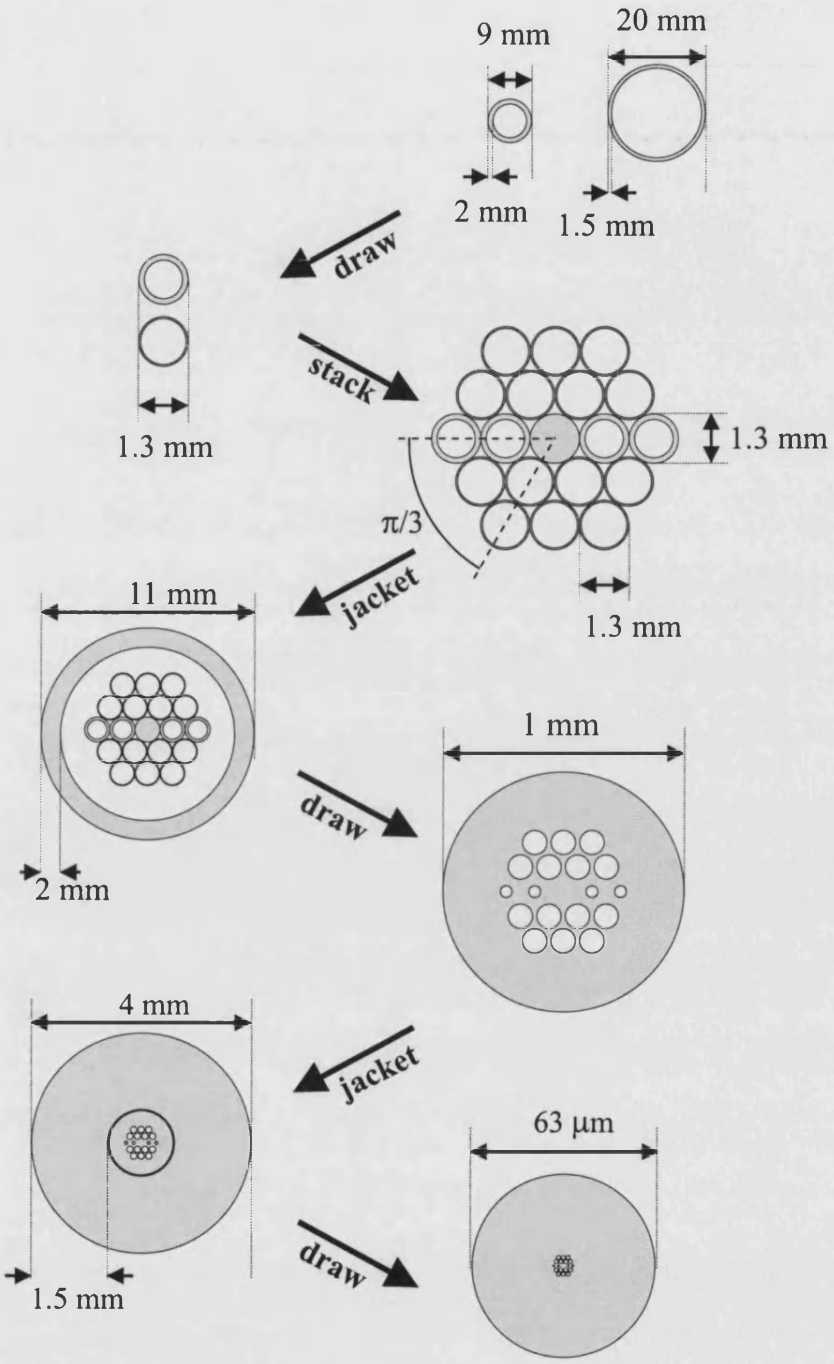

Figure 6.2: Example of a fabrication diagram for a Highly Birefringent PCF

an effective elliptical core can be fabricated. The fibre had a pitch (center to center distance between the holes) of $\Lambda = 1.96\ \mu m$ and a hole diameter of $d_1 = 0.40\ \mu m$ for the small holes and $d_2 = 1.16\ \mu m$ for the large ones. The external fibre diameter was 63 μm. It is clearly seen how the thicker wall capillaries have

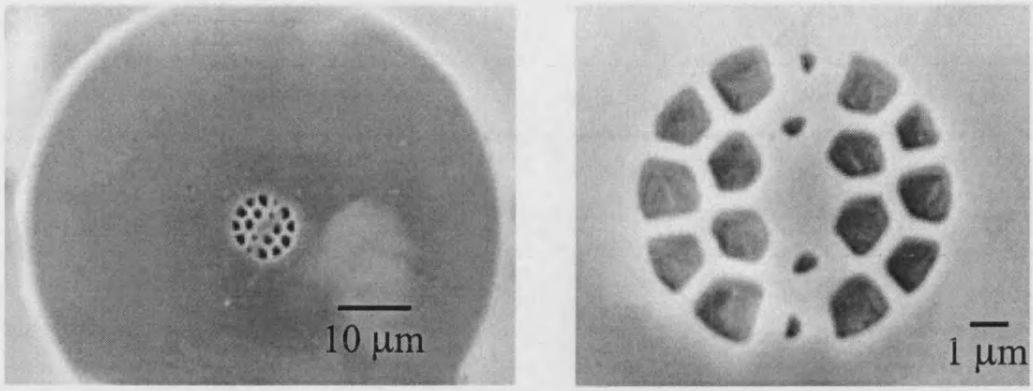

Figure 6.3: Scanning electron micrograph of an example of a Highly Birefringent PCF (Fibre IV)

given the extra silica needed to achieve an elliptical core.

6.3 Modelling

Using the dimensions measured from the scanning electron micrograph the fibre is modelled. We have used two methods to model the structure: a full vector numerical model based on the plane-wave method [4] and a beam propagation method.

For the plane-wave method model, a theoretical unit supercell (Figure 6.4b) or a high contrast bitmap (Figure 6.4c) is used as the input for a Fortran routine. This unit cell is mapped with plane waves and the problem is resolved as an eigenvalue problem. The other method is a commercial beam propagation method software (BeamProp) on which a structure similar to Figure 6.4 (b) is modelled.

It is worth noting that even though my work has been purely experimental, there has been a lot of effort during the last few years on improving this kind of structure from a theoretical point of view [24, 25, 26, 27].

For this case I used a vector numerical model based on the plane-wave method, implemented by Dr Jesus Arriaga, to model our structure. The calculations showed that the fibre was single mode at 1540 nm, which was confirmed exper-

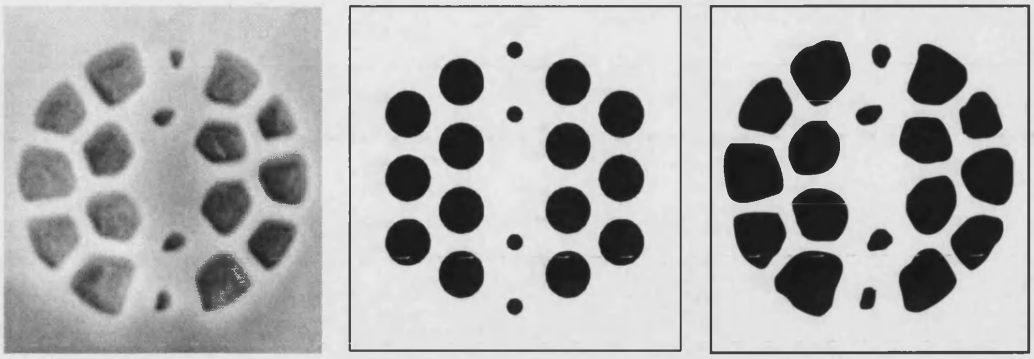

(a) (b) (c)

Figure 6.4: Modelling structures of a Highly Birefringent PCF

imentally and which made it easy to study its beat length. The calculated beat length was $L_B = 0.56$ mm as shown in Figure 6.5

6.4 Characterisation of the fibres

All the Hi-Bi photonic crystal fibres have been characterised. Depending on the desired application, their guidance properties, effective area, polarisation beat-length, losses and dispersion have been studied. In the next subsections a detailed explanation of all these techniques is given.

6.4.1 Guidance properties

The guidance properties of fibre IV were investigated experimentally using a tunable diode laser. The near and far field patterns were studied by imaging the output face of the fibre onto a vidicon camera. Figure 6.6(a) shows a contour map of the observed near-field intensity pattern (excitation wavelength 1540 nm), while the corresponding computed pattern is shown in Figure 6.6(b). Both plots show a mode that is well confined to the core region and elongated in the direction of the small air holes. In that direction, the air-filling fraction is smaller so the fundamental mode sees a higher effective index in the cladding, while the apparent

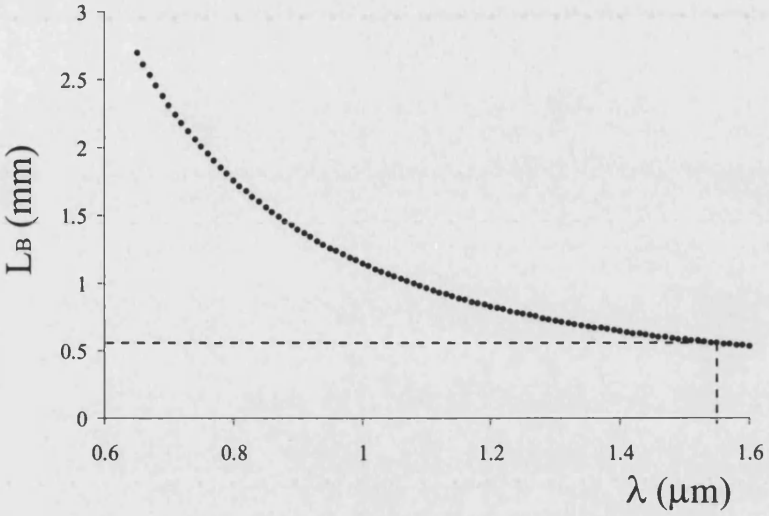

Figure 6.5: Calculated beatlength for fibre IV

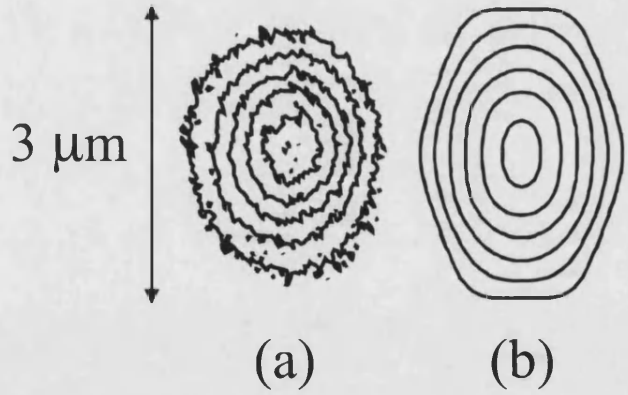

Figure 6.6: (a) Experimental and (b) theoretical contour maps of the near field pattern of the fibre used in the experiment. The experimental contours correspond to 20% steps in the intensity, and the vertical axis corresponds to the direction of the small air-holes. The profiles of the two polarization modes in the fibre are indistinguishable

core size is also larger.

6.4.2 Losses

The main loss mechanisms in PCFs are the same as in conventional fibres: absorption, radiation and confinement.

Losses are measured using a cut back technique. Light from a broadband source (400nm-1600nm) is coupled into several meters of fibre and the transmission spectrum is recorded using an optical spectrum analyser. Then the fibre is cut back to an arbitrarily short length and the transmission spectrum is recorded once more. The difference between the transmission characteristics, normalised by the length that has been cut, gives the loss characteristics.

The losses for fibre IV (see Section 4.4) were not measured, but in general the two period structures fabricated during this Thesis were lossy compared to conventional fibres and recently fabricated PCFs. This is mainly due to two reasons. Firstly, the fact that they had only two periods of air holes, and specially the presence of the small air hole near the core region, made the confinement losses high. Secondly, the fabrication of some of the fibres was not as carefully done as it can be, and then imperfections in the structure and dust in the capillaries and preforms were present. These made the scattering losses to be high.

6.4.3 Effective Area

In order to study the effective area of the fibres, an experimental setup as shown in Figure 6.7 was used. The method employed consists on studying the near field pattern of the fibre whilst using an interferometer to calibrate the image recorded in the CCD camera. For each measurement, two different images of the near field pattern were recorded which differ only in the image position on the CCD array. Then, counting the number of fringes obtained as the image moved across the array (produced by the interferometer which was connected with the translation stage holding the fibre) we could accurately relate the size of the array pixels with the actual displacement. The relationship for the distance between fringes

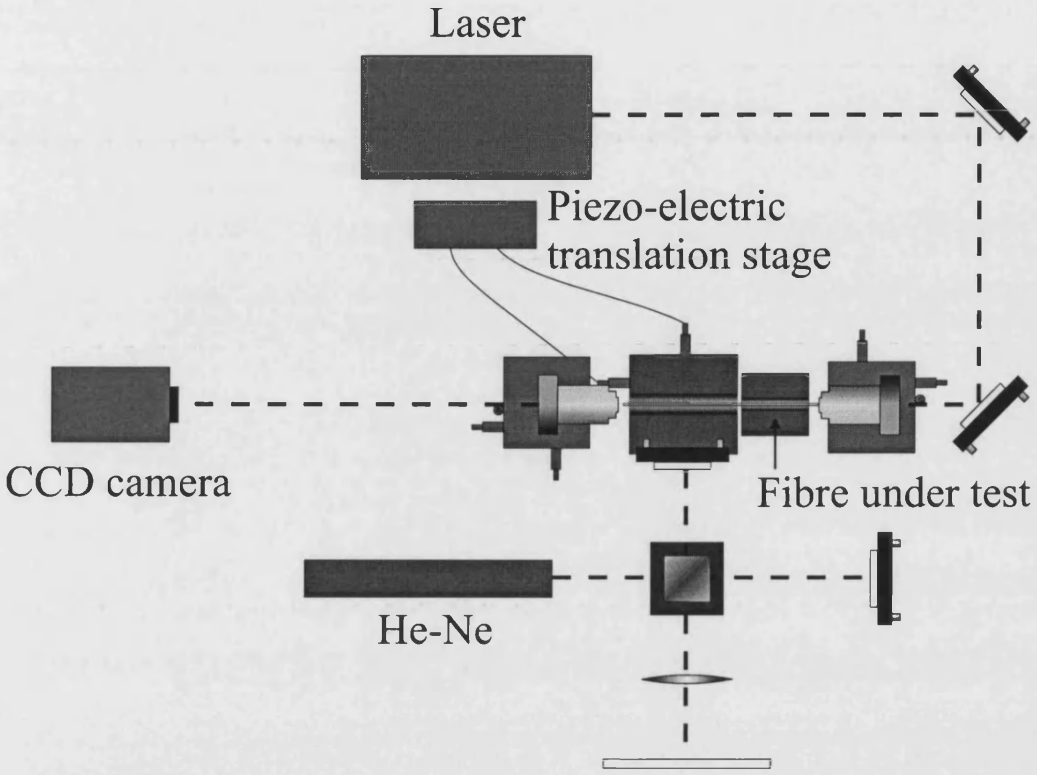

Figure 6.7: Experimental set-up for measuring the effective area

in an interferogram is

$$\Delta d = \frac{N\lambda_0}{2} \tag{6.1}$$

with N the number of fringes and λ_0 the wave length of the laser was used. Using this calibration method and Equation 6.1 several measurements were taken for different wavelengths. The results are summarized in Figure 6.8.

Looking at Figure 6.8, it is seen how the errors added during the experiment lead to a considerable scattering in the measurements. Nevertheless, the increase of the effective area with wavelength is observed. This scattering of the measured points could be caused by several factors. First of all, it has been assumed a linear response on intensity of the CCD. When assuming a linear response for the camera, the intensity ranges from '0' level for the background to '1' level for the maximum intensity. Then, the background of the image is subtracted in order to isolate the mode profile. If the response of the camera would depart greatly from linear, part of the mode profile could have been treated as background and being filtered before the analysis. Another reason is that if the positioning of

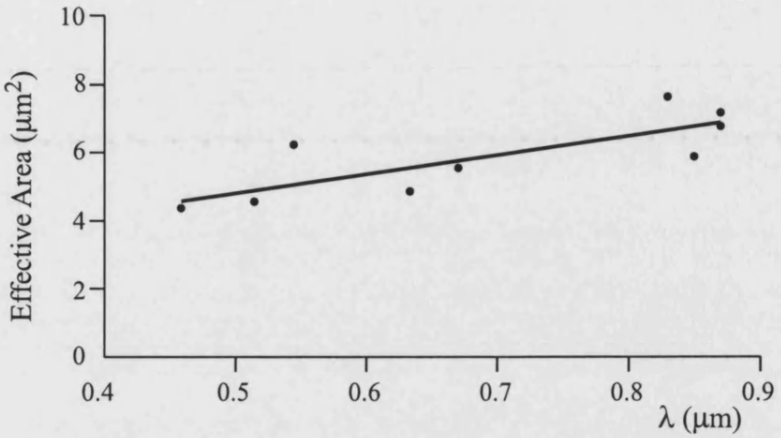

Figure 6.8: Wavelength dependence of the effective area of the Hi Bi PCF

the fibre is not completely perpendicular to the camera, a defocusing will occur when scanning across the CCD array leading to a wrong value for the A_{eff}. Another source of error could be the assumption that the modal distributions are symmetrical with central maxima. The algorithm used to calculate the EA searched for the maximum on intensity assuming that it was on the centre and then used it for positioning the pattern. Then, any departure from the centre position would result in a wrong calculation of the scale of the A_{eff}. At the same time, the fibre was not single mode at these shorter wavelengths and therefore, even though the fundamental mode was excited in all the measurements, there could be some error induced by the presence of higher order modes.

6.4.4 Dispersion

The dispersion of fibre IV was modelled instead of being measured using the method explained in the previous chapter (see Section 5.3). The fibre was modelled using a supercell (Figure 6.4b) and showed anomalous dispersion at wavelengths longer than $1020nm$ and $970nm$ for the two eigenmodes respectively. The dispersion characteristics can be seen in Figure 6.9. It is seen that the zero dispersion wavelengths of the eigenmodes of this fibre are shifted towards the near infrared compared to pure silica and conventional fibres. Considering the relatively large air holes in the cladding the dispersion characteristics can be explained again using the same arguments as in Chapter 5.

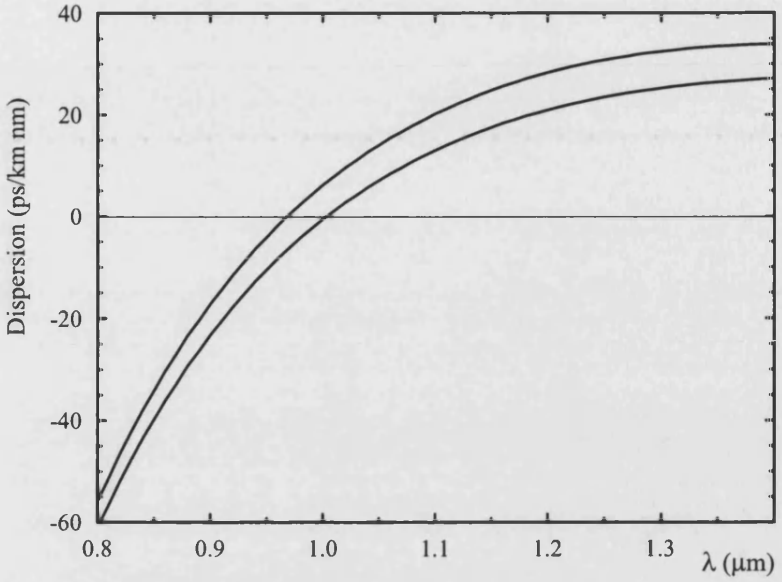

Figure 6.9: Dispersion of fibre IV ($\Lambda = 1.96\ \mu m$, $d_1 = 0.40\ \mu m$ and $d_2 = 1.16\ \mu m$)

6.4.5 Measurement of the beat length

Two different direct methods for measuring the beat length of the fibre were attempted. First, we tried to observe the beat length directly by observing the fibre from the side. When light is propagating in the fibre, an accurate way of measuring birefringence is to count the number of beat lengths by viewing the light emitted from the fibre caused by Rayleigh scattering [5].

As seen in Figure 6.10, if both the fundamental modes in the fibre are launched with equal amplitude (i.e., with the direction of polarization of the light at 45^o to the birefringent axes), the polarization along the fibre progresses from linear to elliptical to circular to elliptical to linear and so on.

When the fields propagate along the fibre, they emit radiation as they drive scattering dipoles. Therefore, the periodic light pattern can be seen by looking at the fibre at an angle of 90^o to the direction of polarization of the light launched into the fibre (see Figure 6.11). The experimental setup, shown in Figure 6.12, was first tested with commercial HI-Bi fibre.

The commercial Hi-Bi fibre used in the experiment was Bow-Tie fibre provided

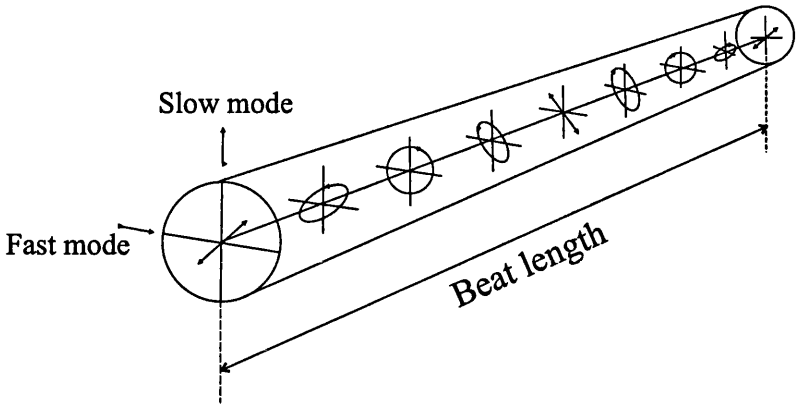

Figure 6.10: Schematic illustration of evolution of light polarization along a birefringent fibre when the input beam is linearly polarized at 45 with respect to the axes

by Fibercore Limited with a beat length of 1 mm at 633 nm. The results are illustrated in Figure 6.11. Figure 6.11(c) shows the fibre orientated at 90° to the direction of polarization of the light and a clear beat pattern can be seen. Figure 6.11(d) is the fibre rotated an extra +45° and the beat pattern is not as clear as before, as we are able to see light scattered from both polarizations. Figure 6.11(e) is the fibre rotated another 45°. The beat pattern is seen again but created this time by the orthogonal polarization as we are now looking on the direction on which the radiation corresponding to the scattered light by the orthogonal mode is maximum. Therefore the complementary pattern to (c) is seen.

Once the method was tested, the experiment was carried out for the Hi-Bi photonic crystal fibre. No beat pattern could be seen as light that is Rayleigh-scattered from the fibre core is subsequently rescattered into different directions by the surrounding air holes.

Secondly, we used an elasto-optic method: the periodic lateral force technique described by K. Takada et al [5, 28]. This technique consists on applying a lateral force on different positions of the fibre when one of the polarization modes is excited. As a result of the force, a coupling in between both polarization modes will occur and placing an analyzer at 45° with the principal axis at the output, a sinusoidal output of the form

$$P = \Lambda + \Omega \sin[\Delta\beta(L - z)] \tag{6.2}$$

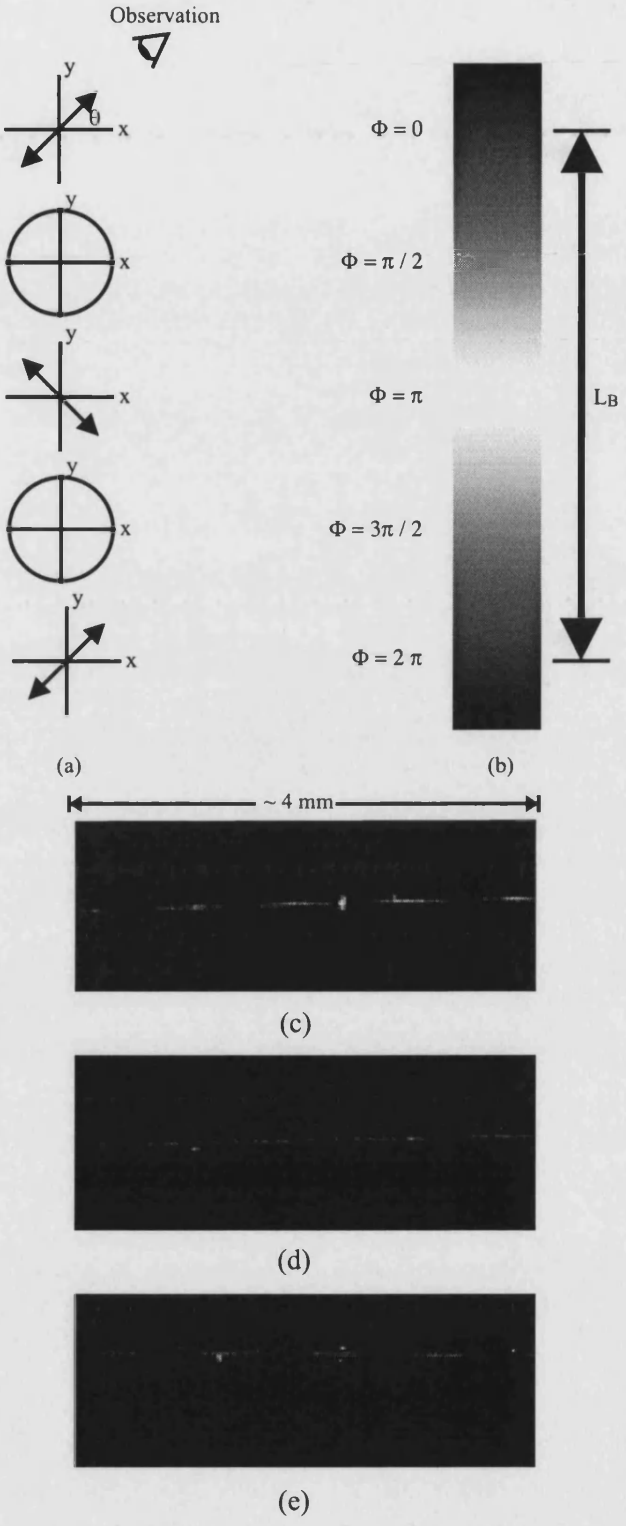

Figure 6.11: Beat length: (a) State of polarisation versus ϕ (z); (b) scattered intensity observed normal to the fibre angle θ and beat patterns observed from the side of the fibre at (c) 90^o , (d) $90^o + 45^o$, and (e) $+90^o + 90^o$ with respect to the direction of polarization of light

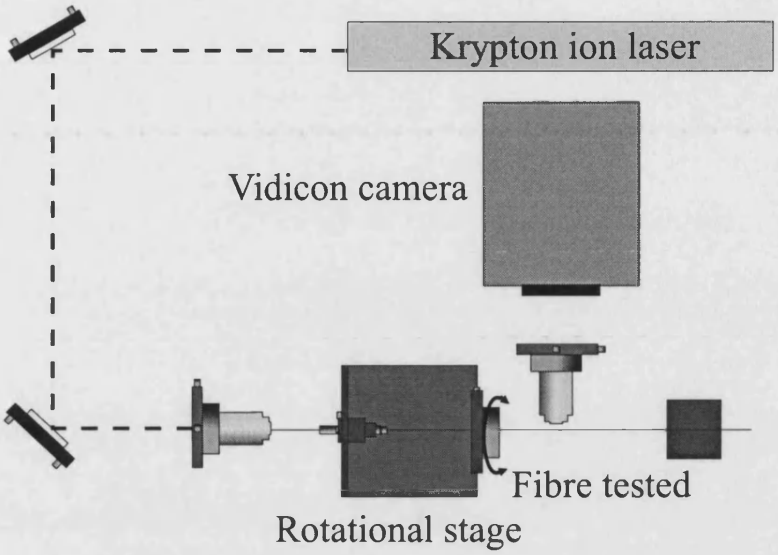

Figure 6.12: Experimental set up for the visual observation of the beat pattern

will be detected, where Λ and Ω are quantities related to the analyser. As we did before, the experimental setup (Figure 6.13) was first tested with the commercial Hi-Bi fibre. The force was applied using a tip attached to a piezo controller. The DC voltage controlled the mean pressure applied into the fibre and then a low sinusoidal signal was overlapped to increase the sensitivity in the detection stage.

The results obtained are shown in Figure 6.14. Fitting equation 6.2 a beat length $L_B = 1.08$ mm was found. Once being tested, the method was used to measure the beat length of the Hi-Bi photonic crystal fibre, but we were again unable to measure it. We attribute this once again to the holey cladding, which is unable to transmit uniaxial stress to the core owing to its strong mechanical anisotropy.

Conventional direct methods having proved to be inappropriate, we were forced to use an indirect approach. We launched light from a tunable diode laser (polarized at 45^o to the principal axes) into a fixed length L of fibre, and monitored the output polarization state as a function of wavelength. The fibre was laid on a flat metal base to avoid bending effects. A polarizer was placed at the output end with its transmission axis aligned at 45^o to the axes of the fibre, and the wavelength was scanned in small steps. Figure 6.15 shows the experimental setup.

The results for a scan from 1530 to 1540 nm are shown in Figure 6.16, showing clear polarization beating for a fibre of length L = 860 mm.

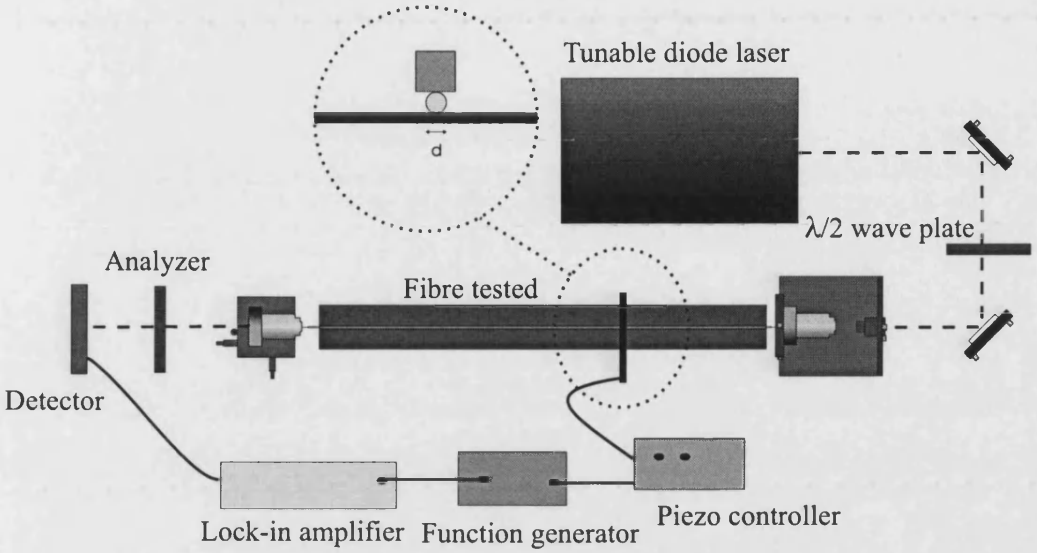

Figure 6.13: Experimental setup for the lateral force technique. The force is applied using a Ta wire of diameter d = 0.125 mm driven by a piezo controller.

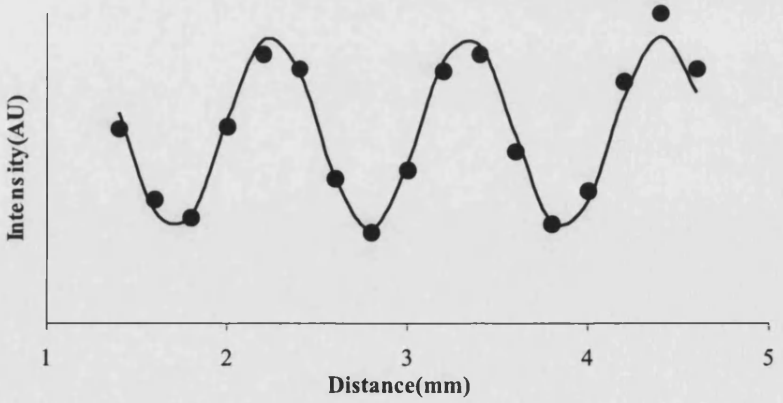

Figure 6.14: Experimental (points) and fitted (line) polarization beat out of the commercial Hi-Bi fibre

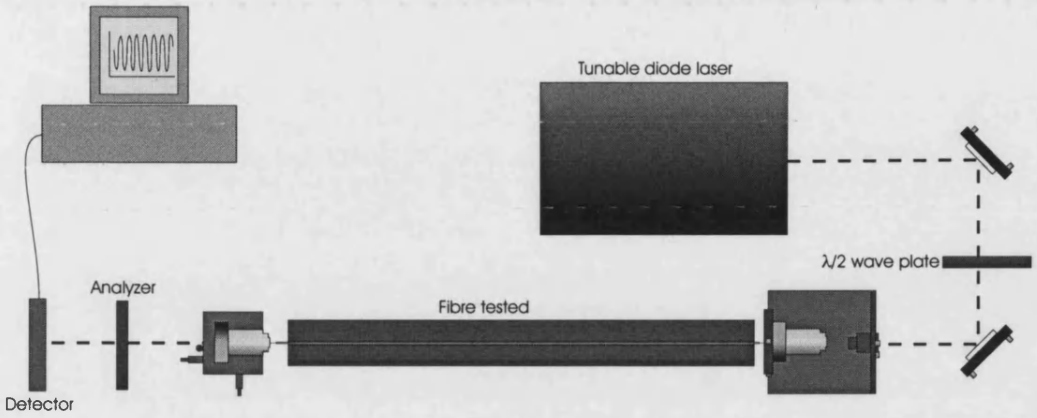

Figure 6.15: Experimental set-up for the wavelength scan technique

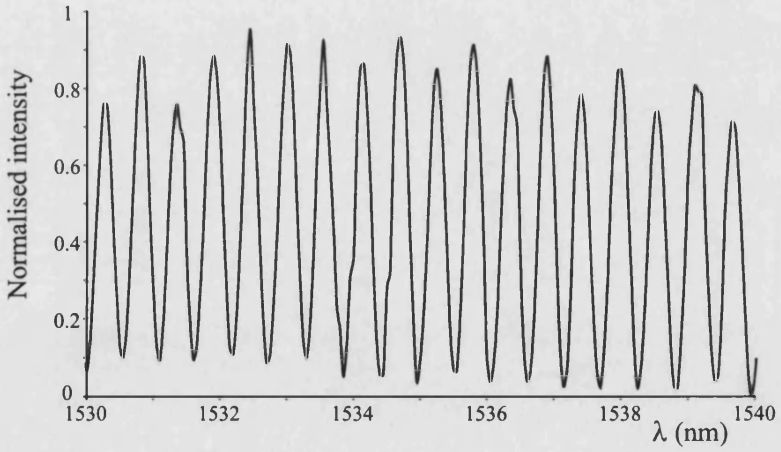

Figure 6.16: Typical plot of the signal transmitted through a polarizer placed at the end of the fibre. The fibre length was 860 mm. Note that the overall transmitted intensity is constant

To relate the observed beat period, $\Delta\lambda = 0.55 \pm 0.01$ nm, to the beat length, L_B, we consider the difference in phase between the modes after a length of fibre, L,

$$\phi = (\beta_x - \beta_y)L = \frac{2\pi L}{L_B} \tag{6.3}$$

using Equation 4.5 for L_B. Differentiating this phase with respect to wavelength and making the total phase change equal to 2π leads to

$$\Delta\lambda = \frac{L_B^2}{L\left|\frac{dL_B}{d\lambda}\right|} \tag{6.4}$$

In order to evaluate this expression for our experimental case, an assumption must be made about the wavelength dependence of L_B. If we assume $L_B \propto \lambda^k$ there is a simple closed form solution for the beat length, given by

$$L_B^{Approx} = \frac{(\Delta\lambda)Lk}{\lambda} \tag{6.5}$$

where L is the actual length of the fibre and λ is the central wavelength of the scan.

A least-squares fit of $L_B \propto \lambda^k$ to values of L_B between 1400 and 1700 nm calculated using our theoretical model (see Figure 6.5), gave $k = 1.38 (R^2 = 0.9992)$. Using this value in Equation 6.5, the observed beating then gives $L_B^{Approx} = 0.42 \pm 0.04$ mm and a modal birefringence $n_x - n_y = 3.7 \times 10^{-3}$ by equation 4.5.

This beat length is more than six times shorter than the beat length of typical conventional high birefringence fibres (see e.g., Newport 1999/2000 catalogue.)

The numerical model was also used to calculate the expected spectral beat period, $\Delta\lambda$. From the theoretical model, we calculated $dL_B/d\lambda = -510$ and $L_B = 0.56$ mm at a wavelength of 1540 nm. Equation 6.4 then gives a theoretical value of $\Delta\lambda = 0.72$ nm, for L = 860 mm as in the experiment. This value can be considered to be in good agreement with the measurement as the model assumes a perfect structure instead of the real one, as shown in Figure 6.4 (b). At the same time, the agreement with the model shows that the most important contribution to the birefringence is form birefringence.

6.5 Polarisation rocking filter

This section presents the results obtained for the fabrication and characterisation of polarisation rocking filters using highly birefringent PCFs. My contribution focused on the fabrication and handling of the fibres whilst the filters were fabricated and characterised with Dr George Kakarantzas. Optical fiber rocking filters are structures that rotate the polarisation state of a linearly polarised optical field launched along one of the principal axes of a birefringent fibre. This is achieved by periodic rotation of the principal axes through a small rocking angle for a length equal to half a polarisation beat length. The periodic rotation can be simply a mechanical twist of the fibre [29] or a periodic exposure of the fibre's photosensitive core to UV light [30]. These perturbations are repeated along the fiber at a period equal to the beat length. Because the beat length is wavelength dependent, there is a resonant wavelength at which the beat length equals the rocking period. At this wavelength, resonant coupling between polarisation states is possible.

Periodic mechanical twisting of the fibre was used to make the rocking filters. A section of the fibre, about 1 cm, was held fixed by two clamps with one of the clamps resting on the arm of a rotational motor that was oscillating through a fixed angle with a constant speed at a given frequency. The twist built into the fibre was accomplished with the heat generated from a fast scanning focused CO_2 laser beam [31]. It is necessary that the temperature due to CO_2 laser heating is sufficiently high to introduce a significant deformational twist while avoiding the collapse of the holes of the PCF. This was achieved using sweep rates faster than the hole collapse relaxation time. For a given rocking angle, the twist period can be defined by two parameters, the sweep rate of the laser beam and the rocking frequency of the motor. For the present experiments we used a rocking angle of 7^0. When the twist period is set, the number of periods can easily be determined by varying the sweep length of the laser beam. There was enough deformational twist generated by the process to be seen by visual inspection of the fibre. The experimental set up is shown in Figure 6.17

A scanning-electron micrograph of fibre used in the experiment is shown in Figure 6.18. The fibre had a pitch $\Lambda = 1.46\mu m$ and hole diameters of $d_1 = 0.54\mu$ m for the small holes and $d_2 = 1.14\mu m$ for the large ones. The external fibre diameter was $125\mu m$. The estimated beatlength from supercell simulations at $\lambda = 1550nm$

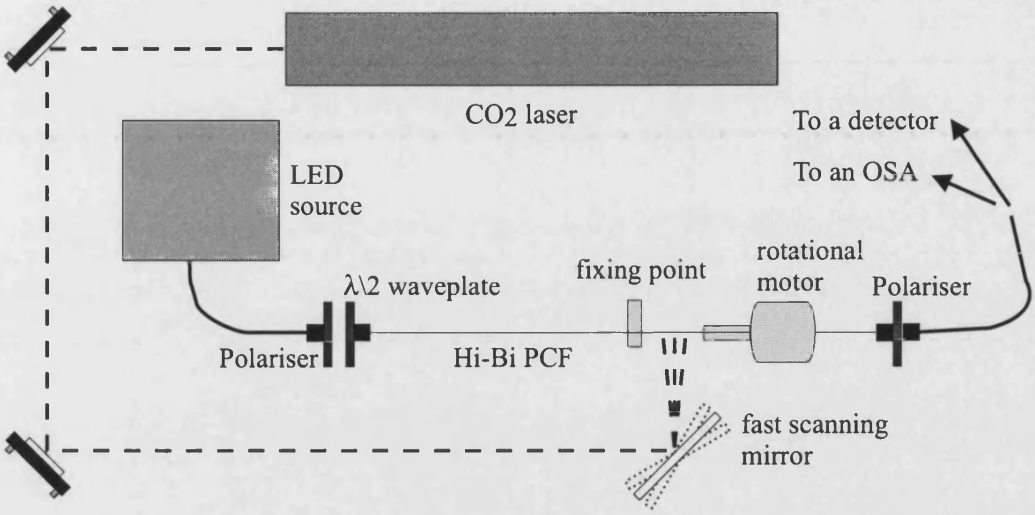

Figure 6.17: Experimental set up for the fabrication of rocking filters

is $L_B = 410\mu m$, which gives a birefringence of $B = 3.8 \times 10^{-3}$.

The transmission spectra of the rocking filters were measured by launching polarised light from a broadband LED source along one of the birefringent axis of the fibre and then monitoring the signal after passing through a second polariser with an optical spectrum analyser. Figure 6.19 shows the transmission spectra of two rocking filters made on two different pieces of the same fibre. The filters were made using different period lengths of $480\mu m$ (grey line) and $420\mu m$ (black line) using laser beam sweep rates of 7 mm/s and 5.5mm/s with the wavelengths for maximum conversion being 1554 nm and 1264 nm respectively. This is also an excellent way to measure of beatlength of the fibre directly. Very good coupling efficiencies were achieved with only 20 periods, total device length of $7mm$ and total fabrication time of 1 second.

The bandwidth of a rocking filter can be estimated from the number of twist periods. The bandwidth is approximately the inverse of the number of full period sections [29]: $\Delta\lambda/\lambda\ N-1$ where $\Delta\lambda$ is the bandwidth at FWHM, λ is the resonant wavelength and N is the number of periods. The predicted bandwidth for the long and short wavelength rocking filter is 78 nm and 63 nm respectively, which are with good agreement with the measured 70 nm and 55 nm.

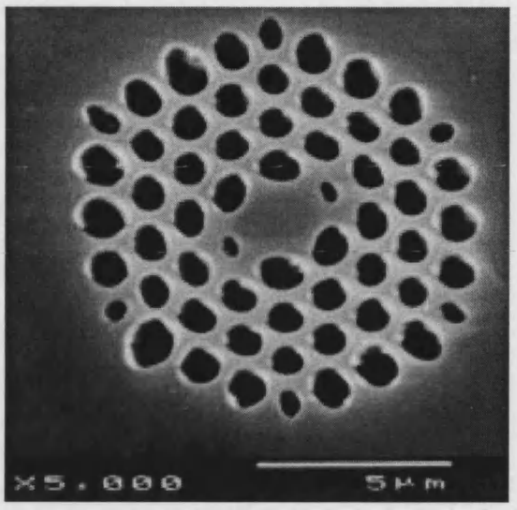

Figure 6.18: Scanning electron micrograph of fibre V

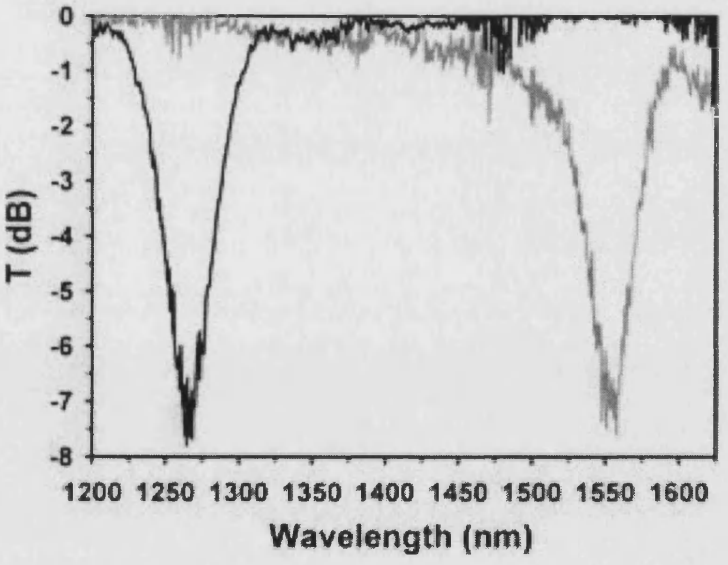

Figure 6.19: Polarisation coupling spectra for rocking filters with period lengths of $480\mu m$ (grey line) and $420\mu m$ (black line) fabricated on fibre V

6.6 Conclusion

We have shown how to develop a photonic crystal fibre with a high modal birefringence. Several techniques for characterising these kind of structures have been shown.

A beat length of 0.4 mm at 1540 nm has been demonstrated. We have also shown that the unusual optical properties of the PCF cladding are accompanied by unique mechanical properties, making it difficult to measure the beat length directly. Unlike conventional optical fibres with solid cladding materials, PCFs permit easy incorporation of large optical and mechanical inhomogeneities by altering the geometry, size and position of the cladding holes.

We have presented results for the fabrication of rocking filters in non-photosensitive highly birefringent PCF for the first time. Very good coupling efficiencies were achieved for lengths as short as 7 mm. Furthermore, a new and highly versatile fabrication method using periodic mechanical twisting of the fibre along with heating from a scanning CO_2 laser beam has been implemented. One of the great advantages of the method is that there is not an upper limit to the range of rocking angles that can be used, in contrast with the UV-written rocking filters. As a consequence, the number of coupling steps can be reduced and even shorter (and hence very broadband) rocking filters can be fabricated.

Chapter 7

Highly birefringent photonic crystal fibres: Nonlinear characterisation

7.1 Introduction

The massive nonlinearity and unusual group velocity dispersion characteristics that can be achieved in PCFs make them spectacular vehicles for nonlinear fiber optics.

With the aim of getting a deeper understanding of the nonlinear characteristics of PCFs, a family of Highly Birefringent PCFs were fabricated which showed anomalous group velocity dispersion in the wavelength window of the laser available to us. These kind of fibres were chosen to avoid unwanted polarisation effects during the experiments. Most of the PCFs previously used to study nonlinear processes in PCF have exhibited some birefringence due to small departures from their symmetry. Doing experiments on structures where a deliberate birefringence has been introduced, ensures that only one of the polarisation eigenmodes is excited and therefore there is no cross effect between eigenmodes.

In this Chapter experimental evidence of soliton transmission and soliton self-frequency shift in Highly Birefringent PCFs are presented.

7.2 Pulse characterisation methods

To fully characterise the transmission of the pulses propagating down the fibres, they have to be characterised in the frequency and in the time domain. Pulses from a modelocked Ti:sapphire laser oscillator (Coherent Mira900) were launched into the fibre at different wavelengths. The pulses were 200 fs in duration with a repetition frequency of 76 MHz. Output spectra were measured using a grating-based optical spectrum analyser (Ando AO-6315B). The resolution was set to 5 nm and spectra were measured across the full range of interest for each case. The absolute power measured is nominally calibrated over the entire range, however there are some notable artifacts associated with the broad measurement bandwidth, requiring different detectors and discrimination of overlapping grating orders. These artefacts were of no relevance to the results presented here. The time domain characteristics of the pulses were measured using an optical autocorrelator.

Even the fastest optical detectors are unable to measure pulse durations shorter than a few tens of picoseconds. Therefore, the only thing fast enough to measure these pulses is the pulse itself. This can be done by performing an autocorrelation in a crystal of the pulse with itself, using a nonlinear detection mechanism. The most common form of autocorrelation is by second harmonic generation. However, recently it has been shown that an LED is a suitable nonlinear element for characterising femtosecond pulses. The first experimental set up implemented can be seen in Figure 7.1.

The autocorrelator consists on a Michelson interferometer with one of the mirrors mounted on a speaker. The speaker was drive at low frequency and allowed us to get autocorrelation traces in real time. A commercially available LED was used as the nonlinear detection system. The mechanism for the nonlinear effect in LEDs and photodiodes is two-photon absorption [32, 33]. Two-photon absorption works to convert the optical signal at the fundamental wavelength directly into the photocurrent. An electron in the valence band of a semiconductor absorbs two photons, which give it enough energy for promotion to the conduction band. Hence, the photons must have a minimum energy of half the bandgap energy, so that two could move an electron from the top of the valence band to the lowest level of the conduction band. The wavelength limit of this is when the photon energy is equal to the bandgap energy, so the photons are absorbed directly. For

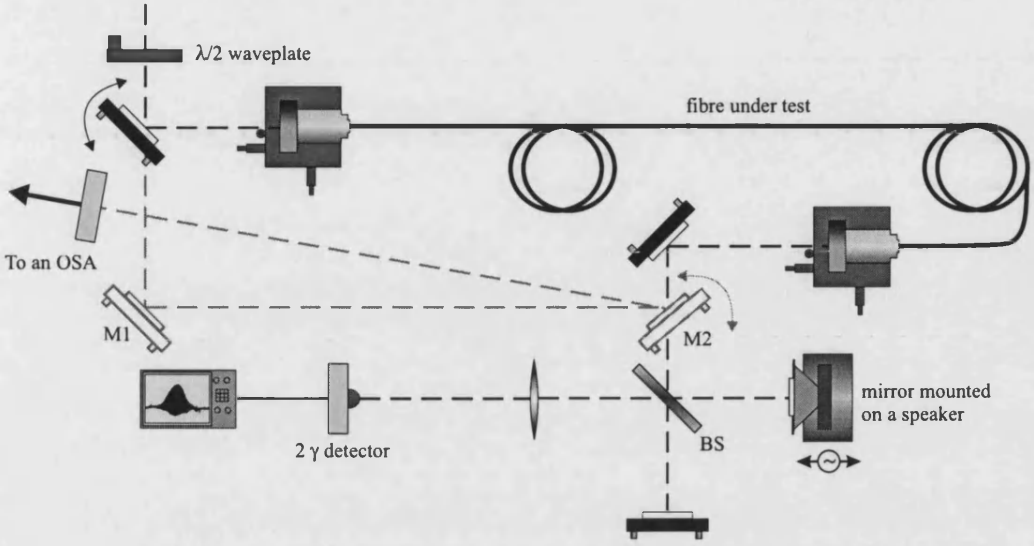

Figure 7.1: Experimental set-up of the autocorrelator based on a two-photon detection system

measurements at other wavelength ranges, it is possible to use other photodiodes with band gap energies that satisfy the two-photon condition. The use of a two-photon photodiode has the advantage that it transforms the autocorrelation signal into an electrical current with a single device and that the system is far easier to align and less expensive than systems based on a doubling crystal.

The beam coming from a mode-locked Ti:sapph laser is launched into the fibre after passing through a half wave-plate to match the polarisation of the beam with the main polarisation axis of the fibre. The output of the fibre is analysed with the optical spectrum analyser and with the autocorrelator. In order to align and calibrate the system, mirrors M1 and M2 bring the laser beam straight into the autocorrelator. When using the laser beam, a very clear interferometric autocorrelation of the laser pulses is seen. As the wavelength of the laser is known we can accurately calibrate and measure in the time domain by resolving the recorded pattern down to the interferometric fringes (see Figure 7.2). The time scale shown in Figure 7.2 corresponds to the time scale of the oscilloscope.

The problem encountered with that kind of configuration was that the energy threshold needed to get autocorrelation traces was too high and therefore autocorrelation traces of the pulses coming out of the fibre could not be recorded because of their low energy. A new autocorrelator was implemented as shown in

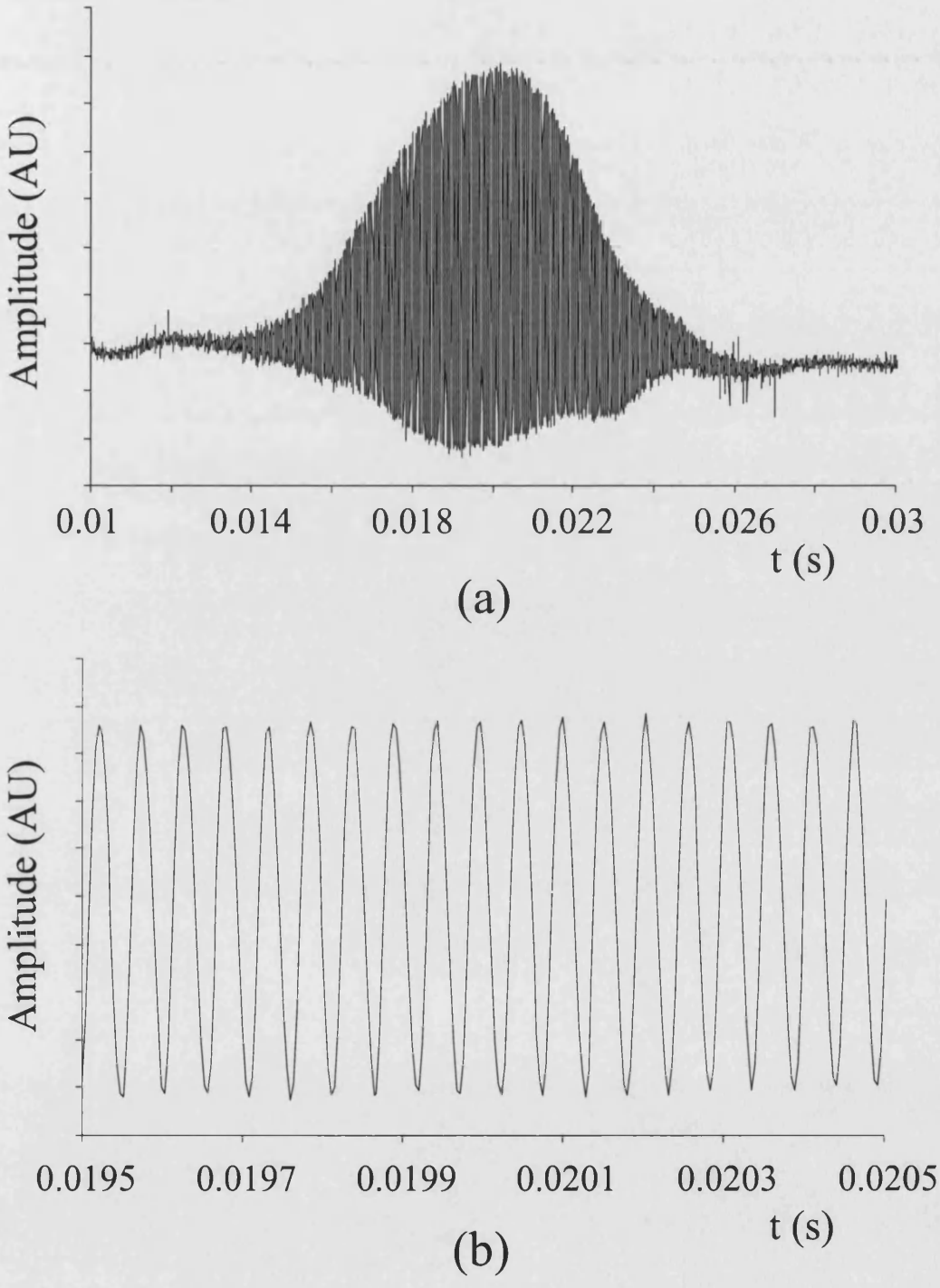

Figure 7.2: (a) Interferometric autocorrelation trace and (b) resolved interferometric fringes of the pulses from a Ti:sapph laser

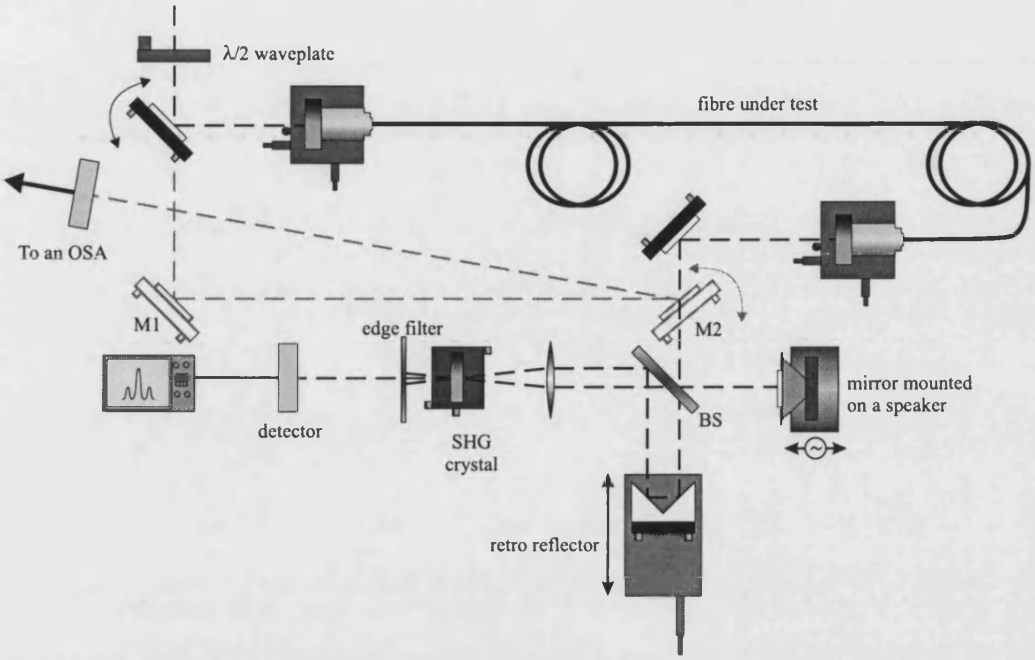

Figure 7.3: Experimental set-up of the autocorrelator based on a second harmonic generation detection system

Figure 7.3

The input pulse passes through a Michelson type arrangement and the correlation of the pulses is designed to occur within the nonlinear crystal (BBO). Pulses in one arm of the interferometer have a temporal delay t relative to the other arm. Translating one of the mirrors about a point of coincidence varies the optical delay in the interferometer. Real-time monitoring of the autocorrelation function is accomplished by mounting one of the mirrors on an loudspeaker which is made to scan at 5 Hz. As the speaker moves in and out the path length for the second half of the pulse is changed, so a delay is introduced into its arrival time at the crystal. When the path lengths for the two pulses are equal, the pulses will exactly coincide at the crystal and the amount of second harmonic light generated will be a maximum. As the speaker changes the delay, the second harmonic generation will drop. The speaker frequency is much less than the pulse repetition frequency, so the autocorrelation trace is made up from the second harmonic produced from many pulses, each subject to a different delay time. Since the intensity of SH is proportional to the product of the intensities of the two beams, its measurement as a function of relative time delay between them would provide the autocorrelation function. The pulse duration can be deduced

from the FWHM of the autocorrelation function provided the hyperbolic secant pulse shape is assumed.

Once more, the beam coming from a Ti:sapp laser was launched into the fibre after matching the polarisation of the beam with the main polarisation axis of the fibre. The output of the fibre was analysed with the optical spectrum analyser and with the autocorrelator.

Two different kinds of Highly Birefringent PCFs were used for the experiments. The first fibre (fibre VI) is the equivalent of a cob-web fibre with polarisation-maintaining PCFs, i.e. an elliptical core surrounded by an array of very large holes. With these kinds of structures nonlinear effects are enhanced as they effectively are silica cores suspended in air by very thin silica webs. Therefore you can approximate the structure by assuming that the fibre behaves as an isolated strand of silica surrounded by air [34]. As explained later, the losses of this fibre proved to be very high (around 60 dB/m) and so a second fibre was fabricated. Fibre V (the same structure used for the rocking filter experiments explained in Chapter 6) consists of an elliptical core region surrounded by 4 periods of air holes acting as the cladding (see Section 4.4). The losses of the fibre were measured as well. The fiber had a relatively high loss of around 0.3 dB/m in the wavelength region from 800nm to 1 μm, with higher losses at shorter wavelengths and smaller losses at 1.5 μm as seen in Figure 7.4. These losses were a vast improvement compared to the previous structure.

7.3 Soliton transmission

A Ti:sapphire laser was used to launch pulses (850 nm, 76 MHz repetition rate) of different energies into fibre VI. A half wave-plate was used to adjust the linear polarization state at the input. The output of the fibre was then analysed using an intensity autocorrelator and an optical spectrum analyser. Once the polarisation axes of the fibre were determined, we analysed the output of the fibre for different input powers for both polarisations. First, the output pulse duration at relatively low input energies was investigated. Figure 7.5 shows the results from the autocorrelator for both polarisations. As the input power increases the output pulse width decreases. This can be explained in terms of the linear chromatic

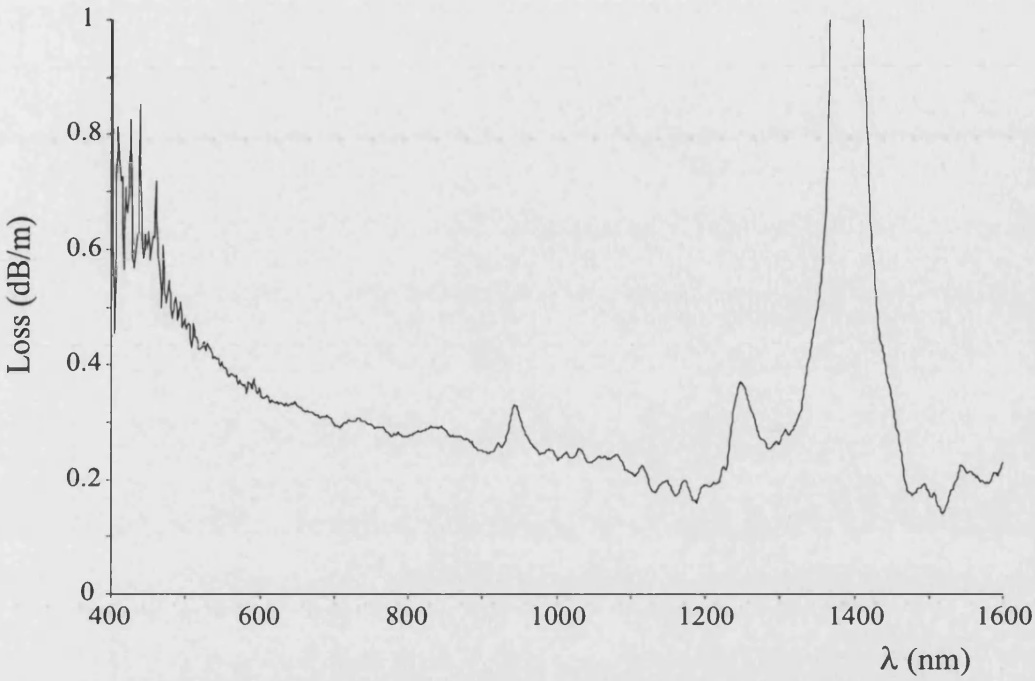

Figure 7.4: Measured losses of fibre V

dispersion and self phase modulation starting to compensate each other. After reaching a minimum, the pulse starts spreading again. From the modelling, and knowing that the modes have an effective area of 4.4 μm^2, the soliton energies can be calculated (see Section 4.4.2). The corresponding average powers for the fundamental soliton are 0.65 mW and 1.21 mW respectively. This obviously does not match the results obtained. This mismatch can be mainly attributed to the high losses of fibre VI. The measured loss at the pump wavelength was 60 dB/m and therefore it is clear that most of the power is lost during propagation, making reliable power measurements very difficult. At higher energies, typical two-peak autocorrelation traces were detected, showing the spectrum analyser that they corresponded to soliton self frequency shifts. Due to the losses once more, it was not possible to do a detailed study with power or to do a reliable cut-back measurement to study the frequency shift.

For all the above, a second structure, fibre V, with significantly lower losses, was fabricated. The results are shown in Figure 7.6. Both polarisation eigenmodes show similar behavior with power. At low energies (up to 0.1mW average power) the pulse is substantially broadened by linear dispersion (output pulse length greater than 1ps for the eigenmode with the longer zero dispersion wavelength).

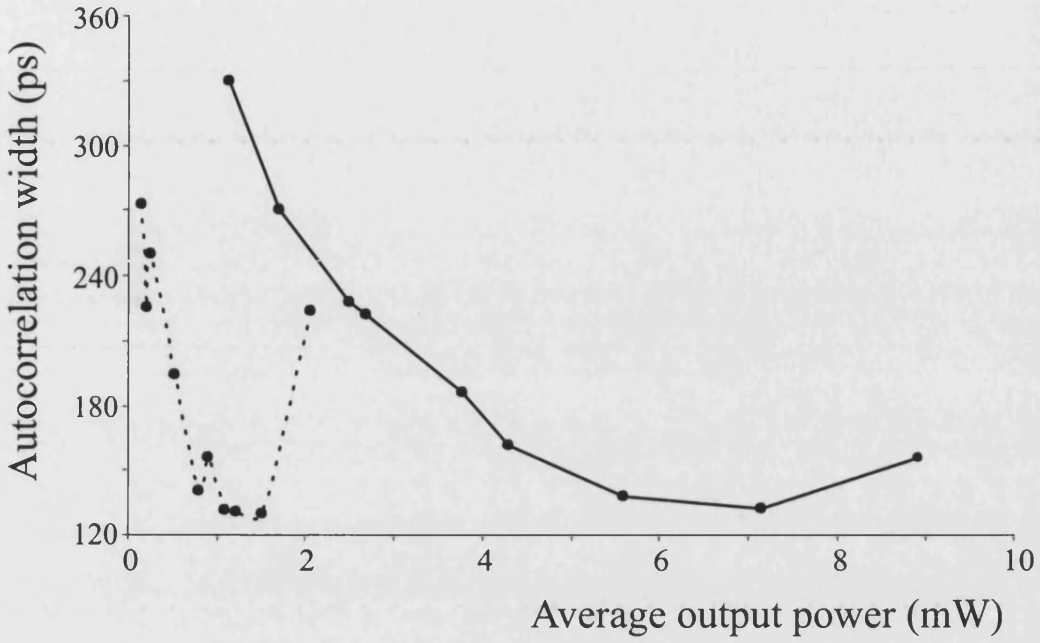

Figure 7.5: Autocorrelation width for different powers for both polarisation eigenmodes of fibre VI

The pulse then compresses down to around 90 fs at an average output power just below 1mW, corresponding to an input power of around 1.4mW (according to the losses for a 6 m piece of fibre). These values can be identified with excitation of the fundamental solitons for each case. It is seen that the data for the autocorrelation traces for the eigenmode with the shorter zero dispersion wavelength (squares) is not as conclusive as the other mode.

7.4 Soliton self-frequency shift

When the power is increased, it is observed how the soliton starts shifting in frequency (see Figure 7.7) [35, 36]. This shift is very pronounced and with just 5 mW average power, a shift of almost 100 nm is observed. Figure 7.7 (a) shows the spectra for different powers. It clearly shows that as the power is increased (traces 1 through 7) the wavelength shift increases as expected. It is worth noting that this results are for a fixed length of fibre and therefore the same effect would be expected for a fixed power and different lengths of fibre. Soliton self-frequency shift in PCF was reported later as well by other research groups [37, 38, 39].

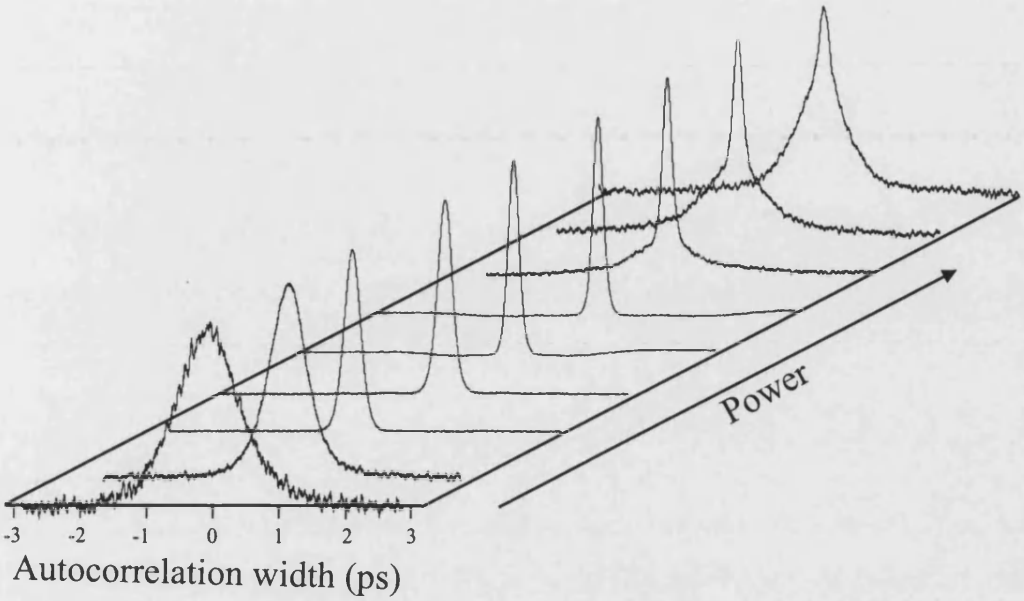

(a)

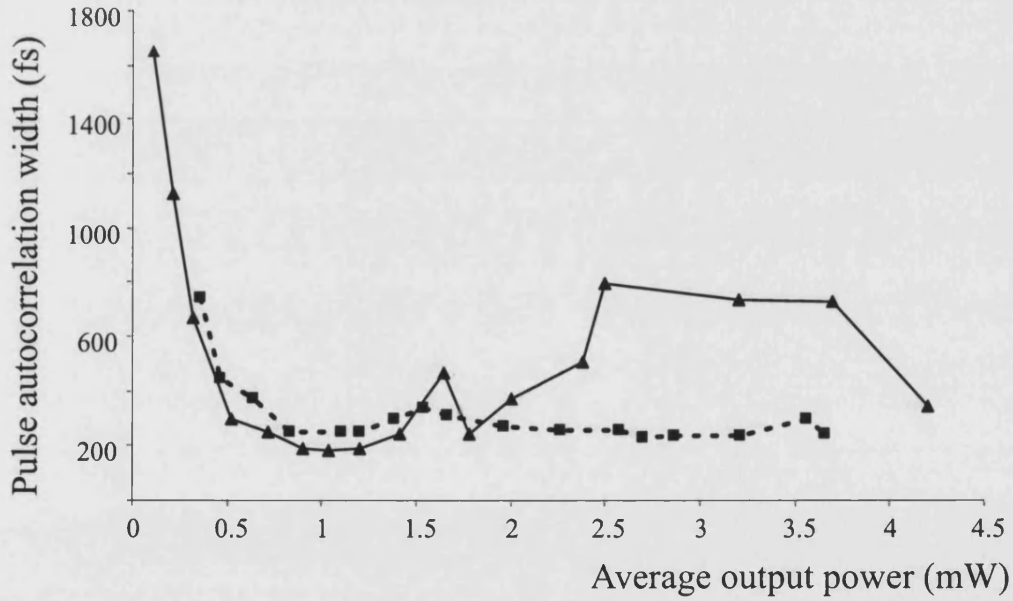

(b)

Figure 7.6: (a) Autocorrelation traces for the eigenmode with longer zero dispersion wavelength and (b) autocorrelation width of both polarisation eigenmodes of fibre V at different powers

Finally, it can be seen how after a pronounced shift, trace 7 shows a second peak emerging from the pump region. This phenomenon will be explained in the next chapter.

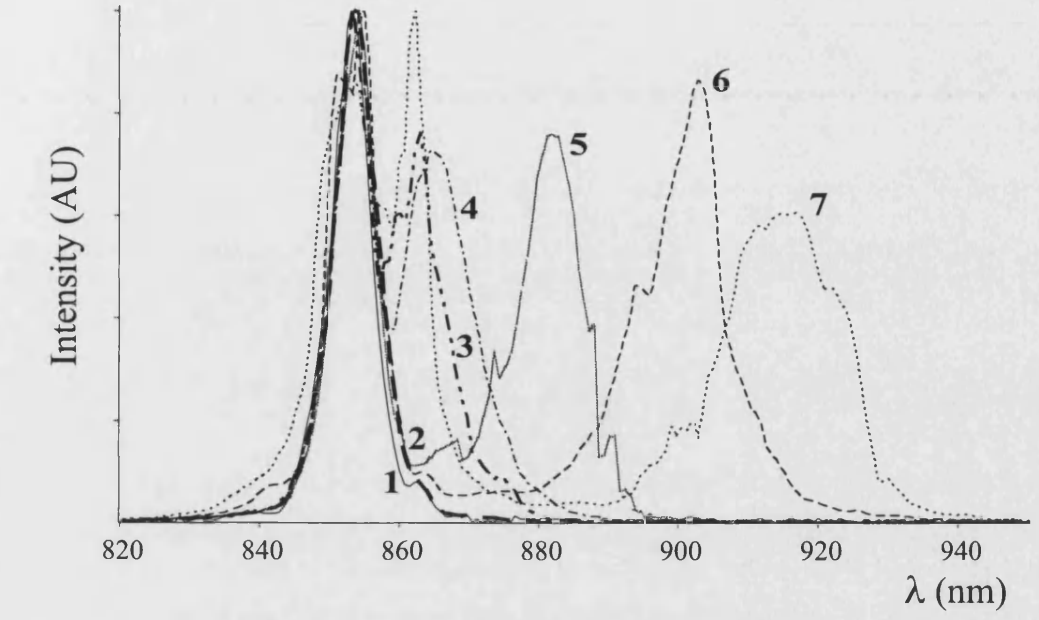

(a)

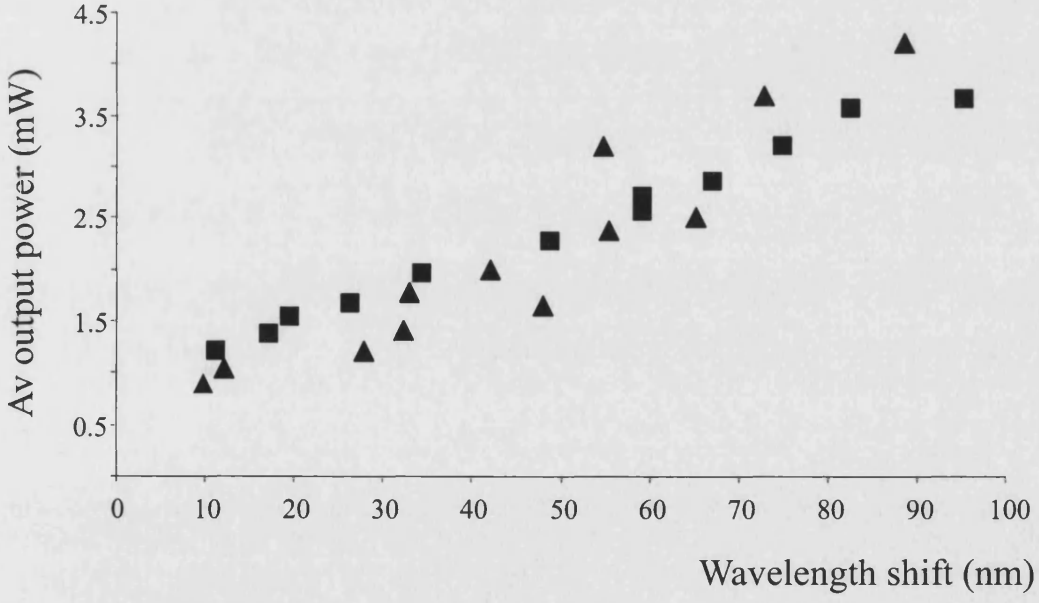

(b)

Figure 7.7: (a) Spectral measurements for the eigenmode with longer zero dispersion wavelength and (b) soliton self frequency shift of both polarisation eigenmodes of fibre V at different powers

7.5 Conclusions

Soliton propagation in the near infrared and soliton self-frequency shift in Highly Birefringent PCFs have been demonstrated . Whilst normal PCFs can exploit the modified dispersion characteristics attainable in these structures for demonstrating soliton transmission in the near infrared [40], Highly Birefringent PCFs allows one to co-propagate solitons on both polarisation eigenmodes at once with negligible cross-talk. This opens new opportunities for telecomunication applications of these kind of structures [20].

Soliton self-frequency shift has been observed and shows how, due to the high nonlinearity of these structures, very low power thresholds are needed for very efficient soliton wavelength shifts. This technique provides a convenient and novel source for femtosecond pulses in a wide wavelength range.

Chapter 8

Supercontinuum generation in highly birefringent photonic crystal fibres

8.1 Introduction

For the last two years, supercontinuum (SC) generation in photonic crystal fiber (PCF) by ultrashort pulse propagation has become a subject of intense worldwide study. This is mainly because the pulse energies required to generate a SC are very low, and the spatial purity and intensity of the SC (which is generated in the fundamental mode of the optical fiber) are very high. First demonstrated by Ranka *et al.* [41], the frequency spectrum can stretch more than two octaves from the UV into the infrared and has found applications in fields such as frequency metrology [42] and optical coherence tomography [43].

In this chapter results for the experimental study of the mechanism for SC generation when pumping a PCF with femtosecond and picosecond pulses are shown. I will first present results for low power spectra, showing evidence for an important mechanism for SC generation when pumping with femtosecond pulses: Soliton breaking is accompanied by the generation of phase-matched radiation at shorter wavelengths than the pump, leading to an ultrabroad SC. Then, results for high power spectra will be presented. Well-characterised polarization-

maintaining fibers have been used to perform the experiments at different pump wavelengths and for different fiber lengths, in order to understand the role of these parameters. We present results showing the generation of supercontinua even when the fibre is pumped in the normal dispersion regime, where we can identify some elements of the same physical mechanism.

Preliminary results for SC generation when pumping with picosecond pulses are shown at the end of the chapter.

8.2 Pulse breaking

The role of pulse breaking in the generation of new frequency components has been extensively studied in conventional fibers. Beaud *et al.* [44] performed experiments using picosecond pulses in the vicinity of the zero dispersion wavelength of a conventional optical fiber. Although the input powers used were sufficient to generate high order solitons, they observed temporal and spectral break-up of the input pulse, leading to pulse narrowing and a series of solitonic features that shifted to lower frequencies due to Raman effects. In 1989, Islam *et al.* [45], reported femtosecond distributed soliton spectra using picosecond pump pulses in the anomalous dispersion regime of a conventional fiber. Their results show how modulation instability is responsible for pulse break up, creating several solitons. These then collide to form intense narrow pulses which frequency shift due to Raman effects. Averaging over these frequency shifted solitons yields a spectrum spanning 300 nm.

The development of PCFs in the last few years has resulted in SC spectra extending not only to the long wavelength side of the pump, but also to much higher frequencies. For the last two years there has been a lot a research interest on the subject, experimental and theoretical, which has mainly concentrated on the characterisation of the spectra generated by these kind of structures and the influence of parameters such as the pulse duration and the pump wavelength, the chirp, and more recently, the coherence and noise characteristics [46, 47, 48].

Regarding the physical mechanism behind SC generation a unified simple explanation is still to come based on known nonlinear mechanisms such as Raman

amplification, modulation instability or four-wave mixing. Some work to date includes Husakou, Herrmann and co-workers [49, 50] and their proposal of fission of higher-order solitons into redshifted fundamental solitons and blueshifted nonsolitonic radiation.

8.3 Supercontinuum generation with femtosecond pump pulses

All the experiments described here were performed using a tunable Ti:sapphire laser (76 MHz repetition rate, 200 fs FWHM pulse duration), launched in one of the polarization eigenmodes of the fibres. Three different kinds of Highly Birefringent PCFs were used in the experiments: Fibre V, Fibre VI and Fibre VII (see Section 4.4). A zero order half wave-plate was used to adjust the linear polarization state at the input. The output of the fiber was then analysed using an intensity autocorrelator (based on second harmonic generation) and an optical spectrum analyser. The polarisation state of the output was analyzed to ensure that the light remained in the same polarisation axis as it was launched in.

The experiments at low power were carried out for different pump wavelengths in different lengths of fibre. The first experiments were done pumping at 850 nm in a 6 meter length of fibre. Then, experiments for a longer piece of fibre (16 m) for different pump wavelengths were done. After these, experiments to test the stability with length and to test the generation of SC in the normal dispersion regime were done.

8.3.1 Low power experiments

Pump at 850 nm for a fibre length of 6 m

Results for a 6 m length of fiber V and a pump wavelength of 850 nm are presented first. The eigenmode with the smaller anomalous dispersion (20 ps/nm.km) at the pump wavelength was excited and the output of the fiber analysed for different input powers. We showed in Chapter 7 how at low energies the pulse is

substantially broadened by linear dispersion and then compresses down. This value of 66 W(corresponding to an input peak power of about 92 W) correspond to the fundamental soliton energy. Then, a pronounced pulse splitting and soliton shelf frequency shift (SSFS) was observed for higher input powers above the first soliton energy. A shift of up to 120 nm was observed for a peak output power of 203 W (corresponding to Figure 8.1, output peak powers from 68 W to 203 W). As the power was increased further a second separate peak split off from the pump and also started shifting in frequency. At the same time, the original self-shifting soliton that appeared at a lower power kept shifting towards longer wavelengths (Figure 8.1, 289 W output power). The generation of a second self-shifting peak is accompanied by the appearance of a blue-shifted peak at a wavelength around 600nm. As the input power was increased further, a third new spectral peak developed, being fully independent at around 618 W output power. It is worth noting that the relationship between the measured output powers and the input powers and calculated powers becomes complicated by the nonlinear losses in this regime (the soliton features at longer wavelengths have lost a significant fraction of their energy through Raman scattering). Further increases in power lead to further self-frequency shifts in the existing peaks and the appearance of new peaks. These are accompanied by the appearance of new blue-shifted peaks as well. At yet higher pump energies (e.g. 6 kW peak power) all those peaks merge to give a continuous spectrum of peaks - a broadband supercontinuum. For high powers, pulse break up occurs after an increasingly short propagation length, so that just a few centimeters of fibre are required to observe supercontinuum generation [41]. At the higher powers, pulse breakup is surely accompanied by other nonlinear mechanisms such as modulation instability [45] and four-wave mixing which serve to diffuse the distinctive features observed at low energies. Previous studies reported shot to shot variations on their spectra [45, 51]. We were unable to study this effect and therefore our observations correspond to output spectra averaged over a great number of pulses.

Having observed these effects in the frequency domain, we used the autocorrelator to study the fiber output in the time domain [47, 48]. The autocorrelation results showed that the appearance of new peaks in the frequency domain corresponds to new pulses generated in the fiber that propagate at different speeds. An example is presented in Figure 8.2 showing the output of the autocorrelator at different pulse energies.

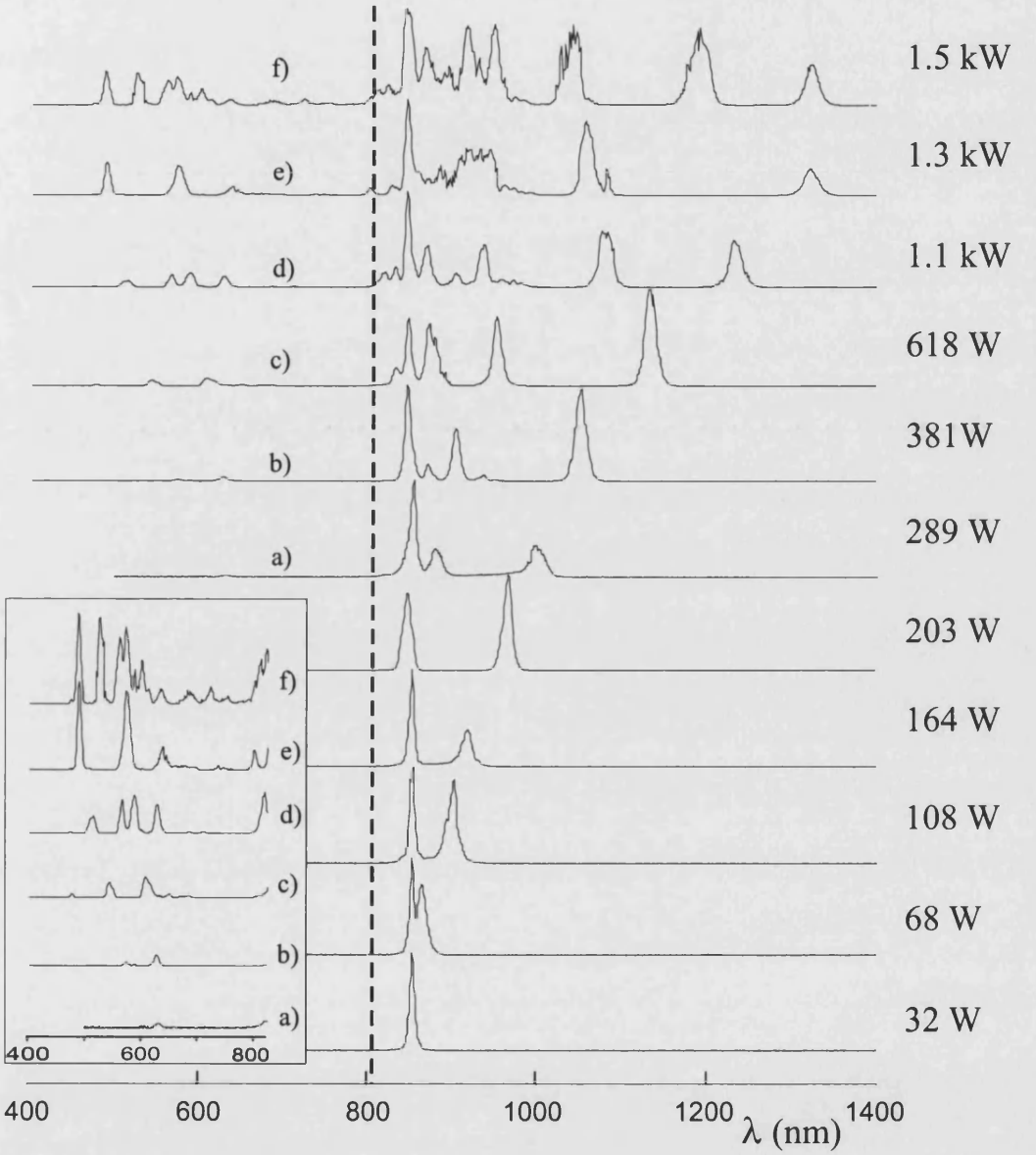

Figure 8.1: Recorded spectra at a pump wavelength of 850 nm for different peak powers coming out of fibre V. The dotted line indicates the zero dispersion wavelength at 806 nm. (Inset) Detail of the spectra from 400 nm to 800 nm

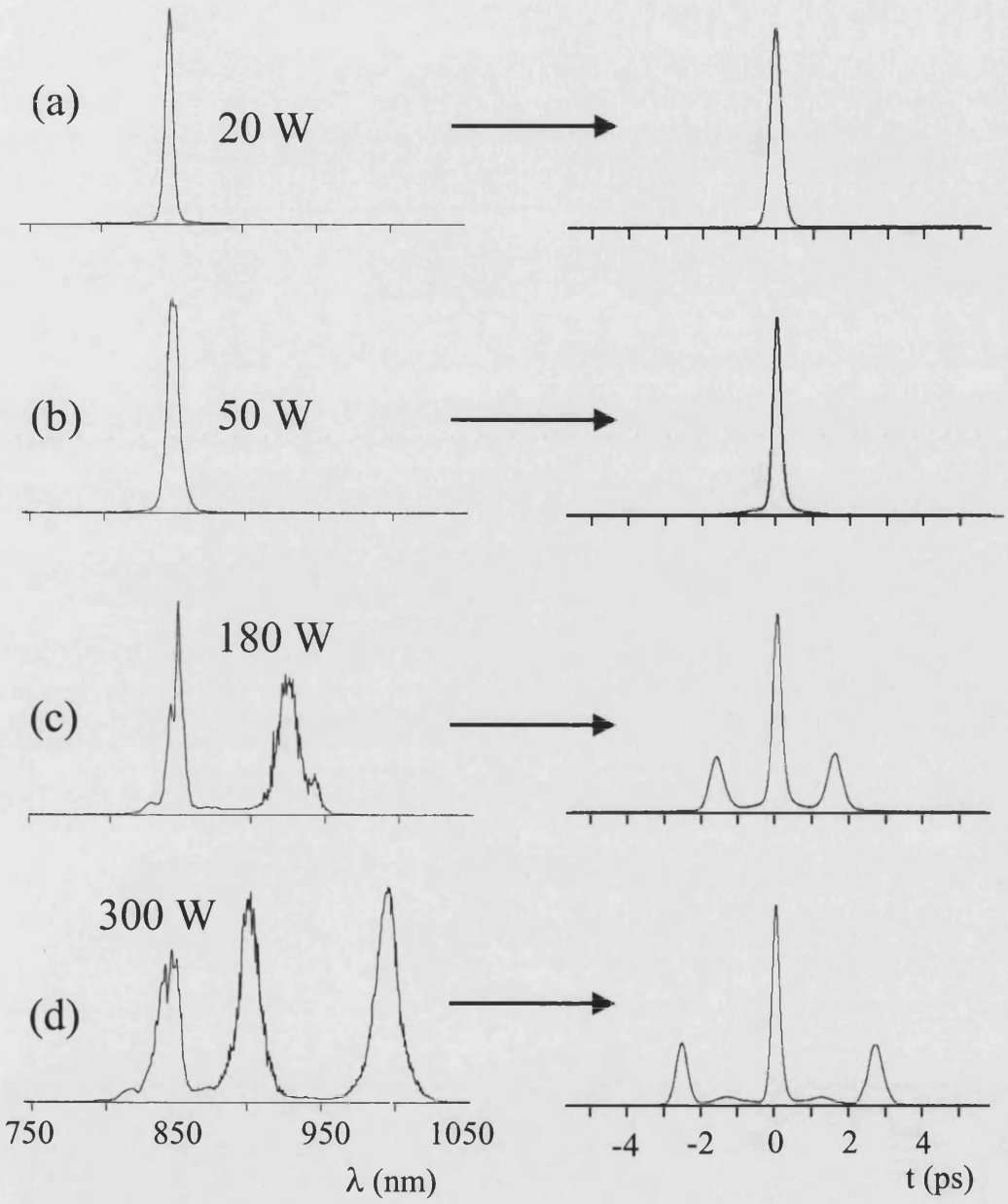

Figure 8.2: Measured autocorrelator signals and spectra for fiber V for different output peak powers

By considering the powers at which we were working, the appearance of this series of new spectral peaks can be explained in terms of the fission of higher-order solitons [49,50]. Looking once more at Figure 8.1, it is clear that, around the second soliton energy (289 W output power), we get two very well-defined peaks in addition to the pump. The autocorrelator confirms these as corresponding to discrete pulses. Furthermore, at the peak power corresponding to N = 3 we observe three spectral peaks (618 W output power) and four peaks (1.1 kW output power) for N = 4. Above the second soliton energy spectral components in the short wavelength part of the spectrum are observed, which can be attributed to nonsolitonic radiation generated during soliton fission. Although the physics underlying the appearance of these short-wavelength bands is not yet completely clear, their positions agree with the numerical simulations reported by Husakou and Herrmann.

Figure 8.3 shows the phase mismatch between the generated fundamental solitons at the pump frequency ($\omega_s = \omega_p$) and the nonsolitonic blue-shifted radiation for different pump wavelengths according to the theory described in 49 and 50. The phase ϕ_s of the soliton at a frequency ω_s and that of the nonsolitonic radiation ϕ_r at ω are given by ϕ_s=n(ω_s)ω_sL/c + $n_2 I_0 \omega_s$L/2c - ω_sL/v_s and ϕ_r = n(ω)ωL/c - ωL/v_s, where n is the effective index, L is the fiber length, c is the speed of light in vacuum, n_2 is the nonlinear refractive index of silica, I_0 is the intensity and v_s is the group velocity of the soliton.

Pump at 817 nm for a fibre length of 16 m

Next, results for the spectra observed as a function of pump wavelength, using a 16 m length of fibre V are presented. Figure 8.4 shows the spectra from a 16 m piece of fibre for a pump wavelength of 817 nm. For this pump wavelength the dispersion (D) is 5 ps/nm.km, yielding a calculated peak power for fundamental soliton formation of 5 W. The first trace was recorded at an output power of 39 W. This corresponds to an energy level above the fourth soliton energy, explaining the appearance of at least 3 distinct peaks around the pump wavelength and a small peak at shorter wavelengths. As the input average power increases, new solitons appear and shift towards longer wavelengths whilst new wavelength components are created in the short wavelength part of the spectrum building up the supercontinuum.

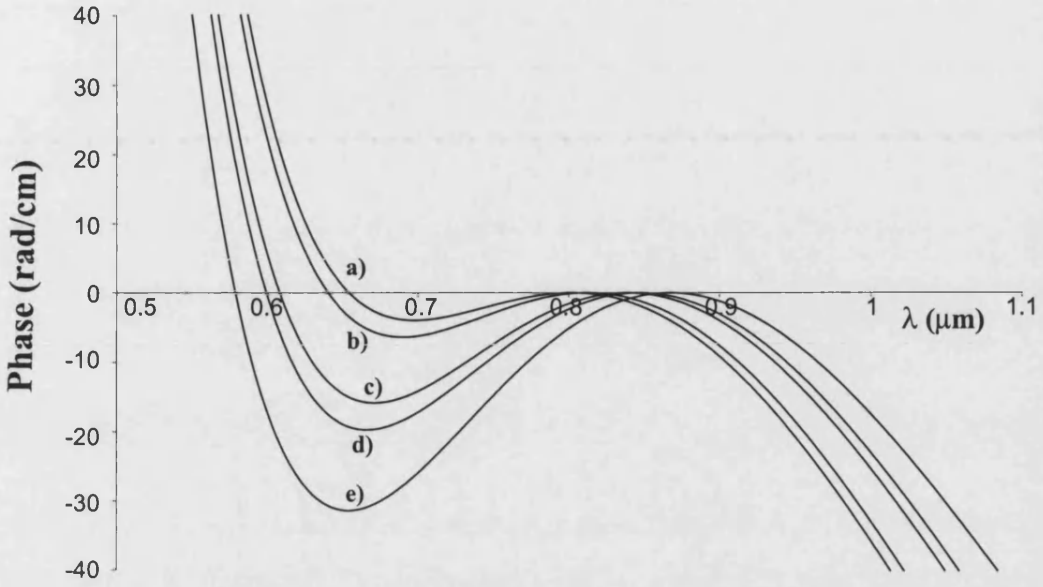

Figure 8.3: Phase mismatch between nonsolitonic radiation and solitons at (a) zero dispersion wavelength, 806 nm, (b) 817 nm, (c) 842 nm and (d) 850 nm and (e) 870 nm, for fibre V

Pump at 842 nm for a fibre length of 16 m

Figure 8.5 shows broadly similar results for a pump wavelength of 842 nm. The value of D for this wavelength is D = 16 ps/nm.km, giving a peak power for the fundamental soliton of 16 W. The phase matching is not as flat as in the previous case and therefore we expect to see less radiation in the region between the pump and the phase-matched wavelength. This is indeed the case, even when the power is increased. It is seen how the pulse breaking mechanism is still responsible for the generation of the supercontinuum.

Pump at 870 nm for a fibre length of 16 m

The fibre was pumped at 870 nm, yet further from the zero dispersion wavelength at 806 nm. The resulting spectra for different powers can be seen in Figure 8.6. In this case, D = 27 ps/nm.km. There is a large phase mismatch for the shorter wavelengths close to the pump and therefore the spectrum shows a well-defined minimum in the generated nonsolitonic radiation in this wavelength band. Once more, multiple self-frequency shifting solitons and the radiation at shorter

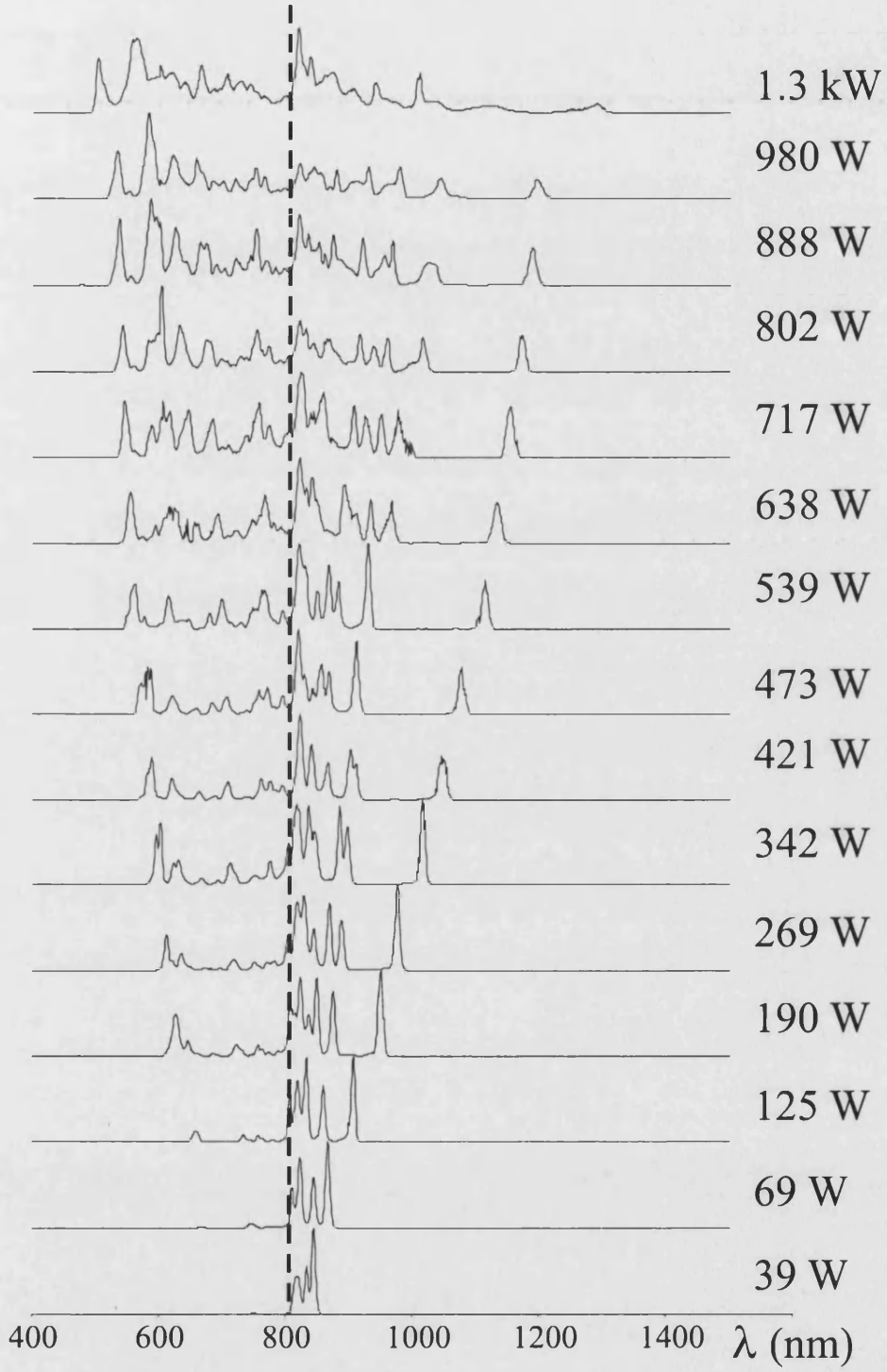

Figure 8.4: Recorded spectra at a pump wavelength of 817 nm for different peak powers coming out of the fibre. The dotted line indicates the zero dispersion wavelength at 806 nm

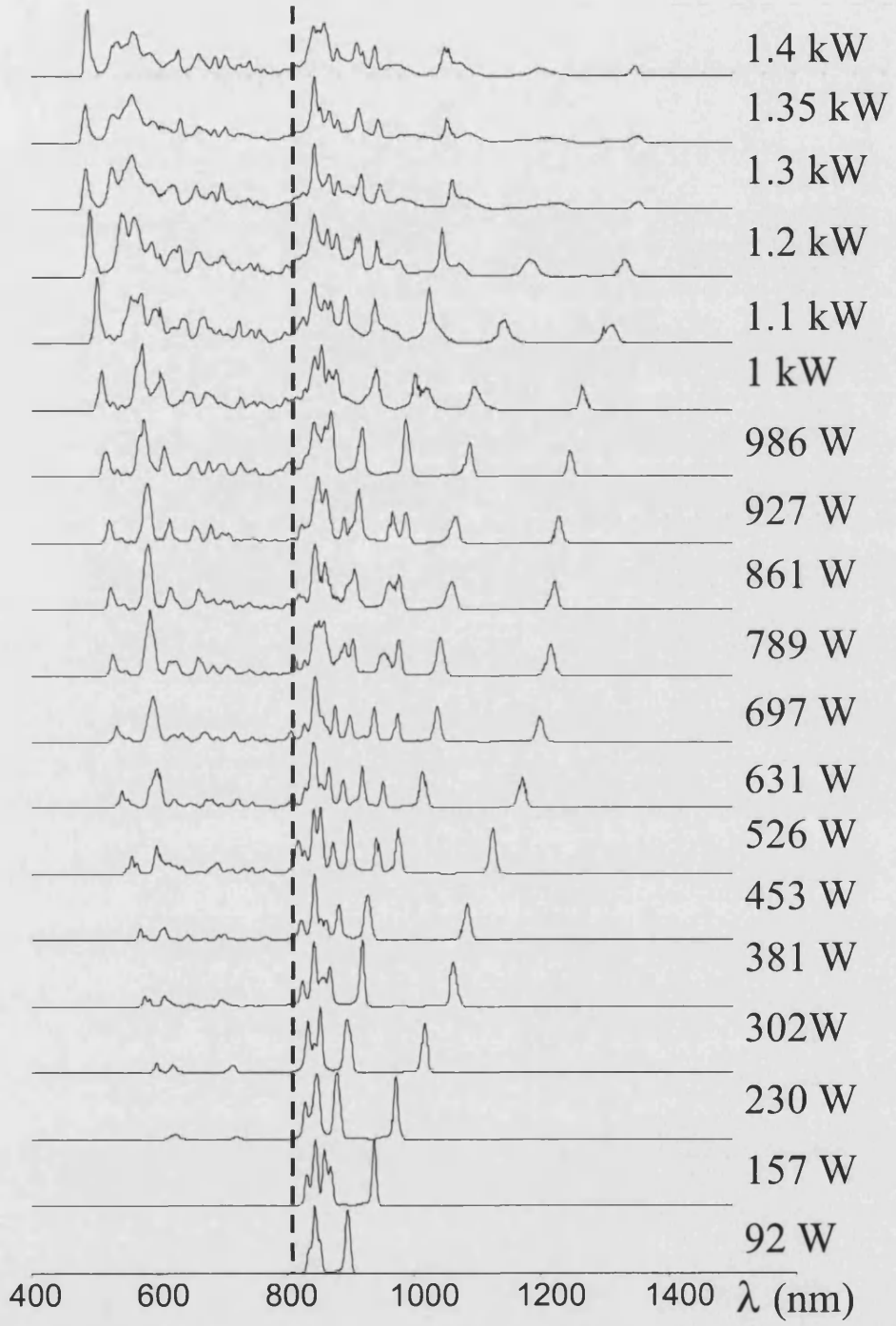

Figure 8.5: Recorded spectra at a pump wavelength of 842 nm for different peak powers coming out of fibre V. The dotted line indicates the zero dispersion wavelength at 806 nm

wavelengths produce a broad spectrum.

Pump at 842 nm for a different fibre lengths

In order to give some insight into the instability of higher-order soliton propagation in such a system, a study of the spectral evolution of a pulse along the fibre length in the regime N > 1 was performed. Figure 8.7 shows output spectra recorded when fibre V was cut back from a length of 39 cm in 3 cm steps for an input power of 150 W (between the second and third soliton powers). For a 6 cm long piece, the spectral distribution shows asymmetric features due to the interaction between Raman scattering and linear and nonlinear dispersion. As the pulse propagates, it becomes unstable and then breaks up emitting nonsolitonic radiation as seen in the 9 cm and the 12 cm long pieces. As the length is further increased, the newly formed soliton starts shifting in frequency and blue-shifted radiation appears at the phase-matched wavelength. It should be noted that this range of fiber lengths spans those previously reported used for SC generation in similar fibers [41].

Pump at 753 nm for a fibre length of 16 m

Having studied the process of SC generation when pumping in the anomalous dispersion regime, the laser was tuned to pump fiber V at 753 nm, at which wavelength the dispersion D = -30 ps/nm.km - that is to say, the GVD is normal. Hence soliton formation is not expected . Figure 8.8 shows the spectra recorded for different powers. The first traces show a progressive broadening of the pump, which we attribute to self-phase modulation. As the power is increased, a small peak appears just before the zero-dispersion wavelength and then some of the energy is transferred into the anomalous dispersion regime. It is worth noting that the observed frequency difference is not consistent with direct Raman scattering [3] and the spectral feature shifts with intensity. As the power was increased (230W), more energy is transferred to this peak and a solitonic feature is formed as energy spills across the zero-GVD wavelength. Further increases in the power lead to a shift of this soliton and the appearance of new frequency shifted solitons on the longer wavelength side of the zero dispersion point. These new components at longer wavelengths are accompanied by the appearance of

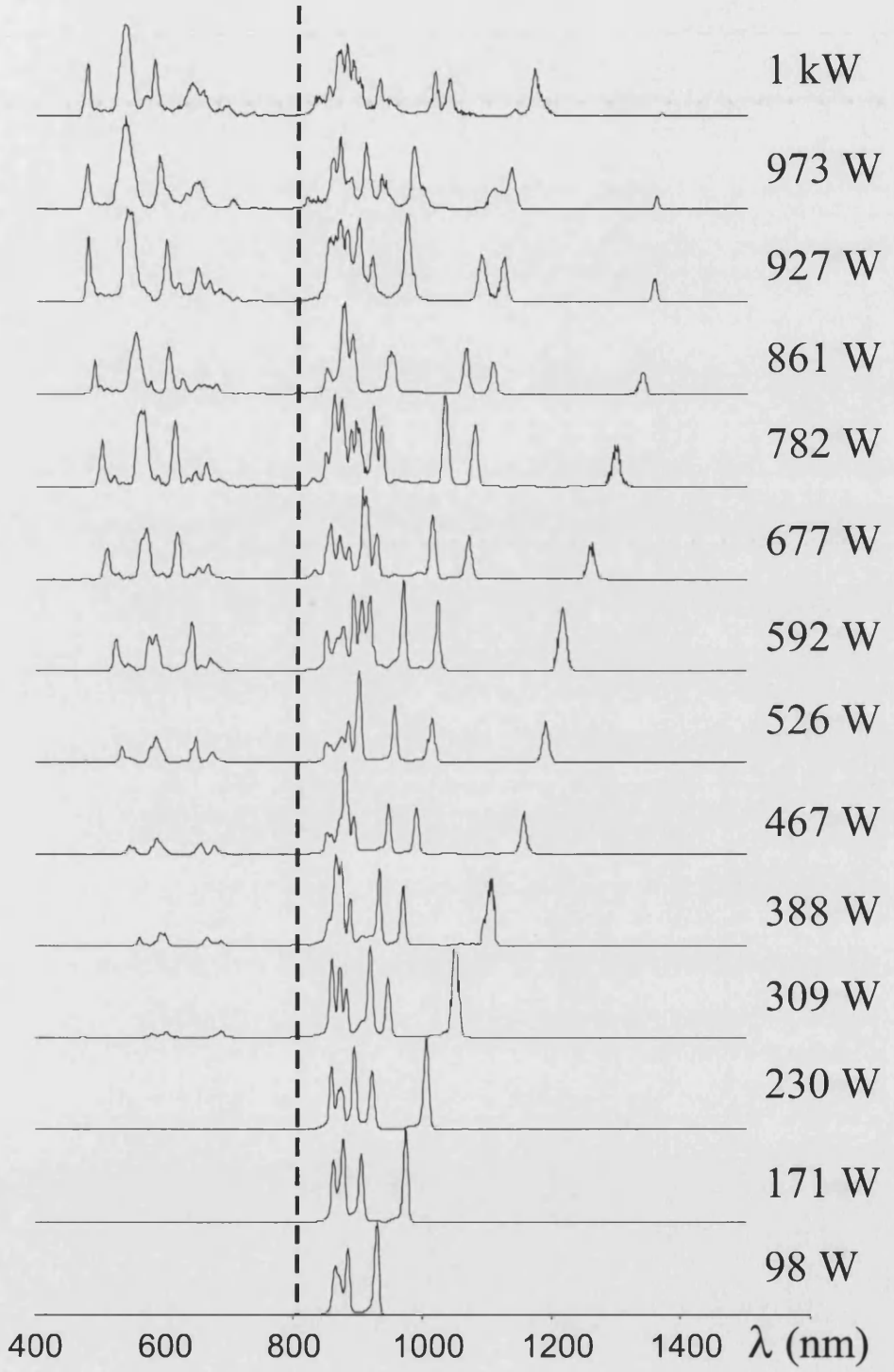

Figure 8.6: Recorded spectra at a pump wavelength of 870 nm for different peak powers coming out of the fibre. The dotted line indicates the zero dispersion wavelength at 806 nm

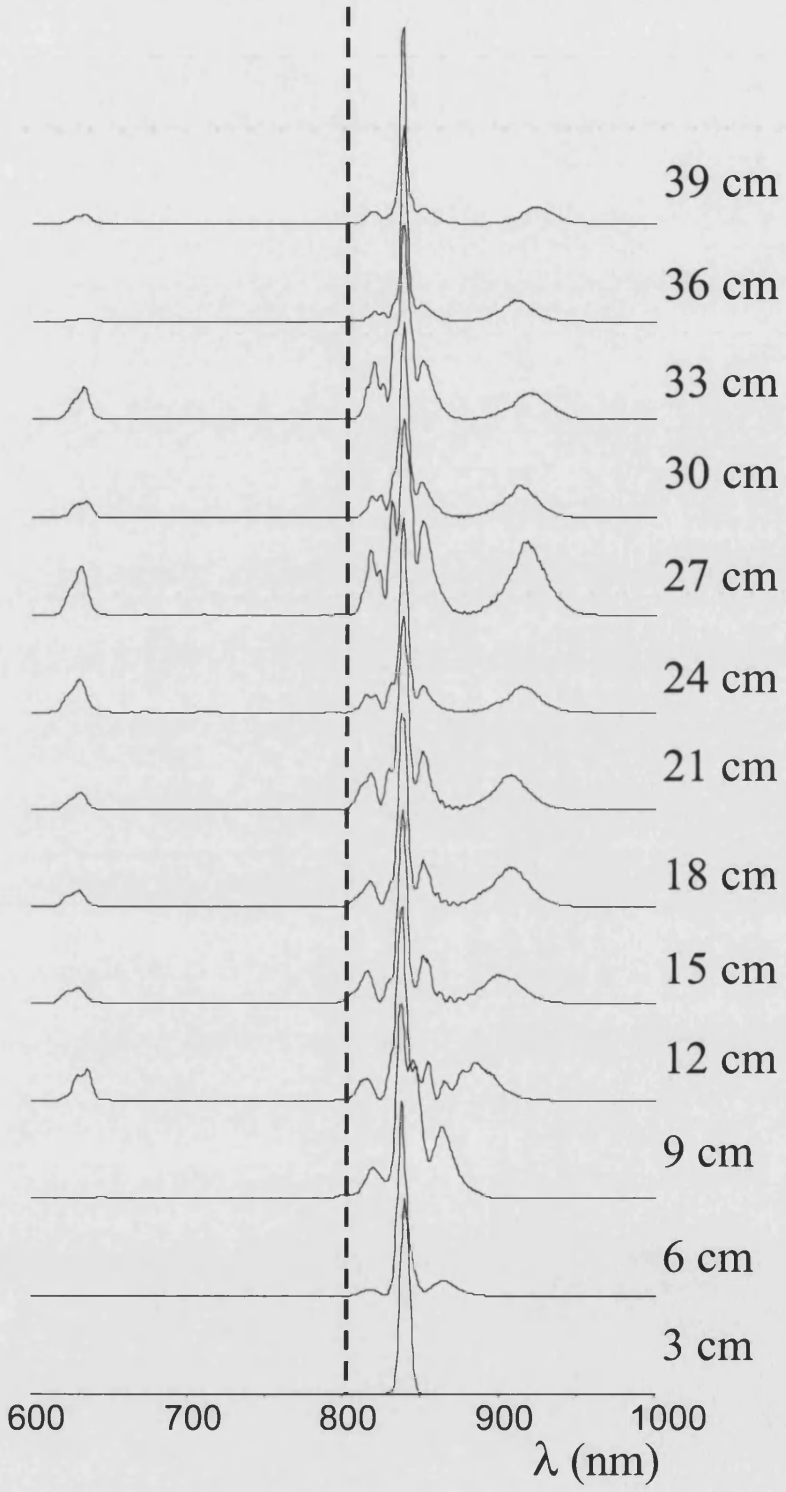

Figure 8.7: Recorded spectra for different lengths of fibre V at constant output peak power of 150 W pumping at 842 nm. The fibre is progressively cut back in 3cm steps

new short-wavelength peaks as well. Therefore it is seen that when pumping in the normal side of D but close to the D = 0 wavelength, self-shifting fundamental solitons nonetheless arise from energy transferred beyond the zero dispersion point, leading to the generation of a continuum of radiation.

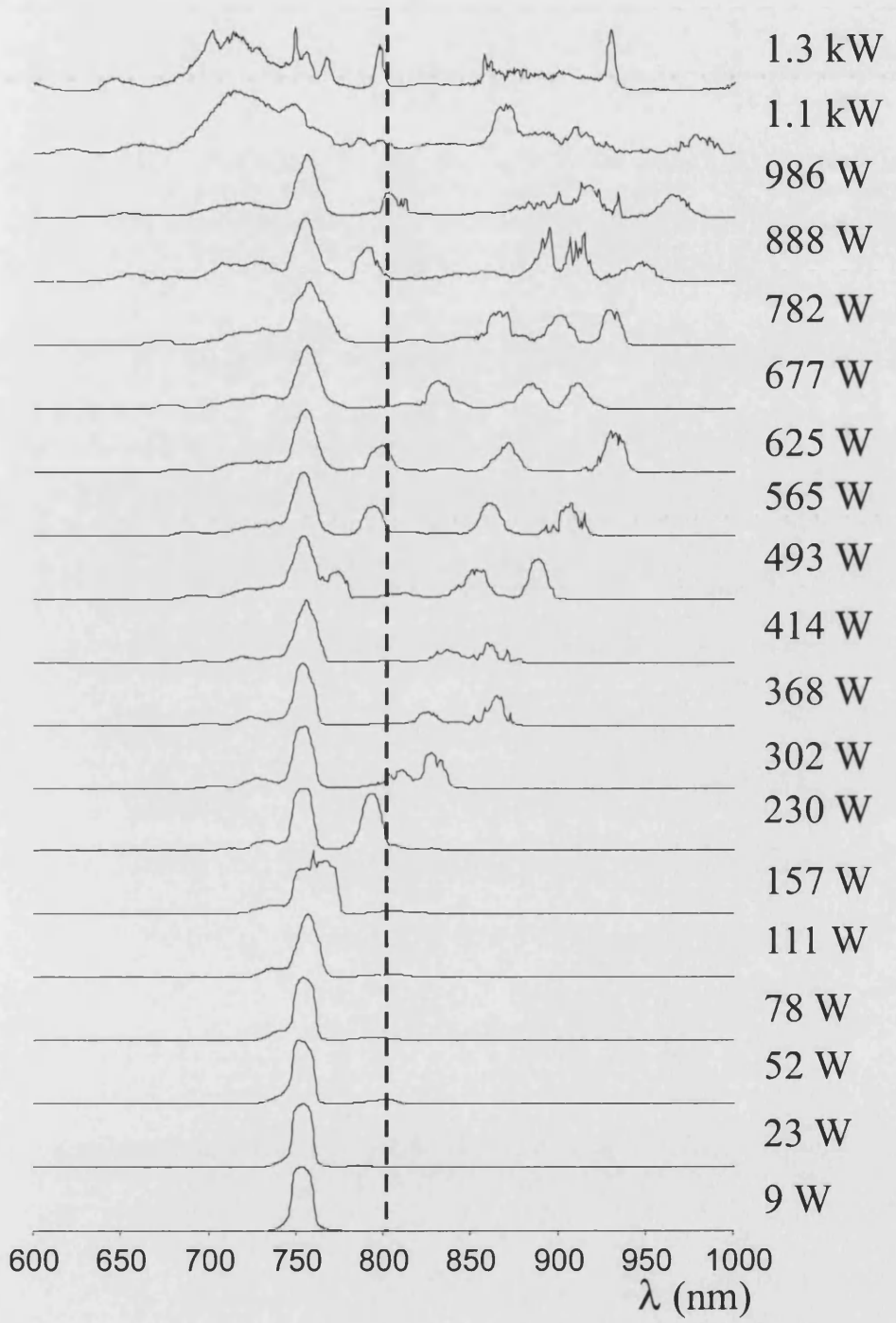

Figure 8.8: Recorded spectra at a pump wavelength of 753 nm for different peak powers coming out of fibre V. The dotted line indicates the zero dispersion wavelength at 806 nm

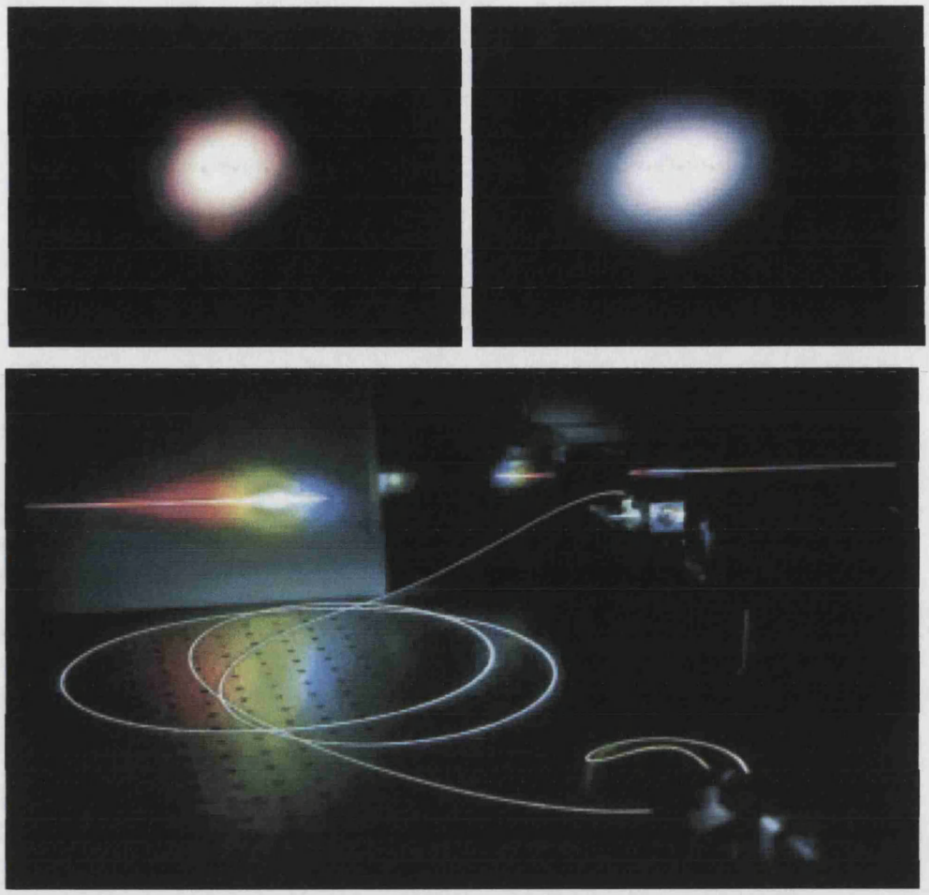

Figure 8.9: Far field patterns and spectrum after a grating of the output of a Highly-Birefringent PCF

8.3.2 High power experiments

Once the mechanism for SC generation has been understood when pumping with 200 femtosecond pulses, we can explore all the different characteristics when working at high powers. Most of the applications for SC generation are based in the great bandwidth attainable in these structures and that is achieved working at higher powers than reported in the previous section. A typical far field pattern and spectrum at high powers can be seen in figure 8.9.

It is seen how a very efficient spectrum can be generated in these structures. Typical spectra for high power for fibre VI can be seen in 8.10. It is clearly seen how a very efficient spectrum is generated for both polarisation eigenmodes. The spectra tend to flatten out loosing the solitonic features characteristic al low

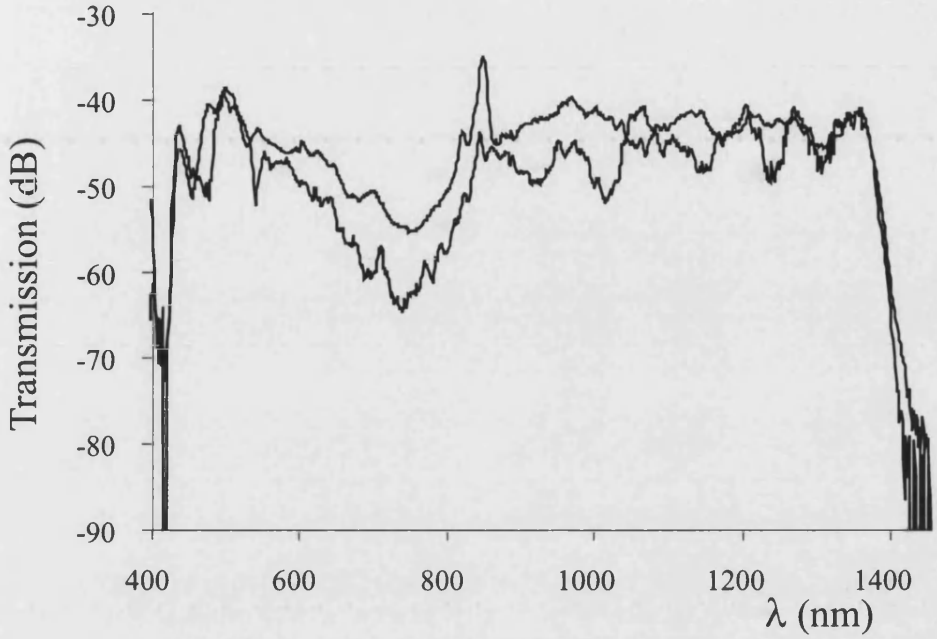

Figure 8.10: SC generated in fibre VI at high power for the two polarisation eigenmodes when pumping in the anomalous dispersion regime

powers. It can be seen as well , how due to the difference on soliton energies in between modes, one of the spectra has flattened out more than the other.

When comparing spectra at high powers, the characteristics identified at low power experiments still can be seen. The spectra present a less "spiky" appearance, but for example, looking at Figure 8.11 it is seen how pumping fibre VII in the anomalous dispersion regime (Figure 8.11 (a)) results in a more efficient generation of radiation than pumping in the normal regime (Figure 8.11 (b)). As explained before, for both situations SC is generated, but when pumping in the anomalous dispersion regime the solitonic features are formed directly from the pump and then they shift in frequency instead of having to transfer energy to the longer side of the zero dispersion wavelength. Therefore, for similar powers, we can get very different SC when pumping in the normal or the anomalous dispersion regime.

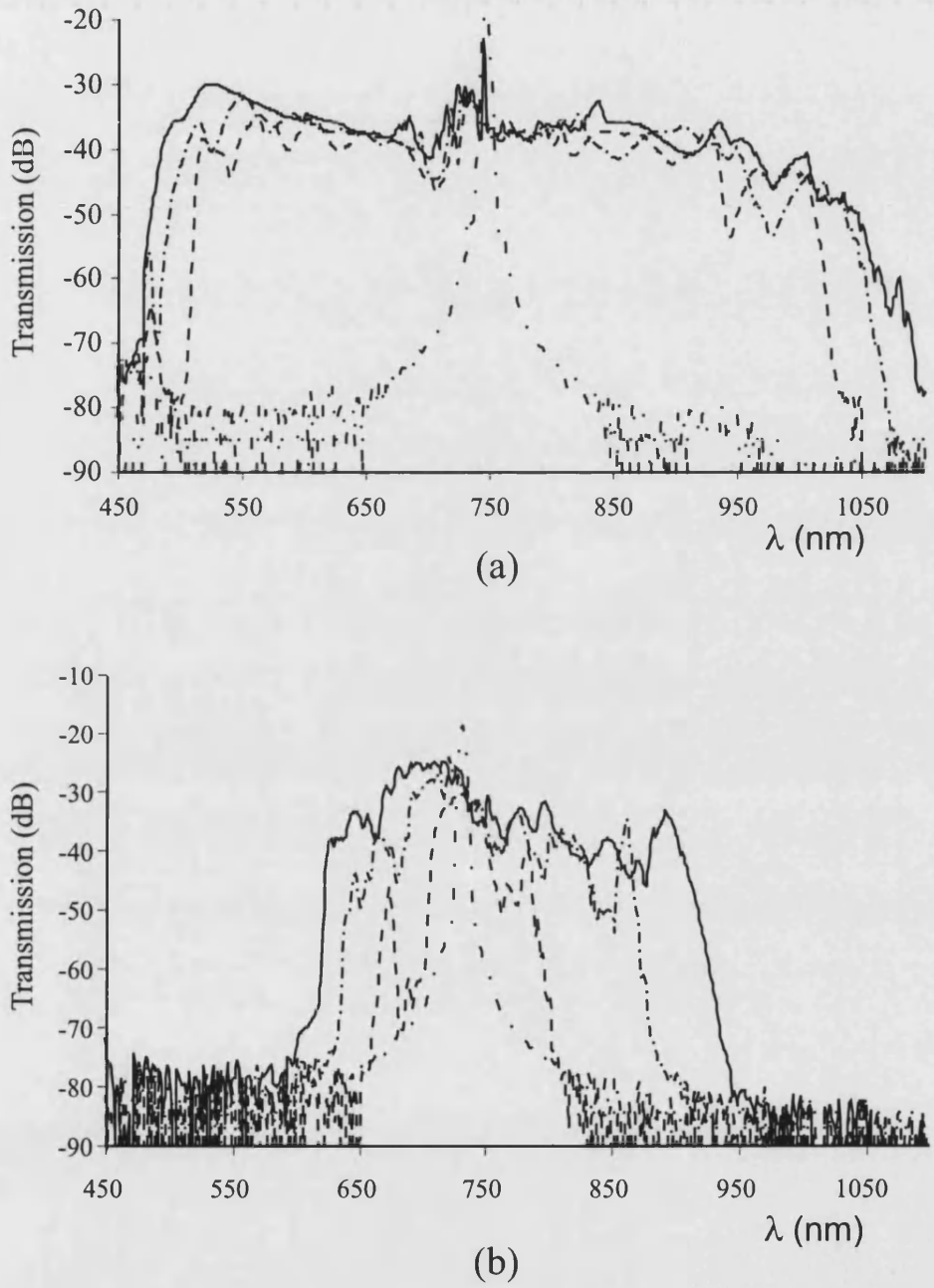

Figure 8.11: SC generated in fibre VII at different high powers when pumping in the (a) anomalous and (b) normal dispersion regime

8.4 Preliminary results of Supercontinuum generation with picosecond pump pulses

For the past two years, the research on SC generation has mainly focused on SC generation when pumping with femtosecond pulses. There has been some work done when pumping PCFs with 60 picosecond pump pulses [46] but at a wavelength into the normal dispersion regime.

The cavity of our Ti:sapp laser (Coherent Mira 900) was changed in order to operate it at picosecond pulses and being tuneable from 780 nm to 950 nm. Several preliminary experiments for different wavelengths and powers were performed in a 16 m piece of fibre V. The fibre nonlinearity coefficient γ was evaluated giving a value $\sim 33\ W^{-1}m^{-1}$ using $n_2 = 2.4 \times 10^{-20}m^2/W$ [3] and an estimated effective area of $A_{eff} = 5.58\ \mu m^2$. The laser pulses were 1 ps long (based on the Coherent specifications). The light was launched in the eigenmode with longer zero dispersion wavelength (806 nm) using a half-wave plate and the output was analysed using an optical spectrum analyser.

Figure 8.12 shows the spectra for different peak powers (spanning from 13 W to 340 W) when pumping fibre V with picosecond pulses at a wavelength of 813 nm. Considering the above parameters for the fibre, the upper limit for the frequency broadening expected from self-phase modulation is [3]

$$\Delta\omega(t) = -\omega_0 \frac{n_2 L}{c} \frac{dI(t)}{dt} \tag{8.1}$$

This indicates that the maximum frequency shift expected from the SPM of 570 W input peak power (corresponding to the highest input powers used in the experiments) 1 ps pulses propagating in the 16 m piece of fibre is $|\Delta\omega| \sim 0.13\omega_0$. This corresponds to $\Delta\lambda \sim 100nm$ and cannot account for the frequency bandwidth of the experimental results.

Next, we can evaluate the influence of SRS and parametric four-wave mixing. Assuming a launched power of around 570 W and phase-matching, a parametric gain of $g_p = \gamma P \sim 190/m$ and a raman gain half of that value, $g_r \sim 95/m$ [3], makes the 16 m of fibre long enough for the generation and merging of new spectral components.

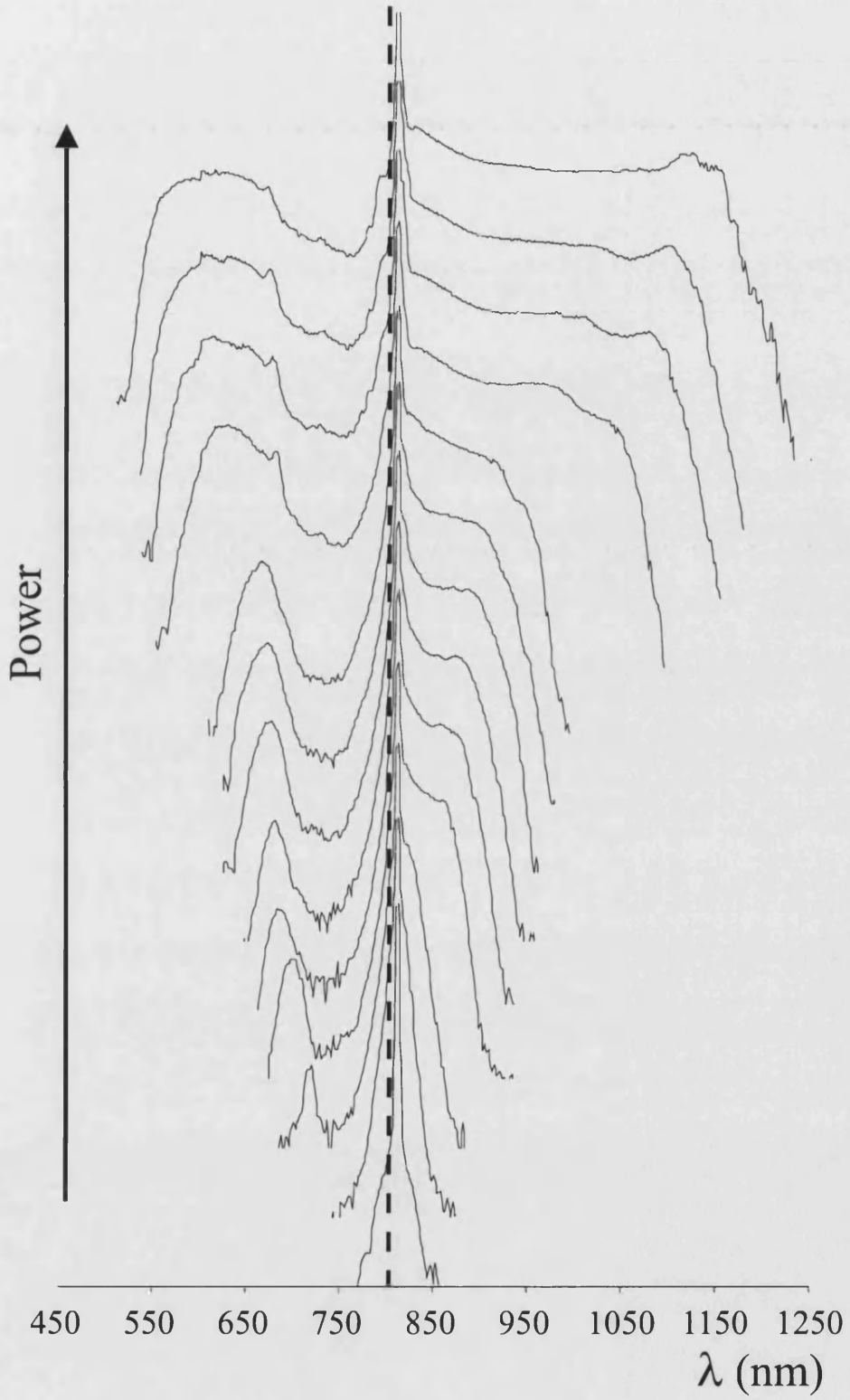

Figure 8.12: Recorded spectra when pumping with picosecond pulses at a pump wavelength of 813 nm for different peak powers coming out of fibre V. The lower trace corresponds to 13 W and the higher corresponds to 340 W and they are equally spaced in power. The dotted line indicates the zero dispersion wavelength at 806 nm

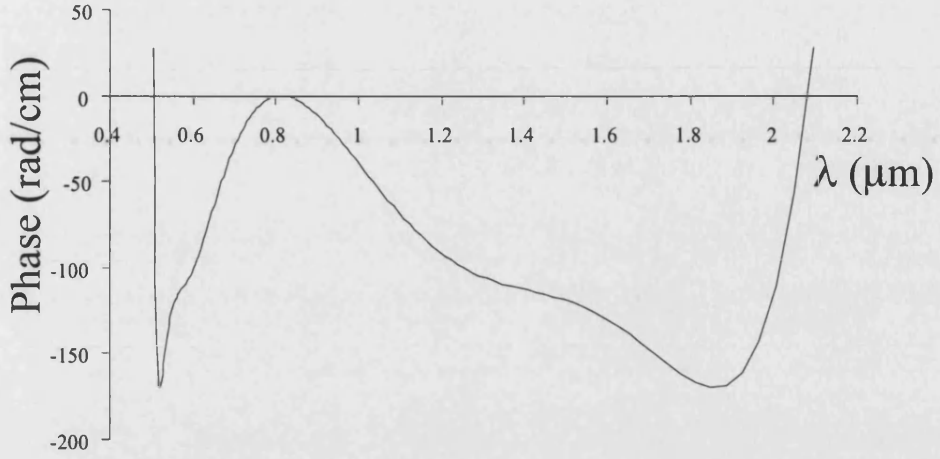

Figure 8.13: Phase matching diagram for degenerate four-wave mixing at a pump wavelength of 813 nm

In contrast to SRS, parametric four-wave mixing is associated with a phase match condition. Figure 8.13 shows the evaluation of the phase matching condition for degenerate four-wave mixing. It is seen how the phase-matching condition occurs for a $\lambda \sim 500$ nm, which does not correspond to the spectral peak at $\lambda \sim 700$ nm for low powers in Figure 8.12. The phase matching shown in Figure 8.13 corresponds to the linear case. If an intensity dependent term is introduced to evaluate the nonlinear phase-matching case, the curve does not shift enough to meet the experimentally observed peak.

Similar results are obtained when pumping fibre V at a wavelength of 800 nm. The results for different powers spanning between 13 W and 260 W can be seen in figure 8.14.

The last set of data presented (see Figure 8.15) correspond to the case of pumping yet further into the normal dispersion regime at a wavelength of 783 nm. In this case, it is seen how SRS and parametric four-wave mixing is responsible for the generation of new frequencies at both sides of the pump wavelength at low powers. Those spectral features then grow as the power is increased.

A summary of the observed effects is shown in Figure 8.16. These preliminary results show that the mechanism for generating SC when pumping with picosecond pulses differs from the case of pumping with femtosecond pulses. The mechanism for generating new frequency components is still not clear. When pumping in the

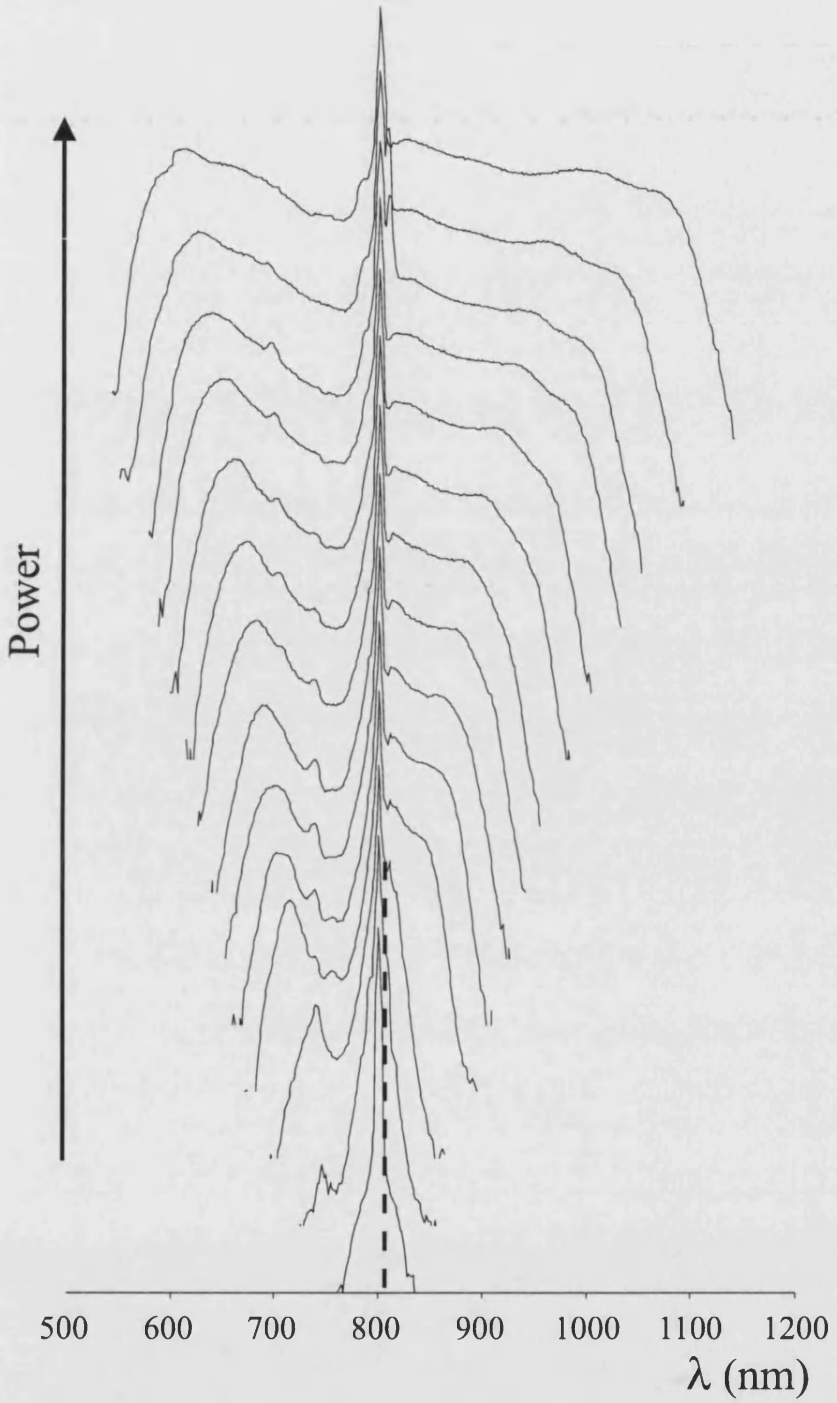

Figure 8.14: Recorded spectra when pumping with picosecond pulses at a pump wavelength of 800 nm for different peak powers coming out of fibre V. The lower trace corresponds to 13 W and the higher corresponds to 260 W and they are equally spaced in power. The dotted line indicates the zero dispersion wavelength at 806 nm

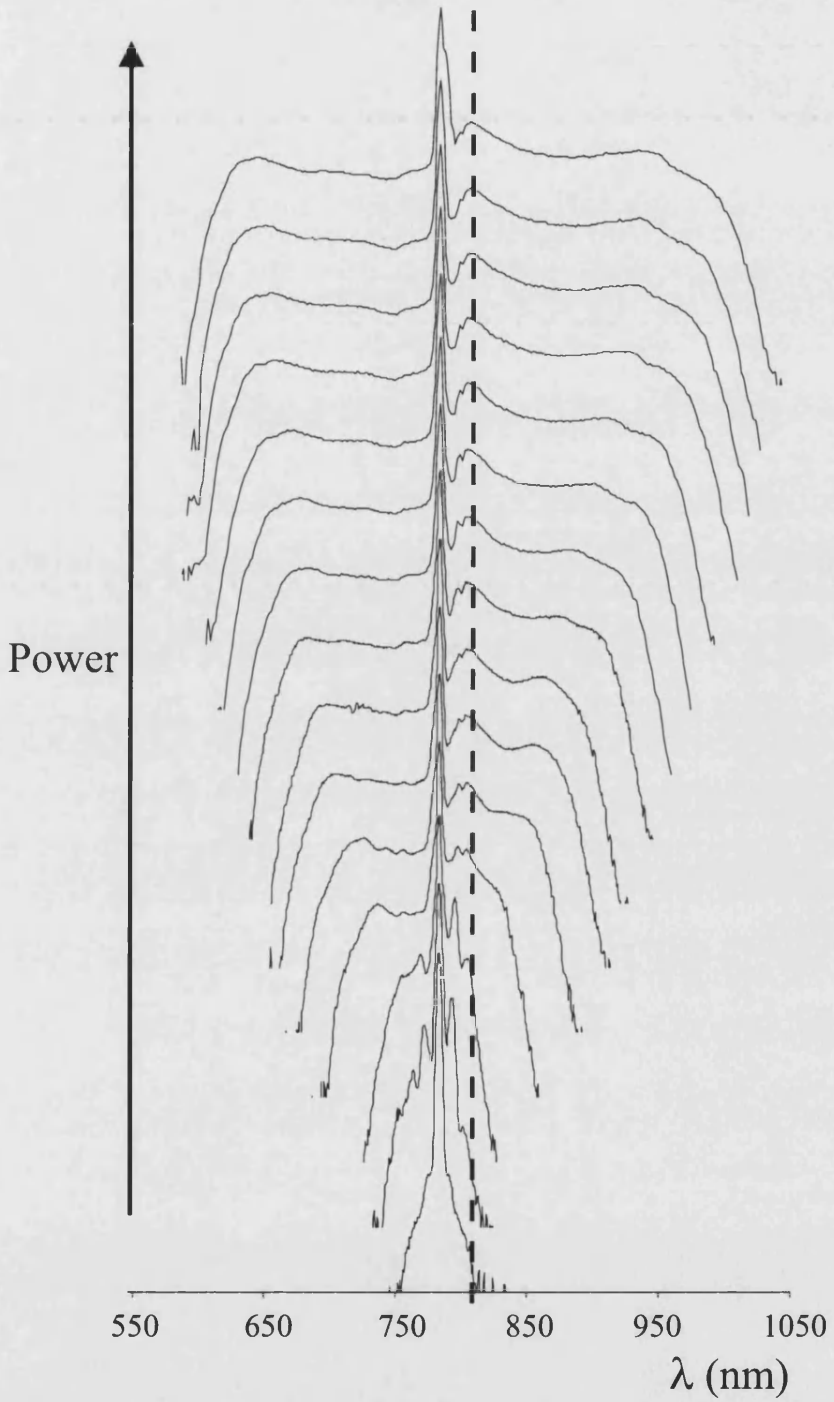

Figure 8.15: Recorded spectra when pumping with picosecond pulses at a pump wavelength of 783 nm for different peak powers coming out of fibre V. The lower trace corresponds to 10 W and the higher corresponds to 184 W and they are equally spaced in power. The dotted line indicates the zero dispersion wavelength at 806 nm

normal dispersion regime and away from the zero dispersion point (Figure 8.15) new frequency components appear at both sides of the pump and then grow when the power is increased. This behavior is similar to the one reported in reference [46] and could be attributed to SRS and parametric four-wave mixing.

The interesting behavior appears when pumping near the zero dispersion wavelength (Figures 8.14 and 8.12). For both cases (pumping in the anomalous or the normal dispersion regime) a short wavelength band appears at relatively low powers. That sideband cannot be attributed to modulation instability. Conventional SRS does not appear to be the phenomenon responsible for it either. Only the anti-Stokes band is created and that suggests that a more complicated phase matching process (due to the proximity to the zero dispersion wavelength) is taking place.

As explained before, these are just preliminary result and a more detailed study for different wavelengths is needed. It will also be interesting to do some realistic modelling of the propagation of ultra-short pulses in order to evaluate the phase-matching conditions and the relevance of each of the nonlinear processes involved.

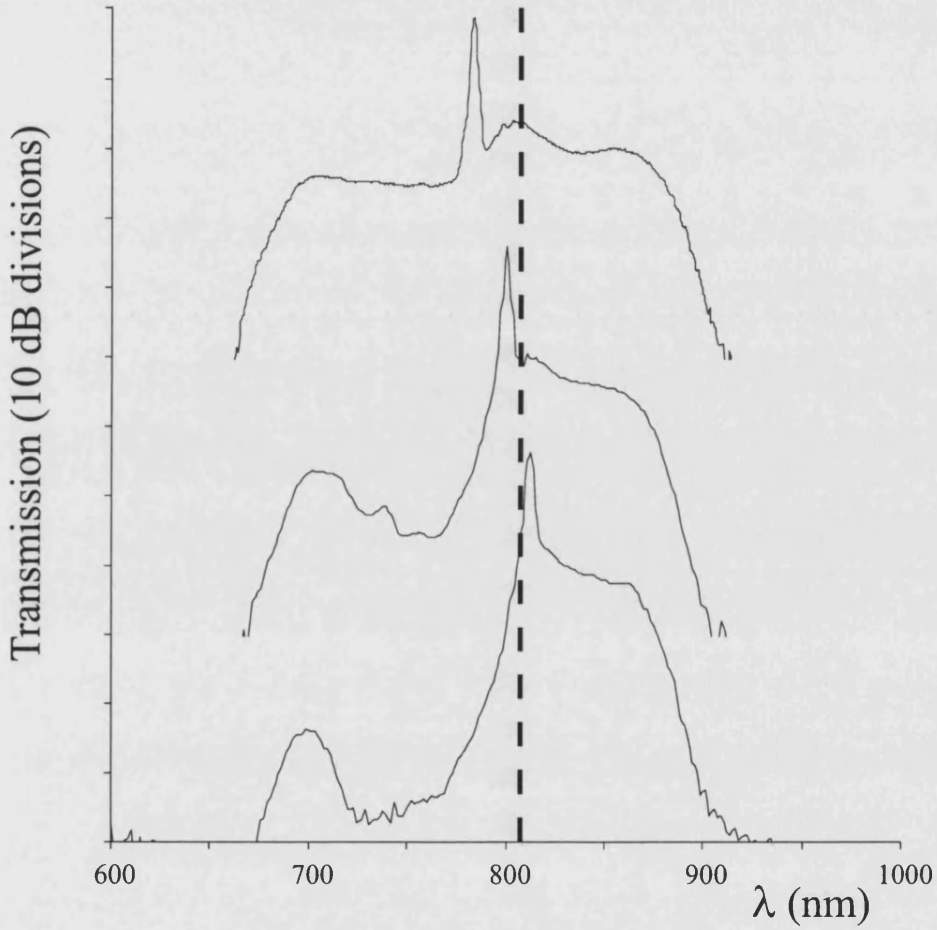

Figure 8.16: Recorded spectra when pumping with picosecond pump pulses at different wavelengths for the same peak power coming out of fibre V. The dotted line indicates the zero dispersion wavelength at 806 nm

8.5 Conclusions

Detailed experiments have been carried out to study the behavior of ultrashort pulses in photonic crystal fibers in order to elucidate the mechanisms for supercontinuum generation in these structures. To avoid unwanted polarization effects, the experiments were performed using well characterised polarization-maintaining fibers.

When pumping with femtosecond pulses, for low powers the experimental evidence shows that, as in conventional fibers, Raman scattering leads to the break-up of higher-order solitons, which is accompanied by the generation of radiation at shorter wavelengths than the pump, leading eventually to an ultrabroad supercontinuum. The mechanism has been tested for different pumps at both sides of the zero dispersion wavelength. In every case, it has been seen how as the power is increased new solitonic features are formed and more radiation is emitted in the short wavelength range. It has been seen how when pumping in the normal dispersion regime, where the formation of bright solitons is not allowed, the mechanism consists on transferring energy to the anomalous dispersion side in order to form these solitons.

For most of the applications of the SC spectrum, wide and flat spectra are required. It has been shown how these spectra can be obtained by sending high powers down the fibres. These high powers correspond to N $>>1$ and therefore several solitons will be formed in the anomalous part of the spectrum radiating in the normal part of the spectrum. At the same time, different parametric processes can take place between the new spectral features allowing for the formation of new wavelengths that will contribute to the flattening of the spectrum. The other factor to be considered is the length of the fiber. It has been shown how the break up process takes place in the first few centimeters of the fiber. Nevertheless, increasing the length of the fibre will allow the solitonic features to self-frequency shift to longer wavelengths and therefore a more efficient spectrum is generated.

Preliminary results when pumping with picosecond pulses have been presented. The effect responsible for SC generation in this regime is still unclear.

Chapter 9

Summary and future work

9.1 Summary

This thesis focused on the fabrication and the characterisation of linear and non-linear phenomena in photonic crystal fibres and more specifically in a new family of polarisation preserving PCFs: Highly Birefringent photonic crystal fibres.

Modified Dispersion PCFs

Several fibres with unusual GVD characteristics have been demonstrated. It has been demonstrated that the zero dispersion wavelength of PCFs can be shifted to the visible and near infrared, where both pure silica and conventional fibres exhibit normal dispersion, by carefully choosing the parameters of the fibres. It has been demonstrated that the dispersion of photonic crystal fibres can be shifted to different wavelengths by changing the air hole size and the core diameter. The unusual GVD characteristics shown by these structures has shown to have a strong effect on the non-linear response of the fibres to ultra short optical pulses. Shifting the anomalous dispersion regime to shorter wavelengths enables the observation and study of solitons in the Ti:Sappire laser wavelength window (700-1000nm). The dispersion shifted fibres have shown as well a new nonlinear phenomenon, the generation of ultra broad supercontinuum in optical fibres.

Highly Birefringent PCFs

We have shown how to develop a new family of photonic crystal fibres with a high modal birefringence. Several techniques for characterising these kind of structures have been shown. Very short beat lengths have been demonstrated. We have also shown that the unusual optical properties of the PCF cladding are accompanied by unique mechanical properties, making it difficult to measure the beat length directly. Using these structures, we have presented results for the fabrication of rocking filters in non-photosensitive highly birefringent PCF for the first time. Very good coupling efficiencies were achieved for very short lengths. Furthermore, a new and highly versatile fabrication method using periodic mechanical twisting of the fibre along with heating from a scanning CO_2 laser beam has been implemented.

Soliton propagation

Several Highly Birefringent PCFs with zero dispersion wavelengths in the near infrared have been fabricated. Soliton propagation in the near infrared and soliton self-frequency shift in these structures have been demonstrated. Soliton self-frequency shift has been observed and showed how, due to the high nonlinearity of these structures, very low power thresholds are needed for very efficient soliton wavelength shifts. This technique provides a convenient and novel source for femtosecond pulses in a wide wavelength range. Whilst normal PCFs can exploit the modified dispersion characteristics attainable in these structures for demonstrating soliton transmission in the near infrared, Highly Birefringent PCFs provide the polarisation control as an extra feature for telecomunication networks.

Supercontinuum generation with femtosecond pump pulses

Detailed experiments have been carried out to study the behavior of ultrashort pulses in photonic crystal fibers in order to elucidate the mechanisms for supercontinuum generation in these structures. To avoid unwanted polarization effects, the experiments were performed using well characterised polarization-maintaining PCFs. When pumping with femtosecond pulses, for low powers the

experimental evidence shows that, as in conventional fibers, Raman scattering leads to the break-up of higher-order solitons, which is accompanied by the generation of radiation at shorter wavelengths than the pump, leading eventually to an ultrabroad supercontinuum. The mechanism has been tested for different pumps at both sides of the zero dispersion wavelength. In every case, it has been seen how as the power is increased new solitonic features are formed and more radiation is emitted in the short wavelength range. It has been seen how when pumping in the normal dispersion regime, where the formation of bright solitons is not allowed, the mechanism consists on transferring energy to the anomalous dispersion side in order to form these solitons.

Supercontinuum generation with picosecond pump pulses

Preliminary results when pumping with picosecond pulses have been shown.

9.2 Future work

The field of photonic crystal fibres is still a relatively new area in the field of optical fibres and therefore new possibilities of design and applications are still open. Following there are some of the current topics of interest in the area.

Nonlinear optics in PCF has become, over the past years, a field of increasing interest mainly due to SC generation. The different mechanisms responsible for SC when pumping with different sources and the coherence properties of the spectrum are some of the topics on which many research groups are working. SC provides a very powerful tool for metrology and OCT and a lot of effort has been put into this fields in order to get better sources.

Flat dispersion PCFs is becoming an area of increasing interest. Flat dispersion PCFs have been theoretically [52] and more recently experimentally demonstrated [53]. It has been shown how choosing the right parameters for the fabrication of photonic crystal fibres, the dispersion can be greatly modified from that of pure silica and conventional fibres. This thesis focused on shifting the zero dispersion wavelength towards the near infrared and the visible, but PCFs with flat disper-

sion over a wide wavelength range can be fabricated. This structures should be great vehicles for nonlinear applications as relatively easy phase matching can be obtained for a wide wavelength range. Another potential application for flat dispersion PCFs are parametric fibre amplifiers as the overlap of pump and idle will be enhanced.

PCFs with doped cores is becoming an area of increasing interest as well. The possibility of exploiting the properties of PCFs and the advantage of having a doped core for laser applications opens a wide range of potential application. Fibre lasers and amplifiers can be fabricated and novel double-clad structures can be tested exploiting the versatility of our air hole technology.

Nevertheless, band gap guidance photonic crystal fibres will probably be the main research interest in the years to come. The properties and the potential applications that these kind of structures offer are of great interest. The low dispersion given by these structures as the light is confined in air and the fact that there is no physical interface for loosing part of the power when coupling the light into the fibre, makes these structures very interesting for high power laser's transmission. Although being a great fabrication challenge, the tailoring of the band gap (ranging from a few tenths of nanometers to very wide wavelength ranges) will allow these structures to find endless applications. The fact that the light is guided in a hollow core, that can be filled with other materials and gases, offers as well a great variety of applications for sensing purposes and the study of nonlinear effects in gases.

References

[1] K.C.Kao and G.A.Hockham. Dielectric-fibre surface waveguides for optical frequencies. *Proc. IEE*, 113:1151, 1966.

[2] S.R. Nagel, J.B.MacChesney, and K.L. Walker. An overview of the modified chemical vapor deposition (mcvd) process and performance. *IEEE Journal of Quantum Electronics*, page 459, 1982.

[3] Govind P. Agrawal. *Nonlinear Fiber Optics.* Academic Press, 2001.

[4] Allan W. Snyder and John D. Love. *Optical Waveguide Theory.* Chapman and Hall, 1983.

[5] R. B. Dyott. *Elliptical Fibre Waveguides.* Artech House, 1995.

[6] D. N. Payne, A. J. Barlow, and J. J. Ramskov-Hansen. Development of low-and high-birefringence optical fibers. *Journal of Quantum Electronics*, QE-18:477, 1982.

[7] I.P. Kaminov. Polarization in optical fibers. *Journal of Quantum Electronics*, QE-17:15, 1981.

[8] A. W. Snyder and Xue-Heng Zheng. Optical fibers of arbitrary cross sections. *JOSA A*, 3:600, 1986.

[9] F. M. Mitschke and L. F. Mollenauer. Discovery of the soliton self-frequency shift. *Optics Letters*, 11:659, 1986.

[10] J. P. Gordon. Theory of the soliton self-frequency shift. *Optics Letters*, 11:662, 1986.

[11] J.C. Knight, T.A.Birks, P.St.J. Russell, and D.M. Atkin. All-silica single-mode optical fiber with photonic crystal cladding. *Optics Letters*, 22:1547, 1996.

[12] J.C. Knight, T.A.Birks, P.St.J. Russell, and D.M. Atkin. All-silica single-mode optical fiber with photonic crystal cladding. errata. *Optics Letters*, 22:961, 1997.

[13] R.F. Cregan, B.J. Mangan, J.C. Knight, T.A. Birks, P.St.J. Russell, P.J. Roberts, and D.C. Allan. Single-mode photonic band gap guidance of light in air. *Science*, 285:1537, 1999.

[14] T.A.Birks, J.C. Knight, , and P.St.J. Russell. Endlessly single-mode photonic cystal fiber. *Optics Letters*, 22:961, 1997.

[15] J.C. Knight, T.A.Birks, P.St.J. Russell, and J.P. de Sandro. Properties of photonic crystal fiber and the effective index model. *JOSA A*, 15:748, 1998.

[16] M.J. Gander, R. McBride, J.D.C. Jones, D. Mogilevtsev, T.A. Birks, J.C. Knight, and P.St.J. Russell. Experimental measurement of group velocity dispersion in photonic crystal fiber. *Electronic Letters*, 35:63, 1999.

[17] D. Mogilevtsev, T.A. Birks, and P.St.J. Russell. Group velocity dispersion in photonic crystal fibers. *Optics Letters*, 23:1662, 1998.

[18] M. Tateda, N. Shibata, and S. Seikai. Interferometric method for chromatic dispersion measurement in a single-mode optical fiber. *IEEE Journal of Quantum Electronics*, QE-17:404, 1981.

[19] A.A. Michelson. *Studies in Optics.* The University of Chicago Press, 1968.

[20] K. Suzuki, H. Kubota, S. Kawanishi, M. Tanaka, and M. Fujita. High-speed bi-directional polarisation division multiplexed optical transmission in ultra low-loss (1.3 dB/km) polarisation-maintaining photonic crystal fibre. *Electronics Letters*, 37:1399, 2001.

[21] K. Suzuki, H. Kubota, S. Kawanishi, M. Tanaka, and M. Fujita. Optical properties of a low-loss polarization-maintaining photonic crystal fiber. *Optics Express*, 9:676, 2001.

[22] T.P. Hansen, J. Broeng, S.E.B. Libori, E. Knudsen, A. Bjarklev, J.R. Jensen, and H. Simonsen. Highly birefringent index-guiding photonic crystal fibers. *IEEE Photonics Technology Letters*, 13:588, 2001.

[23] V. Ramaswamy, W.G. French, and R.D. Standley. Polarization characteristics of noncircular core single-mode fibers. *Applied Optics*, 17:3014, 1978.

[24] M.J. Steel and R.M. Osgood Jr. Elliptical-hole photonic crystal fibers. *Optics Letters*, 26:229, 2001.

[25] M.J. Steel and R.M. Osgood Jr. Polarization and dispersive properties of elliptical-hole photonic crystal fibers. *Journal of Lightwave Technology*, 19:495, 2001.

[26] J. Broeng, D. Mogilevtsev, S.E. Barkou, and A. Bjarklev. Polarization-preserving holey fibers. In *CLEO Pacific Rim Proceedings, Paper MA 1-3*, 2001.

[27] S. Kawanishi and K. Okamoto. Polarization maintaining holey optical fiber. In *IEICE Society Conference 2000, Paper B-10-153 (in Japanese)*, 2000.

[28] K. Takada, J. Noda, and R. Ulrich. Precison measurement of modal birefringence of highly birefringent fibers by periodic lateral force. *Applied Optics*, 24:4387, 1985.

[29] R.H. Stolen, A. Ashkin, W. Pleibel, and J.M. Dziedzic. In-line fiber-polarization-rocking rotator and filter. *Optics Letters*, 9:300, 1984.

[30] P.St.J. Russell and D.P. Hand. Rocking filter formation in photosensitive high birefringent optical fibers. *Electronics Letters*, 26:1846, 1990.

[31] G. Kakarantzas, T.A. Birks, and P.St.J. Russell. Structural long period gratings in photonic crystal fibers. *Optics Letters*, 27:1013, 2002.

[32] D. T. Reid, M. Padgett, C. McGowan, W. E. Sleat, and W. Sibbett. Light-emitting diodes as measurement devices for femtosecond laser pulses. *Optics Letters*, 22:233, 1997.

[33] P. Loza-Alvarez, W. Sibbett, and D. T. Reid. Autocorrelation of femtosecond pulses from 415-630 nm using GaN laser diode. *Electronics Letters*, 36:1, 2000.

[34] J.C. Knight, J. Arriaga, T.A. Birks, A. Ortigosa-Blanch, W.J. Wadsworth, and P.St.J. Russell. Anomalous dispersion in photonic crystal fibre. *IEEE Photonic Technolgy Letters*, 12:807, 2000.

[35] F. M. Mitschke and L. F. Mollenauer. Discovery of the soliton self-frequency shift. *Optics Letters*, 11:659, 1986.

[36] J. P. Gordon. Theory of the soliton self-frequency shift. *Optics Letters*, 11:662, 1986.

[37] B. R. Washburn, S. E. Ralph, P. A. Lacourt, J. M. Dudley, W. T. Rhodes, R. S. Windeler, and S. Coen. Tunable near-infrared femtosecond soliton generation in photonic crystal fibres. *Electronics Letters*, 37:1510, 2001.

[38] X. Liu, C. Xu, W. H. Knox, J. K. Chandalia, B. J. Eggleton, S. G. Kosinski, and R. S. Windeler. Soliton self-frequency shift in a short tapered air-silica microstructure fiber. *Optics Letters*, 26:358, 2001.

[39] I. G. Cormack, D. T. Reid, W. J. Wadsworth, J. C. Knight, and P.St.J. Russell. Observation of soliton self-frequency shift in photonic crystal fibre. *Electronics Letters*, 38:167, 2002.

[40] W. J. Wadsworth, J. C. Knight, A. Ortigosa-Blanch, J. Arriaga, E. Silvestre, and P. St. J. Russell. Soliton effects in photonic crystal fibres at 850 nm. *Electronics Letters*, 36:53, 2000.

[41] J. K. Ranka, R. S. Windeler, and A. J. Stentz. Visible continuum generation in air-silica microstructure optical fibers with anomalous dispersion at 800 nm. *Optics Letters*, 25:25, 2000.

[42] R. Holzwarth, T. Udem, T. W. Hänsch, J.C. Knight, W.J. Wadsworth, and P.St.J. Russell. Optical frequency synthesizer for precision spectroscopy. *Physical Review Letters*, 85:2264, 2000.

[43] I. Hartl, X. D. Li, C. Chudoba, R. Ghanta, T. Ko, J. G. Fujimoto, J. K. Ranka, and R. S. Windeler. Ultrahigh-resolution optical coherence tomography using continuum generation in an air-silica microstructure optical fiber. *Optics Letters*, 26:608, 2001.

[44] P. Beaud, W. Hodel, B. Zysset, and H.P. Weber. Ultrashort pulse propagation, pulse breaking and fundamental soliton formation in a single mode optical fiber. *Journal of Quantum Electronics*, QE 23:1938, 1987.

[45] M. N. Islam, G. Sucha, I. Bar Joseph, M. Wegener, J.P. Gordon, and D.S. Chemla. Femtosecond distributed soliton spectrum fibers. *JOSA B*, 6:1149, 1989.

[46] S. Coen, A. H. L. Chau, R. Leonhardt, J. D. Harvey, J. C. Knight, W. J. Wadsworth, and P. St. J. Russell. Supercontinuum generation by stimulated

raman scattering and parametric four wave mixing in photonic crystal fibers. *JOSA B*, 19:753, 2002.

[47] I. G. Cormack, D. T. Reid, W. J. Wadsworth, J. C. Knight, and P.St.J. Russell. Observation of soliton self-frequency shift in photonic crystal fibre. *Electronics Letters*, 38:167, 2002.

[48] B. R. Washburn, S. E. Ralph, P. A. Lacourt, J. M. Dudley, W. T. Rhodes, R. S. Windeler, and S. Coen. Tunable near-infrared femtosecond soliton generation in photonic crystal fibres. *Electronics Letters*, 37:1510, 2001.

[49] A. V. Husakou and J. Herrmann. Supercontinuum generation of higher-order solitons by fission in photonic crystal fibers. *Physical Review Letters*, 87:203901, 2001.

[50] J. Herrmann, U. Griebner, D. Nickel, A. Husakou, J. C. Knight, W. J. Wadsworth, P. St. J. Russell, N. Zhavoronkov, and G. Korn. Experimental evidence for supercontinuum generation by fission of higher-order solitons in photonic fibers. *Physical Review Letters*, 88:173901, 2002.

[51] X. Gu, M. W. Kimmel, E. Zeek, P. OShea, R. Trebino, and R. S. Windeler. Cross-correlation frequency-resolvedoptical- gating measurements of ultra-broadband continuum from microstructure optical fiber. In *XIII International Ultrafast Meeting, Paper WA2*, 2002.

[52] A. Ferrando, E. Silvestre, J.J. Miret, and P. Andres. Nearly zero ultraflattened dispersion in photonic crystal fibers. *Optics Letters*, 25:790, 2000.

[53] W.H. Reeves, J.C. Knight, P.S.J. Russell, and P.J. Roberts. Demonstration of ultra-flattened dispersion in photonic crystal fibers. *Optics Express*, 10:609, 2002.

Appendix A

Publication List

A.1 Publications in journals

1. *Soliton effects in photonic crystal fibres at 850 nm*
W.J.Wadsworth, J.C. Knight, A. Ortigosa - Blanch, J. Arriaga, E. Silvestre and P.St.J. Russell, Electronics Letters, 36 (1), pp 53-55, 2000.

2. *Anomalous dispersion in photonic crystal fiber*
J.C. Knight, J. Arriaga,T.A. Birks, A. Ortigosa - Blanch, W.J. Wadsworth and P.St.J. Russell, IEEE Photonic Technology Letters, 12 (7), pp 807-809, 2000.

3. *Highly birefringent photonic crystal fibres*
A. Ortigosa - Blanch, J.C. Knight, W.J. Wadsworth, J. Arriaga, B.J. Mangan, T.A. Birks and P.St.J. Russell, Optics Letters, 25 (18), pp 1325-1327, 2000.

4. *Supercontinuum generation in photonic crystal fibres and optical fibre tapers - A novel light source*
W.J. Wadsworth, A. Ortigosa - Blanch, J.C. Knight, T.A. Birks, T - P.M. Man and P.St.J. Russell, JOSA B, 19 (9), pp 2148-2155, 2002.

5. *Pulse breaking and supercontinuum generation with 200 fs pump pulses in photonic crystal fibers*
A. Ortigosa - Blanch, J.C. Knight, P.St.J. Russell, JOSA B, 19 (11), pp 2567-

2572, 2002.

6. *Structural rocking filters in highly birefringent photonic crystal fiber*
G. Kakarantzas, A. Ortigosa-Blanch, T. A. Birks, P.St.J. Russell, L.Farr, F. Couny and B.J. Mangan. Optics Letters (In press)

7. *Four-wave mixing instabilities in photonic crystal and tapered fibers*
F. Biancalana, D.V. Skryabin and A. Ortigosa-Blanch. Submitted to JOSA.

8. *Highly birefringent photonic crystal fibres*
A. Ortigosa - Blanch, J.C. Knight, W.J. Wadsworth, J. Arriaga, B.J. Mangan, T.A. Birks and P.St.J. Russell, Optics and Photonics News (Optics in 2001) vol 12 (12), p17 (2001).(Invited)

A.2 International conferences

1. *Soliton effects and supercontinuum generation in photonic crystal fibres at 850nm*
W.J. Wadsworth, J.C. Knight, A. Ortigosa - Blanch, J. Arriaga, E. Silvestre, B.J. Mangan and P.St.J. Russell, LEOS 1999, San Francisco (USA), paper PD 1.5.

2. *Soliton propagation at short wavelengths in photonic crystal fibres*
W.J. Wadsworth, J.C. Knight, A. Ortigosa - Blanch, B.J. Mangan and P.St.J. Russell, CLEO/QELS 2000, San Francisco (USA), paper QFA2.

3. *Progress in photonic crystal fiber waveguides*
J.C. Knight,T.A. Birks, B.J. Mangan, W.J. Wadsworth, A. Ortigosa - Blanch, J. Arriaga, E. Silvestre and P.St.J. Russell, PECS workshop (Japan), 2000. (Invited).

4. *Soliton propagation at 850 nm and white light supercontinuum generation in photonic crystal fibres*
W.J. Wadsworth, J.C. Knight, A.Ortigosa - Blanch and P.St.J. Russell, IOP Louchborough (UK), September 2000.

5. *Characterisation of photonic crystal fibers*
T.A. Birks, J.C. Knight, B.J. Mangan, A. Ortigosa - Blanch and P.St.J. Russell, Symposium on Optical Fiber Measurements, Boulder (USA), September 2000. (Invited).

6. *White light supercontinuum generation in photonic crystal fibres and optical fibre tapers*
W.J. Wadsworth, J.C. Knight, T.A. Birks, A. Ortigosa - Blanch, B.J. Mangan, and P.St.J. Russell, Mini-Sym posium on Applications of Fast, Low Level Light Detection, Grasmere (UK), October 2000. (Invited).

7. *Highly birefringent photonic crystal fibres*
A. Ortigosa - Blanch, J.C. Knight, W.J. Wadsworth, J. Arriaga, B.J. Mangan, T.A. Birks and P.St.J. Russell, Mini-Symposium on Applications of Fast, Low Level Light Detection, Grasmere (UK), October 2000. (Invited).

8. *Ultrashort pulse propagation in highly birefringent photonic crystal fibres*
A. Ortigosa - Blanch, J.C. Knight, W.J. Wadsworth, B.J. Mangan, and P.St.J. Russell, CLEO/QELS 2001, Baltimore (USA), paper JTuC.

9. *Supercontinuum generation in highly birefringent photonic crystal fibres*
A. Ortigosa - Blanch, J.C. Knight, W.J. Wadsworth, B.J. Mangan, and P.St.J. Russell, PREP2001, Keele (UK), April 2001 (Prize of Best Paper in the Photonics track of PREP 2001).

10. *Photonic crystal fibres for non linear aplications*
W.H. Reeves, W.J. Wadsworth, A. Ortigosa - Blanch, J.C. Knight, and P.St.J. Russell, In-fibre Bragg gratings and special fibres, Coventry (UK), October 2001.

11. *Nonlinear effects in highly birefringent photonic crystal fibres*
A. Ortigosa - Blanch, J.C. Knight, and P.St.J. Russell, Optics and nonlinear optics of microstructured and nanostructured materials, London (UK), November 2001.

12. *Pulse dynamics in polarisation-maintaining photonic crystal fibers*
A. Ortigosa - Blanch, J.C. Knight, and P.St.J. Russell. 13th International Conference in Ultrafast Phenomena, Vancouver (Canada), May 2002. Poster WD

41

13. *Photonic crystal fibers: Speeding up the ultrafast*
P.St.J. Russell A. Ortigosa-Blanch, W.J. Wadsworth and J.C. Knight. 13th International Conference in Ultrafast Phenomena, Vancouver (Canada), May 2002. Paper WA 1(Invited)

14. *Soliton dynamics in polarisation-maintaining photonic crystal fibers*
A. Ortigosa - Blanch, J.C. Knight, and P.St.J. Russell, PREP 2002, Nottingham (UK), April 2002.

15. *Group velocity dispersion in photonic crystal fibres*
W.H. Reeves, W.J. Wadsworth, A. Ortigosa - Blanch, J.C. Knight, and P.St.J. Russell, PREP 2002, Nottingham (UK), April 2002.

16. *Optical fibres using photonic crystals*
J C Knight, T.A. Birks, B.J. Mangan, A. Ortigosa - Blanch, W.J. Wadsworth, P. St. J. Russell, IQEC / LAT 2002, Moscow (Russia), June 2002, Paper QTuM2 (Invited)

17. *Properties and applications of photonic crystal fibres*
W.J. Wadsworth, J.C. Knight, R.M. Percival, G. Bouwmans, A. Ortigosa-Blanch, W.H. Reeves and P.St.J. Russell, IQEC / LAT 2002, Moscow (Russia), June 2002 Paper QThH1 (Invited)

18. *Rocking filter formation in non photosensitive highly birefringent photonic crystal fibres*
G. Kakarantzas, A. Ortigosa - Blanch, T.A. Birks, J C Knight and P. St. J. Russell, ECOC 2002 Copenhagen (Denmark), September 2002, Paper S1.04

19. *Rocking filters in non photosensitive highly birefringent photonic crystal fibres*
G. Kakarantzas, A. Ortigosa - Blanch, T.A. Birks, J C Knight and P. St. J. Russell, Photon 2002, Cardiff (UK), September 2002

20. *New trends in photonic crystal fibre research: Micro-structuring along the third dimension*
G. Kakarantzas, A. Ortigosa - Blanch, T.A. Birks, J. C. Knight and P. St. J.

Russell, XVIII PCSSP-MS, Heraklion (Greece), September 2002

A.3 Publications

Following there is a copy of the work published during this Thesis in peer reviewed journals. The reproduction of these documents has been allowed under the copyright agreements made with the Optical Society of America (OSA), the Institute of Electronics and Electrical Engineering (IEEE) and the Institute of Electrical Engineering (IEE).

Soliton effects en photonic crystal fibres at 850 nm
Electronics Letters, 36 (1), pp 53-55 (2000)

Soliton effects in photonic crystal fibres at 850 nm

W.J.Wadsworth, J.C. Knight, A. Ortigosa - Blanch, J. Arriaga, E. Silvestre and P.St.J. Russell,

Electronics Letters, 36 (1), pp 53-55 (2000)

Soliton effects en photonic crystal fibres at 850 nm
Electronics Letters, 36 (1), pp 53-55 (2000)

Soliton Effects in Photonic Crystal Fibres at 850 nm

W.J. Wadsworth, J.C. Knight, A. Ortigosa-Blanch, J. Arriaga, E. Silvestre and P.St.J. Russell.

Optoelectronics Group, Department of Physics, University of Bath, Bath, BA2 7AY, UK.
Tel: +44-1225-826826 Ext. 4368 Fax: +44-1225-826110 email: w.j.wadsworth@bath.ac.uk

Abstract:
Soliton effects are observed at 850 nm in a pure silica photonic crystal fibre with group velocity dispersion (GVD) characteristics unattainable in conventional fibre. Zero GVD is obtained at 740 nm.

Introduction: Photonic crystal fibre (PCF) is optical fibre with a more-or-less regular array of microscopic air holes running along its length. Proposed in 1992, the first working example was made in 1996 [1]. In this paper we consider PCF in which light is guided at a missing (filled in) air hole in an array of holes, which guides by modified total internal reflection[1]. The unusual dispersion properties of the cladding, with its array of air holes, imparts novel dispersion properties to the guided mode[2].

Solitons allow the propagation of ultrashort optical pulses over long distances in optical fibres without dispersive spreading of the pulse. They occur in optical fibres with positive Kerr nonlinearity and anomalous group velocity dispersion (GVD). In any waveguide the total GVD is made up from the material dispersion and a contribution from the waveguide dispersion. In conventional fibre, waveguide dispersion can only be normal when the fibre is single mode, so anomalous GVD can only be obtained in conventional fibre when the dispersion of silica is anomalous, at wavelengths longer than 1.28 μm. Solitons have been observed in the communications band at 1.55 μm[3].

In PCF, however, the waveguide dispersion can be anomalous whilst the fibre remains strictly single-mode[2,4]. This brings the exciting possibility of generating solitons at wavelengths within the tuning range of Ti:sapphire in the near infrared. Similar fibre has also been shown experimentally to generate supercontinua over the visible and infrared[5]. We have fabricated PCF with parameters in the range suggested by previous calculations[2] and we have observed soliton effects over several metres of fibre. We have also compared calculated and measured values of the GVD over a broad spectral range.

Experiment: Modified dispersion PCF was fabricated from pure silica capillaries and rods in a manner similar to that previously reported[1] (Figure 1). The guided mode is tightly confined to the solid defect because the air filling fraction in the photonic crystal cladding is high. It is therefore not necessary to have more than a few periods of the cladding lattice in order to obtain a low-loss waveguide. Fibres were fabricated with two rows of air holes in a triangular lattice surrounding a central solid

core 'defect'. A solid silica jacket was added to increase the outer diameter of the fibre to 60 μm. The inner ring of air holes have a centre-to-centre spacing of $\Lambda = 1.8$ μm and hole diameter $d = 1.5$ μm ($d/\Lambda = 0.8$). This fibre is not strictly single mode at 850 nm (it supports 6 modes) but the second and higher order modes are difficult to excite, leaky and strongly uncoupled from the fundamental mode and are thus rarely observed experimentally. It is easy to achieve the condition where there is good coupling of the light into the fibre (coupling efficiency 50 %), and the output is clearly only in the fundamental mode. It is important to note that there does exist a range of PCF parameters (Λ and d/Λ), close to those used here, where the fibre is strictly single mode and has a GVD similar to that reported here.

A cut-back measurement of the fibre loss was made at 850 nm, where the loss was 80±40 dB km^{-1}. GVD in the fibre was measured by low-coherence interferometry using a white light source. Soliton effects were observed by propagating pulses from a modelocked Ti:sapphire laser (*Coherent* MIRA 900) through several metres of fibre. Output pulse widths were determined by autocorrelation and spectra were also measured

Results: Modelling of the fibre was performed by re-arranging Maxwell's equations as an eigenvalue problem for the propagation constant, β, and expanding the electromagnetic field in a plane wave basis[6,7]. The structure considered was an infinite periodic array of round holes with a single hole removed. Figure 2 shows the measured and calculated GVD for the fibre. The zero dispersion wavelength has been shifted from 1.28 μm in bulk silica to 0.74 μm in the PCF. Agreement between calculation and measurement is good even though the actual 2-period cladding structure is very different from the infinitely periodic cladding modelled.

The expected soliton characteristic length is slightly over 1 m for 200 fs pulses propagating at 850 nm in this fibre. The measured linear loss is too small to affect the propagation of solitons in the fibre on this length scale (0.08 dB m^{-1})[3]. A 3.1 m length of fibre, representing several soliton lengths, was used to facilitate unambiguous observation of the fundamental soliton. This distance allows linear GVD to lengthen the pulse substantially whilst giving time for any initial chirp or deviation from a pure $sech^2$ intensity profile in the input pulse to evolve into a soliton pulse[8]. Autocorrelation widths of the pulses at the fibre output are shown in figure 3, along with the full traces for the widest and narrowest pulses. The powers given are the average power of the 76 MHz pulse train at the fibre output (1000 μW corresponds to ~66 W peak power, 0.013 nJ pulse energy). At low power (<110 μW) the pulse is broadened to 800 fs by the linear GVD. As the power is increased self-phase modulation (SPM) begins to counteract the effects of GVD and the output pulse narrows to a minimum (140 fs at 1350 μW). At higher power, the pulse shape changes and lengthens slightly (300 fs at 3500 μW), then narrows again to 168 fs at 5100 μW. The ratio of the two powers for minimum pulse width is close to the predicted 4:1 for the fundamental and second soliton, although further characterisation would be required to identify these pulses precisely as the first two soliton orders.

The spectra of the output showed a peak at 850 nm which was little changed up to 2000 μW. At higher powers the main peak developed side lobes. At powers

above 1300 μW there were also other spectral components, red-shifted by more than 10 nm. These are generated by processes other than SPM and thus are not part of the soliton propagation, except as a loss mechanism. The temporal dependence of these features is eliminated from the autocorrelation traces by the spectral response of the non-linear crystal. At still higher powers a range of non-linear effects give rise to many spectral components extending from the ultraviolet to the infrared.

Conclusion: Soliton effects have been observed at 850 nm in a pure silica PCF designed to have anomalous GVD at this wavelength. The large GVD (50 ps nm^{-1} km^{-1}) and short pulse length (<200 fs) allow these effects to be seen over only a few metres of fibre. The fundamental soliton was observed and the second soliton was identified despite other accompanying non-linear effects. The measured GVD is very close to the calculated values which aids design of new fibres with certain dispersion properties, in particular fibres which are strictly single mode whilst retaining anomalous GVD in this spectral region.

The authors acknowledge the contribution from the research group headed by Miguel Andres at Universitat de Valencia, Spain, to the development of the numerical model used in figure (2).

References

[1] Knight, J.C., Birks, T.A., Russell,P.St.J. and Atkin D.M.: "All-silica single-mode fiber with photonic crystal cladding," Opt. Lett., 1996, **21**, pp1547-1549; Errata, Opt.Lett., 1997, **22**, pp484-485

[2] Mogilevtsev, D., Birks, T.A and Russell, P.St.J.: "Group-velocity dispersion in photonic crystal fibres," Opt. Lett., 1998, **23** (21), pp1662-1664

[3] Mollenhauer, L.F., Stolen, R.H. and Gordon, J.P.: "Experimental observation of picosecond pulse narrowing and solitons in optical fibres", Phys.Rev. Lett., 1980, **45**, pp1095-1098

[4] Gander, M.J., McBride, R., Jones, J.D.C., Mogilevtsev, D., Birks, T.A., Knight, J.C. and Russell, P.St.J.: "Experimental measurement of group velocity dispersion in photonic crystal fibre," Electron. Lett., 1999, **35** (1), pp63-64

[5] Ranka, J.K., Windeler, R.S. and Stentz, A.J.: "Efficient visible continuum generation in air-silica microstructure optical fibers with anomalous dispersion at 800 nm, " CLEO'99 postdeadline paper CPD8, Baltimore, May 1999

[6] Ho, K.M., Chan, C.T. and Soukoulis, C.M.: "Existence of a photonic band gap in periodic dielectric structures", Phys. Rev. lett., 1990, **65** (25), pp3152-3155

[7] Ferrando, A., Silvestre, E., Miret, J.J., Monsoriu, J.A. , Andres, M.V., Russell, P.StJ.: "Designing a photonic crystal fibre with flattened chromatic dispersion", Electron. Lett., 1999, **35** (4), pp325-327

[8] Blow, K.J. and Doran, N.J.: "Non-linear propagation effects in optical fibres: Numerical studies" in "Optical solitons- Theory and experiment" Taylor, J.R. ed., (Cambridge University Press, Cambridge, UK, 1992)

Soliton effects en photonic crystal fibres at 850 nm
Electronics Letters, 36 (1), pp 53-55 (2000)

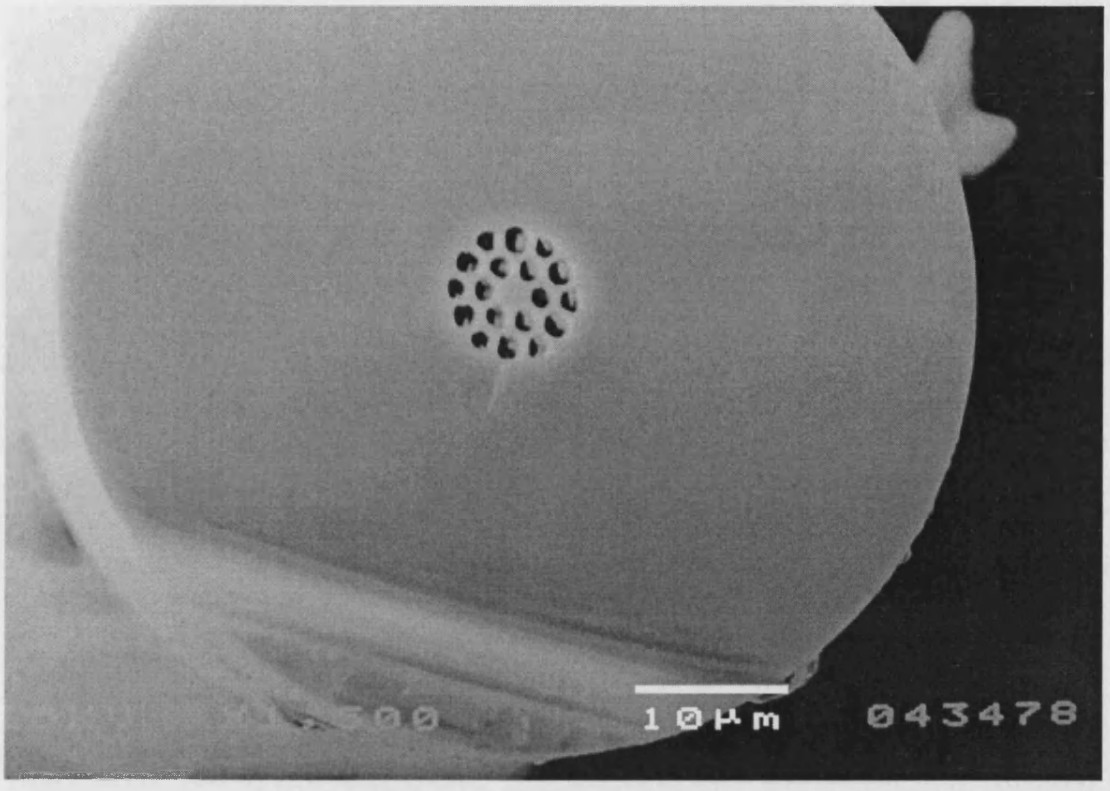

Figure 1: Scanning electron micrograph of the PCF used for the experiments described in this paper. $\Lambda = 1.8$ µm, $d = 1.5$ µm, $d/\Lambda = 0.8$, core diameter 2 µm.

Soliton effects en photonic crystal fibres at 850 nm
Electronics Letters, 36 (1), pp 53-55 (2000)

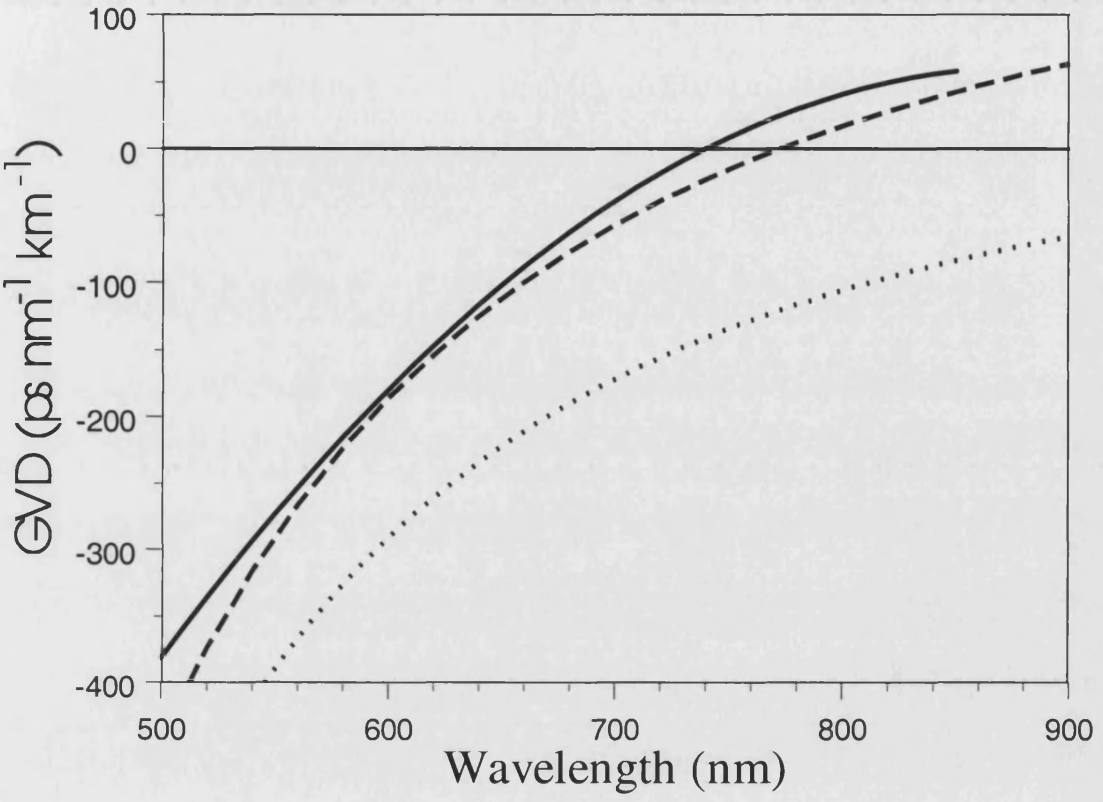

Figure 2: GVD of the PCF. Solid line – measured GVD for the fibre shown in figure 1. Dashed line – calculated GVD for the fundamental mode of an infinite photonic crystal with a missing air hole defect with $\Lambda = 1.8\ \mu m$, $d/\Lambda = 0.8$. Dotted line – GVD of bulk silica (the GVD of conventional fibres must lie below this line if they are to remain single mode).

Soliton effects en photonic crystal fibres at 850 nm
Electronics Letters, 36 (1), pp 53-55 (2000)

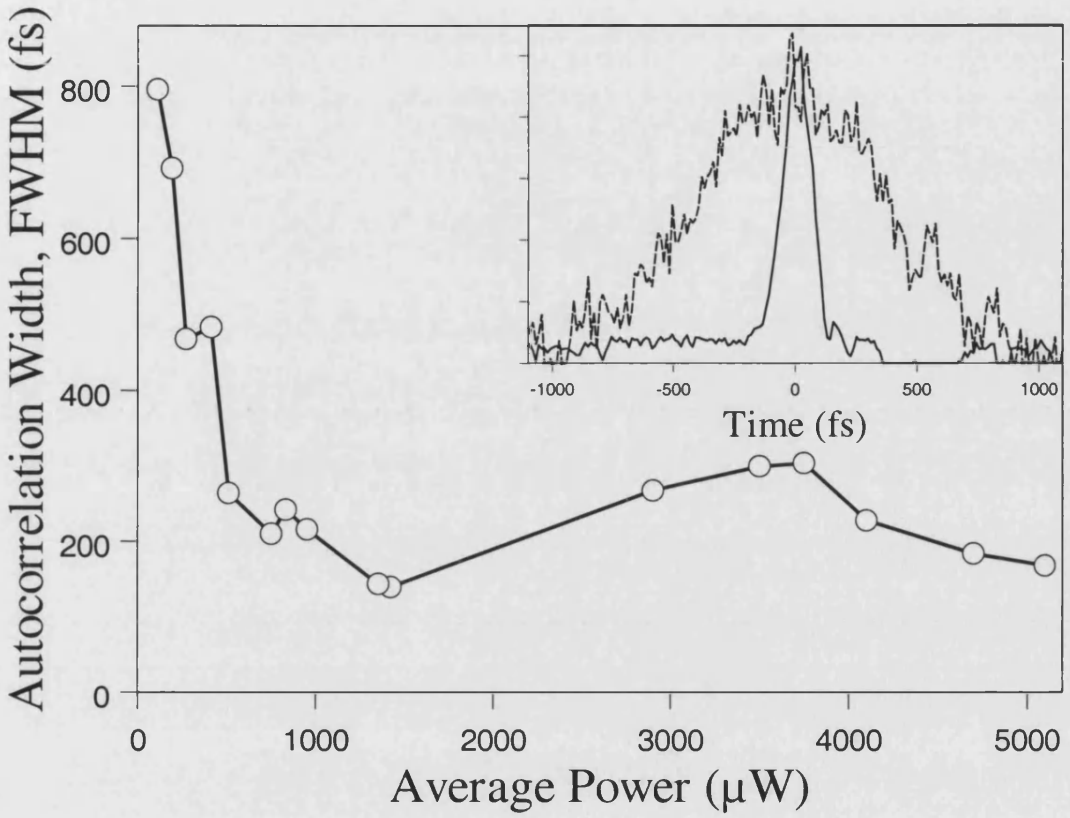

Figure 3: Autocorrelation widths of the pulses output from the fibre for various power levels. Inset: Traces of the pulses at 110 μW (dashed line) and 1350 μW (solid line).

Anomalous dispersion in photonic crystal fiber

J.C. Knight, J. Arriaga,T.A. Birks, A. Ortigosa - Blanch, W.J. Wadsworth and P.St.J. Russell

IEEE Photonic Technology Letters, 12 (7), pp 807-809, 2000.

Anomalous Dispersion in Photonic Crystal Fiber

J. C. Knight, J. Arriaga, T. A. Birks, *Member, IEEE*, A. Ortigosa-Blanch, W. J. Wadsworth, and P. St. J. Russell

***Abstract*—We describe the measured group-velocity dispersion characteristics of several air-silica photonic crystal fibers with anomalous group-velocity dispersion at visible and near-infrared wavelengths. The values measured over a broad spectral range are compared to those predicted for an isolated strand of silica surrounded by air. We demonstrate a strictly single-mode fiber which has zero dispersion at a wavelength of 700 nm. These fibers are significant for the generation of solitons and supercontinua using ultrashort pulse sources.**

***Index Terms*—Nonlinear optics, optical fiber dispersion, photonic crystal fiber.**

I. Introduction

THE group-velocity dispersion (GVD) characteristics of periodically microstructured silica fiber (photonic crystal fiber or PCF) are currently a topic of interest because of their significance in both linear [1]–[3] and especially nonlinear [4], [5] fiber optics. Photonic crystal fiber is a generic term describing a single-material fiber technology in which light guidance is due to roughly periodic morphological microstructuring of the fiber cladding rather than chemical doping. In one realization, photonic crystal fiber has a more-or-less periodic array of air holes in cross section, being invariant along its length, while a region of pure silica embedded within the array forms a waveguiding core. Waveguiding occurs because the "holey" fiber cladding effectively has a lower refractive index than the pure silica core, resulting in total internal reflection at the core-cladding interface [6], [7]. We refer to this as an index-guiding or total-internal reflection guiding fiber to distinguish it from other photonic crystal fibers which guide light due to a photonic band gap. (Such photonic band gap fibers [8] are not the subject of this letter.)

The unusual GVD features arise as a result of the very strong waveguide dispersion attainable in index-guiding PCF. The overall fiber dispersion can be made anomalous at wavelengths where both the GVD of pure silica and that of conventional single-mode fibers is normal [3]. This has recently enabled the demonstration of soliton propagation and superbroad white-light generation [4], [5] in these fibers. In this paper, we describe the dispersion properties of several PCF structures and demonstrate that the zero-GVD point in such fibers can be engineered over a very wide wavelength range extending from 500 nm.

II. The Fibers

Our photonic crystal fibers are made using a process similar to that described previously [6]. An electron micrograph of one of the fibers investigated here is shown in Fig. 1(a). For large-air-hole fibers, the core diameter D is usefully (albeit arbitrarily) defined as the shortest dimension of the solid silica region—approximately 1 μm in Fig. 1(a). The silica bridges which support the core and join it to the cladding structure have a thickness of roughly 120 nm. One would anticipate that the properties of this fiber might be relatively well predicted by approximating it as a single silica strand surrounded by air [1]—to first approximation, the thin silica bridges can be neglected. A different fiber structure is shown in Fig. 1(b). This fiber has a nominal core diameter of approximately 1.5 μm, this core being formed by a missing hole within a triangular array of holes. The silica bridges are about 380 nm wide. We can characterize the structure in terms of the diameter d of the air holes and the pitch

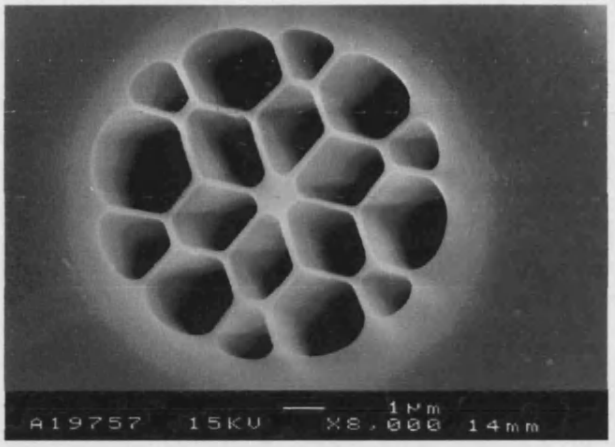

(a)

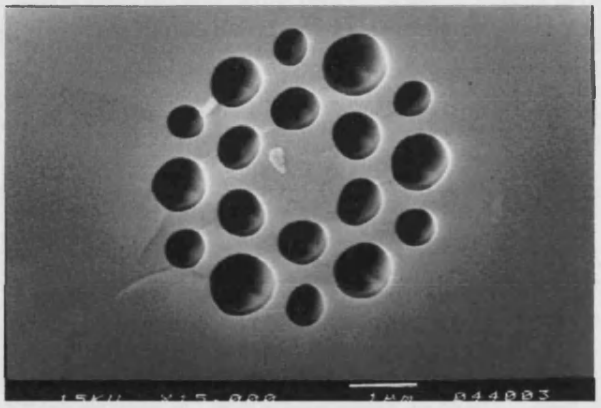

(b)

Fig. 1. (a) Scanning electron micrograph of a cleaved end-face of a photonic crystal fiber with very large air holes. The core diameter D (defined in the text) is 1 μm. The fine silica bridges supporting the core are roughly 120 nm in width. (b) A micrograph of a second PCF structure, where the air holes are significantly smaller. The core diameter is 1.5 μm, and the air holes are 0.62 μm in diameter.

Manuscript received February 29, 2000.

The authors are with the Optoelectronics Group, Department of Physics, University of Bath, Bath BA2 7AY, U.K.

Publisher Item Identifier S 1041-1135(00)05623-8.

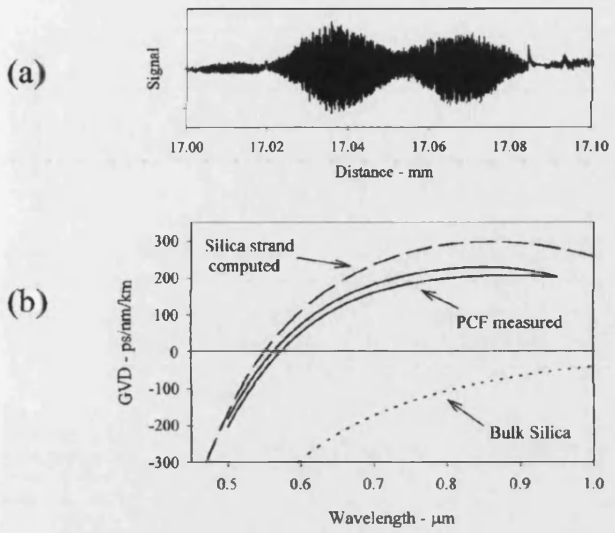

Fig. 2. (a). White-light fringes recorded after transmission of a 10-nm spectrum through a 13-mm length of the fiber shown in Fig. 1(a). The two sets of fringes apparent in the figure correspond to the two polarization states of the fundamental guided mode, as has been verified using a linear polarizer. (b) Group velocity dispersion curve obtained by measuring the shift of the fringes in (a) with wavelength (solid lines) and a computed curve for a solid silica strand surrounded by air with a diameter equal to that of the core of the fiber used (broken line). The dotted curve in the bottom right-hand corner indicates the GVD of pure silica in this wavelength region.

Λ of the periodic array. Such structures have previously been studied in some detail [2], [6], [7]. The core diameter D is then given by $D = 2\Lambda - d$ (assuming circular air holes). The fiber in Fig. 1(b) has $d = 0.62$ μm and $\Lambda = 1$ μm.

III. Experiments

We have measured the dispersion of the fundamental guided mode of the two structures shown in Fig. 1(a) and (b) and of several other fibers similar to that in Fig. 1(b) by using low-coherence interferometry. This has enabled us to perform measurements of group delay—and hence GVD—over a very broad spectral range from 500 to 1500 nm using a single short piece of fiber. Our experimental arrangement is similar to that described previously [9]. The measurements have been performed on short lengths (typically 10–40 mm) of fiber. An interferogram observed from a 13-mm length of the fiber in Fig. 1(a) is shown in Fig. 2(a). The two sets of fringes (recorded at 600 nm using a 10-nm bandpass filter and a tungsten lamp) are due to the different group velocities for the two polarization modes. This has been confirmed by the use of a linear polarizer. In both cases, the near- and far-field patterns of the guided mode are very similar and indicate fundamental-mode propagation. The large polarization-mode dispersion is an indication of the strong polarization dependence attainable in such fibers—the departures from perfect hexagonal symmetry in Fig. 1(a) are unintentional and relatively small. Similar effects were not observed for fibers with smaller air holes.

Results for the fiber shown in Fig. 1(a) are shown in Fig. 2(b). The known GVD of pure silica and the calculated GVD for a fine circular strand of silica surrounded by air (where the diameter of this strand is $D = 1$ μm, equal to the core in the PCF) are

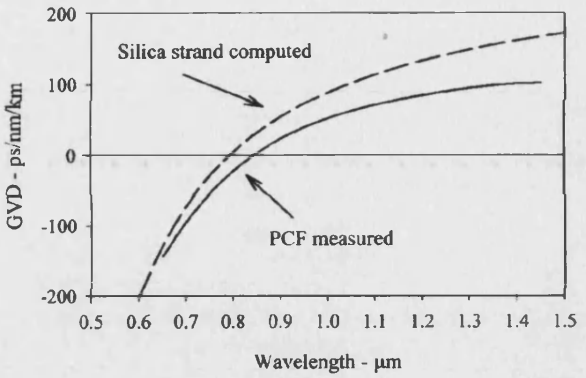

Fig. 3. Measured GVD from the fiber structure shown in Fig. 1(b) (solid line) and the corresponding computed curve for an isolated silica fiber (dashed line).

TABLE I
Summary of the Measured Fiber Parameters and the Corresponding Measured Zero-GVD Wavelengths. Fibers 1 and 3 Are Those Shown in Fig. 1(a) and (b). The Core Sizes Given Are Those Measured Directly on the Electron Micrograph. They Differ from Those Derived from the Measured Pitch and Hole Size Because the Air Holes Are Not Always Perfectly Circular. The Stated Air Hole Sizes Are Always Those Measured Along the Longest Dimension

Fiber number	Pitch (μm)	Air hole size (μm)	Core size (μm)	Measured GVD-zero wavelength (nm)	GVD-zero wavelength of a silica rod (nm) of same size
1	-	-	1	565	552
2	0.8	0.4	1.25	700	600
3	1.0	0.62	1.45	660	639
4	1.58	1.24	2.0	740	717
5	1.85	1.1	2.6	840	793

shown on the same graph. This latter curve was obtained using the known variation of silica index with wavelength and solving the exact eigenvalue equation to find the propagation constant of the guided mode. The agreement between the observed GVD and that computed for a plain silica fiber is very good, considering the degree of the approximation, the arbitrary definition of the core size and the uncertainty in the measured size of the fiber (measurements taken directly from the electron micrographs). A second set of results, recorded from the fiber in Fig. 1(b), are shown in Fig. 3. These demonstrate a similar broad agreement with the predicted behavior from the simple model, but the departures from the predicted performance are increased. The two sets of fringes for the two polarization modes were not resolved for this fiber (the fiber length used was 30 mm). Several general conclusions can be drawn from these measurements, and from the measurements on other fibers as summarized in Table I and illustrated in Fig. 4

For large-air-hole fibers the wavelength of zero-GVD and the overall shape of the GVD curve can be well approximated by assuming that the fiber behaves as an isolated strand of silica surrounded by air. This allows one to use a curve such as that shown in Fig. 4 (computed for a circular silica strand) to design a PCF structure which will have zero GVD at a particular wavelength. (In Fig. 4, the presence of two lines on the plot for small values of the core size indicates a finite region of anomalous dispersion for those sizes, i.e., the dispersion is anomalous

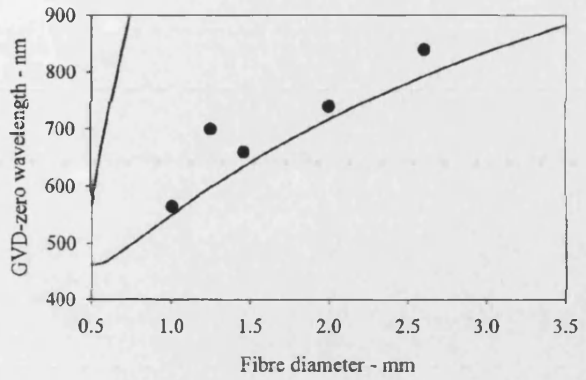

Fig. 4. Zero-GVD wavelength as a function of fiber core diameter, computed for an isolated strand of silica. The presence of two curves for small values of the diameter indicates a finite wavelength range in which an anomalous GVD is found. This curve can be used as a design tool for fabricating PCF structures with a particular GVD characteristic. The data points indicate the measured zero-GVD wavelengths for the fibers described in Table I. The single point which is substantially off the theoretical line is the single-mode fiber (fiber 2 in Table I).

between the two lines only.) Furthermore, this zero-GVD wavelength can be engineered to any wavelength from 500 nm to 1.3 μm, by fabricating a structure with the appropriate core size.

The differences between the predictions of this simple model and the actual fiber response are that the actual zero-GVD point occurs at a longer wavelength than predicted, and that the maximum anomalous GVD is not as high as predicted (see Figs. 2 and 3). The actual wavelength offset of the zero-GVD point in a particular structure is likely to be larger at longer wavelengths, because a given inaccuracy in the value of the computed waveguide dispersion will cause a larger wavelength error where the material dispersion slope is less.

The GVD slope around the zero-point is also reduced by reducing the air hole size. This makes it possible to design comparatively flat anomalous dispersion curves at wavelengths beyond about 800 nm, when compared to a plain silica fiber.

The differences in zero-GVD wavelength and in absolute anomalous GVD between the simple model and the experimental measurements must be attributed to the silica bridges joining the fiber core to the rest of the structure, and are expected to increase for smaller air holes and larger silica bridges. Such smaller air holes are required if the fiber is to be single-mode. Numerical modeling [10] has shown that fiber 2 in Table I is strictly single mode over a very broad wavelength range, extending from at least 300 nm. (This is in contrast to previous "experimentally single mode" fibers [4], which in principle support several modes.) The measured GVD is nonetheless fairly close to that of a pure silica strand.

IV. Conclusion

Photonic crystal fibers can be fabricated to have unusual dispersion characteristics, making them useful for nonlinear applications such as soliton generation and propagation, soliton lasers, supercontinuum generation, and ultrashort pulse compression. Using the results of this study one can approximate the fiber parameters required to produce a desired dispersion characteristic. We have demonstrated experimentally that anomalous dispersion can be obtained at wavelengths well below 600 nm in these structures and that anomalous GVD can be obtained at wavelengths as short as 700 nm in a strictly single-mode fiber structure.

References

[1] T. A. Birks, D. Mogilevtsev, J. C. Knight, and P. St. J. Russell, "Dispersion compensation using single-material fibers," *IEEE Photon. Technol. Lett.*, vol. 11, pp. 674–676, June 1999.

[2] A. Ferrando, E. Silvestre, J. J. Miret, J. A. Monsoriu, M. V. Andres, and P. St. J. Russell, "Designing a photonic crystal fiber with flattened chromatic dispersion," *Electron. Lett.*, vol. 35, pp. 325–327, 1999.

[3] M. J. Gander, R. McBride, J. D. C. Jones, D. Mogilevtsev, T. A. Birks, J. C. Knight, and P. St. J. Russell, "Experimental measurement of group velocity dispersion in photonic crystal fiber," *Electron. Lett.*, vol. 35, pp. 63–64, 1999.

[4] J. K. Ranka, R. S. Windeler, and A. J. Stentz, "Visible continuum generation in air-silica microstructure optical fibers with anomalous dispersion at 800 nm," *Opt. Lett.*, vol. 25, pp. 25–27, 2000.

[5] W. J. Wadsworth, J. C. Knight, A. Ortigosa-Blanch, J. Arriaga, E. Silvestre, and P. St. J. Russell, "Soliton effects in photonic crystal fibers at 850 nm," *Electron. Lett.*, vol. 36, pp. 53–55, 2000.

[6] J. C. Knight, T. A. Birks, P. St. J. Russell, and D. M. Atkin, "All-silica single-mode optical fiber with photonic crystal cladding," *Opt. Lett.*, vol. 21, pp. 1547–1549, 1996.

[7] T. A. Birks, J. C. Knight, and P. St. J. Russell, "Endlessly single-mode photonic crystal fiber," *Opt. Lett.*, vol. 22, pp. 961–963, 1997.

[8] J. C. Knight, J. Broeng, T. A. Birks, and P. St. J. Russell, "Photonic band gap guidance in optical fibers," *Science*, vol. 282, pp. 1476–1549, 1998. R. F. Cregan, B. J. Mangan, J. C. Knight, T. A. Birks, P. St. J. Russell, D. Allen, P. J. Roberts, "Single-mode photonic band gap guidance of light in air," *Science*, vol. 285, pp. 1537–1539, 1999.

[9] M. Tateda, N. Shibata, and S. Seikai, "Interferometric method for chromatic dispersion measurement in a single-mode optical fiber," *IEEE J. Quantum Electron.*, vol. QE-17, pp. 404–407, Mar. 1981.

[10] T. A. Birks, D. Mogilevtsev, J. C. Knight, P. St. J. Russell, J. Broeng, P. J. Roberts, J. A. West, D. C. Allan, and J. C. Fajardo, "The analogy between photonic crystal fibers and step-index fibers," presented at the OFC'99, Paper FG4-1, 1999.

Highly birefringent photonic crystal fibres

A. Ortigosa - Blanch, J.C. Knight, W.J. Wadsworth, J. Arriaga, B.J. Mangan, T.A. Birks and P.St.J. Russell

Optics Letters, 25 (18), pp 1325-1327 (2000)

Highly birefringent photonic crystal fibers

A. Ortigosa-Blanch, J. C. Knight, W. J. Wadsworth, J. Arriaga, B. J. Mangan, T. A. Birks, and P. St. J. Russell

Optoelectronics Group, Department of Physics, University of Bath, Claverton Down, Bath BA2 7AY, UK

Received April 19, 2000

We report a strongly anisotropic photonic crystal fiber. Twofold rotational symmetry was introduced into a single-mode fiber structure by creation of a regular array of airholes of two sizes disposed about a pure-silica core. Based on spectral measurements of the polarization mode beating, we estimate that the fiber has a beat length of approximately 0.4 mm at a wavelength of 1540 nm, in good agreement with the results of modeling. © 2000 Optical Society of America

OCIS codes: 060.2420, 230.4000, 060.2280, 060.2270, 060.2310.

Conventional circularly symmetric optical fibers do not maintain the polarization state of the guided mode along their length. Although they are nominally isotropic, small twists, bends, and other stresses impose unknown and uncontrolled birefringence on the fiber, so the polarization of the fiber output is unpredictable. Highly birefringent fibers (in which strong birefringence is deliberately introduced during the fiber fabrication) are much more resilient to such environmental factors. The polarization beat length L_B is a measure of the birefringence and is defined as

$$L_B = \frac{2\pi}{\beta_x - \beta_y} = \frac{\lambda}{n_x - n_y}, \tag{1}$$

where β_x and β_y are the propagation constants of the two modes and n_x and n_y are the refractive index that each mode sees, with shorter L_B corresponding to stronger birefringence. The required birefringence can be achieved in either of two ways: The shape of the refractive-index profile that defines the waveguide can be made noncircular (form or shape birefringence) or the material that forms the fiber can itself be made birefringent, typically by introduction of stresses as in bow-tie or PANDA fibers.[1,2]

Silica photonic crystal fiber[3] (PCF) has an array of microscopic airholes running along its length. In the type considered here, a single missing airhole within the array forms a region of raised refractive index that guides light by total internal reflection. The large index contrast and the two-dimensional nature of the microstructure greatly widen the range of waveguide parameters attainable, compared with conventional fiber technology, and this has facilitated the creation of, for example, "endlessly single-mode" fibers[4] and fibers with anomalous group-velocity dispersion in the visible region.[5,6] PCF can potentially be made highly birefringent: The large index contrast facilitates high form birefringence, and the stack-and-draw fabrication process permits the formation of the required microstructure near the fiber core. Relatively weak birefringence in similar structures as a result of accidental departures from circular symmetry has already been reported.[3,6] In this Letter we report a realization of a highly birefringent monomode PCF.

We fabricated the fiber by stacking an array of silica capillaries and rods, as previously reported.[3] Anisotropy was introduced into the fiber by careful positioning of capillaries with the same external diameter but different wall thicknesses, leading to different airhole sizes in the cladding of the final fiber and twofold rotational symmetry. A solid silica jacket was added to increase the diameter and the strength of the fiber. A scanning-electron micrograph of the fiber is shown in Fig. 1(a). The fiber had a pitch (center-to-center distance between the holes) of $\Lambda = 1.96\ \mu$m and a hole diameter of $d_1 = 0.40\ \mu$m for the small holes and $d_2 = 1.16\ \mu$m for the large ones. The external fiber diameter was 63 μm.

Using these dimensions, we modeled the fiber by using a full vector numerical model based on the plane-wave method.[7] The photonic crystal structure was modeled as a supercell [Fig. 1(b)]. The calculations showed that the fiber was single mode at 1540 nm, which was confirmed experimentally and which made it easy to study the fiber's beat length. The calculated beat length was $L_B = 0.56$ mm, far shorter than in conventional high-birefringence fibers.

The guidance properties of the fiber were investigated experimentally with a tunable diode laser. We studied the near- and far-field patterns by imaging the output face of the fiber onto a vidicon camera.

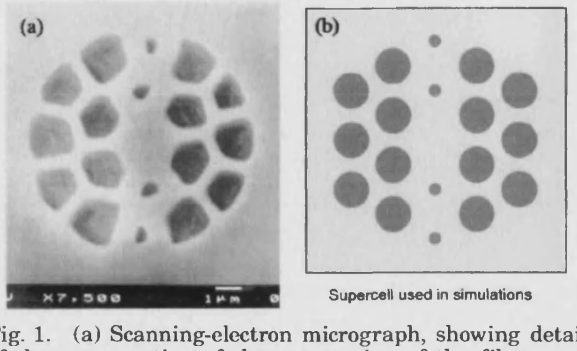

Fig. 1. (a) Scanning-electron micrograph, showing detail of the cross section of the core region of the fiber used in the experiment. The central silica region, surrounded by airholes, acts as the fiber core. (b) Idealized structure used in the numerical modeling.

0146-9592/00/181325-03$15.00/0

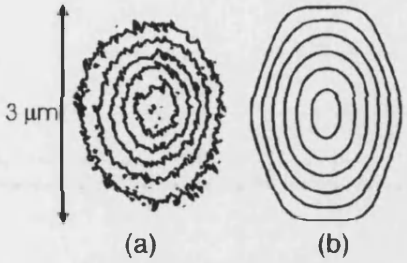

Fig. 2. (a) Experimental and (b) theoretical contour maps of the near-field pattern of the fiber used in the experiment. The contours correspond to 20% steps in the intensity, and the vertical axis corresponds to the direction of the small airholes. The profiles of the two polarization modes in the fiber are indistinguishable.

Figure 2(a) shows a contour map of the observed near-field intensity pattern (excitation wavelength, 1540 nm); the corresponding computed pattern is shown in Fig. 2(b). Both plots show a mode that is well confined to the core region and elongated in the direction of the small airholes. In that direction the air-filling fraction is smaller, so the fundamental mode sees a higher effective index in the cladding; the apparent core size is also larger.

Two direct methods for measuring the beat length of the fiber were attempted, both of which we found to work well for conventional high-birefringence fiber. First we tried to observe the beat length directly by observing the fiber from the side.[1] No variation could be seen, because light that is Rayleigh scattered from the fiber core is subsequently rescattered into different directions by the surrounding airholes. Second, we used an elasto-optic method (the periodic lateral force technique[1,8]) but were still unable to measure the beat length in the highly birefringent PCF. We attribute this outcome once again to the holey cladding, which is unable to transmit uniaxial stress to the core owing to its strong mechanical anisotropy.

Conventional direct methods having proved to be inappropriate, we were forced to use an indirect approach. We launched light from a tunable diode laser (polarized at 45° to the principal axes) into a fixed length L of fiber and monitored the output polarization state as a function of wavelength. The fiber was laid upon a flat metal base to prevent bending. A polarizer was placed at the output end with its transmission axis aligned at 45° to the axes of the fiber, and the wavelength was scanned in small steps. The results for a scan from 1530 to 1540 nm are shown in *Fig. 3; clear polarization beating for a fiber of length* $L = 860$ mm was seen.

To relate the observed beat period, $\Delta\lambda = 0.55 \pm 0.01$ nm, to the beat length, L_B, we consider the difference in phase between the modes after a length of fiber, L:

$$\phi = (\beta_x - \beta_y)L = 2\pi L/L_B, \tag{2}$$

where we use Eq. (1) for L_B. Differentiating the phase with respect to wavelength and making the total phase change equal to 2π lead to

$$\Delta\lambda = \frac{{L_B}^2}{L\left|\frac{dL_B}{d\lambda}\right|}. \tag{3}$$

To evaluate this expression for our experimental case, we must make an assumption about the wavelength dependence of L_B. If we assume that $L_B \propto \lambda^k$, there is a simple closed-form solution for the beat length, given by

$${L_B}^{\text{Approx}} = \frac{(\Delta\lambda)Lk}{\lambda}, \tag{4}$$

where L is the actual length of the fiber and λ is the central wavelength of the scan.

A least-squares fit of $L_B \propto \lambda^k$ to values of L_B from 1400 to 1700 nm calculated with our theoretical model gave $k = -1.38$ ($R^2 = 0.9992$). With this value used in Eq. (4), the observed beating then gives ${L_B}^{\text{Approx}} = 0.42 \pm 0.04$ mm and a modal birefringence $|n_x - n_y| = 3.7 \times 10^{-3}$ from Eq. (1). This beat length is more than six times shorter than the beat length of typical conventional high-birefringence fibers (see, e.g., the Newport 1999–2000 catalog[9]).

We also used our model to calculate the expected spectral beat period, $\Delta\lambda$. From the theoretical model we calculated $dL_B/d\lambda = -510$ and $L_B = 0.56$ mm at a wavelength of 1540 nm. Equation (3) then gives a theoretical value of $\Delta\lambda = 0.72$ nm for $L = 860$ mm, as in the experiment. This value can be considered to be in good agreement with the measurement, as the model assumes a perfect structure instead of the real one, as shown in Fig. 1. At the same time, the agreement with the model shows that the most important contribution to the birefringence is form birefringence.

In conclusion, we have developed a photonic crystal fiber with a high modal birefringence and a beat length of 0.4 mm at 1540 nm. We have also shown that the unusual optical properties of the PCF cladding are accompanied by unique mechanical properties, making it difficult to measure the beat length directly. Unlike conventional optical fibers with solid cladding materials, PCF's permit easy incorporation of large optical and mechanical inhomogeneities by altering the geometry, size, and position of the cladding holes.

This study is supported by the U.K. Engineering and Physical Sciences Research Council. T. A. Birks

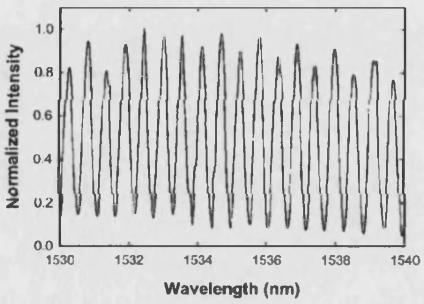

Fig. 3. Typical plot of the signal transmitted through a polarizer placed at the end of the fiber. The fiber length was 860 mm. Note that the overall transmitted intensity is constant.

is a Royal Society University Research Fellow. A. Ortigosa-Blanch's e-mail address is pypao@bath.ac.uk.

References

1. R. B. Dyott, *Elliptical Fiber Waveguides* (Artech House, Boston, Mass., 1995).
2. D. N. Payne, A. J. Barlow, and J. J. Ramskov Hansen, J. Quantum Electron. **QE-18,** 477 (1982).
3. J. C. Knight, T. A. Birks, P. St. J. Russell, and D. M. Atkin, Opt. Lett. **21,** 1547 (1996); errata **22,** 484 (1997).
4. T. A. Birks, J. C. Knight, and P. St. J. Russell, Opt. Lett. **22,** 961 (1997).
5. J. C. Knight, J. Arriaga, T. A. Birks, A. Ortigosa-Blanch, W. J. Wadsworth, and P. St. J. Russell, IEEE Photon. Technol. Lett. **12,** 807 (2000).
6. J. K. Ranka, R. S. Windeler, and A. J. Stenz, Opt. Lett. **25,** 25 (2000).
7. A. Ferrando, E. Silvestre, J. J. Miret, P. Andres, and M. V. Andres, Opt. Lett. **24,** 276 (1999).
8. K. Takada, J. Noda, and R. Ulrich, Appl. Opt. **24,** 4387 (1985).
9. Newport Corporation, Irvine, Calif.

Supercontinuum generation in photonic crystal fibres and optical fibre tapers-A novel light source
JOSA B, 19 (9), pp. 2148-2155, 2002

Supercontinuum generation in photonic crystal fibres and optical fibre tapers – A novel light source

W.J. Wadsworth, A. Ortigosa - Blanch, J.C. Knight, T.A. Birks, T – P.M. Man and P.St.J. Russell

JOSA B, 19 (9), pp. 2148-2155, 2002

Supercontinuum generation in photonic crystal fibers and optical fiber tapers: a novel light source

William J. Wadsworth, Arturo Ortigosa-Blanch, Jonathan C. Knight, Tim A. Birks, T.-P. Martin Man, and Phillip St. J. Russell

Optoelectronics Group, Department of Physics, University of Bath, Bath BA2 7AY, UK

Received November 30, 2001; revised manuscript received February 27, 2002; accepted March 14, 2002

Broadband continua extending from 400 to 1600 nm are generated in photonic crystal fibers and in tapered conventional optical fibers. The continuum is generated in the fundamental fiber mode. Femtosecond pulses from an unamplified Ti:sapphire laser with energies up to 4 nJ are used, and the resultant spectra from several photonic crystal fibers and taper structures are compared and analyzed. © 2002 Optical Society of America

OCIS codes: 060.2400, 060.4370.

1. INTRODUCTION

There has recently been great interest in the applications of white-light supercontinua generated by femtosecond pulses in photonic crystal fibers (PCFs) and in tapered optical fibers.[1–11] The low pulse energies required for generation of the continuum, its coherently pulsed nature, and its high spatial brightness in the fundamental mode of an optical fiber make this continuum an ideal source for applications such as frequency metrology,[12–16] femtosecond-pulse phase stabilization,[12] optical coherence tomography,[17,18] ultrashort pulse compression, spectroscopy of materials and photonic structures, and fiber characterization. Supercontinuum spectra have been observed from PCFs and tapered-fiber structures with a wide range of pump pulse lengths from 25 fs to 60 ps or even to 800 ps and with pump wavelengths in the visible or the near infrared.[1,4,8,13,19] The present authors and others previously demonstrated supercontinuum spectra spanning more than two optical octaves from 380 nm in the ultraviolet, through the visible, to 1600 nm in the infrared from pulses approximately 200 fs long and as little as 5 nJ energy, propagating either in PCFs or in tapered conventional telecommunications fiber.[2] In this paper we compare the properties of the spectra produced in various PCFs and tapered fibers with particular attention to tailoring spectra to applications of this novel source.

A PCF is a silica optical fiber with an ordered array of microscopic air holes running along its length. The guidance properties of the fiber are determined by the size and pattern of the air holes and the solid-silica regions rather than by the properties of bulk optical glass, as in conventional fiber.[20] Here we consider PCF in which light is guided by modified total internal reflection[20,21] at a missing (filled-in) air hole in an array of holes. It was predicted that such a structure with a small core (of the order of 1 μm) and large air holes would display unique group-velocity dispersion (GVD), with anomalous GVD in single-mode PCFs at wavelengths much shorter than are attainable in conventional single-mode fiber.[22] In fact, single-mode guidance is not necessary for many applications of white-light generation, as is discussed below, which greatly widens the range of GVD available for study.[19,23,24]

A PCF with large air holes and a small solid-silica core is physically similar to a strand of silica surrounded by air. If a section of conventional optical fiber is heated and stretched in a flame, the diameter of the fiber may be reduced to such an extent that the core becomes too small to confine the light and the mode spreads out to be guided at the external surface of the cladding. A fiber tapered in this way to a waist diameter of a few micrometers has the GVD characteristics required for the generation of continua similar to those seen in PCF.[2,10,18]

Here we compare the spectra generated from (a) a PCF with a regular array of air holes on a triangular lattice and a ratio of air-hole diameter d to hole pitch Λ of $d/\Lambda = 0.4–0.8$, (b) tapered optical fibers with taper-waist diameters of 1–3 μm, and (c) a PCF variant in which the air holes are so large as to leave a core surrounded by air and suspended by thin (~100-nm) glass bridges with core diameters of 1–3 μm. Figure 1 shows scanning electron micrographs (SEMs) of representative structures of the three devices.

2. EXPERIMENT

PCFs were fabricated in a manner similar to that previously reported.[20,21] Pure-silica capillaries were stacked around a solid-silica rod. The stack was then drawn down into a fiber: [Figs. 1(a) and 1(c)]. A solid-silica jacket was added to increase the external fiber diameter to 60–100 μm for ease of handling. With different stacking and drawing techniques fibers with various hole diameters d, hole-to-hole pitches Λ, and solid core diameters d_{core} could be fabricated for the two types of structure shown in Figs. 1(a) and 1(c).

Fiber tapers were fabricated by heating and stretching standard telecommunications fiber (Corning, SMF 28) or

0740-3224/2002/092148-08$15.00

other step-index fiber in a flame. A traveling-flame technique was used to produce tapers with short adiabatic transition regions and a long, 95-mm, uniform-diameter waist region.[2,25] Waists with controlled variations in their diameters and fused taper couplers could also be produced by this technique. The tapers were placed in a plastic housing for physical protection and to prevent losses caused by dust settling on the waist region. Losses of such tapers are typically of the order of 0.1 dB.

The mode-propagation constants and thence phase velocity, group velocity, and GVD, of the fiber devices were calculated. For tapers the analytical mode-propagation equation was solved numerically for a circular silica fiber in air. For periodic PCFs and free-strand-type PCFs a plane-wave supercell expansion[23,24] was used. Plane-wave expansions were generated both for idealized regular PCF structures and for actual fabricated fibers by use of bit-map index-profile images from electron micrographs of the fiber cross section.

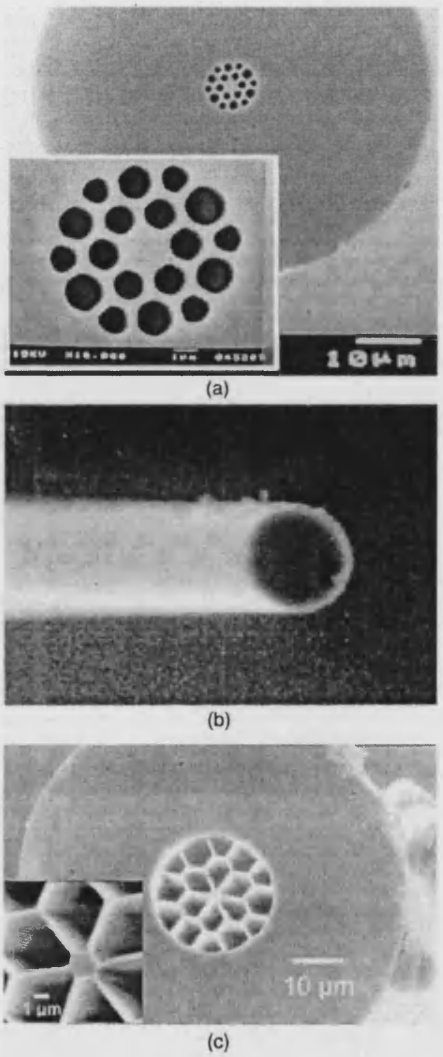

Fig. 1. SEMs of the fibers used for the experiments described in this paper: (a) regular-array PCF, where $\Lambda = 1.74\ \mu m$, $d/\Lambda = 0.8$, and $d_{core} = 2.0\ \mu m$; (b) waist of a tapered conventional fiber, where the waist diameter is 6 μm and the tapers used had waist diameters of 1–3 μm; (c) free-strand PCF, where $d_{core} = 1.9\ \mu m$.

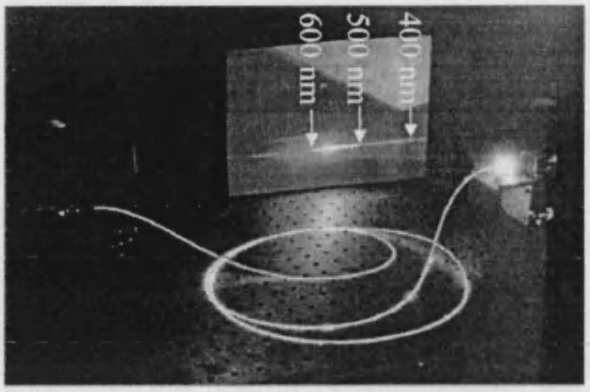

Fig. 2. Photograph of white-light supercontinuum generation in a PCF. Femtosecond pulses at 850 nm from the Ti:sapphire laser enter the fiber from the left. The output beam is dispersed by a grating onto the screen behind it.

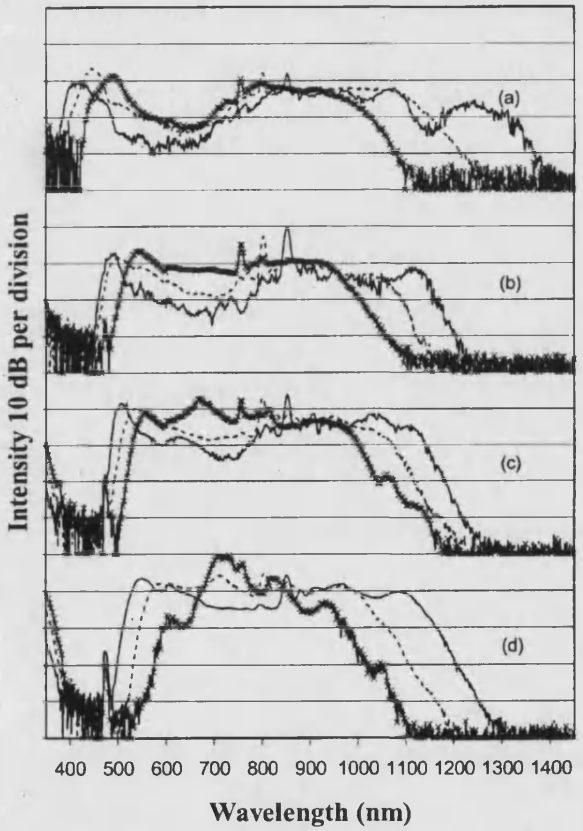

Fig. 3. Dependence of output spectrum on fiber and pump wavelength at high power, ~210 mW with a 90-mm length. Strand-type PCF: (a), (b), (c), (d) $d_{core} = 1.6, 1.9, 2.1, 2.5\ \mu m$, respectively. Input wavelengths: 850 nm, solid curves; 800 nm, dotted curves; 750 nm, crosses.

The group delay, hence the GVD, of the fiber devices was also measured over a broad range from 500 to 1500 nm by low-coherence interferometry.[23,26] There is gener-

ally very close agreement between the calculated and the measured values of GVD, a fact that gives credence to nonlinear optical predictions derived from calculated values of modal indices.

For white-light generation, pulses from a mode-locked Ti:sapphire laser oscillator (Coherent, Model Mira900) were launched into the fiber (Fig. 2). To prevent optical feedback into the Ti:sapphire laser from the input face of the fiber, an optical isolator was used. The pulses emitted by the laser were less than 200 fs in duration and were chirped by the normal dispersion of the isolator and the launch optics. The pulse-repetition frequency was 76 MHz.

Output spectra were measured with a grating-based optical spectrum analyzer (Ando, Model AO-6315B). The resolution was set to 5 or 10 nm, and spectra were measured across the full range of the instrument from 350 to 1750 nm. The absolute power measured was nominally calibrated over the entire range; however, there were some notable artifacts associated with the broad measurement bandwidth that requires different detectors and discrimination of overlapping grating orders. The artifacts of importance to the results presented here are a step change in intensity (which can be quite large) at a wavelength of 600 nm [see, e.g., Figs. 3(c) and 3(d) (solid curves)], an isolated peak at 475 nm (25–30 dB below the peak intensity of the spectrum [e.g., Figs. 3(c) and 3(d), all three traces], an apparent increase in intensity from 400 to 350 nm and from 1700 to 1750 nm [e.g., Figs. 3(d) (all three traces) and 4 (all traces)], and an apparent ultraviolet signal at $\lambda/2$ at 30 dB below peak intensity [e.g., Fig. 5(d) (crosses)]. It should be noted, however, that other isolated peaks [such as that at 550 nm in Figs. 5(b) and 5(c) (solid curves)] are real, as one can easily verify by dispersing the fiber output onto a screen by use of a grating.

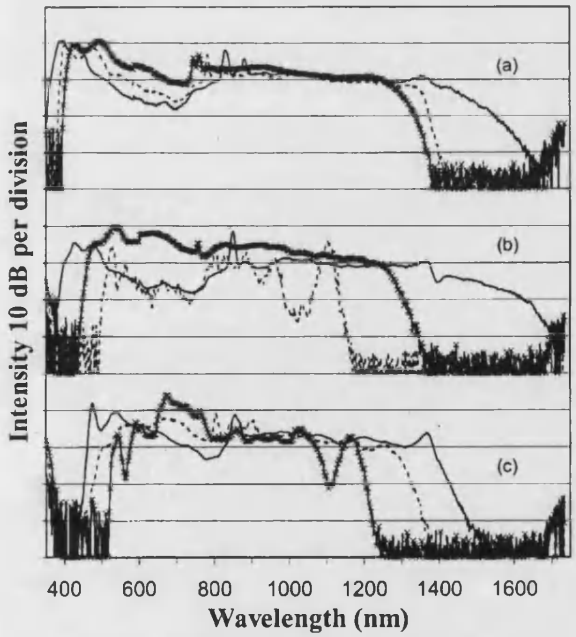

Fig. 4. Dependence of output spectrum on the fiber and the pump wavelength at high power, ~200 mW with a 1-m length. Strand-type PCF: (a), (b), (c), (d) d_{core} = 1.6, 1.9, 2.1, 2.5 μm, respectively. Input wavelength, 850 nm, solid curves; 800 nm, dotted curves; 750 nm, crosses.

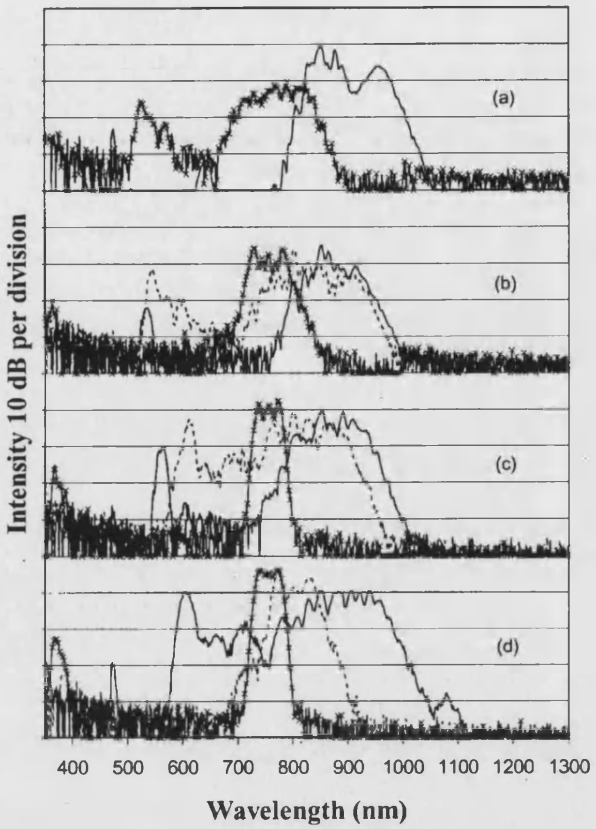

Fig. 5. Dependence of output spectrum on fiber and pump wavelength at low power, ~50 mW with a 90-mm length. Strand-type PCF: (a), (b), (c), (d) d_{core} = 1.6, 1.9, 2.1, 2.5 μm, respectively. Input wavelengths: 850 nm, solid curves; 800 nm, dotted curves; 750 nm, crosses.

3. RESULTS

A. Dispersion

Figure 6 shows the calculated GVDs for circular fiber tapers of various diameters along with the measured GVDs of several PCFs. From these figures it is clear that the GVDs of optical fiber tapers and of PCFs are in the same region but that, while there can be marked similarities, there can be significant differences [see, e.g., curve (f) in Fig. 6]. Optical fiber tapers and free-strand PCFs are clearly structurally similar [Figs. 1(b) and 1(c)] and would be expected to have similar GVD properties. In Fig. 6 the PCFs represented by curves (a) and (d) are free-strand structures with core diameters of 1.0 and 2.5 μm, respectively, and they have similar dispersion curves to those calculated for free-silica strands of these diameters. Periodic PCF [Fig. 1(a)] affords an extra degree of freedom; as well as the diameter of the solid core, we can control the sizes of the holes surrounding the core (or, equivalently, control the widths of the silica bridges supporting the core), hence the effective index step. Thus we have greater control of the dispersion properties, permitting

GVD curves like curve (f) of Fig. 6. Periodic PCFs can also be used to create fibers that are strictly single mode but retain interesting GVD properties. For example, curve (f) of Fig. 6 is a single-mode fiber. The double GVD trace [curve (a) of Fig. 6] arises from the form birefringence of this free-strand PCF, which has a core diameter of 1 μm.[23]

B. Fiber Modal Properties

It is well known that the larger the refractive-index step from core to cladding, the more modes are guided, in general, in a fiber waveguide. With the large silica–air index step used in the fibers discussed in this paper, most structures are highly multimode, even with extremely small core diameters of 1–2 μm. This is not as much of a problem as one might think. In few-moded fibers such as these it is still possible to launch light almost entirely into the fundamental mode. In conventional fibers used in the few-moded regime the propagation constants of many modes are similar, which means that small perturbations of the fiber (e.g., bending) are sufficient to couple light from one mode into others. Light that is launched into one mode soon becomes distributed among many fiber modes.

In the fibers discussed here, however, the same large index step and small core that yield interesting dispersion properties also help with the modal properties. Although there may be many modes allowed in a fiber taper or a free-strand PCF, these modes have very different propagation constants (or modal indices). For example, a fiber of the type shown in Fig. 1(c), with $d_{\text{core}} = 2.5$ μm, has a calculated fundamental-mode effective index of $n_1 = 1.44$ and a second mode index of $n_2 = 1.41$ at a wavelength of $\lambda = 0.8$ μm. Thus the beat length L_B between the modes is

$$L_B = \frac{1}{(\beta_1 - \beta_2)} = 5\ \mu\text{m}, \tag{1}$$

with propagation constants $\beta_n = 2\pi n_n/\lambda$. With such a short beat length, coupling the modes together requires large perturbations, which cannot be achieved through normal bending (with typical radii of more than 2 mm). Thus, if light is launched into one mode of the fiber (whether that be the fundamental mode or some higher mode) the light will continue to propagate in that mode without coupling to other modes. In this way, we can conduct experiments in the fundamental mode of a multimode PCF or taper without worrying about the existence of other modes.

Adiabatic transitions on an optical fiber taper provide further assistance. Light in the fundamental mode of the untapered fiber is transformed into the fundamental mode of the taper and then is transformed back again into the fundamental mode of the untapered fiber at the output. Thus, if the untapered fiber is single mode at the input wavelength, light can be coupled into only the fundamental mode of the taper waist. Any light of other wavelengths generated in the fundamental mode of the taper will also exit in the fundamental mode of the untapered output fiber; however, if this light is at a short wavelength that is below the single-mode cutoff of the untapered fiber it may be coupled to higher-order modes if the output fiber pigtail is long and bent. The present authors and others have previously shown[2] that the type of fiber used to create a taper has no effect on the output spectrum, as the residual core is too small to have any effect on the properties of the taper waist. It is therefore usually possible to select a fiber that is single mode for the continuum wavelengths required for a particular application and then to make the necessary taper from this fiber. In this way single-mode output may be ensured.

Finally, regular PCFs can be designed to have interesting GVD properties, while supporting only one mode.[22,24] The index step can be high, with relatively large air holes, but any mode other than the fundamental mode may leak out between the holes where there is no index step at all.[21] In these fibers there are no higher-order modes to worry about.

C. White-Light Generation

We investigated how the fiber size, type, dispersion, and length affect the supercontinuum spectrum generated at various input power levels with different pump wavelengths. Table I lists the fiber structures used. Because of the large range of possible parameters under which supercontinuum generation may be observed, we first

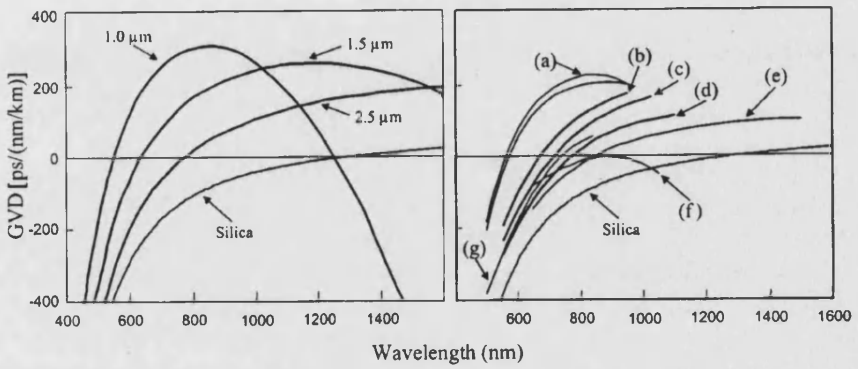

Fig. 6. Calculated GVD of silica strands (fiber taper waists) of left, various diameters, and right, with the measured GVD of various PCFs; and GVD of bulk silica (solid curves.) Fibers (a), (b), (c), (d) free-strand PCF with $d_{\text{core}} = 1.0, 1.6, 1.9, 2.5$ μm and (e), (f), (g) regular-array PCF $d_{\text{core}} = 1.5, 1.5, 2.1$ μm, respectively.

Table 1. Properties of Fiber Structures

	Property		
Fiber Type	Length	Waist	Core
Tapers	90 mm	1.5, 1.8, 2.0, 2.5 μm	
	250 mm	3–4 μm	
Free-strand PCFs	90 mm		1.6, 1.9, 2.1, 2.5 μm
	1 m		1.6, 1.9, 2.1, 2.5 μm
Other PCFs	90 mm–1 m		1.5–3 μm

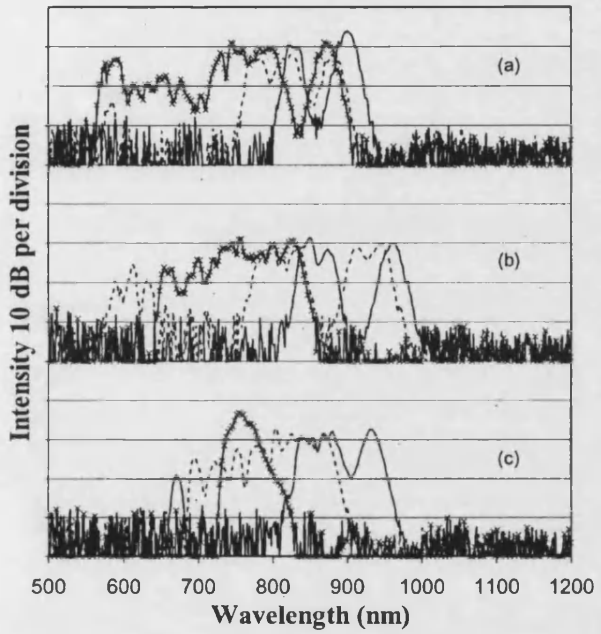

Fig. 7. Dependence of output spectrum on the fiber and the pump wavelength at low power, ~10 mW with a 1-m length. Strand-type PCF: (a), (b), (c), d_{core} = 1.9, 2.1, 2.5 μm, respectively. Input wavelengths: 850 nm, solid curves; 800 nm, dotted curves; 750 nm, crosses.

present measurements from a selection of fibers and then draw comparisons and further conclusions.

Figures 3, 4, 5, and 7 show the output spectra from 90-mm and 1-m lengths of four free-strand PCFs with respective core diameters of 1.6, 1.9, 2.1, and 2.5 μm. The full measured GVD curves for d_{core} = 1.6, 1.9, 2.5 μm are shown in as curves (b), (c), and (d), respectively, in Fig. 6. The GVD zero points are $\lambda_{GVD=0}$ = 675, 720, 775 nm for these three fibers, and GVD zero is estimated to be 750 nm for d_{core} = 2.1 μm. This type of fiber is easily controlled in fabrication to allow for a clean comparison of the effects of varying $\lambda_{GVD=0}$ and λ_{pump}. Pump wavelengths of 750, 800, and 850 nm were used. GVD parameters D at 750 nm are 70, 25, and −21; at 800 nm they are 105, 55, and 14; at 850 nm they are 130, 85, and 40 ps nm^{-1} km^{-1} for d_{core} = 1.6, 1.9, 2.5 μm, respectively.

Clearly the broadest spectra are seen when $\lambda_{pump} \gg \lambda_{GVD=0}$, where $D \gg 0$ [e.g., the solid curves in Figs. 3(a), 4(a), and 4(b)]. In these cases the spectra at low pump powers exhibit substantial broadening to the infrared side of the pump wavelength together and an isolated intensity peak in the visible [e.g., the solid curves in Figs. 5(a), 5(b), and 5(c), with isolated peaks at 650, 540, and 565 nm, respectively]. As the power is increased, the visible peak broadens and shifts to the blue, and the spectral gap between the peak and the broad infrared spectrum also fills in. At high power the spectrum is continuous but still displays a marked dip in intensity (to as much as 20 dB) in the red and an intense component in the blue–ultraviolet [e.g., all curves in Figs. 3(a) and solid curves in Figs. 3(b) and 3(c)].

Although spectra generated for $\lambda_{pump} = \lambda_{GVD=0}$ or even $\lambda_{pump} < \lambda_{GVD=0}$ are relatively narrow, they also tend to be much better in terms of spectral flatness [e.g., crosses in Figs. 3(b), 4(a), and 4(b) and dotted curve in Fig. 3(d)]. Fiber (f) in Fig. 6, with a GVD curve that reaches zero but is never anomalous, is still able to generate a 600-nm-wide spectrum (Fig. 8) and is particularly insensitive to the pump wavelength because the third-order dispersion is small in the 800–900-nm region.

In all cases, the spectral width increases with both length and power, and the spectra tend to become flatter at higher power, as illustrated in Fig. 9 for fiber (e) of Fig. 6. The spectral width is characterized by the wavelengths at which the power drops 20 dB from the peak. These wavelength points are then plotted against power for several fiber lengths. It is clear that, once the spectrum extends to the blue–ultraviolet, it requires increasingly more power or length to generate further wavelengths. This result is hardly surprising, as the phase velocity, the group velocity, and the GVD all diverge from the values at the pump wavelength particularly rapidly in the ultraviolet. One of the most noticeable differences among the fibers is the characteristic length or power required for approaching a saturated spectral width. This analysis of the full spectral width does, of course, hide the detail of the shape of the spectrum. The full effect on the spectral shape as well as on the absolute width of two discrete lengths and powers can be seen by comparison of Figs. 5 and 7 or 3 and 4, which illustrate the effect of increasing the length from 90 mm to 1 m at low and high

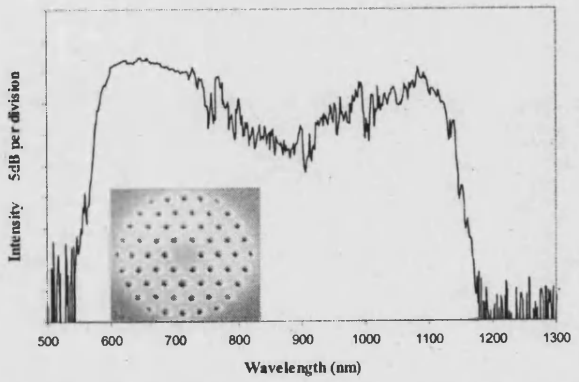

Fig. 8. Output spectrum of a 1-m length of fiber (f) of Fig. 6 pumped with 200 mW of power at 850 nm. The spectrum for the 800-nm pump wavelength is indistinguishable from this spectrum. Inset, SEM of the core region of the fiber with a core diameter of 1.5 μm.

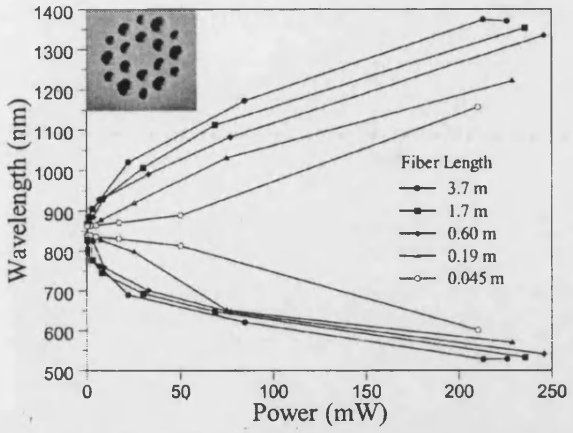

Fig. 9. Spectral width (−20 dB, or 1% intensity points) of the supercontinuum generated in a PCF with various launched powers and fiber lengths. Fiber parameters: core diameter, 1.5 μm; hole diameter, 0.62 μm. Inset, SEM of the core region of the fiber.

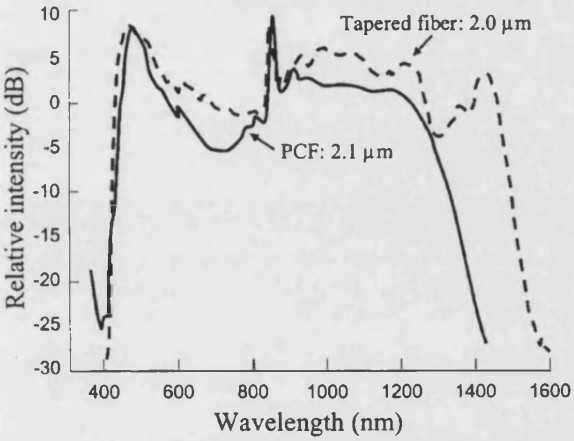

Fig. 10. Comparison of the spectra generated in a free-strand PCF and a tapered fiber. Core diameters, 2.1 and 2.0 μm, respectively; length, 90 mm; average power, 350-mW; pump wavelength, 850 nm.

power, or Figs. 5 and 3 or 7 and 4, which illustrate the effect of increasing the power at fixed lengths of 90 mm and 1 m. A particular point to note is that, as the length or the power is increased, not only does the full width of the spectrum increase but the spectral fluctuations in intensity become filled in. A smooth spectrum is of particular importance for applications that use the supercontinuum simply as a broadband source; however, there is anecdotal evidence that the smooth spectrum comes at the price of reduced coherence, a fact that has precluded use of the broadest spectra for metrological applications.

The free-strand PCFs discussed above are a close analog of tapered optical fibers; however, although a PCF may be of any length, the waist region of a taper is generally limited to lengths at less than 100 mm.[25] Supercontinuum generation in tapered fibers is treated in detail in Ref. 2. For the purpose of the current discussion the output spectrum for a taper diameter of 2.0 μm is shown in Fig. 10, along with the spectrum for a free-strand PCF with d_{core} = 2.1 μm of the same length. As expected, the spectra are almost identical because the dispersion curves are the same. By using the Corning SMF-28 fiber output tail of our fiber tapers to couple directly into the spectrum analyzer, we were able to determine that the absolute spectral power density is typically of the order of 0.5 mW/nm.

The limited length of a fiber taper is not a great impediment to supercontinuum generation in structures with core diameters near 2 μm. It is quite possible to push the output bandwidth down to 380 nm in the ultraviolet and correspondingly to 1.6 μm in the infrared. However, supercontinuum generation in a PCF can make up for low power or unfavorable GVD by use of extended length. We have developed a new technique for fabrication of fiber tapers that can be used to create taper waists as much as 1 m long with sufficiently small waist diameters for supercontinuum generation.[10] Spectra extending from below 400 nm to beyond 1600 nm have been measured in these structures as well.

4. ANALYSIS

The range of spectra here shows many features that are amenable to phenomenological explanation. That this is so is of use in selecting a fiber–laser combination for a particular purpose. A deeper understanding of the processes involved requires further investigation of the initial broadening processes. It has already been noted that many different regimes of pulse energy and wavelength yield continuum spectra but that the ways in which the spectrum builds up can be radically different. For example, for 60-ps pulses in the normal GVD regime there is clear silica Raman generation before the sudden onset of a supercontinuum.[3,4] Spectral Raman peaks are not seen in the femtosecond regime when the intrinsic pulse width spans much of the Raman gain spectrum. Instead, direct Raman pumping of the low-frequency side of the pulse leads to continuous transfer of energy from shorter to longer wavelengths in an effect known as the Raman self-frequency shift. Several of the present authors recently observed[27] the strong self-frequency shift of fundamental solitons in polarization-maintaining PCFs[28] at low pump energies. Figure 11 shows that the formation of self-shifting solitons can be observed in PCFs even when the polarization and the chirp of the pump pulse are not controlled. In this figure, single and then multiple red-shifted peaks appear as the power is increased from very low levels. The onset of the supercontinuum is then seen as the appearance of blue-shifted radiation [the peaks near 600 nm in Figs. 11(b) and 11(c) (solid curves)]. We studied in detail the breakup of pulses with energy corresponding to the nth soliton into n fundamental soiltons and blue-shifted radiation[27] to verify this recently identified mechanism for the formation of supercontinuum spectra.[7,11] In other cases the low-power spectra have the clear hallmarks of self-phase modulation [see Figs. 5(b)–5(d) (crosses) and 5(d) (dotted curve)], which is usually observed when the pump wavelength is close to zero GVD in either the normal or the anomalous region for the fiber.

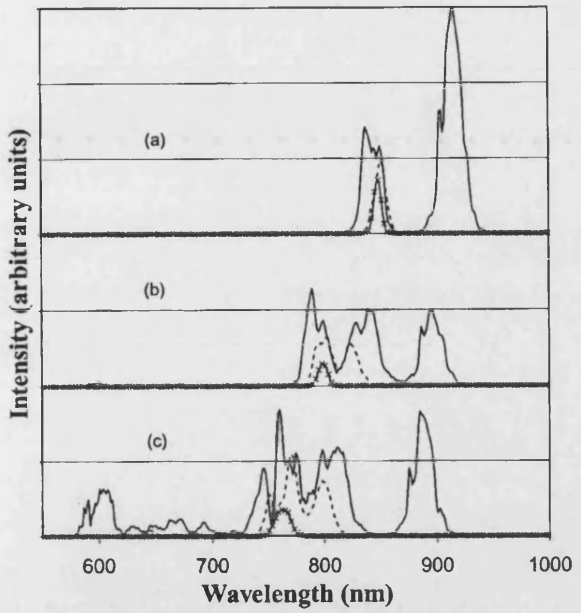

Fig. 11. Dependence of output spectrum on the pump wavelength and the power. Strand-type PCF, d_{core} = 1.9 μm, 1-m length. (a), (b), (c) Input wavelengths 850, 800, and 750 nm, respectively. Pump powers: 10 mW, solid curves; 3 mW, dotted curves; 1 mW, crosses. The vertical scale is linear and was adjusted for each plot to separate the curves.

Considerable further experimental and theoretical study is required in order to elucidate the various broadening mechanisms and the ways in which they may be affected by pulse length and fiber design. For applications of metrology it is particularly important to calculate or measure the coherence of the spectrum under different conditions.

The many nonlinear processes that cause the broadening of pulses in optical fibers account for the wide range of conditions under which a continuum is observed in PCF. The high nonlinearity (which is due to the large index contrast that is attainable) causes substantial broadening by self-phase modulation, Raman scattering, or modulational instability. Thereafter, the significance of the precise pump wavelength is lost and the unusual GVD curves, because of their effect on the phase matching of radiation at low and high frequencies, enable several optical processes to occur.

It is thus clear that, for low powers and weak broadening, matching the fiber to the pump laser and the application is a critical matter. The spectra in Figs. 5 and 7 are widely different depending on the combination of pump wavelength and fiber GVD. At high powers, which generate broad spectra, the fiber-to-fiber differences are less pronounced but are still visible in the basic features of the spectrum. The effects of the pump wavelength, which were so obvious at low power, are confined to the extremes of the spectra in this high-power regime (Figs. 3 and 4). Selection of the most appropriate fiber for a particular purpose must then include consideration of details such as spectral and temporal noise and the strength of particular important wavelengths in the spectrum. Integration of supercontinuum generation into the rest of an experiment is also a prime consideration, and it is here that tapered conventional fibers can offer distinct advantages in some situations. A particular current application is in optical coherence tomography, for which the instrument is frequently entirely fiber based and the ability simply to splice a supercontinuum source to the input is highly attractive. In other situations in which free-space coupling or dissimilar fiber splicing is tolerable, PCFs of both kinds can offer advantages. The extra free parameters of a regular-array PCF offer the possibility of more closely tailoring the fiber dispersion (both GVD and third-order dispersion) to a particular application and also permit supercontinuum generation in strictly single-mode fibers in some cases. We also recently developed a highly birefringent PCF,[27,28] which generates polarized continua with spectral properties that depend on the input polarization because of the different dispersions of the polarization modes. Free-strand PCF offers no different characteristics from the active part of a fiber taper, but it does not suffer from the dispersive effects of the up and the down transition regions. This can be important for short-pulse applications and for applications for which a small amount of broadening in a few millimeters of fiber is required. In these cases the transition overhead of a few centimeters that is required for a taper is unacceptable.

The most common general use of fiber tapers is as fused couplers, and the current authors and others have recently shown that such couplers can be fabricated with the waist dimensions required for continuum generation.[9] In the simplest cases, these devices act as continuum generators followed by a passive couplers, but asymmetric null couplers can also be used for access to the dispersion parameters of higher-order modes. In a null coupler two dissimilar fibers are tapered together to a common waist. The fundamental mode of the larger fiber is transformed to the fundamental mode of the waist and exits again in the same fiber. The fundamental mode of the smaller fiber is transformed to the second mode of the waist. These second modes have greater waveguide dispersion for a given waist diameter or similar dispersion for a greater waist diameter than the fundamental modes. For example, the GVD curves for the second mode, $TE_{0,1}$, of a 3.0-μm taper and the fundamental mode, $HE_{1,1}$, of a 1.8-μm taper are almost identical. Fused fiber couples therefore allow us access to new GVD regimes or to similar GVD for larger structures, which could be useful in increasing the maximum output power in the continuum.

5. CONCLUSIONS

Supercontinuum generation in PCF and tapered fibers provides a novel light source that is finding many uses throughout physics. The initial spectral-broadening processes, which occur at low power in PCFs and fiber tapers, can be explained well as being simple nonlinear processes. A broad analysis of the effects of fiber and laser parameters on the full supercontinuum spectrum is helpful in predicting which laser–fiber combination will yield the desired features for a particular application.

The wide range of structures that have been demonstrated to yield broad output spectra—regular PCF, free-

strand PCF, short-tapered fiber, extended-length fiber tapers, and fused tapered fiber couplers—provides a wide range of possible fiber parameters. This is important both for supercontinuum generation, for which different fiber dispersions will be appropriate for different pump laser sources or desired output spectra, and for integration of the source into real applications.

W. J. Wadsworth is a Royal Society University Research Fellow. W. J. Wadsworth's e-mail address is w.j.wadsworth@bath.ac.uk.

REFERENCES

1. J. K. Ranka, R. S. Windeler, and A. J. Stentz, "Visible continuum generation in air–silica microstructure optical fibers with anomalous dispersion at 800 nm," Opt. Lett. **25**, 25–27 (2000).
2. T. A. Birks, W. J. Wadsworth, and P. St. J. Russell, "Supercontinuum generation in tapered fibers," Opt. Lett. **25**, 1415–1417 (2000).
3. S. Coen, A. H. L. Chau, R. Leonhardt, J. D. Harvey, J. C. Knight, W. J. Wadsworth, and P. St. J. Russell, "White-light supercontinuum with 60-ps pump pulses in a photonic crystal fiber," Opt. Lett. **26**, 1356–1358 (2001).
4. S. Coen, A. H. L. Chau, R. Leonhardt, J. D. Harvey, J. C. Knight, W. J. Wadsworth, and P. St. J. Russell, "Supercontinuum generation by stimulated Raman scattering and parametric four-wave mixing in photonic crystal fibers," J. Opt. Soc. Am. B (to be published).
5. R. Holzwarth, M. Zimmermann, Th. Udem, T. W. Hänsch, P. Russbüldt, K. Gäbel, R. Poprawe, J. C. Knight, W. J. Wadsworth, and P. St. J. Russell, "White-light frequency comb generation with a diode-pumped Cr:LiSAF laser," Opt. Lett. **26**, 1376–1378 (2001).
6. F. G. Omenetto, A. J. Taylor, M. D. Moores, J. Arriaga, J. C. Knight, W. J. Wadsworth, and P. St. J. Russell, "Simultaneous generation of spectrally distinct third harmonics in a photonic-crystal fiber," Opt. Lett. **26**, 1158–1160 (2001).
7. J. Herrmann, U. Griebner, D. Nickel, A. Husakou, J. C. Knight, W. J. Wadsworth, P. St. J. Russell, N. Zhavoronkov, and G. Korn, "Experimental evidence for low-intensity supercontinuum generation by fission of higher-order solitons in photonic crystal fibers," Phys. Rev. Lett. **88**, 173901 (2001).
8. L. Provino, J. M. Dudley, H. Maillotte, N. Grossard, R. S. Windeler, and B. J. Eggleton, "Compact broadband continuum source based on microchip laser pumped microstructured fibre," Electron. Lett. **37**, 558–560 (2001).
9. T. A. Birks, D. Bahloul, W. J. Wadsworth, and P. St. J. Russell, "Supercontinuum generation in fused fibre couplers," in *Conference on Lasers and Electro-Optics 2001*, Vol. 56 of OSA Trends in Optics and Photonics Series (Optical Society of America, Washington, D.C., 2001), paper CThH1.
10. T. P. M. Man, T. A. Birks, W. J. Wadsworth, and P. St. J. Russell, "Fabrication of indefinitely long tapered fibers for supercontinuum generation," in *Nonlinear Guided Waves and Their Applications*, Vol. 55 of OSA Trends in Optics and Photonics (Optical Society of America, Washington, D.C., 2001), paper WB4.
11. A. V. Husakou and J. Herrmann, "Supercontinuum generation of high-order solitons by fission in photonic crystal fibres," Phys. Rev. Lett. **87**, 203901 (2001).
12. D. A. Jones, S. A. Diddams, J. K. Ranka, A. Stentz, R. S. Windeler, J. L. Hall, and S. T. Cundiff, "Carrier-envelope phase control of femtosecond mode-locked lasers and direct optical frequency synthesis," Science **288**, 635–639 (2000).
13. R. Holzwarth, J. Reichert, Th. Udem, T. W. Hänsch, J. C. Knight, W. J. Wadsworth, and P. St. J. Russell, "An optical frequency synthesiser for precision spectroscopy," Phys. Rev. Lett. **85**, 2264–2267 (2000).
14. R. Holzwarth, M. Zimmermann, Th. Udem, T. W. Hänsch, A. Nevsky, J. von Zanthier, H. Walther, J. C. Knight, W. J. Wadsworth, P. St. J. Russell, M. N. Skvortsov, and S. N. Bagayev, "Absolute frequency measurement of iodine lines with a femtosecond optical synthesizer," Appl. Phys. B **73**, 269–271 (2001).
15. S. A. Diddams, D. J. Jones, J. Ye, S. T. Cundiff, J. L. Hall, J. K. Ranka, and R. S. Windeler, "Direct rf to optical frequency measurements with a femtosecond laser comb," IEEE Trans. Instrum. Meas. **50**, 552–555 (2001).
16. S. A. Diddams, D. J. Jones, J. Ye, T. Cundiff, J. L. Hall, J. K. Ranka, R. S. Windeler, R. Holzwarth, T. Udem, and T. W. Hansch, "Direct link between microwave and optical frequencies with a 300 THz femtosecond laser comb," Phys. Rev. Lett. **84**, 5102–5105 (2000).
17. I. Hartl, X. D. Li, C. Chudoba, R. Ghanta, T. Ko, J. G. Fujimoto, J. K. Ranka, R. S. Windeler, and A. J. Stentz, "Ultrahigh-resolution optical coherence tomography using continuum generation in an air-silica microstructure optical fiber," Opt. Lett. **26**, 608–610 (2001).
18. I. Hartl, P.-L. Hsiung, T. H. Ko, J. G. Fujimoto, T. A. Birks, W. J. Wadsworth, U. Bünting, and D. Kopf, "High resolution OCT imaging using a spectrally broadened femtosecond Nd:glass laser," in *Conference on Lasers and Electro-Optics*, Vol. 73 of OSA Trends in Optics and Photonics Series (Optical Society of America, Washington, D.C., 2002), paper CThI3.
19. W. J. Wadsworth, J. C. Knight, A. Ortigosa-Blanch, J. Arriaga, E. Silvestre, and P. St. J. Russell, "Soliton effects in photonic crystal fibres at 850 nm," Electron. Lett. **36**, 53–55 (2000).
20. J. C. Knight, T. A. Birks, P. St. J. Russell, and D. M. Atkin, "All-silica single-mode fiber with photonic crystal cladding," Opt. Lett. **21**, 1547–1549 (1996); errata **22**, 484–485 (1997).
21. T. A. Birks, J. C. Knight, and P. St. J. Russell, "Endlessly single-mode photonic crystal fiber," Opt. Lett. **22**, 961–963 (1997).
22. D. Mogilevtsev, T. A. Birks, and P. St. J. Russell, "Group-velocity dispersion in photonic crystal fibers," Opt. Lett. **23**, 1662–1664 (1998).
23. J. C. Knight, J. Arriaga, T. A. Birks, A. Ortigosa-Blanch, W. J. Wadsworth, and P. St. J. Russell, "Anomalous dispersion in photonic crystal fiber," IEEE Photonics Technol. Lett. **12**, 807–809 (2000).
24. A. Ferrando, E. Silvestre, J. J. Miret, J. A. Monsoriu, M. V. Andres, and P. St. J. Russell, "Designing a photonic crystal fibre with flattened chromatic dispersion," Electron. Lett. **35**, 325–327 (1999).
25. T. A. Birks and Y. W. Li, "The shape of fiber tapers," J. Lightwave Technol. **10**, 432–438 (1992).
26. M. Tateda, N. Shibata, and S. Seikai, "Interferometric method for chromatic dispersion measurement in a single-mode optical fiber," IEEE J. Quantum Electron. **QE-17**, 404–407 (1981).
27. A. Ortigosa-Blanch, J. C. Knight, and P. St. J. Russell, "Pulse breaking and supercontinuum generation with 200 fs pump pulses in photonic crystal fibers," submitted to J. Opt. Soc. Am. B.
28. A. Ortigosa-Blanch, J. C. Knight, W. J. Wadsworth, J. Arriaga, B. J. Mangan, T. A. Birks, and P. St. J. Russell, "Highly birefringent photonic crystal fibers," Opt. Lett. **25**, 1325–1327 (2000).

Pulse breaking and supercontinuum generation with 200 fs pump pulses in photonic crystal fibers

A. Ortigosa - Blanch, J.C. Knight, P.St.J. Russell

JOSA B , 19 (11), pp 2567-2572, 2002

Pulse breaking and supercontinuum generation with 200 fs pump pulses in photonic crystal fibers
JOSA B (in press)

Pulse breaking and supercontinuum generation with 200 fs pump pulses in photonic crystal fibers

A. Ortigosa-Blanch, J.C. Knight, P.St.J. Russell

Optoelectronics Group, Department of Physics, University of Bath,
Claverton Down, Bath, BA2 7AY, UK

Abstract

We have carried out a detailed experimental study of the behaviour of 200 fs pulses in highly nonlinear photonic crystal fiber in order to elucidate the mechanisms for supercontinuum generation. To avoid unwanted polarization effects, our experiments were performed using polarization-maintaining fiber. The experimental evidence shows that, as in conventional fibers, Raman scattering leads to the break-up of higher-order solitons, which is accompanied by the generation of radiation at shorter wavelengths than the pump, leading eventually to an ultrabroad supercontinuum.

OCIS codes: (060.5530) Pulse propagation and Solitons; (060.4370) Nonlinear optics, fibers; (060.2310) Fiber Optics

INTRODUCTION

For the last two years, supercontinuum (SC) generation in photonic crystal fiber (PCF) by ultrashort pulse propagation has become a subject of intense world-wide study. This is mainly because the pulse energies required to generate a SC are very low, and the spatial purity and intensity of the SC (which is generated in the fundamental mode of the optical fiber) are very high. First demonstrated by Ranka *et al.* in 2000 [1], the frequency comb can stretch more than two octaves from the UV into the infrared and has found applications in fields such as frequency metrology [2] and optical coherence tomography [3].

The role of pulse breaking in the generation of new frequency components has been extensively studied in conventional fibers. Beaud *et al.* [4] performed experiments using psec pulses in the vicinity of the zero dispersion wavelength of a conventional optical fiber. Although the input powers used were sufficient to generate high-order solitons, they observed temporal and spectral break-up of the input pulse, leading to pulse narrowing and a series of solitonic features that shifted to lower frequencies due to Raman effects. In 1989, Islam *et al* [5], reported fsec distributed soliton spectra using psec pump pulses in the anomalous dispersion regime of a conventional fiber. Their results show how modulation instability is responsible for pulse break-up, creating several solitons. These then collide to form intense narrow pulses which frequency shift due to Raman effects. Averaging over these frequency shifted solitons yields a spectrum spanning 300 nm.

The development of PCFs in the last few years has resulted in SC spectra extending not only to the long wavelength side of the pump, but also to much higher frequencies. In this paper we study experimentally the mechanism for SC generation when pumping a PCF with femtosecond pulses. We report how soliton breaking is accompanied by the generation of phase-matched radiation at shorter wavelengths than the pump, leading to an ultrabroad SC. We have used a well-characterised polarization-maintaining fiber to perform the experiments at different pump wavelengths and for different fiber lengths, in order to understand the role of these parameters. We also present results showing the generation of supercontinua when the fibre is pumped in the normal dispersion regime, where soliton formation is not allowed but we can identify some elements of the same physical mechanism.

THE FIBRES

Photonic crystal fibers have a regular array of air holes running along their length and are typically made from pure silica glass. A missing (i.e., filled in) air hole within the array acts as the guiding core. PCFs have shown remarkable linear and especially nonlinear properties due to the combination of very small effective areas and anomalous dispersion in the near-infrared [1, 6, 7].

With the aim of understanding the physical processes governing ultrashort pulse propagation and supercontinuum generation in such fibers, we have performed a series of measurements using polarisation-maintaining PCF. The fiber was fabricated as previously reported [8,9]. A scanning electron micrograph of the fibre is shown in Figure 1 (inset). The structure consists of an elliptical core region surrounded by 4 periods of air holes acting as the cladding. The larger air holes were 1.14 μm in diameter and the smaller air-holes were 0.54 μm in diameter. The distance between the nearest air holes (the pitch) was $\Lambda = 1.46$ μm. A silica jacket was added to the fibre structure leading to an external diameter of 125 μm. The losses for the fiber were around 0.3dB/m in the wavelength region from 800nm to 1μm.

Based on the structure shown, the linear characteristics of the fiber were modelled using a full vector numerical model based on the plane wave method [10]. The computed fiber birefringence (9.07×10^{-4}) – although not as large as some previously reported [9] – is more than sufficient to remove coupling between polarization modes, ensuring that our experiments were performed in a single polarization mode. Figure 1 shows the calculated (dotted lines) dispersion for the structure, which has been confirmed experimentally (points) over a limited wavelength range using low-coherence interferometry [11]. The two polarisation eigenmodes show different linear characteristics, exhibiting anomalous dispersion at wavelengths longer than 781 nm and 806 nm respectively and an effective area of 5.58 μm^2.

All the experiments described here were performed using a tunable Ti:sapphire laser (76 MHz repetition rate, 200 fs FWHM pulse duration), launched in the polarization eigenmode with the longer zero dispersion wavelength (806 nm). A zero-order half

wave-plate was used to adjust the linear polarization state at the input. The output of the fiber was then analysed using an intensity autocorrelator (based on second harmonic generation) and an optical spectrum analyser. The polarisation state of the output was analyzed to ensure that the light remained in the same polarisation axis as it was launched in.

THE EXPERIMENTS

A. The anomalous dispersion regime

We present results (Figure 2) for a 6 m length of fiber and a pump wavelength of 850 nm. We chose the eigenmode with the smaller anomalous dispersion (20 ps/nm.km) at the pump wavelength and analysed the output of the fiber for different input powers. We first investigated the output pulse duration at relatively low input energies. At such energies (up to 6 W peak power) the pulse is substantially broadened by linear dispersion (output pulse length > 1 ps). The pulse then compresses down to 90 fs at a peak output power just below 66 W. We identify this value (corresponding to an input power of about 92 W) with the fundamental soliton energy, in accord with simple theory [7].

As we increased the energy launched into the fiber, interesting features appeared in the recorded spectra. Figure 2 shows the recorded spectra at different powers. A pronounced pulse splitting and soliton shelf frequency shift (SSFS) was observed for input powers above the first soliton energy. A shift of up to 120 nm was observed for a peak output power of 203 W (corresponding to Figure 2, output peak powers from 68 W to 203 W). As the power was increased further a second separate peak split off from the pump and also started shifting in frequency. At the same time, the original self-shifting soliton that appeared at a lower power kept shifting towards longer wavelengths (Figure 2, 289 W output power). The generation of a second self-shifting peak is accompanied by the appearance of a blue-shifted peak at a wavelength around 600nm.

As the input power was increased further, a third new spectral peak developed, being fully independent at around 618 W output power. It is worth noting that the relationship between the measured output powers and the input powers and calculated powers becomes complicated by the nonlinear losses in this regime (the soliton features at longer wavelengths have lost a significant fraction of their energy through Raman scattering). Further increases in power lead to further self-frequency shifts in the existing peaks and the appearance of new peaks. These are accompanied by the appearance of new blue-shifted peaks as well. At yet higher pump energies (e.g. 6 kW peak power) all those peaks merge to give a continuous spectrum of peaks – a broadband supercontinuum. At these higher powers, pulse break up occurs after an increasingly short propagation length, so that just a few centimeters of fibre are required to observe supercontinuum generation [1]. At these higher powers, pulse breakup is surely accompanied by other nonlinear mechanisms such as modulation instability [5] and four-wave mixing which serve to diffuse the distinctive features observed at low energies. Previous studies reported shot to shot variations on their spectra [5]. We were unable to study this effect and therefore our observations correspond to output spectra averaged over a great number of pulses.

Having observed these effects in the frequency domain, we used the autocorrelator to study the fiber output in the time domain [12,13]. The autocorrelation results showed that the appearance of new peaks in the frequency domain corresponds to new pulses generated in the fiber that propagate at different speeds. An example is presented in Figure 3 showing the output of the autocorrelator at a pulse energy corresponding to 164 W output peak power. The correlation trace shows the presence of two distinct peaks in the time domain.

By considering the powers at which we were working, we can explain the appearance of this series of new spectral peaks in terms of the fission of higher-order solitons [14, 15]. Looking once more at Figure 2, it is clear that, around the second soliton energy (289 W output power), we get two very well-defined peaks in addition to the pump. The autocorrelator confirms these as corresponding to discrete pulses. Furthermore, at the peak power corresponding to $N = 3$ we observe three spectral peaks (618 W output power) and four peaks (1.1 kW output power) for $N = 4$. Above the second soliton energy we also observe spectral components in the short wavelength part of the spectrum which we attribute to nonsolitonic radiation generated during soliton fission. Although the physics underlying the appearance of these short-wavelength bands is not yet completely clear, their positions agree with the numerical simulations reported in references 14 and 15.

We next present the spectra observed as a function of pump wavelength, using a 16 m length of the same fiber. Figure 4 shows the spectra from a 16 m piece of fiber for a pump wavelength of 817 nm. For this pump wavelength the dispersion (D) is 5 ps/nm.km, yielding a calculated peak power for fundamental soliton formation of 5 W. The first trace was recorded at an output power of 39 W. This corresponds to an energy level above the fourth soliton energy, explaining the appearance of at least 3 distinct peaks around the pump wavelength and a small peak at shorter wavelengths. As the input average power increases, new solitons appear and shift towards longer wavelengths whilst new wavelength components are created in the short wavelength part of the spectrum.

Figure 5 shows broadly similar results for a pump wavelength of 842 nm. The value of D for this wavelength is $D = 16$ ps/nm.km, giving a peak power for the fundamental soliton of 16 W. The phase matching [15] is not as flat as in the previous case and therefore we expect to see less radiation in the region between the pump and the phase-matched wavelength. This is indeed the case, even when the power is increased.

For the third part of the experiment, we pumped at 870 nm, yet further from the zero dispersion wavelength at 806 nm. The resulting spectra for different powers can be seen in Figure 6. In this case, D = 27 ps/nm.km. There is a large phase mismatch for the shorter wavelengths close to the pump and therefore the spectra shows a well-defined minimum in the generated nonsolitonic radiation in this wavelength band.

In order to give some insight into the instability of higher-order soliton propagation in such a system, we have performed a study of the spectral evolution of a pulse along the

fibre length in the regime N > 1. Figure 7 shows output spectra recorded when the fiber was cut back from a length of 39 cm in 3 cm steps for an input power of 150 W (between the second and third soliton powers). For a 6 cm long piece, the spectral distribution shows asymmetric features apparently due to the interaction between Raman scattering and linear and nonlinear dispersion. As the pulse propagates, it becomes unstable and then breaks up emitting nonsolitonic radiation as seen in the 9 cm and the 12 cm long pieces. As the length is further increased, the newly formed soliton starts shifting in frequency and blue-shifted radiation appears at the phase-matched wavelength. It should be noted that this range of fiber lengths spans those previously reported used for SC generation in similar fibers [1].

Data presented up to this point were acquired at low peak powers and that is the reason for the very distinctive spectral features. Figure 8 shows output spectra from a 16 m long piece of fiber for three different powers. The first spectra (Figure 8(a)) correspond to the highest power trace shown in Figure 5 with an output peak power of 1.4 kW. As the power is increased two main effects take place: the bandwidth of the SC increases, and the very distinctive spectral components tend to smooth (Figure 8(b)), yielding to a much more flattened spectra at even higher energies as shown in trace (c).

B. The normal dispersion regime

Having understood the process of SC generation when pumping in the anomalous dispersion regime, we tuned the laser to pump the fiber at 753 nm, at which wavelength the dispersion $D = -30$ ps/nm.km – that is to say, the GVD is normal. Hence, we do not expect to observe soliton formation. Figure 9 shows the spectra recorded for different powers. The first traces show a progressive broadening of the pump, which we attribute to self-phase modulation. As the power is increased, a small peak appears just before the zero-dispersion wavelength and then some of the energy is transferred into the anomalous dispersion regime. It is worth noting that the observed frequency difference is not consistent with direct Raman scattering [16] and the spectral feature shifts with intensity. As we increased the power (230W), more energy is transferred to this peak and a solitonic feature is formed as energy spills across the zero-GVD wavelength. Further increases in the power lead to a shift of this soliton and the appearance of new frequency shifted solitons on the longer wavelength side of the zero dispersion point. These new components at longer wavelengths are accompanied by the appearance of new short-wavelength peaks as well. Therefore we see that when pumping in the normal side of D but close to the $D = 0$ wavelength, self-shifting fundamental solitons nonetheless arise from energy transferred beyond the zero dispersion point, leading to the generation of a continuum of radiation.

CONCLUSIONS

In conclusion, we have reported experimental evidence supporting the generation of supercontinua in photonic crystal fibres by higher order soliton break-up and associated short wavelength radiation. This process creates new frequency components that ultimately form an ultrabroad spectrum. As previously shown at longer wavelengths, the linear properties of the fiber, such as its modal index and GVD, play a very important

role on the generation of the supercontinuum, as well as the power and the chirp of the input pulses [12]. All the spectra shown in this paper have been generated at low powers, and that is the reason for their rather "spiky" appearance. Many SC applications require a smooth and flat spectrum. This smoothness can be achieved by working at higher powers. Understanding the mechanism for SC generation allows one to tailor the linear properties of the fibers to generate optimum spectra for different applications. All the experiments reported here were performed using pulses of 200 fs. Extensive study of the generation of SC has also been made when pumping with picosecond pulses [17], showing that in this case the main mechanism is stimulated Raman scattering and parametric four-wave mixing. We anticipate that propagation of much shorter pulses would be dominated by different physical effects, leading to different spectra.

REFERENCES:

1. J.K. Ranka, R.S. Windeler and A.J. Stentz: "Visible continuum generation in air-silica microstructure optical fibers with anomalous dispersion at 800 nm", Opt.Lett., **25**, 25(2000)
2. R. Holzwarth, T. Udem, T.W. Hänsch, J.C. Knight, W.J. Wadsworth and P.St.J. Russell: "Optical frequency synthesizer for precision spectroscopy", Phys. Rev. Lett. **85,** 2264(2000)
3. I. Hartl, X. D. Li, C. Chudoba, R. Ghanta, T. Ko, J. G. Fujimoto, J. K. Ranka and R. S. Windeler: "Ultrahigh-resolution optical coherence tomography using continuum generation in an air-silica microstructure optical fiber", Opt. Lett., **26**, 608 (2001)
4. P. Beaud, W. Hodel, B. Zysset and H.P. Weber: "Ultrashort pulse propagation, pulse breaking and fundamental soliton formation in a single mode optical fiber", J. Quantum Electron. **QE-23**, 1938 (1987)
5. M.N. Islam, G. Sucha, I. Bar-Joseph, M. Wegener, J.P. Gordon and D.S. Chemla: "Femtosecond distributed soliton spectrum fibers", JOSA B **6**, 1149 (1989)
6. J. C. Knight, J. Arriaga, T. A. Birks, A. Ortigosa-Blanch, W. J. Wadsworth, P. St. J. Russell: "Anomalous dispersion in photonic crystal fiber", IEEE Photon. Technol. Lett., **12,** 807 (2000)
7. W. J. Wadsworth, J. C. Knight, A. Ortigosa-Blanch, J. Arriaga, E. Silvestre and P. St. J. Russell: "Soliton effects in photonic crystal fibres at 850 nm", Electron. Lett. **36** 53 (2000)
8. J. C. Knight, T. A. Birks, P. St. J. Russell, and D. M. Atkin: "All-silica single-mode optical fiber with photonic crystal cladding", Opt. Lett. **21**, 1547 (1996); errata **22,** 484 (1997).
9. A. Ortigosa-Blanch, J.C. Knight, W.J. Wadsworth, J. Arriaga, B.J. Mangan, T.A. Birks and P.St.J. Russell: "Highly birefringent photonic crystal fibers", Opt. Lett **25**, 1325 (2000)
10. A. Ferrando, E. Silvestre, J.J. Miret, P. Andres, and M.V. Andres: "Full-vector analysis of a realistic photonic crystal fiber", Opt. Lett. **24**, 276 (1999)

Pulse breaking and supercontinuum generation with 200 fs pump pulses in photonic crystal fibers JOSA B (in press)

11. M. Tateda, N. Shibata, and S. Seikai: "Interferometric method for chromatic dispersion measurement in a single-mode optical fiber," IEEE J. Quantum Electronics, **QE-17**, 404 (1981)
12. I.G. Cormack, D.T. Reid, W.J. Wadsworth, J.C. Knight, P.St.J. Russell: Observation of soliton self-frequency shift in photonic crystal fibre", Electron. Lett. **38** 167 (2002)
13. B.R. Washburn, S.E. Ralph, P.A. Lacourt, J.M. Dudley, W.T. Rhodes, R.S. Windeler, S. Coen; "Tunable near-infrared femtosecond soliton generation in photonic crystal fibres", Electron. Lett. **37** 1510 (2001)
14. A.V. Husakou and J. Herrmann: "Supercontinuum generation of higher-order solitons by fission in photonic crystal fibers", Phys. Rev. Lett., **87**, 203901 (2001)
15. J. Herrmann, U. Griebner, D. Nickel, A. Husakou, J.C. Knight, W.J. Wadsworth, P.St.J. Russell, N. Zhavoronkov, G. Korn: "Experimental evidence for supercontinuum generation by fission of higher-order solitons in photonic fibers", Phys. Rev. Lett., **88**, 173901 (2002)
16. G.P. Agrawal: "Nonlinear fiber optics", 3rd edition, Academic Press (2001)
17. S. Coen, A.H.L. Chau, R. Leonhardt, J.D. Harvey, J.C. Knight, W.J. Wadsworth and P.St.J. Russell: "Supercontinuum generation by stimulated Raman scattering and parametric four-wave mixing in photonic crystal fibers", JOSA B 19, 753 (2002)

Pulse breaking and supercontinuum generation with 200 fs pump pulses in photonic crystal fibers
JOSA B (in press)

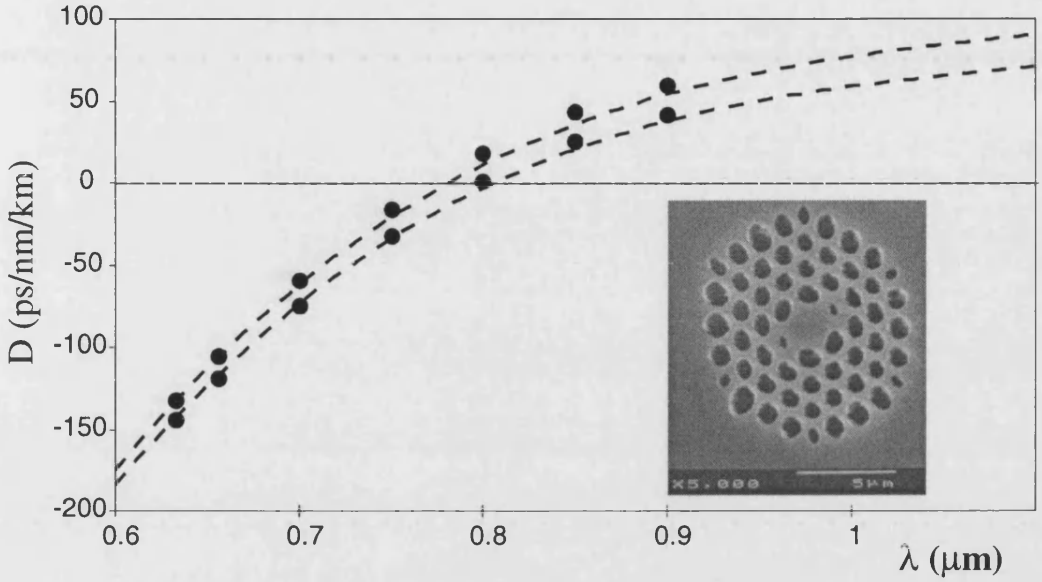

Figure 1 Calculated (dotted line) and measured (points) dispersion for the polarisation eigenmodes of the polarisation-preserving PCF shown in the inset.

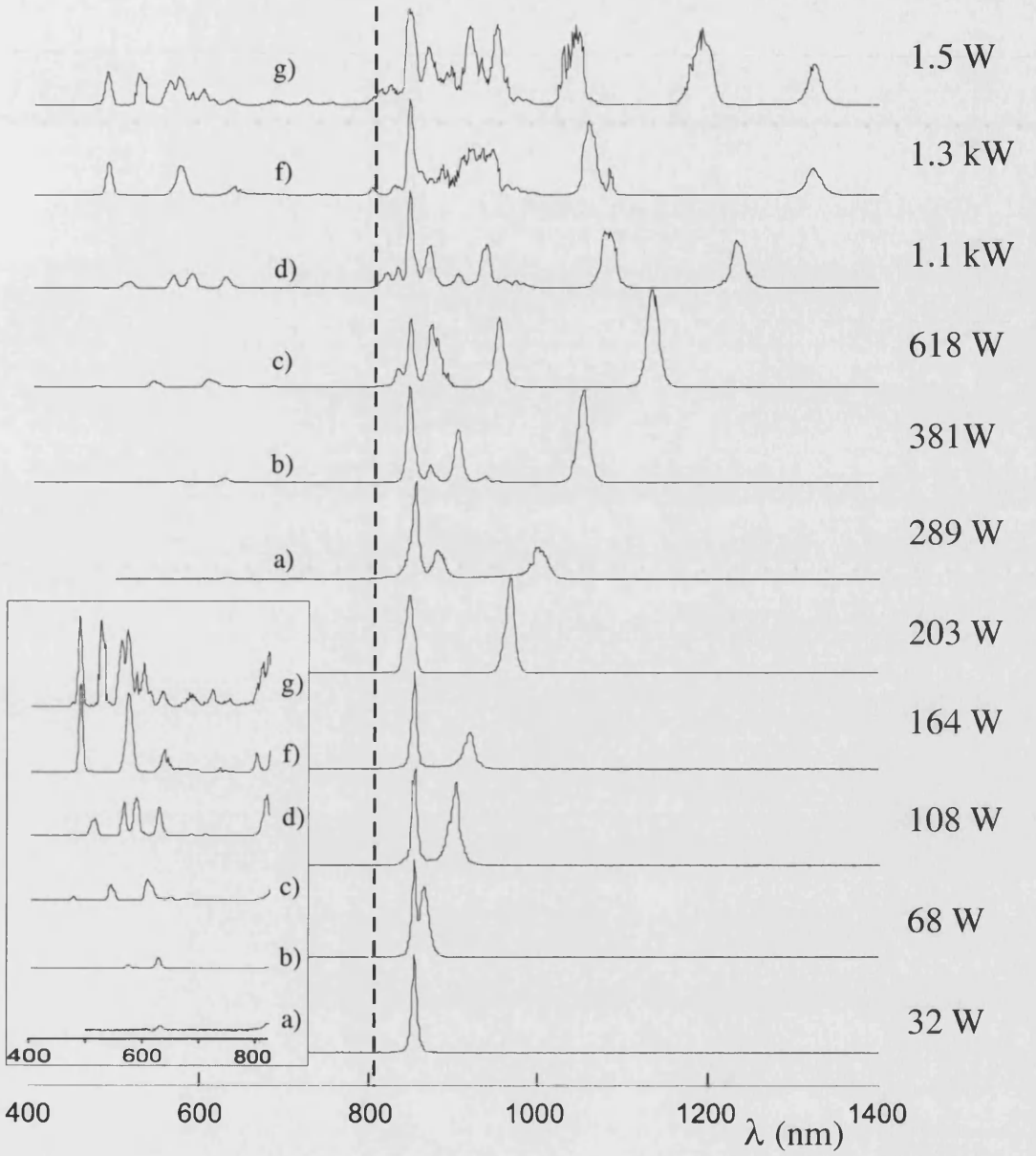

Figure 2 Recorded spectra at a pump wavelength of 850 nm for different peak powers coming out of the fibre. The dotted line indicates the zero dispersion wavelength at 806 nm. (Inset) Detail of the spectra from 400 nm to 800 nm.

Pulse breaking and supercontinuum generation with 200 fs pump pulses in photonic crystal fibers
JOSA B (in press)

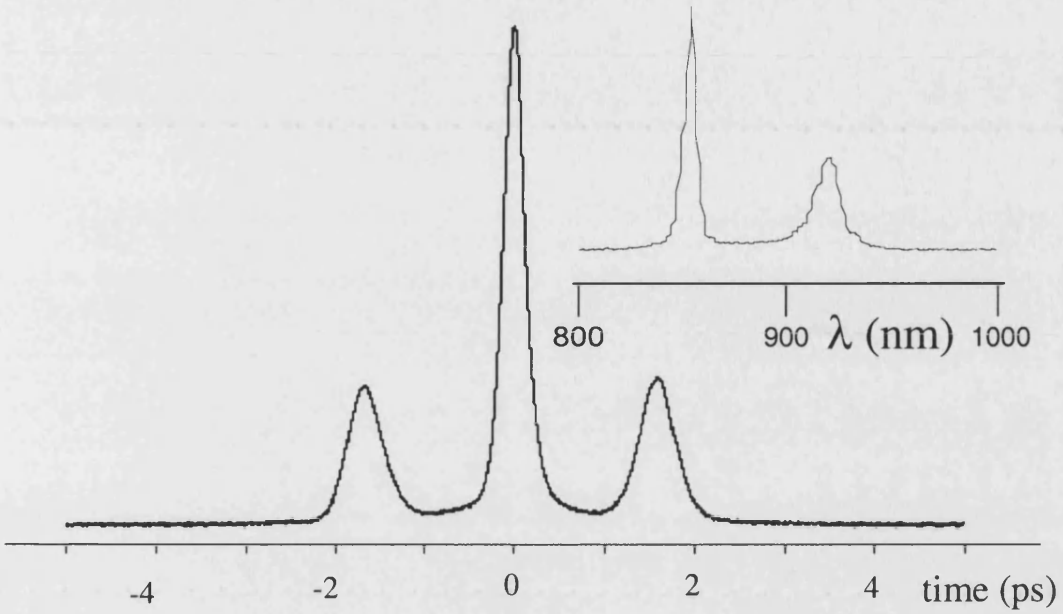

Figure 3. Measured autocorrelator signal and spectrum (inset) of the fiber output at 164 W peak power.

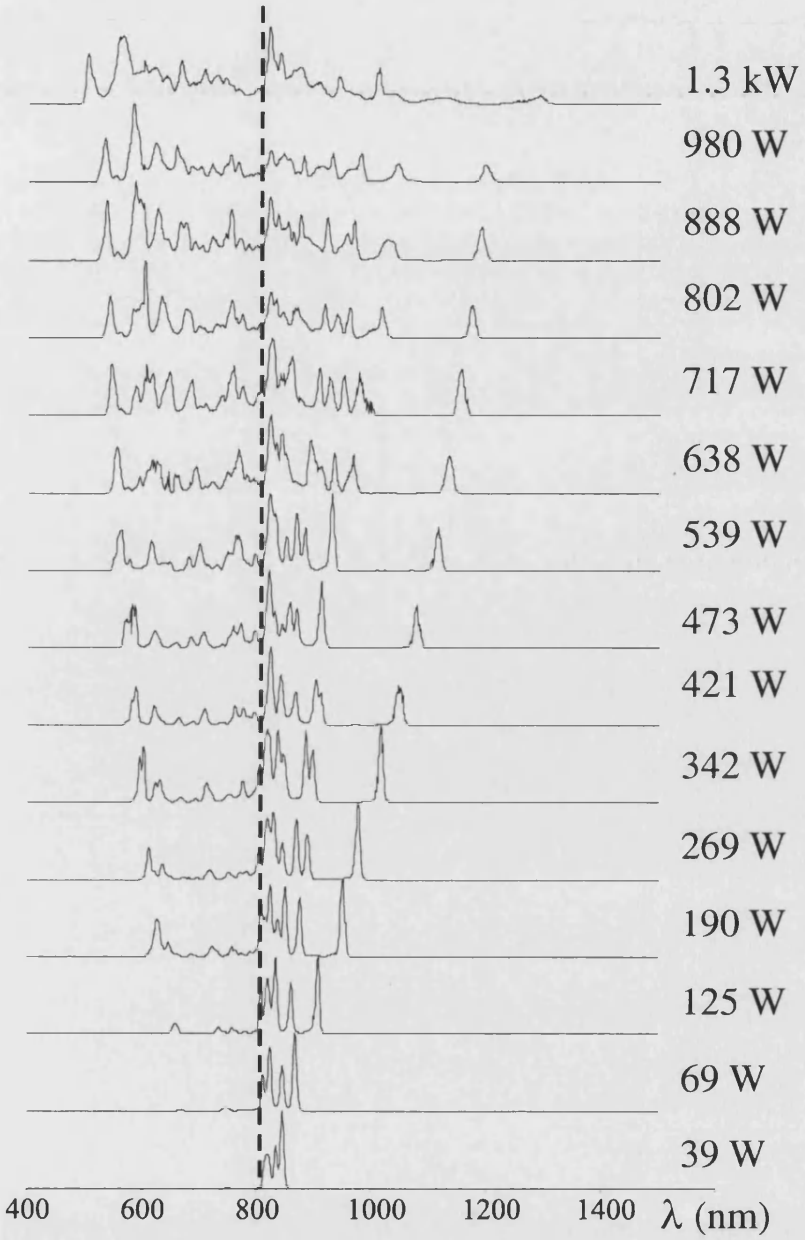

Figure 4 Recorded spectra at a pump wavelength of 817 nm for different peak powers coming out of the fibre. The dotted line indicates the zero dispersion wavelength at 806 nm.

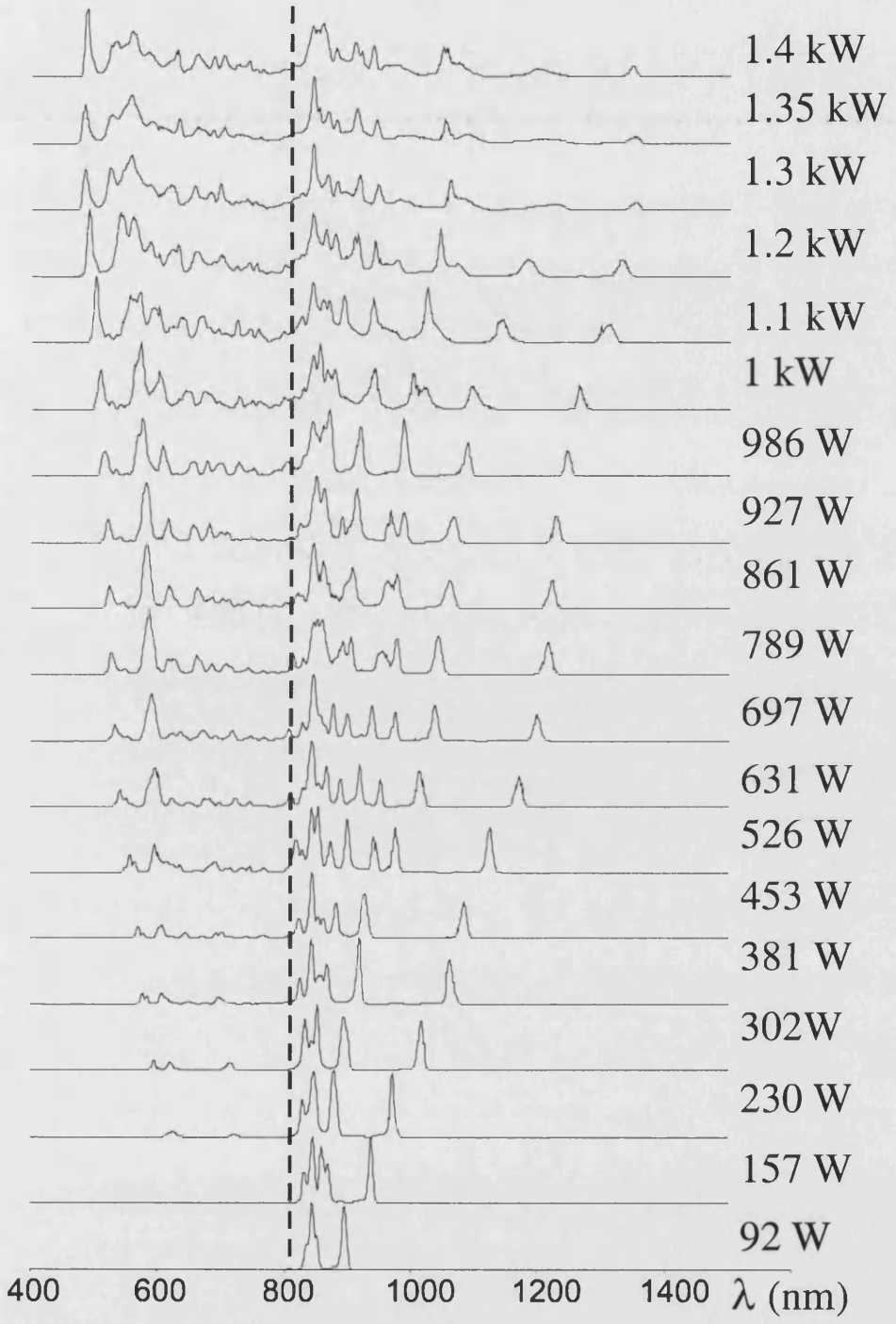

Figure 5 Recorded spectra at a pump wavelength of 842 nm for different peak powers coming out of the fibre. The dotted line indicates the zero dispersion wavelength at 806 nm.

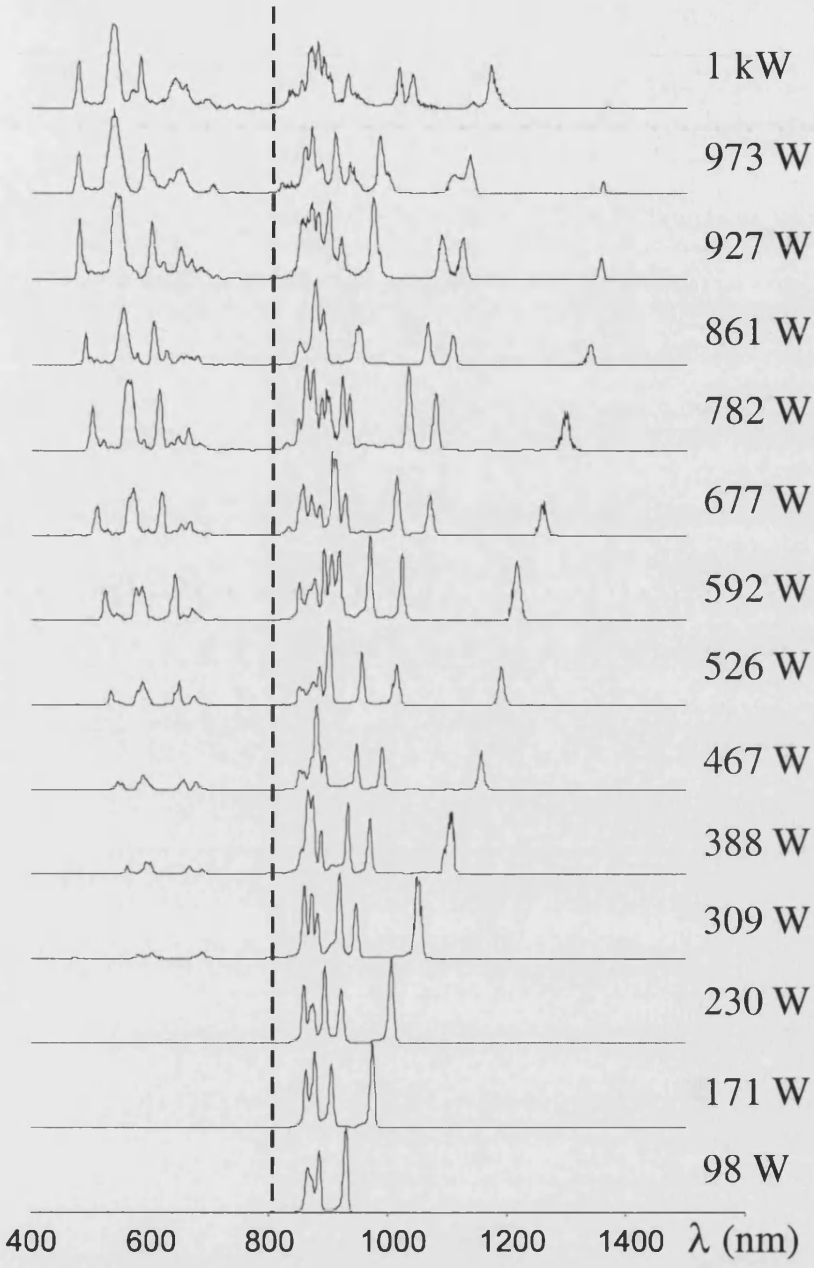

Figure 6 Recorded spectra at a pump wavelength of 870 nm for different peak powers coming out of the fibre. The dotted line indicates the zero dispersion wavelength at 806 nm.

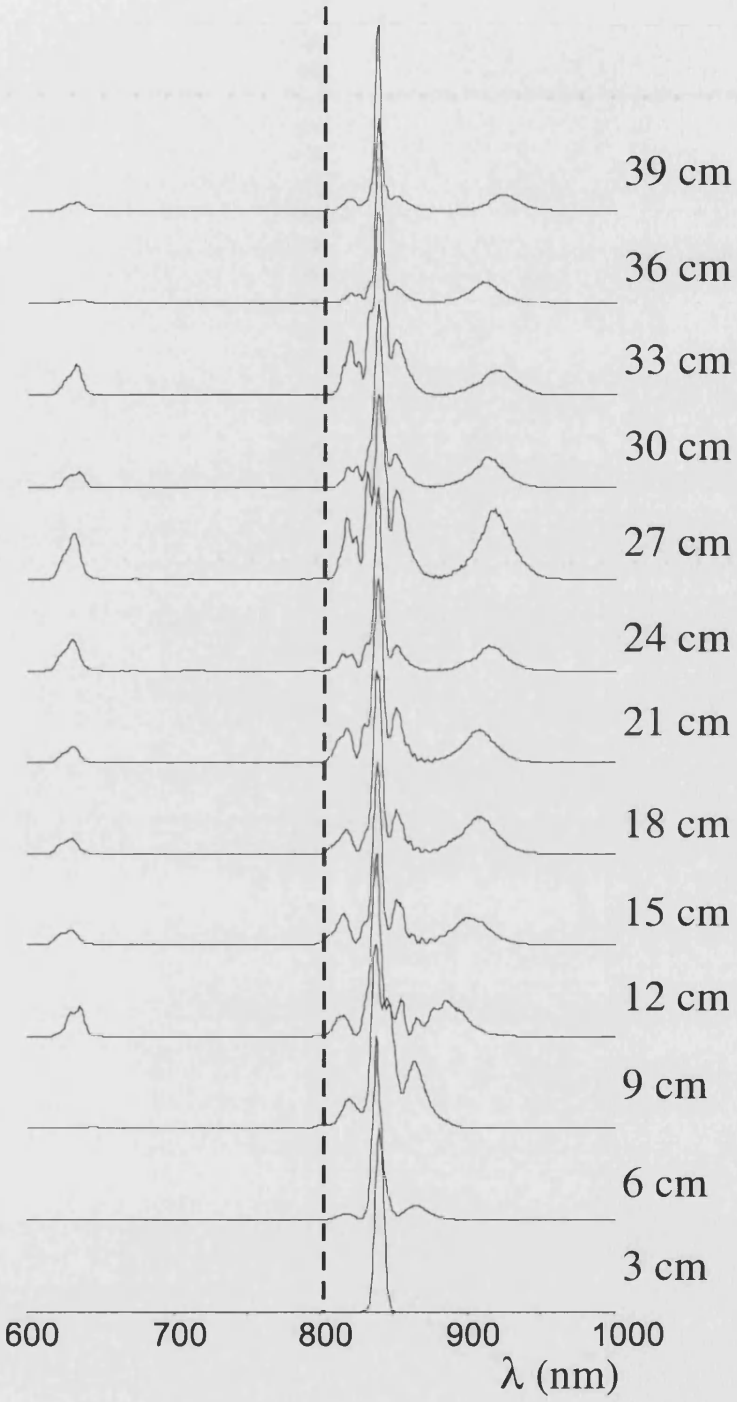

Figure 7 Recorded spectra for different lengths of fibre at constant output peak power of 150 W pumping at 842 nm. The fibre is progressively cut back in 3cm steps.

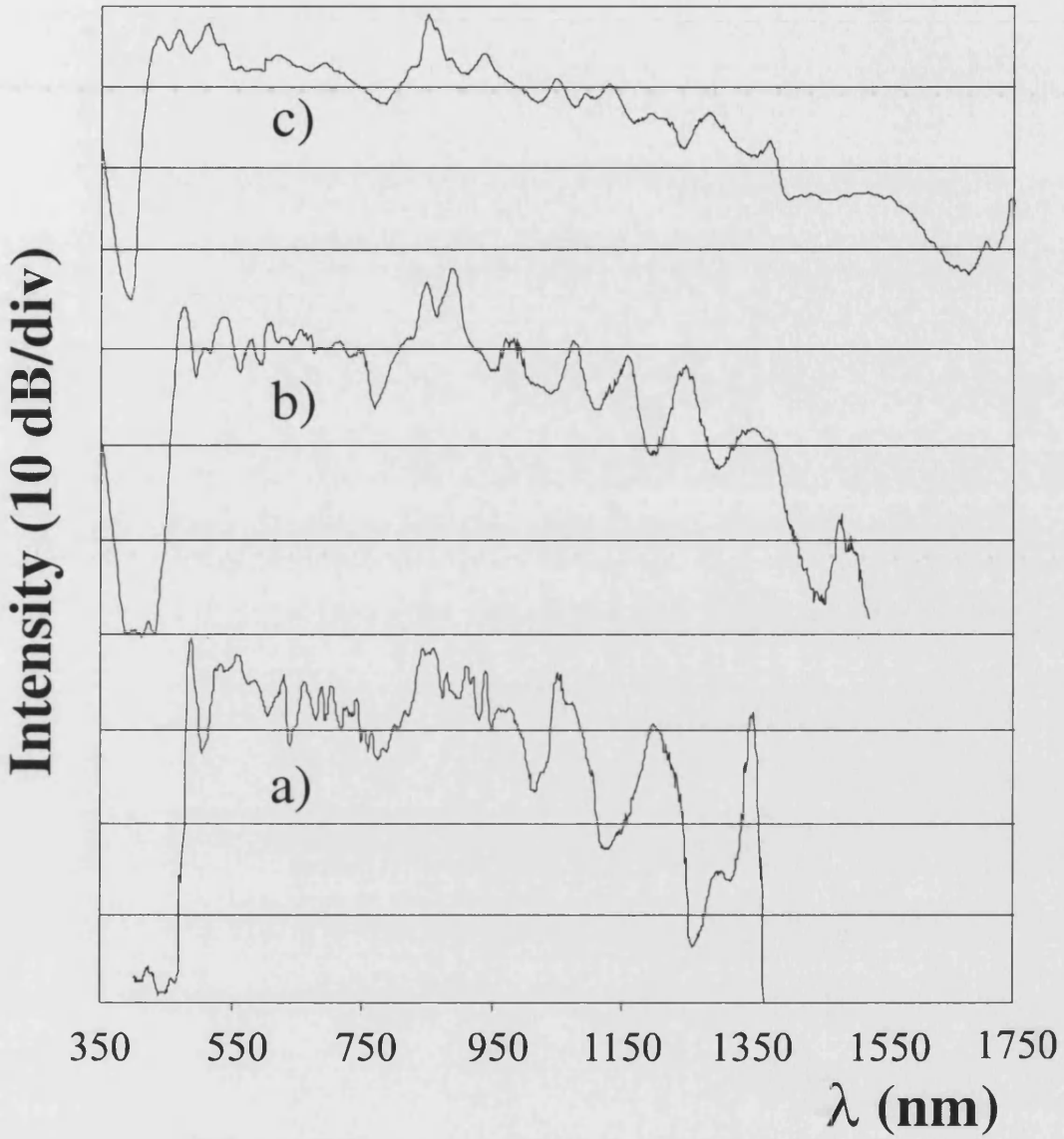

Figure 8 Recorded spectra at a pump wavelength of 842 nm for different peak powers coming out of the fibre: a) 1.4 kW, b) 2.6 kW and c)4.6 kW. The vertical axis is in a logarithmic scale with each division corresponding to 10 dB.

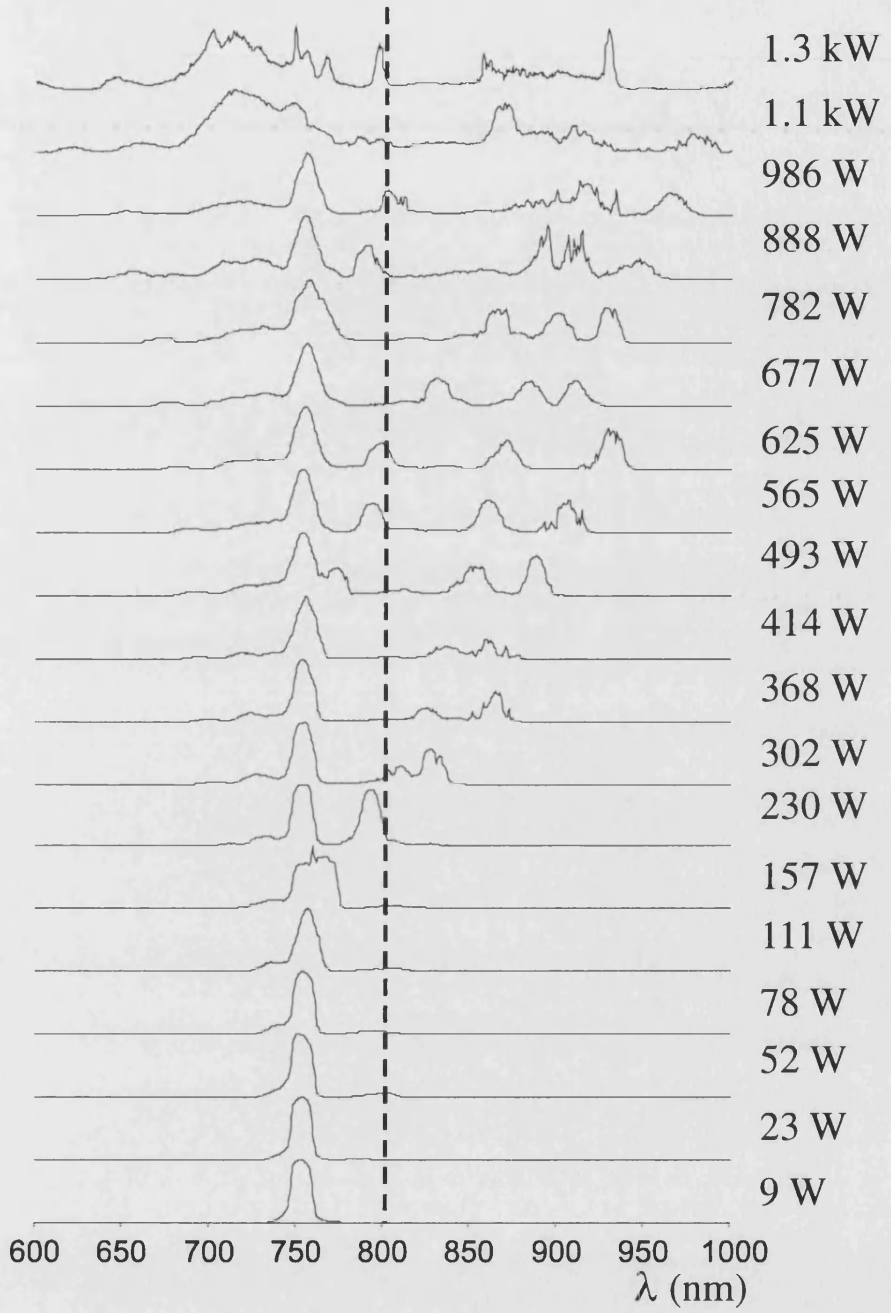

Figure 9 Recorded spectra at a pump wavelength of 753 nm for different peak powers coming out of the fibre. The dotted line indicates the zero dispersion wavelength at 806 nm.

Highly birefringent photonic crystal fibres

A. Ortigosa - Blanch, J.C. Knight, W.J. Wadsworth, J. Arriaga, B.J. Mangan, T.A. Birks and P.St.J. Russell
Optics & Photonics News (Optics in 2001) vol 12 (12), p17 (2001)

Highly Birefringent Photonic Crystal Fibers
Optics & Photonics News (Optics in 2001) vol.12 (12), p 17 (2001)

Highly Birefringent Photonic Crystal Fibers

A. Ortigosa-Blanch, J.C. Knight, W.J. Wadsworth, J. Arriaga, B.J. Mangan, T.A. Birks, and P. St. J. Russell

Optoelectronics Group, Department of Physics, University of Bath,
Claverton Down, Bath, BA2 7AY, UK

Conventional circularly symmetric optical fibers do not maintain the polarization state of the guided mode along their length. Although they are nominally isotropic, small twists, bends and other stresses impose unknown and uncontrolled birefringence on the fiber, so that the polarization of the fiber output is unpredictable. Highly birefringent or polarization-preserving fibers (in which strong birefringence is deliberately introduced during the fiber fabrication) are much more resilient to such environmental factors. The required birefringence can be achieved in two main ways. The shape of the refractive index profile defining the waveguide can be made non-circular (form or shape birefringence) or the material forming the fiber can itself be made birefringent by introducing stresses as in bow-tie or panda fibers [1][2].

Photonic crystal fiber (PCF) [3] is a pure silica optical fiber that has an array of microscopic air holes running along its length. In the PCF considered here, a single missing air hole within the array forms a region of raised refractive index that guides light by a form of total internal reflection. Our fibers are fabricated by stacking silica capillaries and rods as previously reported [3]. PCF can potentially be made very highly birefringent: the large index contrast enables high form birefringence, while the stack-and-draw fabrication process allows the formation of the required microstructure near the fiber core. By careful positioning of capillaries with the same external diameter but different wall thicknesses (leading to different air-hole sizes in the cladding of the final fiber and two-fold rotation symmetry - see Figure1), we have recently formed optical fibers with massive form birefringence [4].

One way of characterizing polarization-preserving fibers is to measure the beatlength, L_B, which corresponds to the length of fiber necessary for introducing a 2π phase change between the polarization eigenmodes. The shorter the beatlength, the better the fiber. We attempted two different known direct methods for measuring the beat length of the fiber but were unable to use them to characterize highly birefringent PCF [4]. We attribute this to the holey structure of the cladding, which acts as a strong optical and mechanical anisotropic medium. Therefore, we used an indirect approach. We launched light from a tunable diode laser (polarized at 45° to the principal axes) into a fixed length L of fiber, and monitored the output polarization state as a function of wavelength. Using the experimental results and a theoretical model [4], a value of $L_B = 0.42 \pm 0.04$ mm and a modal birefringence $|n_x - n_y| = 3.7 \times 10^{-3}$ was found. At the same time, the agreement in between the model and the experimental results showed that the most important contribution to the birefringence was form birefringence.

In conclusion, we have developed a photonic crystal fiber with a very high modal birefringence and a beat length of 0.4 mm at 1540 nm. We have also shown that the unusual optical properties of the PCF cladding are accompanied by unique mechanical properties, making it difficult to access light propagating down the core.

References

1. R. B. Dyott, *Elliptical Fiber Waveguides* (Artech House, Boston, London, 1995).
2. D. N. Payne, A. J. Barlow, and J. J. Ramskov Hansen, "Development of low- and high-birefringence optical fibers," J. Quantum Electron., **QE-18**, 477-88 (1982)
3. J. C. Knight, T. A. Birks, P. St. J. Russell, and D. M. Atkin, "All-silica sigle-mode optical fiber with photonic crystal cladding," Opt. Lett. **21**, 1547-9 (1996); errata **22,** 484 (1997).
4. A. Ortigosa-Blanch, J.C. Knight, W.J. Wadsworth, J. Arriaga, B.J. Mangan, T.A. Birks, and P. St. J. Russell, "Highly birefringent photonic crystal fibers," Opt. Lett. **25**, 1325-7 (2000)

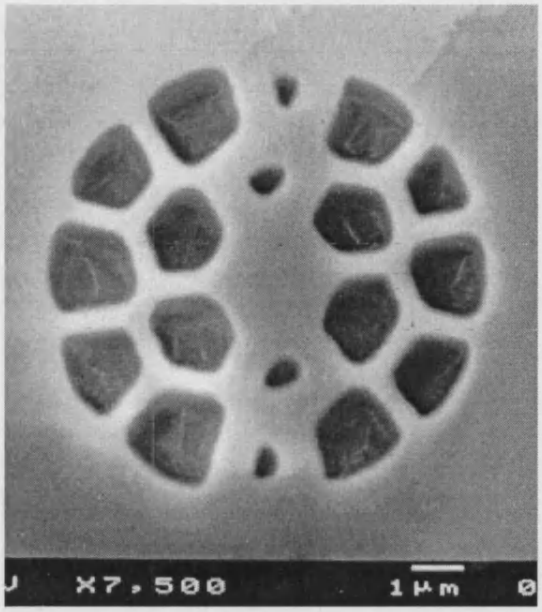

Figure 1. Scanning electron micrograph showing detail of the cross-section of the core region of the fiber used in the experiment.

Structural rocking filters in highly birefringent photonic crystal fiber

G. Kakarantzas, A. Ortigosa-Blanch, T. A. Birks, P.St.J. Russell, L.Farr, F. Couny and B.J. Mangan

Optics Letters (In press)

Structural rocking filters in highly birefringent photonic crystal fiber
Optics Letters (In press)

Structural Rocking Filters in Highly Birefringent Photonic Crystal Fiber

G. Kakarantzas, A. Ortigosa-Blanch, T. A. Birks and P.St.J. Russell
Optoelectronics Group, Department of Physics
University of Bath, Claverton Down
Bath, BA2 7AY, United Kingdom.
Email: G.Kakarantzas@bath.ac.uk

L.Farr, F. Couny and B.J. Mangan
Blaze Photonics Ltd, University of Bath, Claverton Down
Bath, BA2 7AY, United Kingdom.

Abstract
In this letter we report the first example of efficient rocking filter formation in polarisation maintaining photonic crystal fiber. Very high coupling efficiencies (down to –23.5 dB suppression of the input polarisation) and loss <0,02 dB were achieved for lengths as short as 11 mm. Prepared using periodic mechanical twisting and heating using a scanned CO_2 laser beam, the filters are highly compact and they are expected to be temperature stable.

Great scientific and technological interest has recently been drawn to a new type of optical fiber: photonic crystal fiber (PCF) [1]. In contrast to conventional fibers, PCF is made by using just a single material, for example fused silica, and has a regular pattern of tiny air holes running along its length. When an air hole is replaced with solid glass, light can be guided by total internal reflection. The air holes have the effect of reducing the refractive index of the cladding region relative to the core. Confinement occurs because the encircling air holes act as a "mode sieve" blocking the fundamental mode whilst allowing higher-order modes with shorter effective transverse wavelengths to escape into the cladding. As a result, the guiding properties of the fiber are governed primarily by the size, shape and pitch of the air holes, and there is a certain air-filling fraction below which the fiber has no cut-off wavelength and is therefore endlessly single mode [2]. PCF can also be made highly birefringent: The large index contrast facilitates high form birefringence, and the stack-and-draw fabrication process permits the formation of the required microstructure near the fiber core. The realization of a highly birefringent monomode PCF has already been reported [3].

An optical fiber rocking filter is a type of long period grating that rotates the polarisation state of a linearly polarised optical field launched along one of the principal axes of a birefringent fiber. This is achieved by oscillating the principal axes along the fiber through a small rocking angle. The periodic rotation can be simply a mechanical twist of the fiber [4] or a periodic exposure of the fiber's photosensitive core to UV light [5], [6]. If the rocking period equals the polarisation beatlength, resonant coupling between polarisation states is possible. Because the beat length is wavelength dependent, this

generally only happens around a resonant wavelength.

Here, we demonstrate the first example of a rocking filter in a highly birefringent PCF with extinction ratio as high as –23.5dB and insertion loss less than 0.02 dB. We used a technique similar to the one previously reported for long-period gratings [7]. Permanent twists in the fiber's principal axes could be produced by twisting the fibre mechanically and then annealing out the twist by heating at one point in a CO_2 laser beam.

The fiber was fabricated at Blaze Photonics Ltd. by stacking an array of silica capillaries and rods, as previously reported [1]. Anisotropy was introduced into the fiber by careful positioning of capillaries with the same external diameter but different wall thicknesses, leading to different air-hole sizes in the cladding of the final fiber and twofold rotational symmetry [3]. A solid silica jacket was added to increase the diameter and the strength of the fiber. A scanning-electron micrograph of this is shown in Figure 1.

The fiber had a hole pitch (centre-to-centre distance between the holes) of Λ_p=2.23 μm and hole diameters of d_1=1.15 μm for the small holes and d_2=2.15 μm for the large ones. The external fiber diameter was 125μm. The fiber is highly birefringent. The beatlength at λ=1550nm was directly measured [8] to be L_B~600 μm, which gives a birefringence of B~0.00258. Figure 2 shows a schematic diagram of the experimental set up. The fiber was fixed to two in-line clamps with a 2 cm gap between them. One of the clamps rested on the arm of a rotational motor that could oscillate through a fixed angle with a constant speed at a given frequency. The resulting twist is introduced at one point along the fiber using the heat generated from a CO_2 laser beam focused onto the fiber with a 300mm focal length lens. A complete grating is formed by sweeping the beam along the fiber. It is necessary that the temperature and the dwell time of the hot spot are sufficiently high to introduce a significant deformational twist, but not high enough to collapse the holes of the PCF. This was achieved using sweep rates faster than the hole collapse relaxation time.

In all the experiments the mirror was scanned at a speed of 6 mm/s and the rocking filters were fabricated with a single scan. A complete filter could be made in less than 2 seconds. For a given rocking angle, the twist period can be defined by two parameters: the sweep rate of the laser beam and the rocking frequency of the motor. When the twist period is set, the number of periods can easily be determined by varying the sweep length of the laser beam. The wavelength of maximum conversion can be tuned by simply increasing or decreasing the rotation speed of the motor, so that there are more or fewer periods per unit length of fiber and hence shorter or longer twist periods respectively.

The transmission spectra of the rocking filters were measured by launching polarized light from a broadband LED source along one of the birefringent axes of the fiber. After passing through a second polariser the signal was monitored with an optical spectrum analyzer. Figure 3a shows the transmission spectrum from a rocking filter with 25 periods each with a length of 560μm. The resonance wavelength is 1515 nm, the bandwidth at

FWHM is 50 nm and the measured peak conversion efficiency was or 99.5%, representing –23.5 dB extinction. The loss of <0.02 dB was typical of filters made in this way. There was enough deformational twist generated by the process to be seen by visual inspection of the fiber from which the actual twist period could be directly measured. The drive rocking angle amplitude was set by the rotation motor to 5.6°, but not all of this rotation is taken by the fiber. The rocking angle in radians required for 100% conversion can be determined [6] by the relation $\theta = \pi/4N$ where N is the number of rocking periods. Thus, for the rocking filter of Figure 3, the effective twist angle is 1.6°.

Utilising coupled mode theory [9], the transfer of power between two polarisation eigenmodes modes by a periodic perturbation may be analysed. When only one polarisation mode is excited at the start of the interaction region, the fraction of power coupled to the other mode is given by

$$P(z) = (\kappa z)^2 \mathrm{sinc}^2\left\{z\sqrt{\kappa^2 + \delta^2}\right\} \tag{1}$$

where z is the interaction length, κ is the coupling constant and $2\delta=\Delta\beta$ is the detuning parameter of the grating and it is given by

$$\Delta\beta = \beta_x - \beta_y - \frac{2\pi}{\Lambda} \tag{2}$$

β_x and β_y are the propagation constants of the two polarisation eigenmodes and Λ is the perturbation length. Complete power transfer can only occur when $\Delta\beta=0$. This is the longitudinal phase matching condition and is equivalent to matching the spatial period of the perturbation Λ to the beatlength L_b between the two polarisation eigenmodes. At this point, the input polarisation is rotated by $\pi/2$, from which it follows that

$$\kappa L = \pi/2 \tag{3}$$

where L is the length at which maximum conversion occurs. Figure 3b (dot circles) is the measured spectrum of conversion efficiency, and the solid line is the spectrum calculated from Eq. (1), (2) and (3). There is excellent agreement between the experimental and calculated results, with no fitting parameters needed to be adjusted other than the determination of the effective twist angle.

It is evident from the above analysis that the bandwidth for maximum conversion is directly related to the number of periods (or the total length) and the angle of rotation. As a result, broader bandwidths can be obtained using higher twist angles and shorter total lengths. Figure 4 shows the percent power conversion to the orthogonal polarisation versus wavelength for a rocking filter with an effective angle of 3.7° and 12 twist periods (the total device length was ~6.7 mm). This was achieved by increasing the drive amplitude of the rotational motor to 8.5°. The bandwidth of the maximum conversion increases to 98 nm, almost double that from figure 3.

In conclusion, we report for the first time the fabrication of rocking filters in non-

photosensitive highly birefringent PCF. Very good coupling efficiencies up to 99.5% and low loss were achieved for lengths as short as 11 mm. Note, the length of all the previous reported rocking filters was in the range of several cm. This is, to our knowledge, the shortest rocking filter ever reported. The method combines the high birefringence of the PCF which gives sub-millimetre beatlengths, with a new and highly versatile fabrication method using periodic mechanical twisting of the fiber and heating by a scanning CO_2 laser beam. This may lead to a substantial improvement in the performance of optical fiber sensor devices based on rocking filters [10] where the length plays an important role. We also expect the purely mechanical nature of the perturbation to make the filter very insensitive to temperature variations.

This study is supported by the U.K. Engineering and Physical Sciences Research Council.

References

1. J.C. Knight, T.A. Birks, P.St.J. Russell, and D.M. Atkin, "All-silica optical fiber with photonic crystal cladding" Opt. Lett. 21, 1547, (1996); errata 22, 484 (1997).
2. T.A. Birks, J.C. Knight and P.St.J. Russell, "Endlessly single-mode photonic crystal fiber" Opt. Lett. 22, 961, (1997).
3. A. Ortigosa-Blanch, J.C. Knight, W.J. Wadsworth, J. Arriaga, B.J. Mangan, T.A. Birks and P.St.J. Russell, "Highly birefringent photonic crystal fibers" Opt. Lett. 25, 1325, (2000).
4. R.H. Stolen, A. Ashkin, W. Pleibel, and J.M. Dziedzic, "In-line fiber-polarization-rocking rotator and filter" Opt. Lett. 9, 300, (1984).
5. P.St.J. Russell, and D.P. Hand "Rocking filter formation in photosensitive high birefringent optical fibers" Electronics. Lett. 26, 1846, (1990).
6. D.C. Psaila, F. Ouellette, C. Martijn de Sterke, "Characterization of photo induced birefringence change in optical fiber rocking filters" Appl. Phys. Lett. 68, 900, (1996).
7. G. Kakarantzas, T.A. Birks, and P.St.J. Russell, "Structural long period gratings in photonic crystal fibers", Opt. Lett. 27, 1013, (2002).
8. R.B. Dyott, " Elliptical Fiber Waveguides" (Artech House, Boston), (1995).
9. A.Yariv and P.Yeh, "Optical waves in crystals"(John Wiley, New York), (1984).
10. S.E Kanellopoulos, V.A. Handerek and A.J. Rogers "Compact Mach-Zehnder fiber interferometer incorporating photoinduced gratings in elliptical-core fibers" Opt. Lett. 18, 1013, (1993).

Figure Captions

Figure 1. Scanning-electron micrograph, showing the cross section of the fiber used in the experiment.

Figure 2. Schematic diagram of the experimental set up used to fabricate and characterise the rocking filters. L: CO_2 laser, M: Mirror, MA: Motorised Attenuator, LN: Lens, SM: Scanning Mirror, FM: Fiber Mount, RM: Rotational Motor, P: Polariser, A: Analyser, BLS: Broadband LED Source, OSA: Optical Spectrum Analyser.

Figure 3. Polarisation coupling spectra for a rocking filter with 1.6° twist angle and 25 coupling steps (periods) (a) in the original state of polarisation, (b) in the orthogonal state of polarisation: Experiment (circles), Theory (solid line).

Figure 4. Polarisation coupling spectra for a rocking filter with 3.7° twist angle and 12 coupling steps (periods).

Structural rocking filters in highly birefringent photonic crystal fiber
Optics Letters (In press)

Figure 1

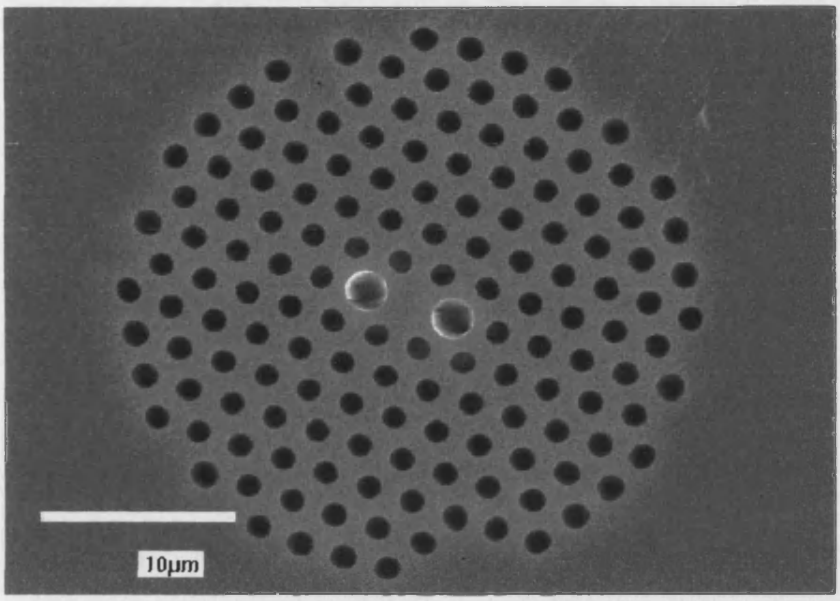

Figure 2

Structural rocking filters in highly birefringent photonic crystal fiber
Optics Letters (In press)

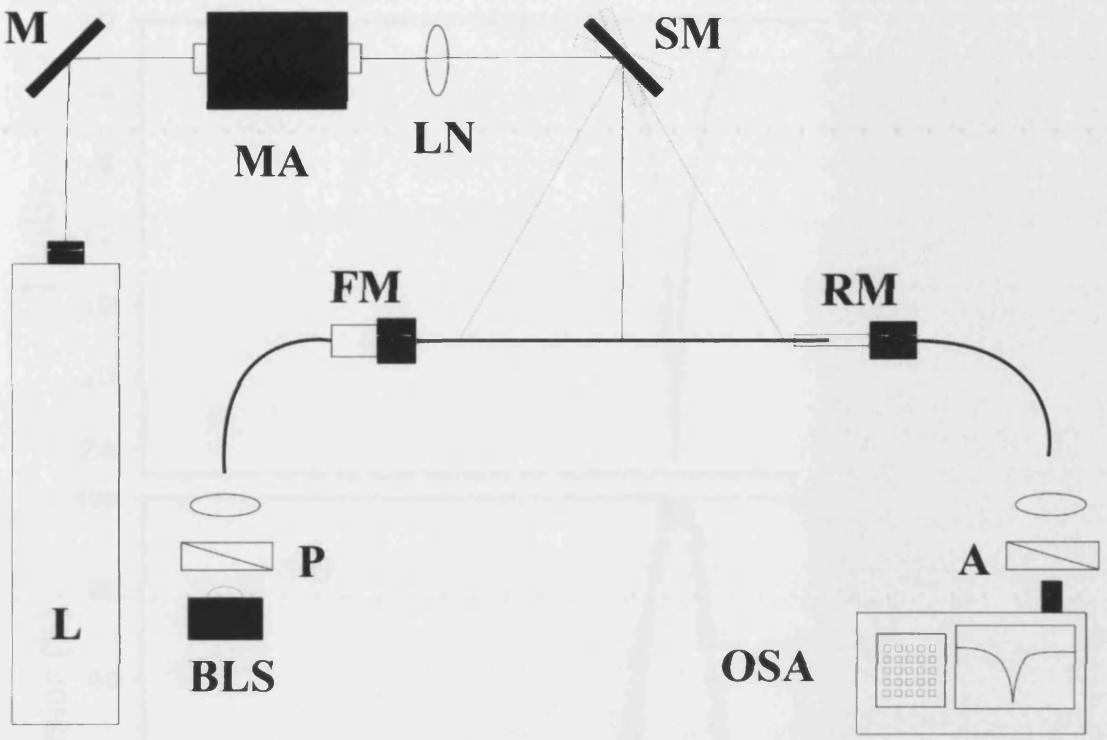

Figure 3

Structural rocking filters in highly birefringent photonic crystal fiber
Optics Letters (In press)

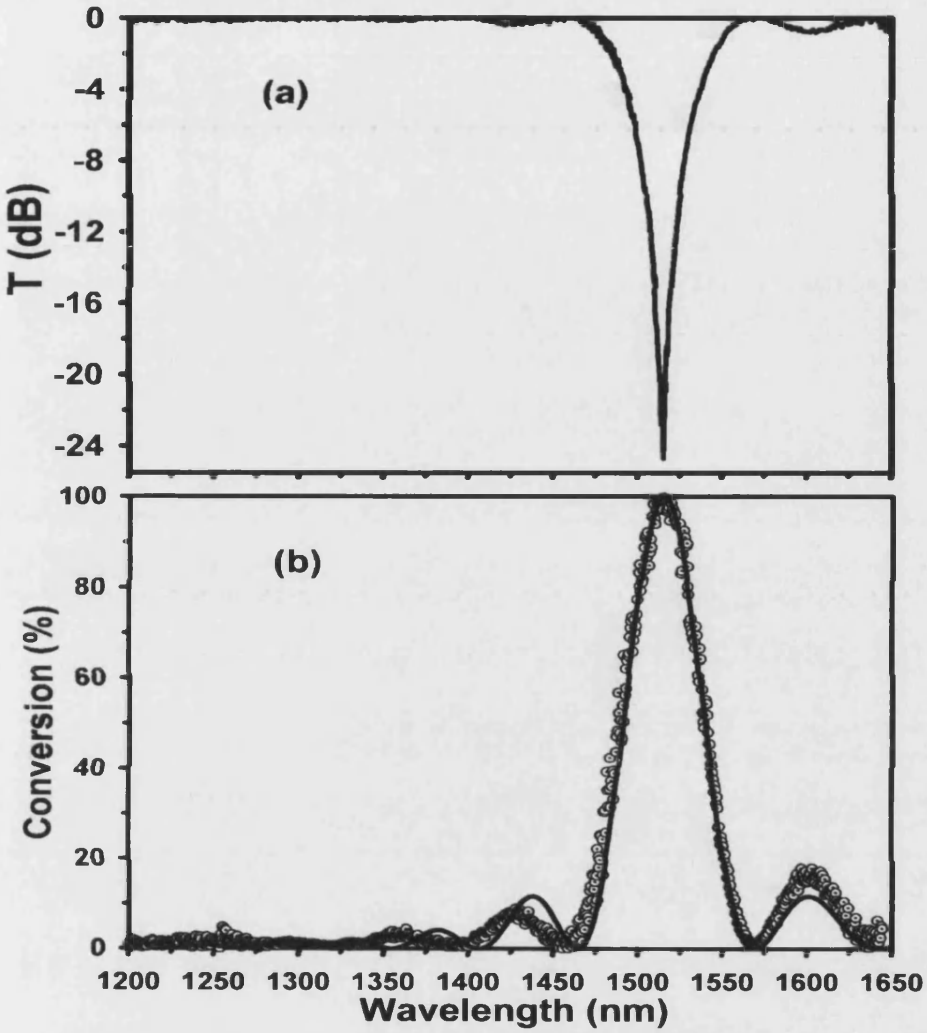

Figure 4

Structural rocking filters in highly birefringent photonic crystal fiber
Optics Letters (In press)